INFORMATION TO USERS

This manuscript has been reproduced from the microfilm master. UMI films the text directly from the original or copy submitted. Thus, some thesis and dissertation copies are in typewriter face, while others may be from any type of computer printer.

The quality of this reproduction is dependent upon the quality of the copy submitted. Broken or indistinct print, colored or poor quality illustrations and photographs, print bleedthrough, substandard margins, and improper alignment can adversely affect reproduction.

In the unlikely event that the author did not send UMI a complete manuscript and there are missing pages, these will be noted. Also, if unauthorized copyright material had to be removed, a note will indicate the deletion.

Oversize materials (e.g., maps, drawings, charts) are reproduced by sectioning the original, beginning at the upper left-hand corner and continuing from left to right in equal sections with small overlaps.

Photographs included in the original manuscript have been reproduced xerographically in this copy. Higher quality 6" x 9" black and white photographic prints are available for any photographs or illustrations appearing in this copy for an additional charge. Contact UMI directly to order.

ProQuest Information and Learning
300 North Zeeb Road, Ann Arbor, MI 48106-1346 USA
800-521-0600

UMI®

Improving the Refrigeration and Gas Liquefaction Performance of Gifford-McMahon and Active Magnetic Regenerative Cryocoolers: A Study of Flow Maldistribution, Unbalance, and Asymmetry

by

Ian Gregory Spearing
B.A.Sc., University of Toronto, 1990
M.A.Sc., University of Victoria, 1995

A Dissertation Submitted in Partial Fulfilment of the
Requirements for the Degree of

DOCTOR OF PHILOSOPHY

in the Department of Mechanical Engineering

We accept this dissertation as conforming
to the required standard

Dr. J.A. Barclay, Supervisor (Department of Mechanical Engineering)

Dr. N. Djilali, Member (Department of Mechanical Engineering)

Dr. S. Dost, Member (Department of Mechanical Engineering)

Dr. J.D. Jones, Outside Member (Simon Fraser University)

Dr. T. Bose, External Examiner (Université du Québec à Trois-Rivières)

Supervisor: Dr. John A. Barclay

Abstract

Cost-effective liquefaction of gases at cryogenic temperatures requires a combined approach of designing efficient refrigeration cycles to generate cooling capacity and designing efficient liquefaction processes to utilize that capacity. This dissertation addresses both approaches for improvement of the liquefaction process. Magnetic refrigeration employing the magnetocaloric effect of ferromagnetic materials has been identified as potentially more efficient and cost-effective than conventional refrigeration systems. One magnetic cycle that shows promise for efficiently achieving cooling over large temperature spans is active magnetic regenerative refrigeration (AMRR). In this cycle the magnetic material serves the dual functions of work input and thermal regeneration, however the operation is complex with coupled fluid, thermal, and magnetic phenomena and a clearer understanding of the regenerative operation is required. Models to elucidate the flow characteristics of the regenerative heat exchangers of rotary AMRR and Gifford-McMahon (GM) systems using a commercially available computational fluid dynamics (CFD) software package are described. Theoretical results are presented to qualify and quantify the effect of maldistributed flow within regenerators. Experimental results of an improved regenerator for the GM system based on the CFD flow simulations are presented. Efforts to develop an improved AMRR thermal model using the commercial package are also described.

The second approach for the design of efficient liquefiers addresses a drawback of the usual embodiment of the AMRR cycle, namely, the provision of cooling at a single temperature which necessitates that cryogenic designs have multiple stages providing cooling over a range of discrete temperatures for an efficient liquefaction process. Use of multiple stages leads to increased expense and complexity. A simple, inexpensive plumbing change of the flow through the regenerator of a single-stage device can significantly increase the overall liquefaction capacity compared to the usual flow configuration making additional staging unnecessary. This dissertation describes the alternative flow arrangement, known variously as "bypass flow," "permanent flow," or "DC flow," which is suitable for all passive and active regenerative refrigeration cycles used as liquefiers. Theoretical results showing increased liquefaction capacity when bypass flow is employed are given for active magnetic regenerative and Gifford-McMahon systems. Experimental results are presented for a single-stage GM refrigerator modified for bypass flow which demonstrates increased liquefaction capacity.

Examiners:

Dr. J.A. Barclay, Supervisor (Department of Mechanical Engineering)

Dr. N. Djilali, Member (Department of Mechanical Engineering)

Dr. S. Dost, Member (Department of Mechanical Engineering)

Dr. J.D. Jones, Outside Member (Simon Fraser University)

Dr. T. Bose, External Examiner (Université du Québec à Trois-Rivières)

Table of Contents

List of Tables

List of Figures

Nomenclature

Symbols

A	regenerator matrix surface area [m^2]
C	fluid heat capacity [$J\cdot kg^{-1}\cdot K^{-1}$]
C_f	fluid heat capacity [$J\cdot kg^{-1}\cdot K^{-1}$]
C_H	solid heat capacity at constant field [$J\cdot kg^{-1}\cdot K^{-1}$]
C_s	solid heat capacity [$J\cdot kg^{-1}\cdot K^{-1}$]
C_v	dimensionless parameter, metering valve flow coefficient
d_s	particle diameter [m]
D	regenerator bed diameter [m]
D_p	particle diameter [m]
f	dimensionless parameter, friction factor
$f_{\Delta T}$	dimensionless parameter, gas expansion temperature change proportionality constant
G	mass flux per unit free flow area [$kg\cdot s^{-1}\cdot m^{-2}$]
h	bulk heat transfer coefficient [$W\cdot m^{-2}\cdot K^{-1}$]
h	fluid enthalpy [$J\cdot kg^{-1}$]
h_R	dimensionless parameter, ratio of fluid latent heat to sensible heat
H	applied magnetic field [$A\cdot m^{-1}$]
H_f	fluid enthalpy [$J\cdot kg^{-1}$]
I_{ε}	dimensionless parameter, regenerator ineffectiveness
k_f	fluid thermal conductivity [$W\cdot m^{-1}\cdot K^{-1}$]
L	regenerator bed length [m]

M	• material magnetization [$A\cdot m^{-1}$]
$\dot{m}$	• fluid mass flow rate [$kg\cdot s^{-1}$]
M_s	• regenerator matrix mass [kg]
Nu	• dimensionless parameter, Nusselt number
P	• regenerator blow period (Chapter 1 only) [s]
P	• pressure [$N\cdot m^{-2}$]
Pr	• dimensionless parameter, Prandtl number
PR_{CH}	• dimensionless parameter, cold head pressure ratio
$\dot{Q}$	• heat absorption/rejection rate [W]
$\bar{q}$	• heat flux vector [$W\cdot m^{-2}$]
R	• radius [m]
R	• electrical resistance [ohm]
Re	• dimensionless parameter, Reynold's number
$\Re$	• gas constant [$J\cdot kg^{-1}\cdot K^{-1}$]
s	• entropy [$J\cdot kg^{-1}\cdot K^{-1}$]
S_E	• energy equation volumetric source term [$W\cdot m^{-3}$]
S_{ui}	• momentum equation volumetric source term [$kg\cdot m^{-2}\cdot s^{-2}$]
S_C	• discretization equation source term constant coefficient [units vary]
S_P	• discretization equation source term active coefficient [units vary]
t	• time [s]
T_C	• cold (reservoir, inlet) temperature [K]
$T_{C,\beta}$	• minimum cold temperature with unbalance [K]
T_H	• hot (reservoir, inlet) temperature [K]
T_f	• fluid temperature [K]
$\overset{\bullet}{T}_f$	• dimensionless fluid temperature
T_s	• solid temperature [K]
$\overset{\bullet}{T}_s$	• dimensionless solid temperature
$\bar{T}_{f,o}$	• average fluid outlet temperature [K]
u	• component of velocity in the x-coordinate direction [$m\cdot s^{-1}$]

u_i	• component of velocity in the i^{th}-coordinate direction [$m \cdot s^{-1}$]
U	• dimensionless parameter, utilization factor
v	• component of velocity in the y-coordinate direction [$m \cdot s^{-1}$]
$\vec{v}$	• velocity vector [$m \cdot s^{-1}$]
x	• distance [m]
V_f	• volume of fluid entrained within a regenerator [m^3]
V_S	• sensor voltage [V]
$\dot{W}$	• work rate [W]

Greek

α	• dimensionless parameter, material porosity
β	• dimensionless parameter, regenerator unbalance factor
γ	• dimensionless parameter, ratio of gas specific heats
δ	• infinitesimal change
Δ	• difference
ΔT_{ad}	• adiabatic temperature change [K]
$\Delta T_{R,net}$	• dimensionless constant, net expansion temperature change proportionality factor
ϵ_T	• error in indicated temperature [K]
ε	• dimensionless parameter, heat exchanger effectiveness
η_C	• dimensionless parameter, refrigerator coefficient of performance
η_{CGR}	• dimensionless parameter, cold gas refrigerator coefficient of performance
η_{th}	• dimensionless parameter, regenerator thermal ratio
$\eta_{th,\beta}$	• dimensionless parameter, regenerator thermal ratio with unbalance
$\eta_{T_{span}}$	• dimensionless parameter, temperature span efficiency
θ	• angular position [radian]
Λ	• dimensionless parameter, regenerator reduced length
μ	• fluid viscosity [$kg \cdot m^{-1} \cdot s^{-1}$]
μ_0	• constant, permeability of free space [$4\pi \times 10^{-7}$ $H \cdot m^{-1}$]
ν_i	• initial condition specific gas volume [$m^3 \cdot kg^{-1}$]
ξ	• dimensionless parameter, regenerator dimensionless distance

Π	• dimensionless parameter, regenerator reduced period
ρ_f	• fluid density [$kg \cdot m^{-3}$]
ρ_s	• solid density [$kg \cdot m^{-3}$]
σ	• volumetric energy generation term [$W \cdot m^{-3}$]
τ	• dimensionless parameter, regenerator dimensionless time
τ_{GM}	• Gifford-McMahon cycle period
τ_{ij}	• viscous stress tensor [$J \cdot m^{-3}$]
ϕ	• an independent variable
ϕ	• angular width (of a rotary regenerator duct region) [radian]
ω	• angular rotation rate [$radian \cdot s^{-1}$]

Subscripts

1	• initial, or at condition 1
2	• final, or at condition 2
ad	• adiabatic
B	• bypass
B,EQ	• thermodynamically equivalent to the bypass value
C	• cold
c_1	• (heat exchanger) cold inlet stream
c_2	• (heat exchanger) cold oulet stream
CH	• cold head
CHT	• conjugate heat transfer component
cold	• during the cold blow
comp	• compressor
exp	• expander
f	• final state
f	• fluid
f	• fluid saturated liquid state
f,o	• fluid outlet
fg	• change of state between saturated liquid and vapour states
g	• fluid vapour state

H	• hot
h_1	• (heat exchanger) hot inlet stream
h_2	• (heat exchanger) hot oulet stream
har	• harmonic mean value
hot	• during the hot blow
i	• ideal
i	• initial state
i	• inner
i	• coordinate direction index
j	• coordinate direction index
mal	• under maldistributed flow
min	• minimum value
o	• outer
P	• for the process gas
R	• for the return line
$\dot{Q}_{EQ}$	• for the thermodynamically equivalent cooling load
R:L	• ideal refrigerator relative to ideal liquefier
s	• solid
sat	• saturated fluid state
sf	• between solid and fluid
T	• at temperature T
uniform	• under uniform flow
ω	• advection component

Superscripts

$'$	• (single prime) hot blow
$''$	• (double prime) cold blow
$''$	• (double prime) per unit area (Chapter 5 only)
$'''$	• (triple prime) per unit volume

Overstrike

¯	(overbar) average
˙	(overdot) rate
*	(star) dimensionless
→	(arrow) vector

Acronyms

AC	Alternating Current
AMR	Active Magnetic Regenerator
AMRR	Active Magnetic Regenerative Refrigerator
AWG	American Wire Gauge
CGR	Cold Gas Refrigerator
CHT	Conjugate Heat Transfer
CNG	Compressed Natural Gas
COP	Coefficient of Performance
DC	Direct Current
FOM	Figure of Merit
GM	Gifford-McMahon
ILU	Incomplete Lower-Upper
LNG	Liquefied Natural Gas
LVDT	Linear Voltage Displacement Transducer
PRT	Platinum Resistance Thermometer
PV	Pressure-Volume
RMS	Root Mean Squared
SC	Superconducting

Acknowledgements

My enduring stay within the Cryofuel Systems Group at the University of Victoria, completing first my Master's degree and herein my Doctorate, was filled with many challenges and rewards. Over the last 8 ½ years I have learned a great deal, and I would like to express my thanks to those who provided innumerable examples for academic and personal betterment. In particular, I would like to express my gratitude to:

- My Supervisor, Dr. John Barclay, for patiently awaiting the final draft of my dissertation as I toiled away at home, missing the expected deadlines and disregarding the encouragement to complete expeditiously.

- Research Associate, Dr. Jeff Hall, who went on to bigger and better things during my early years as a Doctoral student. His generous spirit and down-to-earth sensibility found no match.

- Research Associate, Dr. Edgar Nelson, who went on to bigger and better things during my later years as a Doctoral student. His advice and insight were instrumental in understanding "the big picture."

- Fellow graduate student, Andrew Rowe, who gave bountiful suggestions and advice and who yet toils through many of the same academic challenges I faced.

- Finally, and most of all, my lovely wife, Moira, and our beautiful daughter, Madeleine, who both bring smiles to my face and joy to my life with each moment we spend together. The diagrams were still pesky, but the mornings are no longer cranky. I couldn't have done it without you two.

I would like to acknowledge Natural Sciences and Engineering Research Council of Canada (NSERC), and Centra Gas, Inc., a division of Westcoast Energy, for their support of projects of which this work forms a part. I am also grateful of the generous Fellowship awarded to me by the University of Victoria.

Chapter 1

Introduction

1.1 Objective

This dissertation was performed within the Cryofuel Systems Group at the University of Victoria. Broadly, the aim of Cryofuel Systems and its original founding group, the Institute for Integrated Energy Systems (IES*Vic*), can be stated as the development of energy systems that simultaneously:

- Offer a foundation for economic growth and industrial diversification;
- Cause minimal environmental intrusion, and especially, reduce climate destabilizing emissions, and;
- Provide flexibility and resilience in response to technical, geopolitical, and environmental change.

Towards these goals, Cryofuel Systems is currently engaged in the development of systems for gas purification, cryogenic fuel handling, and advanced refrigeration and liquefaction, with a major emphasis on the development of magnetic refrigeration for the liquefaction of natural gas for vehicular transportation markets.

Aside from one-shot cooling systems used in physics experiments, magnetic refrigeration, based on the magnetic-field-induced temperature changes, or *magnetocaloric effect*, of certain materials, is an immature technology. Development of solutions to practical implementation details, as well as a development of a fundamental theoretical understanding of the active magnetic regenerative refrigerator and the requirements of the gas liquefaction process are required before cost-effective systems can be built. Towards these development requirements, the work embodied in this dissertation had the following objective:

> *The objective of this study was to advance the understanding of the fluid mechanics and thermodynamics describing the processes within passive and active magnetic regenerative refrigerators through theoretical derivation, modelling, and simulation of the regenerative heat exchangers, and to suggest, build, test, and prove practical improvements to these systems by direct experiment.*

The scope of the objective was limited to three specific goals:

1) Determine the extent and impact of flow maldistribution within the 1st-stage regenerator of a commercial Gifford-McMahon refrigerator and develop an improved design;
2) Extend the results of existing thermal models and develop an improved thermo-fluid model of an active magnetic regenerative refrigerator in the context of gas liquefaction, and;
3) Verify by experimentation key results of the above two goals.

A study of the extent and impact of flow maldistribution within the 1st-stage regenerator of a commercial GM refrigerator was carried out by:

1) extension of existing theoretical models of the thermal performance of maldistributed flow regenerators;
2) development of computational fluid mechanics simulations of the 3-dimensional flow patterns within a 1st-stage GM regenerator, for an existing commercial design and a novel design, and;
3) experimental comparison of the performance of the commercial design and the novel design under a range of typical operating conditions.

An extension of the existing thermal models for active magnetic regenerative refrigerators and experimental verification of key liquefier theoretical and simulation results was carried out by:

1) development of theoretical foundations for improved performance of regenerative cryocoolers in gas liquefaction applications;
2) study of the characteristics of magnetic regenerative systems under various operating conditions using existing theoretical thermal simulation computer models;
3) development of computational fluid mechanics simulations of the flow patterns within a 2-dimensional rotary regenerator model using commercially available software with additional user source code;
4) development of a new thermal simulation computer model in conjunction with the fluid mechanics simulations using commercially available software, custom modifications to that software, and additional user source code, and;
5) experimental verification of the theoretical foundations for improved performance of GM and AMR systems in gas liquefaction applications by implementation of the resultant liquefier design modifications to a GM system operating as a simulated gas liquefaction system.

1.2 Motivation

Rapid and convenient transportation has become a mainstay of our developed societies, using vehicles powered primarily by high carbon content fuels. Several researchers [1], [2], [3], [4], [5], [6] have identified economic, geo-political, and environmental benefits to a society that shifts its energy currencies to low carbon content fuels, such as natural gas (NG), and ultimately to carbon-free fuels, such as hydrogen (H_2). Natural gas, as provided by pipeline distribution systems, is composed primarily of methane, which has four atoms of hydrogen for each atom of carbon, the highest ratio of hydrogen to carbon of the hydrocarbon fuels. The exact composition of pipeline natural gas varies, but it has been measured to contain 82.2 - 97.8% methane, with ethane, nitrogen, carbon dioxide, heavier hydrocarbons, and other trace gases and odourants making up the remainder [7].

Recent efforts to introduce NG fuelled vehicles have been hampered, in part, by the limited range of these vehicles due primarily to the low volumetric storage capacity of compressed gas fuel storage tanks. Fuel storage, and hence vehicle range, can be increased by storing the fuel as a liquid rather than as a compressed gas. Liquefied natural gas (LNG) at atmospheric pressure has 2.6 times the volumetric energy density of compressed natural gas (CNG) at 3000 psig. At atmospheric pressure natural gas liquefies at 112 K, considerably below room temperature of 293 K. Liquids below 123 K are known as cryogens, and LNG can thus be termed a cryogenic fuel or *cryofuel*.

To supply LNG to a vehicular fuel market, a supply of natural gas and an inexpensive and efficient refrigeration system for liquefaction are required. Natural gas distribution systems exist in most major North American cities; however, current refrigeration systems in the LNG temperature range are expensive or inefficient, or both. New liquefaction technologies that are less expensive and more efficient are required to reduce the refuelling system cost component of LNG.

The Cryofuel Systems Group at the University of Victoria has identified active magnetic regenerative refrigeration (AMRR) as a viable technique to achieve refrigeration at high efficiencies and competitive capital expense compared to current technologies. A thorough understanding of the thermal and fluid processes within the regenerator is critical to designing and achieving optimal performance at the lowest possible cost for a regenerative magnetic refrigerator.

Refrigeration system improvements and capital cost reductions can additionally be achieved by improvements in any ancillary equipment. For the AMR liquefier proposed by Cryofuel Systems, this includes the regenerator within the Gifford-McMahon refrigerator that is employed for conduction cooling of the superconducting magnet systems required by the magnetic refrigerator. Within the scope of the complete liquefier system, this dissertation focuses on the role of regenerators and their operational impact on the overall liquefaction process under various design conditions. An understanding of the construction and thermal function of the regenerator provides the foundation for this work.

1.3 Regenerative Heat Exchangers

Regenerative heat exchangers, or *regenerators*, are compact heat exchangers in which heat is alternately stored and removed using a heat storage matrix. During the storage phase, commonly called the *hot blow*, hot gas is passed through and gives up its heat to the regenerator matrix. At the end of the hot blow period, the flow of hot gas stops and cold gas flow begins, typically in the opposite direction to the hot gas flow. During the *cold blow*, the cold gas picks up heat previously stored in the regenerator matrix. At the end of the cold blow period, the flow of cold gas stops and the next cycle of hot and cold blows begins.

Figure 1.1 shows a schematic diagram of a single fixed-bed regenerator under periodic hot and cold blow operation as described above. Valves are used to coordinate the hot blow and cold blow gas flow streams, here arbitrarily labelled as "waste" and "process" streams. Distinction of what constitutes a "process" stream or "waste" stream is entirely dependent on the regenerator application.

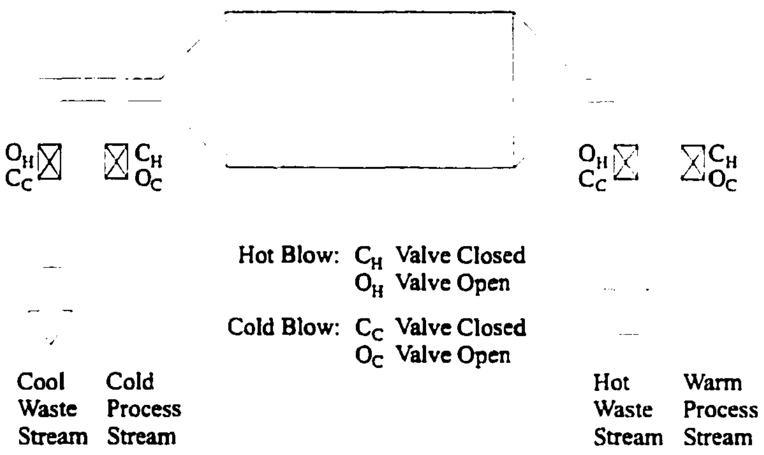

Figure 1.1 Schematic diagram of a fixed-bed counterflow regenerative heat exchanger.

Various modes of regenerator operation can be realized, but a pseudo-steady-state cyclic operation is commonly utilized. This is achieved after a number of repeated, fixed-period hot and cold blows where ultimately after one hot and one cold blow, the temperature at any one point in the matrix or fluid within the regenerator is identical to its value one full cycle earlier. Figure 1.2 shows the variation with time of the matrix temperature and the fluid temperature at some station within the regenerator of Figure 1.1 undergoing cyclic flow reversals after achieving pseudo-steady-state.

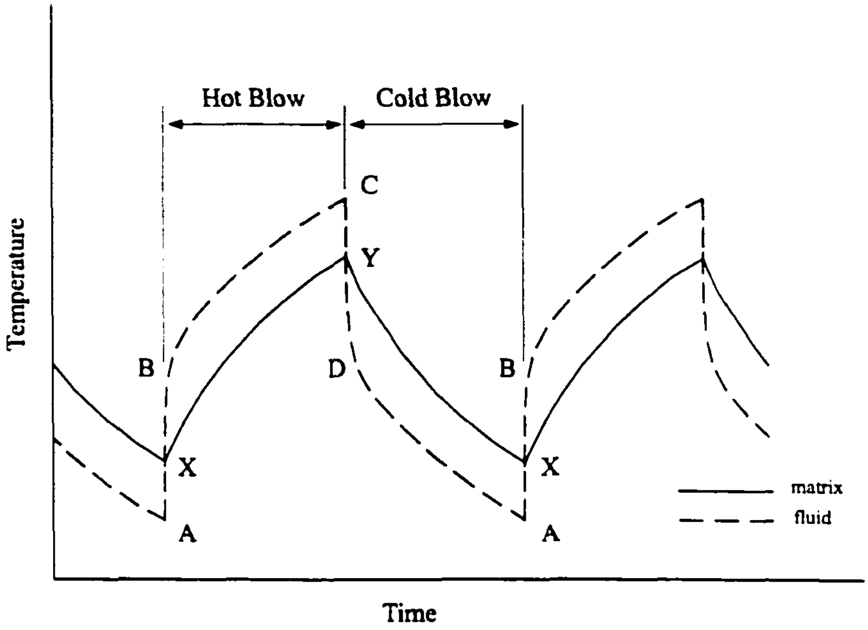

Figure 1.2 Temporal temperature variation of fluid and matrix in a thermal regenerator during hot and cold blows.

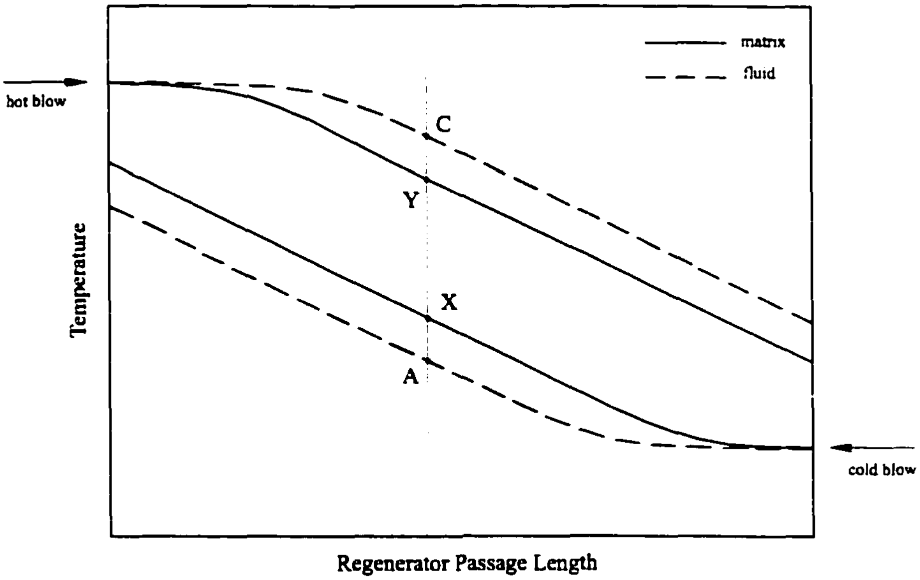

Figure 1.3 Spatial temperature variation of fluid and matrix in a thermal regenerator at the instants of flow reversal.

Figure 1.3 shows the spatial variation of the matrix temperature and fluid temperature at the instants of flow reversal. The upper curves represent the temperature of the fluid and matrix at the end of the hot blow and the start of the cold blow, while the lower curves represent the end of the cold blow and the start of the hot blow. Each station in the matrix, such as the position designated by the vertical line in Figure 1.3, fluctuates between these two sets of curves in a time-dependent manner similar to that shown in Figure 1.2.

1.4 The Ideal Regenerator

1.4.1 Ideal Thermal and Mechanical Properties

The ideal counterflow regenerator can be viewed as a black box device that accepts gas at T_H and cools it to T_C. After some period of time, the flow is reversed and gas enters at T_C and is instantly warmed to T_H. Regardless of the length of time taken for the blow period, gas only leaves at the constant temperature of T_C or T_H. The ideal regenerator is a perfect thermal insulator between the limits of T_H and T_C so that there is no heat leak longitudinally through the device.

The ideal regenerator is also described by its mechanical requirements. The regenerator is perfectly sound structurally to withstand any loads applied to it, including loads applied by the action of the gas flow through it, by external mechanical loading, by internal thermal stresses, or by internal loads from gravitational, magnetic, or electrical fields, for example. The ideal regenerator has no fluid entrained within it because it has zero void volume, and has zero pressure drop associated with the fluid flowing through it.

1.4.2 Implications of Regenerator Ideality

With these lofty design criteria and exotic materials, the designer might conclude that the ideal regenerator will be an expensive component. Fortunately, that is not the case, since the ideal regenerator would cost nothing to produce.

The ideal regenerator is impossible to achieve. To achieve zero pressure drop, the flow would have to be entirely frictionless. Achieving zero void volume would preclude the possibility of flow channels through the matrix in which the fluid would traverse. Achieving instant warming or cooling for a finite gas flow would require the heat transfer coefficient or heat transfer area to be infinite, or the heat capacity of the fluid to be zero. To achieve a constant outlet temperature would require the heat capacity of the matrix to be infinite (which then effectively precludes setting the necessary temperature gradient within the matrix) or the heat capacity of the fluid to be zero. To achieve perfect thermal insulation across the regenerator would require materials of zero thermal conductivity to be used in the construction.

1.5 Practical Regenerators

1.5.1 Practical Thermal and Mechanical Properties

Practical regenerators balance the various conflicting requirements of the ideal regenerator according to their application. Heat transfer and heat transfer area is maximized by use of fine geometries with very high specific areas, such as packed particle beds, parallel plates, perforated plates, wire screens, etched foils, packed wires, and hollow tubes.

The thermal mass of the regenerator matrix for a fixed-volume regenerator is maximized by selection of materials having high volumetric heat capacity. As the regenerator operation temperature dips below ~20-30 K, conventional regenerator materials such as phosphor-bronze, stainless steel, and lead lose their effectiveness as regenerator materials because of a rapid decline in their heat capacities. Figure 1.4 shows the heat capacities of these conventional materials as a function of temperature.

The decline in the heat capacity of conventional regenerator materials at low temperatures is particularly problematic because the heat transfer gas used at these low temperatures, namely helium, exhibits a rise in heat capacity. Figure 1.5 shows the pressure dependent heat capacity of helium at low temperature.

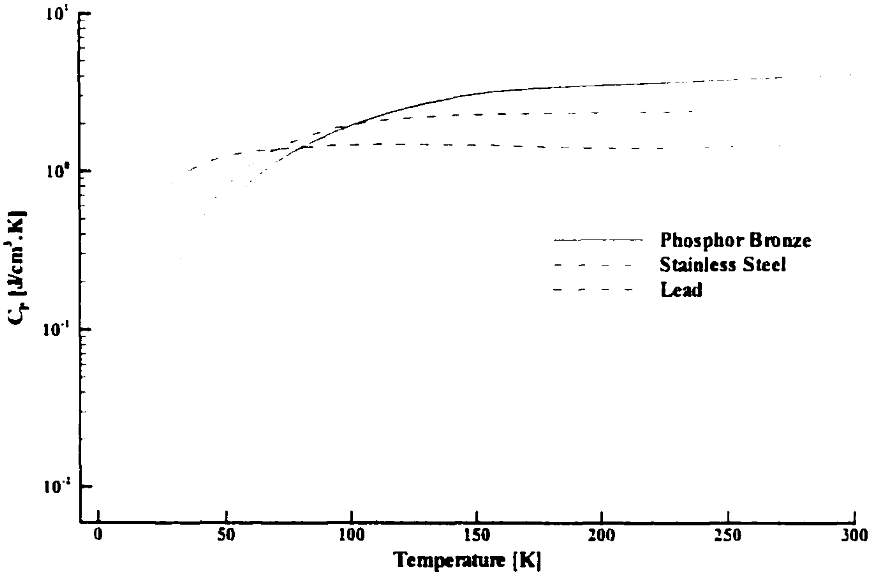

Figure 1.4 Volumetric heat capacity of phosphor-bronze, stainless steel, and lead as a function of temperature.

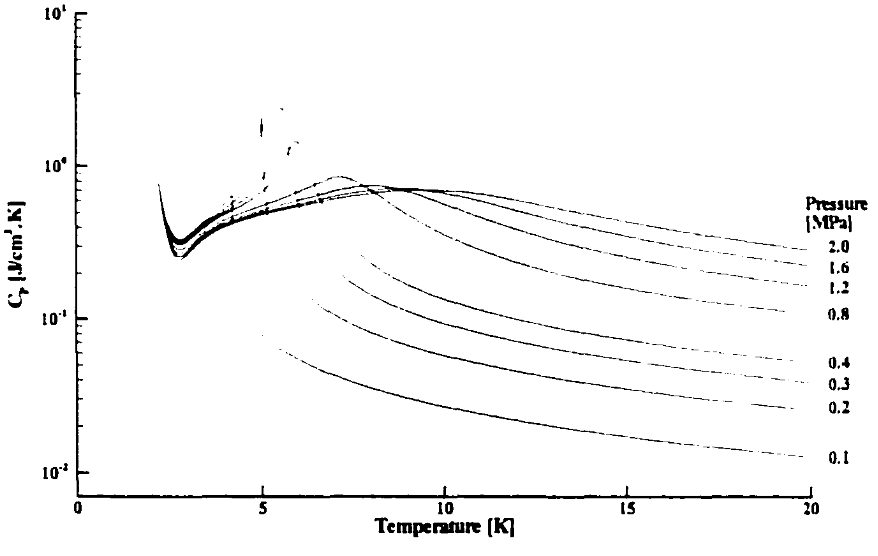

Figure 1.5 Volumetric heat capacity of helium as a function of pressure and temperature near the lambda point.

Nearly 25 years ago, Buschow *et al.* [8] pointed out the potential use of lanthanide materials as replacements to conventional regenerator materials. In the last decade, replacement of the conventional regenerator matrix material with rare-earth/transition metal compounds such as Er_3Ni, $ErNi_{0.9}Co_{0.1}$, $HoCu_2$, and elemental Nd, which exhibit a heat capacity spike at low temperatures due to magnetic ordering, has yielded improved regenerator performance [9,10]. In practice, many of these intermetallic compounds have proven brittle and can experience chipping from thermal and fluid stresses. Chipping and abrasion can lead to a fine dust that clogs the flow channels of the bed, or worse, contaminates the heat transfer gas leading to failure of any associated compression equipment. Researchers have come up with some novel means to prevent these regenerator materials from slowly pulverizing during operation [11].

The porosity of a regenerator is primarily a function of the material geometry selected, with some options offering greater control of the final porosity, which can be used to find a balance between the thermal and pressure drop losses. Some geometries, such as packed particle beds, tend to provide essentially isotropic porosity, whereas others, such as parallel plates, can be considered to have zero porosity perpendicular to the plates.

Some porosity perpendicular to the fluid flow is desirable to allow the flow to redistribute itself evenly across the bed and to counteract the effects of flow channel dimensional variations or constrictions as well as inherent flow instabilities. If the heat transfer gas flowing through the regenerator has a temperature dependent viscosity decreasing with decreasing temperature, then a positive feedback flow instability can develop during the cold blow. In regions where flow is for some reason initially higher than adjacent regions during the cold blow, there will be increased local cooling, leading to decreased local viscosity, which in turn leads to increased flow. Periodic flow interruptions and channels perpendicular to flow help to redistribute the flow and to minimize flow instability maldistribution [12].

Thermal conduction longitudinally through the regenerator is minimized by use of discontinuous media or periodic thermal breaks. Regenerators made by stacking layers of wire screens, for example, where flow is perpendicular to the screens, allow thermal conduction to be minimized in the direction of fluid flow because of the nearly point contacts between successive screens. The relatively high thermal conductivity of screens perpendicular to the fluid flow direction has the secondary benefit of minimizing thermal gradients that might develop across the width of the regenerator due to flow maldistribution, for example.

The heat transfer gas also contributes to longitudinal thermal conduction, and as such, any real regenerator will have a non-zero longitudinal thermal conductivity because of the flow channels. Determining the effective thermal conductivity of a packed bed can become a complicated function of many parameters. Tsotsas and Martin [13] consider a packed bed's thermal conductivity to depend on the thermal conductivity of the solid and gas phases, the porosity, the pressure and temperature of the gas, the particle diameter and size distribution, the mechanical properties of the solid (for contact point area and surface heat transfer properties), the optical properties of the solid (for radiation), and the thermodynamic and optical properties of the gas.

Edwards and Richardson [14] studied the thermal conductivity augmentation from the effect of gas dispersion during flow through the bed. Vortmeyer and Adam [15] reviewed several researchers' work and found that most researchers agree that the effective thermal conductivity consists of an effective conductivity without flow plus a contribution depending on the flow rate, but that there is considerable difference in the observed magnitude of the latter term. Duncan *et al.* [16] provided a number of analytical and empirical relations for the effective thermal conductivity for packed beds.

1.6 Regenerator Configurations

Regenerators may be categorized as either fixed bed or rotary configurations. In fixed bed regenerators, the matrix material is stationary and valves (or some means of gas displacement) are used to alternately direct the hot and cold fluid streams. The regenerator of Figure 1.1 is an example of a fixed bed regenerator. In processes where hot and cold streams must flow at the same instant, two (or more) fixed bed regenerators are used in tandem. While hot gas flows through the first regenerator acting as a thermal store, cold gas flows through the second regenerator acting as a thermal source. After some time, the flow control valves change their open/closed state so that the regenerators reverse their roles. Figure 1.6 shows a schematic diagram of a tandem fixed bed regenerator arrangement. The system can be extended to multiple beds to accommodate unequal hot and cold blow periods and to limit the outlet fluid temperature swing.

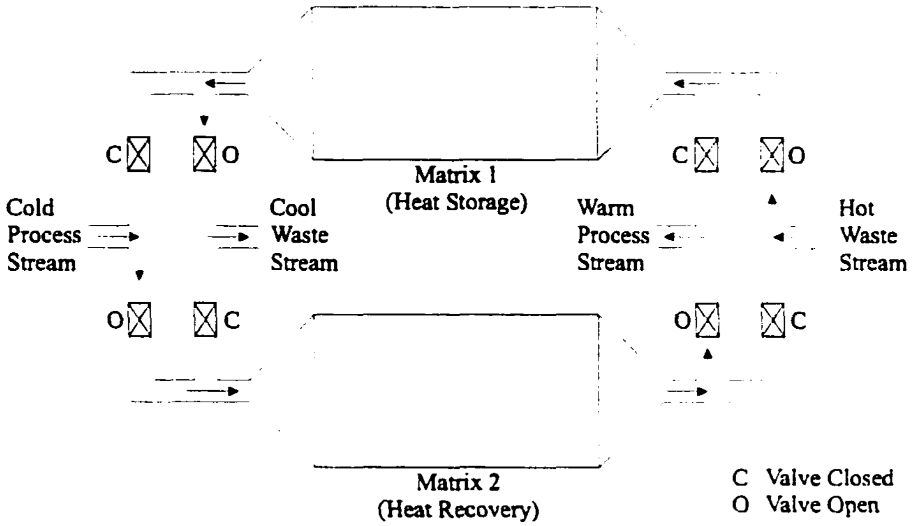

Figure 1.6 Schematic diagram of tandem fixed-bed counterflow regenerative heat exchangers allowing simultaneous hot and cold blow periods.

In contrast to the fixed bed regenerator, the rotary regenerator moves the matrix material past stationary hot and cold blow flow ducts to effect the periodic flow reversal within the regenerator matrix. As a result, the pseudo-steady-state rotary regenerator has a spatial, rather than temporal, variation of fluid outlet temperature. Figure 1.7 shows a schematic diagram of a rotary regenerator where fluid flows axially through the regenerator matrix, while Figure 1.8 shows an arrangement with radial fluid flow through the matrix.

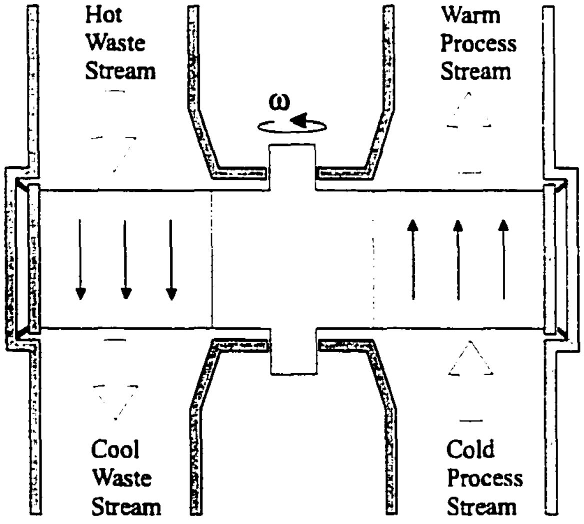

Figure 1.7 Schematic diagram of an axial flow rotary regenerator.

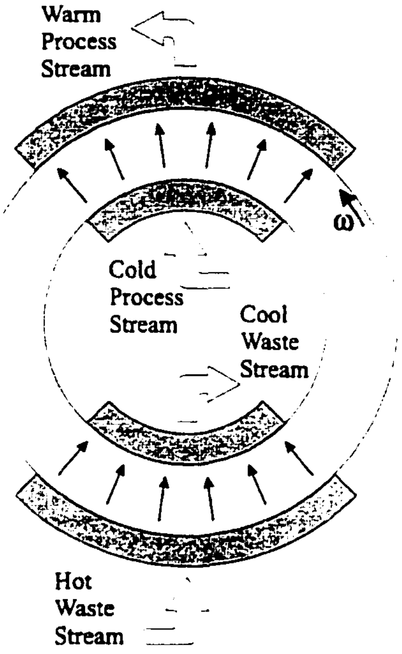

Figure 1.8 Schematic diagram of a radial flow rotary regenerator.

1.7 Regenerator Modelling

1.7.1 General Considerations

A regenerator's function is fairly straightforward; however, its operation is cited as one of the most difficult to analyze mathematically [17]. A complete description of the operation of a regenerator is a complex function of many coupled parameters, including:

- internal matrix geometry (particles, wire screens, thin plates, tubes, wires, etc.);
- external matrix geometry (rectangular, cylindrical, etc.);
- regenerator configuration (fixed bed, rotary);
- mass and heat capacities of matrix material and heat transfer fluid;
- effective thermal conductivity of matrix material and heat transfer fluid;
- effective heat transfer between matrix material and heat transfer fluid;
- radiative properties of matrix material and heat transfer fluid;

- matrix porosity and porosity distribution;
- flow impedance, viscous dissipation, and (mal)distribution;
- heat transfer fluid condensibles or contaminants;
- internal heat generation, chemical reactions, response to external fields, etc.;
- parasitic heat leaks to or from the external environment;
- variations of properties with position, time, temperature, etc.

To make a regenerator analysis tractable, several simplifying assumptions are often made, including:

a) The thermal conductivity of the matrix is zero parallel to the fluid flow and:
    i) infinitely large normal to the fluid flow, or
    ii) finite normal to the fluid flow.
b) The specific heats of the fluid and matrix material are not a function of temperature.
c) The fluids flow in opposite directions, and have inlet temperatures that are constant both over the flow section and with time.
d) The thermal capacity of the gas in the matrix at any instant is negligible compared to the matrix thermal capacity.
e) The heat transfer coefficients and fluid velocities are constant with time and space. (though they may be different for the hot and cold blow fluids).
f) The rate of mass flow of either fluid is constant during the blow period, though it may be different for the two fluids, and the blow periods may be different.
g) Heat transfer by radiation is insignificant.
h) Viscous dissipation is insignificant.
i) There is no internal heat generation.
j) The regenerator is adiabatic with respect to its container and the container to its surroundings.

The validity of these assumptions depends upon the operating conditions and application of the particular regenerator system. Walker [17] gives a summary of common simplifications in regenerator analysis, while Schmidt and Willmott [18] give a more thorough development of regenerator theory and possible simplifications.

1.7.2 Mathematical Model

In the simplest mathematical description, properties are assumed constant with temperature and position, momentum effects are ignored, mass conservation is solved trivially, conduction is considered negligible, and an energy balance governing only the fluid and solid is derived by considering the heat flow rates for a differential volume of the regenerator having a length dx. This gives two coupled partial differential equations describing the solid and fluid temperatures as a function of time and position during a blow period:

Fluid:

$$\dot{m} C_f \frac{\partial T_f}{\partial x} dx + \rho_f \frac{V_f}{L} C_f \frac{\partial T_f}{\partial t} dx = h\left(T_s - T_f\right) \frac{A}{L} dx \tag{1.1}$$

Solid:

$$\frac{M_s}{L} C_s \frac{\partial T_s}{\partial t} dx = h\left(T_f - T_s\right) \frac{A}{L} dx \tag{1.2}$$

where h is the heat transfer coefficient between fluid and matrix, per unit surface area, A is the total matrix surface area, $\dot{m}$ is the fluid mass flow rate, C_f is the specific heat capacity of the fluid, ρ_f is the density of the fluid, V_f is the volume of fluid entrained within the regenerator, L is the matrix length, M_s is the total mass of the matrix material, C_s is the specific heat capacity of the matrix material, and T_s and T_f are the solid and fluid temperatures, respectively. These two equations are applied separately for the hot and cold blow periods, and accordingly, values for h, $\dot{m}$, and C_f may be different for the two periods. To describe both hot and cold blows, the mass flow $\dot{m}$ is always considered positive, and the x-coordinate is measured with respect to the hot inlet during the hot blow and the cold inlet during the cold blow, i.e., increasing in the direction of fluid flow.

Often, the heat capacity effect of any entrained fluid is considered negligible, and Equation 1.1 for the fluid energy balance reduces to:

$$\frac{\partial T_f}{\partial x} = \frac{hA}{\dot{m} C_f L}\left(T_s - T_f\right) \tag{1.3}$$

Also, Equation 1.2 for the solid energy balance can be simplified as:

$$\frac{\partial T_s}{\partial t} = \frac{hA}{M_s C_s}\left(T_f - T_s\right) \tag{1.4}$$

This limited approach provides rudimentary performance data that can be presented in a number of ways, but one of the most common is to express the regenerator operation in terms of two dimensionless parameters (after Hausen [19]) called reduced length, Λ, and reduced period, Π. The reduced length (in the flow direction) is defined by:

$$\Lambda = \frac{hA}{\dot{m} C_f} \tag{1.5}$$

and represents the ratio of the potential rate of heat transfer with the regenerator to the heat capacity rate of the gas flow in the bed. The reduced period is defined by:

$$\Pi = \frac{hAP}{M_s C_s} \tag{1.6}$$

where P is the blow period. The reduced period represents the ratio of the potential heat transfer during a period to the heat capacity of the solid matrix. Frequently, Π and Λ are combined by the quotient:

$$\frac{\Pi}{\Lambda} = U = \frac{\dot{m} C_f P}{M_s C_s} \tag{1.7}$$

and called the utilization factor, representing the ratio of the sensible heat capacity of the fluid per blow to the heat storage capacity of the matrix, i.e., the maximum amount of heat which may be transferred to, or from, the gas to the maximum heat which may be transferred from, or to, the matrix. The greater this ratio, the greater the magnitude of the variation of the fluid and matrix temperatures for each blow period either temporally (for fixed bed) or spatially (for rotary bed).

If the hot and cold blow fluid inlet temperatures are constant with time, and denoted T_H and T_C respectively, dimensionless temperatures can be defined:

$$\dot{T}_f = \frac{T_f - T_C}{T_H - T_C} \qquad (1.8)$$

for the fluid, and:

$$\dot{T}_s = \frac{T_s - T_C}{T_H - T_C} \qquad (1.9)$$

for the solid. Finally, with the introduction of dimensionless distance:

$$\xi = \frac{x}{L} \qquad (1.10)$$

and dimensionless time:

$$\tau = \frac{t}{P} \qquad (1.11)$$

it is possible to describe a large range of regenerator operation by two dimensionless fluid and solid energy balance equations:

Fluid:

$$\frac{\partial \dot{T}_f}{\partial \xi} = \Lambda\left(\dot{T}_s - \dot{T}_f\right) \qquad (1.12)$$

Solid:

$$\frac{\partial \dot{T}_s}{\partial \tau} = \Pi\left(\dot{T}_f - \dot{T}_s\right) \qquad (1.13)$$

The reduced length Λ and reduced period Π can each have different values for the hot and cold blow periods. A notation using single and double primes can be used to distinguish between the hot and cold blow periods, respectively. Using this notation, for the hot blow:

$$\Lambda' = \frac{h'A}{\dot{m}'C_f'} \tag{1.14}$$

$$\Pi' = \frac{h'AP'}{M_s C_s} \tag{1.15}$$

For the cold blow:

$$\Lambda'' = \frac{h''A}{\dot{m}''C_f''} \tag{1.16}$$

$$\Pi'' = \frac{h''AP''}{M_s C_s} \tag{1.17}$$

The energy balance equations describing the regenerator operation are incomplete without some specification of the boundary conditions. The hot and cold fluid inlet temperatures provide two boundary conditions, which in the dimensionless equation formulation are 1 and 0, respectively. Consideration of the cyclic-steady-state provides two reversal conditions. The final temperature at each position within the solid matrix at the end of a blow period is the initial temperature at the start of the next period. With the above-noted convention for the x-coordinate (and therefore also the ξ-coordinate), the reversal condition for the start of the hot period can be stated as:

$$\dot{T}_s'(\xi',0) = \dot{T}_s''\left(\frac{\Lambda''(\Lambda' - \xi')}{\Lambda'}, \Pi''\right) \tag{1.18}$$

Similarly, the reversal condition for the start of the cold period can be stated as:

$$\dot{T}_s^{\bullet}\left(\xi^{\bullet},0\right) = \dot{T}_s'\left(\frac{\Lambda'\left(\Lambda^{\bullet} - \xi^{\bullet}\right)}{\Lambda^{\bullet}},\Pi'\right) \tag{1.19}$$

1.7.3 Balance and Symmetry

The definitions of distinct values for the reduced length and reduced period for the hot and cold blow periods is necessitated by the myriad applications to which regenerators have been applied. The heat transfer gas and its flowrate, and accordingly, its heat capacity and the resultant heat transfer coefficient, as well as the duration of gas flow can be different for the hot and cold blow periods. To help describe all such possibilities of regenerator operation, it is useful to define the terms balance and symmetry.

A regenerator is said to be balanced when the utilization factor as defined by Equation 1.7 evaluated for each of the hot and cold blow periods are equal. When they are unequal, the unbalance factor, β, is given by the ratio of the minimum to maximum utilization factors, *viz*:

$$\beta = \frac{U_{\min}}{U_{\max}} = \frac{\left(\dot{m}C_f P\right)_{\min}}{\left(\dot{m}C_f P\right)_{\max}} \tag{1.20}$$

The unbalance factor represents the ratio of minimum to maximum gas sensible heat capacities of the two periods. Implicit in this definition is the assumption that the value of $M_s C_s$ is equal for the hot and cold blow periods. The unbalance factor can take on any value greater than zero and less than or equal to one, though in most refrigeration applications it will have a value closer to the upper limit.

A regenerator is said to be symmetric when only single values for reduced length and reduced period are required to describe its operation. That is, a regenerator is symmetric if:

$$\Lambda' = \Lambda^{\bullet} \quad \textit{and} \quad \Pi' = \Pi^{\bullet} \tag{1.21}$$

These definitions for balance and symmetry give rise to three classes of regenerator operation:

1) Symmetric-Balanced:

$$\Lambda' = \Lambda'' \ , \ \Pi' = \Pi'' \ \textit{and} \ \beta = 1 \tag{1.22}$$

2) Asymmetric-Balanced:

$$\Lambda' \neq \Lambda'' \ , \ \Pi' \neq \Pi'' \ \textit{but} \ \beta = 1 \tag{1.23}$$

3) Asymmetric-Unbalanced:

$$\Lambda' \neq \Lambda'' \ , \ \Pi' \neq \Pi'' \ \textit{and} \ \beta \neq 1 \tag{1.24}$$

The combination "symmetric-unbalanced" is normally precluded because by the above definitions a symmetric regenerator will always have an unbalance factor $\beta=1$, i.e., balanced. Potentially, if the regenerator matrix is uniformly responsive to some external field during operation, the symmetric-unbalanced case could be realized. In that case, the reduced length and reduced period energy balance equations 1.12 and 1.13 are insufficient to describe the complete regenerator operation and would require an additional term to describe the response of the matrix to the external field. Because the symmetric-unbalanced regenerator is a degenerate case that requires an unlikely set of conditions to be satisfied and a mathematical description beyond the simple Λ-Π analysis, it will not be considered further.

1.7.4 Regenerator Effectiveness and Thermal Ratio

The performance of a regenerator is often reported in terms of its effectiveness. The effectiveness of a regenerator is defined as the ratio of heat transferred during a period to the thermodynamically limited maximum heat transferrable in a counterflow regenerator of infinite heat transfer area operating between the same inlet temperature limits. If the average fluid outlet temperature during the hot blow is denoted as $\bar{T}'_{f,o}$, then the effectiveness for the hot blow period is defined as:

$$\varepsilon' = \frac{\left(\dot{m}C_fP\right)_{hot}\left(T_H - \bar{T}'_{f,o}\right)}{\left(\dot{m}C_fP\right)_{\min}\left(T_H - T_C\right)} \tag{1.25}$$

Similarly, if the average outlet temperature during the cold blow is denoted as $\bar{T}^{\bullet}_{f,o}$, then the effectiveness for the cold blow period is defined as:

$$\varepsilon^{\bullet} = \frac{\left(\dot{m}C_fP\right)_{cold}\left(\bar{T}^{\bullet}_{f,o} - T_C\right)}{\left(\dot{m}C_fP\right)_{\min}\left(T_H - T_C\right)} \tag{1.26}$$

In calculating the effectiveness, $\left(\dot{m}C_fP\right)_{\min}$ is the smaller of the gas sensible heat capacities $\left(\dot{m}C_fP\right)_{hot}$ for the hot blow and $\left(\dot{m}C_fP\right)_{cold}$ for the cold blow. With no heat leaks to or from the regenerator, or other work or heat interactions, at cyclic-steady-state the heat transferred during the hot blow equals the heat transferred during the cold blow, and consequently, the values of effectiveness for hot blow and cold blow are equal.

The thermal ratios, or pseudo-efficiencies, of regenerators are often considered. When the regenerator is balanced, the gas sensible heat capacities are equal. The expressions for effectiveness reduce to the regenerator thermal ratios, given as:

$$\eta'_{th} = \frac{\left(T_H - \bar{T}'_{f,o}\right)}{\left(T_H - T_C\right)} \tag{1.27}$$

for the hot blow, and:

$$\eta^{\bullet}_{th} = \frac{\left(\bar{T}^{\bullet}_{f,o} - T_C\right)}{\left(T_H - T_C\right)} \tag{1.28}$$

for the cold blow. For a balanced regenerator, $\eta'_{th} = \eta^{\bullet}_{th} = \eta_{th}$, but despite their origin in the case of a balanced regenerator, the thermal ratios are often cited for unbalanced regenerators and retain their distinction for hot and cold blows. This causes some confusion in the literature where the terms effectiveness, efficiency, and thermal ratio are used interchangeably.

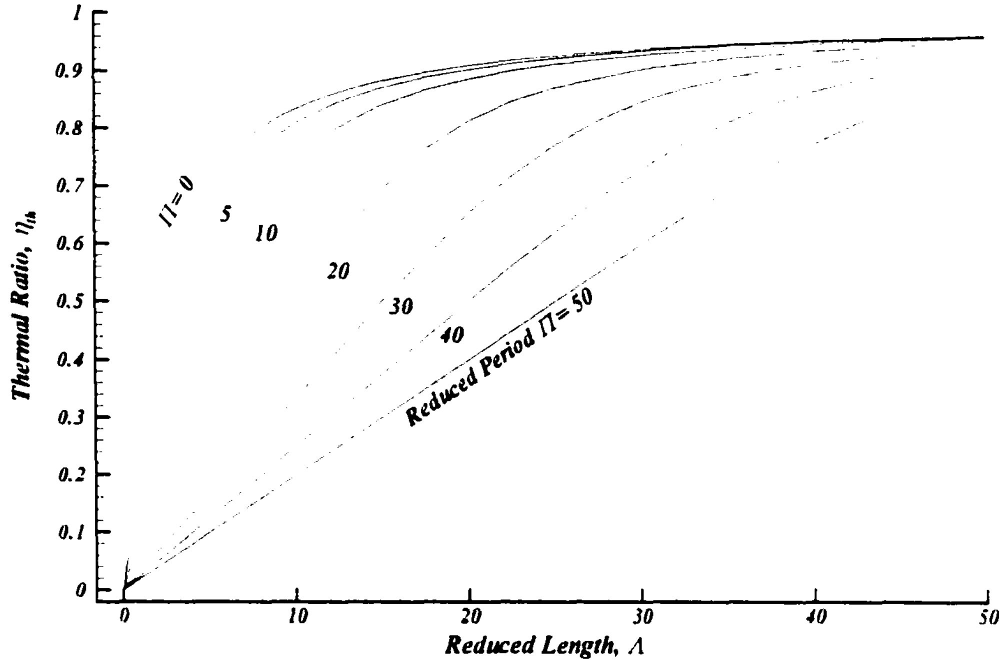

Figure 1.9 Symmetric-balanced regenerator thermal ratio, η_{th}, as a function of reduced length Λ and reduced period Π, after Hausen [19].

The performance data for balanced regenerators is classically presented as the thermal ratio η_{th} as a function of the reduced length Λ and reduced period Π, as shown in Figure 1.9. In the limit of zero reduced period, the thermal ratio is given exactly by:

$$\eta_{th} = \frac{\Lambda}{\Lambda + 2} \tag{1.29}$$

For a non-zero reduced period, the energy balance equations 1.3 and 1.4 (or 1.12 and 1.13) must be solved to determine the thermal ratio. A review of the methods employed to solve the regenerator equations is presented in Chapter 3.

The ineffectiveness is often used to present the regenerator performance data, and is defined as:

$$Ie = 1 - \eta_{th} \qquad (1.30)$$

For high performance regenerators, where η_{th} is nearly unity, the ineffectiveness can be useful to show the strong dependence of cycle performance on regenerator operation, since losses frequently scale with ineffectiveness. As such, a decrease in thermal ratio from 0.995 to 0.990, might seem like a small change, but represents a doubling of the ineffectiveness. Note that the definition is based on the thermal ratio, and not the effectiveness, further clouding the nomenclature with respect to unbalanced regenerators where thermal ratio and effectiveness values are unequal for the larger capacity stream.

1.7.5 Beyond Λ and Π

For many applications, the simple Λ-Π analysis is sufficient to determine the expected regenerator performance, or the expected change in performance under a change in operating conditions for existing equipment. A more detailed mathematical model is required when some or all of the simplifying assumptions do not hold. The following is a summary of conditions under which the simplifying assumptions would and would not be valid

The assumption of thermal conductivity zero parallel to the fluid flow is reasonably valid for matrix materials having very low thermal conductivity, such as ceramic bricks that might be used in Cowper stoves, but is generally not valid for metallic elements, such as parallel plates oriented parallel to the fluid flow. A matrix thermal conductivity infinitely large normal to the fluid flow would likely be valid for perforated plates oriented normal to the fluid flow, and generally would become increasingly questionable with geometries parallel to the fluid flow, such as wires packed parallel to the fluid flow, or ceramic materials. In the case of insulating elements, an additional diffusion equation is required to describe the heat transfer within the elements resulting from the convection heat transfer at their surface from the hot or cold blow.

The assumption of constant specific heats, either of the fluid or the matrix, is valid over "small" temperature spans, provided the temperature span does not include a point of material phase change.

That is, the span could not encompass the liquefaction point for a fluid, or near a magnetic phase change for the matrix for the assumption to be valid. Generally, the definition of a "small" temperature span would be proportionate to the absolute temperature, so that a "small" temperature span near 50 K would be smaller than a "small" temperature span near room temperature. In cryogenic applications, where large temperature spans are encountered, and temperatures can approach absolute zero where properties can change rapidly, the assumption of constant specific heat needs to be used with care.

The assumption of constant fluid inlet temperature is a requirement to maintain linearity of the governing equations for the Λ-Π analysis. The assumption of uniform flow distribution is the subject of research papers [20,21,22] and theses [23,24], including this work in part. Flow maldistribution can have a significant effect on the thermal performance of the regenerator depending on the degree of maldistribution and the nominal Λ-Π operating conditions. The assumption of counter-flow operation of the regenerator is to clarify the mode of operation of the regenerator. Parallel flow regenerators are physically realizable, but due to their intrinsically lower thermal ratios have limited applications.

The assumption of negligible thermal capacity of the gas in the matrix is questionable when the porosity of the matrix is high, or generally when the heat capacity of the gas is large relative to the matrix. In cryogenic applications where the heat capacity of the matrix falls off quickly with decreasing temperature, but the fluid heat capacity is nearly constant or, for helium near the lambda point, increases, this assumption is invalid.

The assumption of constant heat transfer coefficient is reliant on constant fluid thermophysical properties and/or compensating geometrical properties. The validity of this assumption would have to be checked with respect to the specifics of regenerator design and application. For regenerators employing gases for the heat transfer fluid, large density changes associated with large temperature spans can significantly affect the heat transfer coefficient indirectly through a change in gas velocity, as well as more directly through changes in viscosity, thermal conductivity, and heat capacity.

Heat transfer by radiation (internal to the regenerator) is significant in high temperature applications. For room temperature applications and below, the assumption of negligible heat transfer by radiation is likely valid.

The assumption of adiabatic conditions for the regenerator in its housing and its housing with its surroundings is likely invalid when the regenerator is operating at a temperature significantly different from its surroundings. This would encompass high temperature and cryogenic applications, where a significant loss to, or gain from, the surroundings could be experienced. These parasitic loads can be minimized by the use of suitable regenerator containers with insulating properties, and for many applications, additional external insulation.

When the regenerator simplifying assumptions are deemed invalid, the simple regenerator energy balance equations can be modified with additional terms to account for the additional heat fluxes. With the introduction of non-linear terms, the solution of the regenerator equations becomes more complicated. In this work, any additional regenerator energy balance terms will be introduced as required by the systems being described.

Chapter 2

Applications of Regenerators: Gifford-McMahon and Active Magnetic Regenerative Refrigerators

2.1 Introduction

Of the innumerable applications for regenerators, of interest in this work is the application of the device to the systems of Gifford-McMahon (GM) and Active Magnetic Regenerative (AMR) Refrigerators. More specifically, of interest is the thermal and fluid dynamic operation and interdependence, as well as the overall thermal performance of the regenerator under various operating conditions of balance and symmetry. To understand the operation of the regenerator in these applications, it is first necessary to understand the refrigeration cycles in which they are applied.

2.2 The Gifford-McMahon Cycle

2.2.1 Basis of Refrigeration

The Gifford-McMahon (GM) cycle [25] was conceived at A.D. Little, Inc. in the mid 1950's, and introduced commercially in the early 1960's. GM cryocoolers are characterized as "durable and the cooler of choice where size, weight, and efficiency are not of prime importance."[26] The device achieves refrigeration by repeated cycles of Simon isentropic gas expansion. When an ideal gas is isentropically compressed or expanded, there is an accompanying temperature change in the gas according to:

$$\frac{T_i}{T_f} = \left(\frac{P_i}{P_f}\right)^{\frac{\gamma - 1}{\gamma}} \tag{2.1}$$

where T and P are the gas temperatures and pressures, respectively, the subscripts i and f correspond to the initial and final states, respectively, and γ is the ratio of the gas specific heat at constant pressure to specific heat at constant volume. A non-ideal gas will also experience a temperature change from isentropic compression or expansion, the value of which is specific to the gas considered as well as the initial temperature and initial and final pressures. Helium gas expansion in the GM cycle provides cooling, and the large temperature span of the device is made possible by use of a regenerative heat exchanger to pre-cool the gas before expansion.

2.2.2 GM Schematic and Cycle Description

A schematic diagram of a single-stage GM refrigerator having an integral regenerator displacer unit is given in Figure 2.1. A gas compressor, with aftercooler and high and low pressure reservoirs, is used to supply the pressure variations of the cycle. The GM cycle is composed of the following four processes:

1) *Pressure Buildup:* With the regenerator/displacer at the bottom of the cylinder and the exhaust valve closed, the inlet valve is opened. This increases the pressure in the cylinder, filling the regenerator and the void space above the regenerator/displacer.
2) *Intake Stroke:* While maintaining the inlet valve open, the regenerator/displacer is moved from the bottom of the cylinder to the top of the cylinder. This shuttles the gas from above the regenerator/displacer through the regenerator, to the space below the regenerator/displacer. In passing through the regenerator, the gas is cooled, which increases its density. Gas flows through the open intake valve to maintain the high pressure within the cylinder.

3) *Pressure Release and Expansion:* With the regenerator/displacer at the top of the cylinder, the intake valve is closed and the exhaust valve is opened, decreasing the pressure in the cylinder. The pressure drop results in a reduction of the gas temperature level. The cold gas remaining in the bottom of the cylinder below the regenerator/displacer provides the refrigeration for the cycle.

4) *Exhaust Stroke:* With the exhaust valve still open, the regenerator displacer is moved back to the bottom of the cylinder. This shuttles the cold gas from below the regenerator/displacer through the regenerator, to the space above the regenerator/displacer. In passing through the regenerator, the regenerator matrix is cooled and readied for the next cycle, while the gas is warmed. Some of the warm gas, having lower density, exits through the exhaust valve to maintain the low pressure in the cylinder.

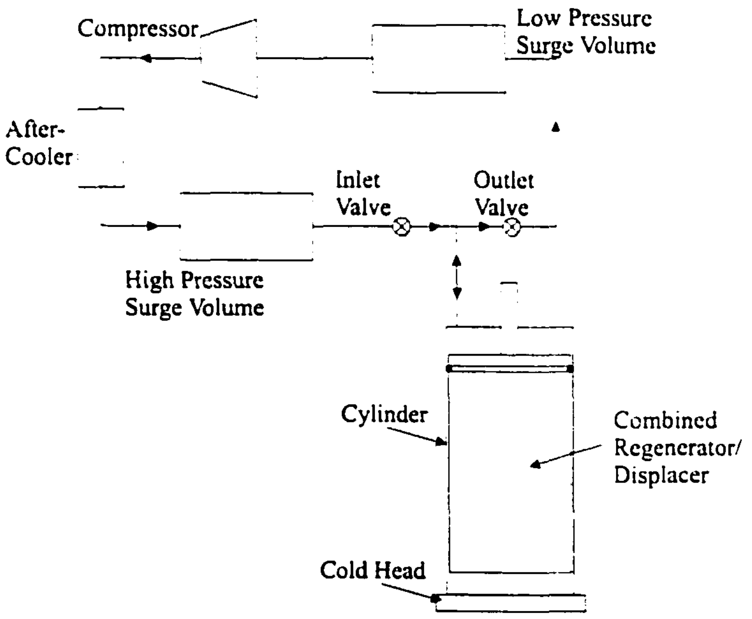

Figure 2.1 Schematic diagram of a single-stage Gifford-McMahon refrigerator.

The temperature-entropy (T-s) diagram for the GM cycle is shown in Figure 2.2. Temperature spans from room temperature to ~20 K are readily achieved in the GM cooler in a single stage. Below ~20 K, two or three stage designs reach temperatures below the normal boiling point of helium at 4.2 K, provided suitable materials are used in the low-temperature regenerators.

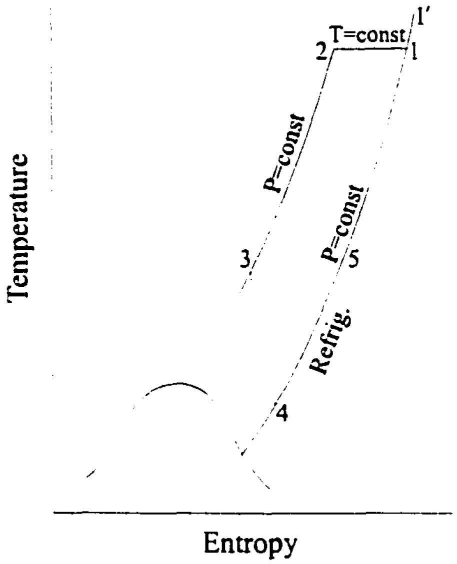

Figure 2.2 Temperature-entropy diagram of the Gifford-McMahon refrigeration cycle.

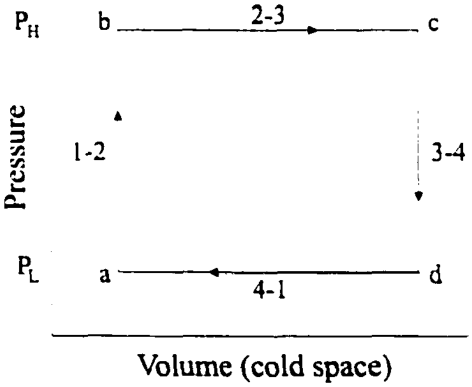

Figure 2.3 Ideal pressure-volume diagram for the cold expansion space of a Gifford-McMahon cycle refrigerator.

The pressure-volume (P-V) diagram for the cold expansion space for the GM cycle is shown in Figure 2.3. The minimum volume is greater than zero to account for void space and clearances between the regenerator/displacer and the cylinder housing. The cycle executes clockwise and the legs of the cycle are numbered corresponding to the process description given above. In practice, the P-V diagram does not exhibit perfectly constant volume and constant pressure processes for the cycle, which tends to "round-out" the P-V diagram.

2.2.3 GM Regenerator Balance and Symmetry

Except at low temperatures, where the working gas, helium, exhibits a strong pressure dependent heat capacity, the normal operation of the regenerator within the GM cycle is essentially balanced and symmetrical. There are some deviations from perfect balance and symmetry imposed by the constraints of the operating conditions in a real device, in particular, the varying mass flow and regenerator hot end and cold end temperatures during the four phases of operation, the void volume of the regenerator and cylinder, and the heat leaks into and along the regenerator.

2.3 Active Magnetic Regenerative Refrigeration

2.3.1 Basis of Magnetic Refrigeration

While the concepts behind refrigeration cycles that utilize gas compression and expansion are widely understood, the concepts behind magnetic refrigeration are less well known. To understand the operation of active magnetic regenerative cycles, an understanding of the basis of magnetic refrigeration is essential.

The magnetocaloric effect, which is the basis for all magnetic refrigerators, has been credited to Warburg [27] who observed the heating and cooling of iron in response to a varying magnetic field. In 1918, Piccard and Weiss [28] experimentally observed the reversible heating and cooling of ferromagnetic nickel near its Curie temperature of 631 K upon application and removal of a magnetic field. The nature of the magnetocaloric effect was explained and its practical use to reach ultra-low temperatures in a process of adiabatic magnetization was suggested independently by Debye [29] and Giauque [30]. In 1933 Giauque [31] and his graduate student were able to use the magnetocaloric effect of paramagnetic materials in a practical device to achieve a cooling temperature of 0.5 K. His method was to isothermally magnetize a paramagnetic salt at 3.5 K and then to adiabatically demagnetize it to achieve 0.5 K. Figure 2.4 illustrates this process on a low-temperature *T-s* diagram.

with process 1 being the isothermal magnetization, and process 2 being the adiabatic demagnetization. This one-shot technique is still in use today to temporarily create ultra-low temperatures for physics experiments.

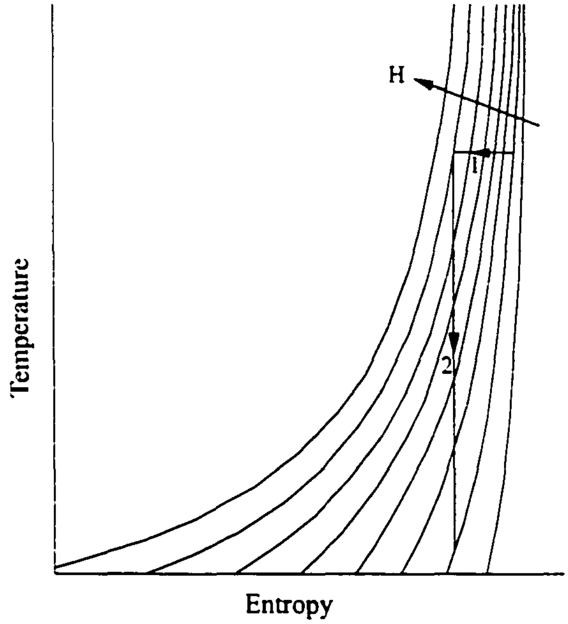

Figure 2.4 Temperature-entropy diagram of a one-shot magnetic cooling process, where *H* gives the applied magnetic field.

The method of Giauque is a one-shot process, and any cooling effect produced is short term. In 1949 Daunt and Heer [32] suggested combining two isothermal and two adiabatic magnetization and demagnetization processes to form a magnetic Carnot heat pump cycle for continuous operation. The magnetic Carnot cycle using a paramagnetic salt is illustrated in Figure 2.5. The process begins by the isothermal magnetization of the working material, thereby rejecting heat from the material and decreasing the material's entropy. The material is then adiabatically demagnetized, decreasing its temperature. Heat is then absorbed by the material during isothermal demagnetization, increasing the material's entropy. Finally, the material is raised to its initial temperature by adiabatic magnetization. In 1954 Heer *et. al* [33] built a continuous magnetic refrigerator approximating the Carnot cycle and achieved temperatures below 0.2 K.

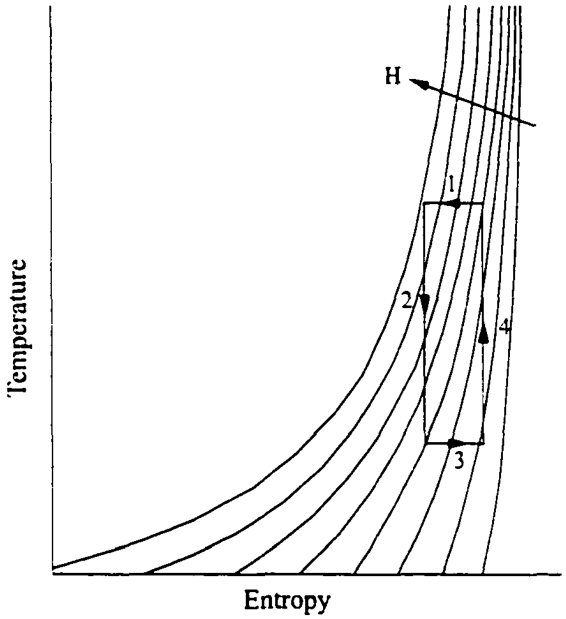

Figure 2.5 Temperature-entropy diagram of a magnetic Carnot cycle for a paramagnetic salt.

2.3.2 Fundamental Relations

The thermodynamics describing the application of the magnetocaloric effect to a refrigeration device can be understood by considering a heat and work interaction for a paramagnetic solid. During magnetization, the dipole moments of the magnetocaloric material oppose changes made in their orientation. The infinitesimal magnetic work transfer interaction for the process is:

$$\delta W = -\mu_0 H dM \tag{2.2}$$

where μ_0 is the permeability of free space, H is the applied magnetic field, and dM is the increase in the magnetization (i.e. total magnetic moment) of the material. The differential change in internal energy of the material in the vicinity of an equilibrium state is the sum of its reversible energy transfer interactions of heat transfer, mechanical work transfer, and magnetic work transfer, *viz*:

$$dU = TdS - PdV + \mu_0 H dM \tag{2.3}$$

where U is the internal energy, T is the temperature, S is the entropy, P is the pressure, and V is the volume. The mechanical work transfer term, PdV, is the familiar work interaction for gas cycle refrigeration systems, while the magnetic work transfer term, $\mu_0 HdM$, is specific to magnetic systems. In magnetic refrigeration systems, the mechanical work transfers from changes in material pressure and volume are negligible compared to the magnetic work transfer from changes in field and magnetization, and the differential change in internal energy can be simplified as:

$$dU = TdS + \mu_0 HdM \tag{2.4}$$

The corresponding relation for the adiabatic demagnetization (magnetization) process gives the resultant cooling (warming) of the magnetic material according to:

$$T_f = T_i - \mu_0 \int_{H_i}^{H_f} \frac{T}{C_H} \left(\frac{\partial M}{\partial T} \right)_H dH \tag{2.5}$$

where C_H is the heat capacity at constant field, $\left(\frac{\partial M}{\partial T} \right)_H$ is the change in material magnetization with temperature at constant field, and the subscripts i and f represent the initial and final states, respectively. Equation 2.5 shows that the adiabatic temperature change is a function of temperature and the limits of applied field change, as well as a function of the material through the properties C_H and $\left(\frac{\partial M}{\partial T} \right)_H$. Figure 2.6 gives the adiabatic magnetization temperature change of gadolinium as a function of initial temperature for an applied field change from 0 up to 10 Tesla, as calculated using a molecular field model. The results from the molecular field model are in agreement with the experimental results of Benford and Brown [34]. From this diagram, the temperature dependence of the magnetocaloric effect is easily discernible, with the peak temperature change corresponding to the material's Curie point.

The adiabatic temperature change in a magnetic material is relatively small, about 1-2 K per Tesla applied field change. The large fields required to generate an appreciable magnetocaloric effect suitable for continuous refrigeration devices are effectively provided using superconducting magnet systems. Such magnet systems, because of their relative complexity and historically high expense, may help explain the lack of commercial magnetic refrigeration systems.

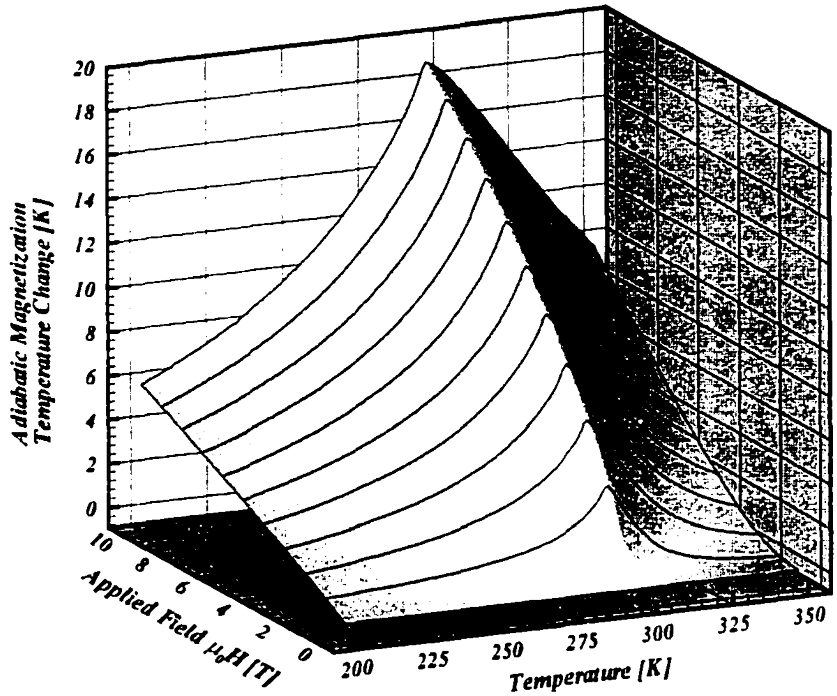

Figure 2.6 Adiabatic temperature change, ΔT_{ad}, of gadolinium as a function of temperature and applied field.

A magnetic refrigeration cycle is made possible by coupling a heat transfer gas to the temperature swings available from the magnetocaloric effect. The heat transfer gas allows a heat load to be picked up by the material when it is cooler than the gas, and allows a load to be rejected when the material is warmer than the gas. Figure 2.7 shows schematically the steps of a possible magnetic refrigeration cycle, and for comparison, the corresponding steps of a gas compression refrigeration cycle.

For a refrigeration cycle to span a temperature range exceeding the magnitude of the magnetocaloric temperature change of the working material, the cycle must include recuperative or regenerative heat exchange. In this work, cycles which employ the magnetocaloric material arranged to act as both active working material and thermal regenerator to achieve the desired temperature span are considered.

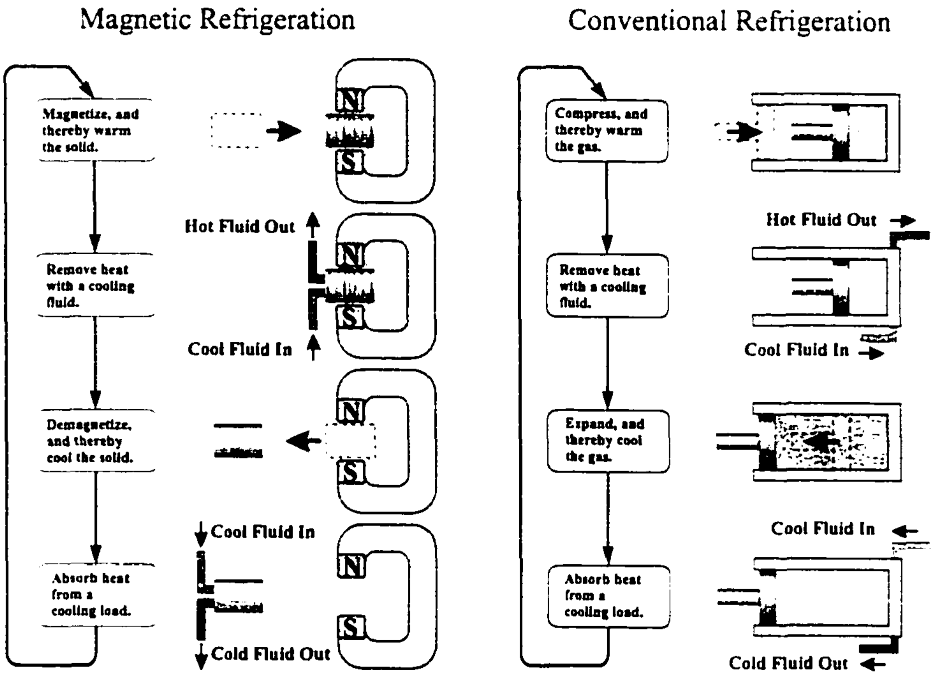

Figure 2.7 Comparison of magnetic refrigeration and conventional gas compression refrigeration.

2.3.3 The Active Magnetic Regenerative Cycle

For optimal heat transfer from the working material to the heat transfer gas in a magnetic cycle, relatively large heat transfer areas are required since the temperature differences available for heat transfer from adiabatic magnetization and demagnetization are relatively small. Similarly, for optimal thermal regenerator performance, large heat transfer areas are required. In a regenerative magnetic cycle, it is possible to integrate the thermal regeneration requirement with the heat load absorption and rejection requirements by arranging the active working material to also function as the thermal regenerator. Because the magnetic material performs both functions of active working material and thermal regenerator, this configuration is known as an Active Magnetic Regenerator, or *AMR*.

Figure 2.8 shows a schematic diagram of an AMR refrigerator that uses a fixed bed of magnetic refrigerant. In the figure, hot and cold heat exchangers sandwich a regenerator bed composed of magnetic material, while pistons shuttle heat transfer fluid periodically and in cooperation with the periodic application of a magnetic field. The periodic magnetic field is accomplished either by use of charge/discharge magnets or by a reciprocal motion with respect to the bed.

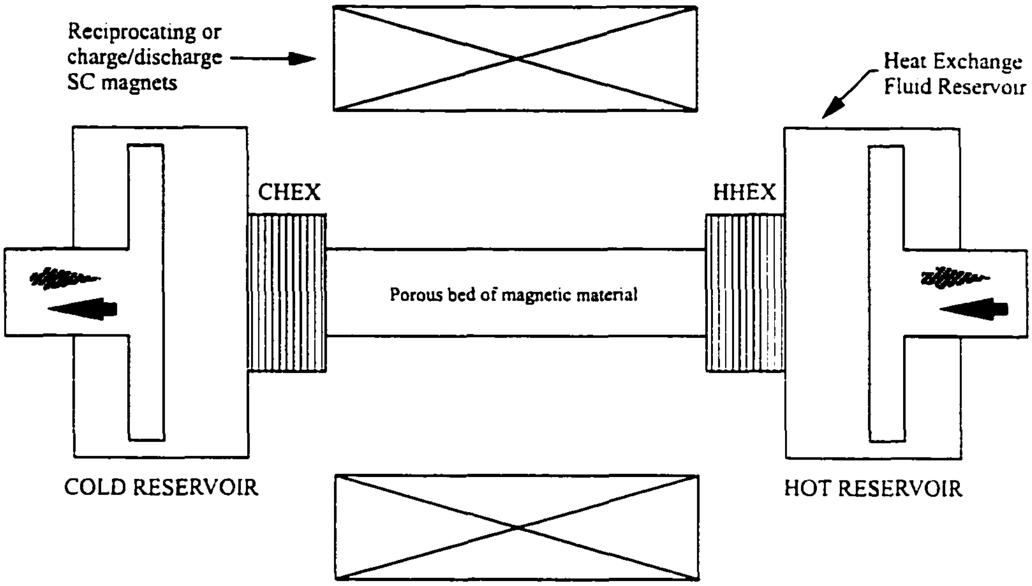

Figure 2.8 Schematic diagram of a fixed-bed active magnetic regenerative refrigerator.

The AMR refrigeration cycle consists of the following four processes:

1) *Adiabatic Magnetization:* With all the fluid in the cold reservoir, the magnet is energized or positioned surrounding the regenerator bed, adiabatically magnetizing the bed and causing the temperature everywhere in the bed to increase by some amount as determined by the local value of the magnetocaloric effect.
2) *Heat Rejection:* While maintaining the bed magnetized, fluid is shuttled from the cold side through the bed to the hot side. In passing through the cold heat exchanger, the fluid accepts the cooling load. In passing through the bed, the fluid is warmed, and the solid is cooled. In passing through the hot heat exchanger, the fluid rejects the heat it received from the load and the regenerator bed.
3) *Adiabatic Demagnetization:* With the fluid now in the hot reservoir, the magnet is discharged, or positioned away from the regenerator bed, adiabatically demagnetizing the bed and causing the temperature everywhere in the bed to decrease by some amount as determined by the local magnetocaloric effect.
4) *Regeneration:* While maintaining the bed demagnetized, fluid is shuttled from hot side to cold side. In passing through the bed, the fluid is cooled and made ready to pick up a cooling load, and the solid is warmed, ready for the next cycle.

The AMR cycle has been variously described as akin to the magnetic reverse-Brayton cycle, where the two constant field heat transfer and two adiabatic magnetization processes for the magnetic material are analogous to two constant pressure heat transfer and two adiabatic compression processes for the gas reverse-Brayton cycle. There is a subtle distinction between the two, however. In the usual reverse-Brayton cycle, the working material provides both the heat transfer function and the work input function, and an element of working material spans the entire temperature range from hot to cold. In the AMR cycle, the working material, the magnetic solid, provides the work input, while the heat transfer circulation gas provides the heat transfer function. A given element of magnetic solid only spans a small portion of the entire temperature span for the device; the heat transfer gas couples the elements to span the entire temperature range.

This subtle distinction between the AMR and magnetic reverse-Brayton cycles is important. The decoupling of the work input and heat transfer functions allows the small, temperature-dependent magnetocaloric effect to be leveraged across a large temperature span by selection of a collection of materials that each maximizes the magnetocaloric effect according to the local operation temperatures within the regenerator.

The decoupling also has import implications for the description of the temperature-entropy diagram for the cycle. Usually, the temperature-entropy diagram describes the cycle executed by a representative unit of the working material. In the case of the AMR, each element of working material undergoes its own local T-s cycle (each following a magnetic reverse-Brayton cycle), with adjacent cycles overlapping. The overall cycle for the working material is described by the envelope of these sub-cycles. Figure 2.9 shows a schematic representation of the overlap in the temperature-entropy cycles of adjacent elements of solid material, with the envelope of these sub-cycles defining the overall T-s cycle for the AMR. For this cycle, no element of working material needs to be active over the entire temperature span; every element can potentially be optimized to operate over its own local temperature span.

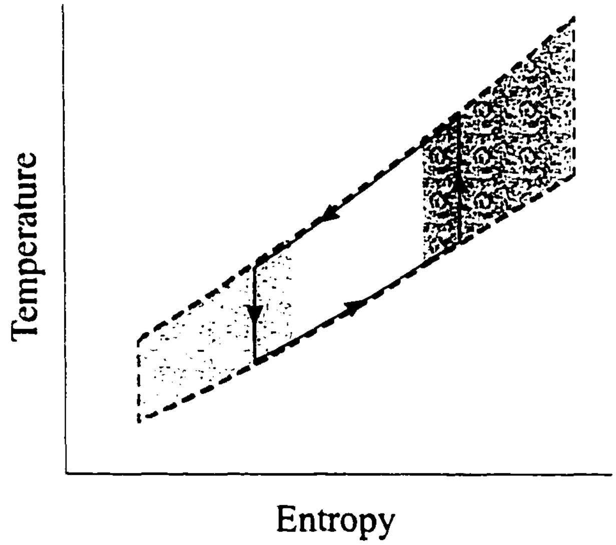

Figure 2.9 Schematic representation of overlapping temperature-entropy cycles of adjacent AMR solid elements defining the envelope of the overall AMR refrigeration cycle.

2.3.4 AMR Regenerator Solid Energy Balance Equation

The basic regenerator equations describing the thermal operation of the regenerator must be modified to account for the magnetic field interaction of the magnetocaloric material. Following the assumptions of the derivation leading to Equation 1.4, and considering only the interaction of the solid with the applied field, the simplest form of the regenerator solid energy balance equation for a magnetocaloric material is given by:

$$\frac{\partial T_s}{\partial t} = \frac{hA}{M_s C_H}\left(T_f - T_s\right) - \frac{\mu_0 T_s}{\rho_s C_H}\left(\frac{\partial M}{\partial T}\right)_H \frac{dH}{dt} \tag{2.6}$$

where ρ_s is the density of the solid, and $\frac{dH}{dt}$ is the change in applied field with time. The fluid energy balance equation is unchanged from Equation 1.3. The coupled regenerator equations embodying the magnetocaloric effect represent a non-linear system, and consequently only numerical methods can be used to determine temperature distributions, fluid output temperatures, and thermal performance.

Equation 2.6 is a particular case of the general solid energy balance equation:

$$\rho\frac{Ds}{Dt} = \frac{1}{T}\left(-\nabla\cdot\vec{q} + \sigma\right) \tag{2.7}$$

where $\frac{Ds}{Dt}$ is the substantive derivative of the specific entropy, s, $\vec{q}$ is the heat flux vector, and σ is the volumetric energy generation term. For the AMR equations, the solid entropy is a function of the temperature and applied field, i.e., $s = s(T, \mu_0 H)$. The volumetric energy generation term, σ, is used to represent the conjugate heat transfer between solid and fluid and any additional source terms, such as electrical eddy current heating. The heat flux vector represents solid conduction based on Fourier's Law of Heat Conduction. Equation 2.7 can be used to derive the AMR solid energy balance equation for any configuration of steady-state or transient AMR, including rotating, stationary, and reciprocating designs.

2.3.5 AMR Regenerator Balance and Symmetry

The normal operation of the regenerator within the AMR cycle is unbalanced and asymmetrical. The application of the magnetic field to the magnetocaloric material causes a decrease in material heat capacity below the material Curie point, and an increase in heat capacity above the Curie point. With equal blow periods, and equal heat transfer coefficients, the reduced period becomes unbalanced due to the change in heat capacity of the solid. When the AMR is operated primarily below the Curie point of the material, $\Pi' > \Pi''$, where the definitions of reduced period are broadened to consider the local variation in properties over differential volumes, and net reduced period is the integral over the period and the volume of the regenerator.

The definition of unbalance factor given as Equation 1.20, which was developed in the context of regenerators where the matrix material was passive, and therefore $M_s C_s$ was constant for the hot and cold periods, is invalid for AMR regenerators. For AMR regenerators, the broader definition is used:

$$\beta_{AMR} = \frac{U_{\min}}{U_{\max}} = \frac{\left(\dot{m} C_f P / M_s C_H\right)_{\min}}{\left(\dot{m} C_f P / M_s C_H\right)_{\max}} \tag{2.8}$$

The reduced length of the AMR regenerator is unaffected by the changes in the solid matrix material, except perhaps via the change in heat transfer coefficient due to varying thermophysical fluid properties with temperature. Since the temperature changes are small from the magnetocaloric effect, the change in effective heat transfer coefficient between the hot and cold blow periods is small, and can usually be neglected. In this case, $\Lambda' = \Lambda''$.

2.3.6 AMR Regenerator Effectiveness

An alternative interpretation of the AMR cycle is possible when only the regenerative aspects of the device are considered and the specifics of the magnetic material field interactions and temperature changes are ignored. Using the definitions of regenerator effectiveness and thermal ratio developed previously as Equations 1.25, 1.26, 1.27, and 1.28, the active regenerator can be considered to be a device which has unequal hot and cold blow effectiveness and thermal ratios, each greater than unity. Because the effectiveness is greater than unity, the AMR regenerator allows the extents of the fluid exit temperatures to equal or exceed the extents of the inlet temperatures.

2.3.7 Rotary Active Magnetic Regeneration

The reciprocating design is not the only possible configuration for the AMR device. The original concept of rotating magnetic refrigerators as conceived by Steyert [35] was taken a step further by the invention of the rotary active magnetic regenerator in 1983 by Barclay [36].

A schematic diagram of a rotary AMR refrigerator (AMRR) is given in Figure 2.10. A circulation pump supplies a flow of heat transfer circulation gas to a ring-shaped regenerator composed of magnetocaloric materials that is rotated through a constant high magnetic field region. As a radial segment of the regenerator enters the high field region, it responds to the field and experiences warming from the magnetocaloric effect. While in the high field region, heat transfer fluid from the cold heat exchanger flows through the segment, picking up heat to be rejected in the hot heat exchanger. As the segment rotates through the high field region, it is continuously cooled by the fluid flow. Eventually, the segment rotates to the area where fluid flow ends, and the segment rotates out of the high field region. Again it responds to the change in field, this time getting cooler. In the zero field region, heat transfer fluid from the hot heat exchanger flows in the opposite direction through the radial segment, regenerating the magnetic material and thereby cooling the fluid so it can absorb a load at the cold heat exchanger. Eventually, the segment rotates to the area where fluid flow ends, material regeneration is complete, and the segment is ready to undergo another cyclic rotation.

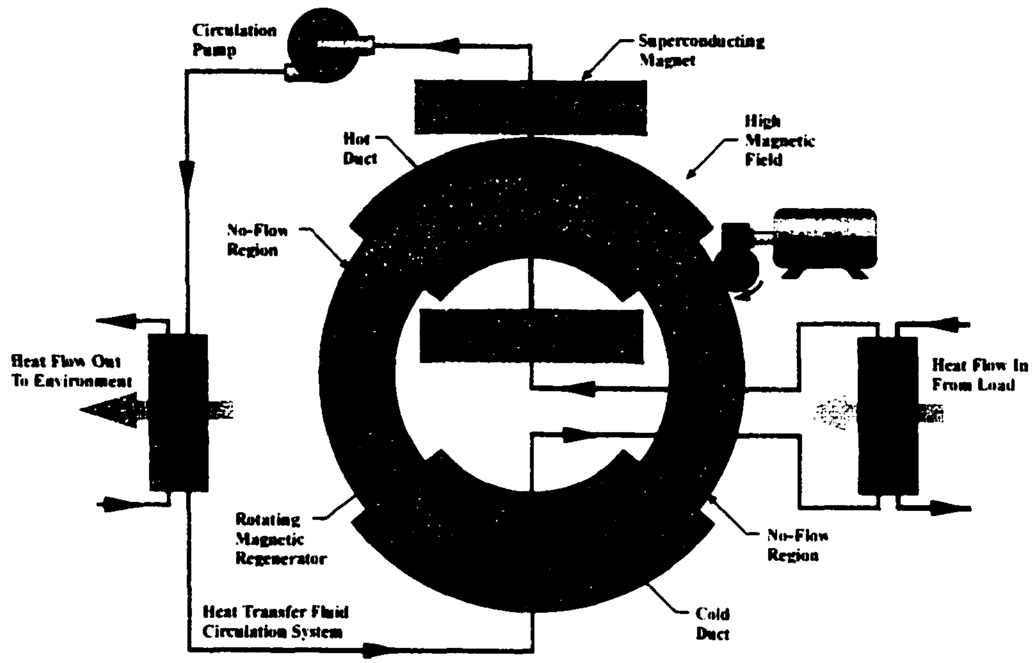

Figure 2.10 - Schematic diagram of a single-stage rotary AMR refrigerator showing key system components.

Both the rotary AMRR and reciprocating AMRR undergo the same thermodynamic processes in a periodic manner. The rotary AMRR, however, achieves periodicity by physical rotation of the magnetic solid through the various phases of operation, while the reciprocating AMRR achieves periodicity by applying the different phases at different times. At any given time, in the rotary AMRR, every phase of the cycle is being applied to some portion of the magnetic solid, whereas in the reciprocating AMRR only one phase of the cycle is being applied to every portion of the magnetic solid. From the point of view of the cold and hot heat exchangers where the cooling load is absorbed and rejected, respectively, the rotary AMRR has constant loads, whereas the reciprocating AMRR has periodic loads. This provides the rotary device with a distinct advantage for most cooling applications where constant cooling is preferred, as well as certain mechanical advantages from steady forces and constant work input.

Chapter 3

Literature Review

3.1 Introduction

The literature relevant to this work can be grouped into four broad categories:

1) Mathematical description of the operation of regenerators and methods of solution of the resultant coupled differential equations;
2) Flow maldistribution within regenerators;
3) Unbalanced and asymmetrical regenerator operation, and;
4) Application of regenerators to refrigeration devices: the Gifford-McMahon cycle and the active magnetic regenerative cycle.

Each of the above topics represents a large body of knowledge with significant overlaps between categories. Accordingly, the literature reported here is a small subset of that body of knowledge with a bias towards those which specifically pertain to the material in this work.

3.2 Regenerator Mathematical Models and Solution Methods

Mathematical models of regenerative heat exchanger thermal operation can vary from rather simple descriptions of the regenerator matrix only to complex descriptions including interactions of the regenerator with the surroundings, transient effects, more detailed descriptions of the solid-fluid interaction, heat diffusion within the solid matrix, and fluid viscous dissipation, for example. For the designer of systems employing regenerative heat exchangers, it is not always necessary to solve the full energy balance equations to predict a proposed regenerator design to an accuracy sufficient for initial design considerations. In these cases, empirical models based on previous solutions to the regenerator energy equations can be used.

3.2.1 Empirical Models

By assuming linear solid temperature profiles, Lubbock and Bowen [37] obtained a correlation for the thermal ratio of symmetric rotary regenerators. Tipler [38] later converted this correlation to dimensionless length and period to give the thermal ratio as a function of utilization and reduced length, *viz*:

$$\eta_{th} = \frac{1}{U}\mathrm{Tanh}\left(\frac{\Lambda}{\Lambda + 2}\right) \tag{3.1}$$

Comparing the thermal ratios obtained from Equation 3.1 with those obtained from Hausen's efficiency chart (reproduced in this work as Figure 1.9), Tipler concluded that the equation will produce an error of less than 4% when the dimensionless period is less than 10. This overstates the accuracy of the relation. The relative error between Tipler's correlation and Hausen's thermal ratio is shown in Figure 3.1, which shows progressively larger maximum error as the reduced period increases. Tipler's stated accuracy is only unconditionally achieved for reduced length greater than ~20.

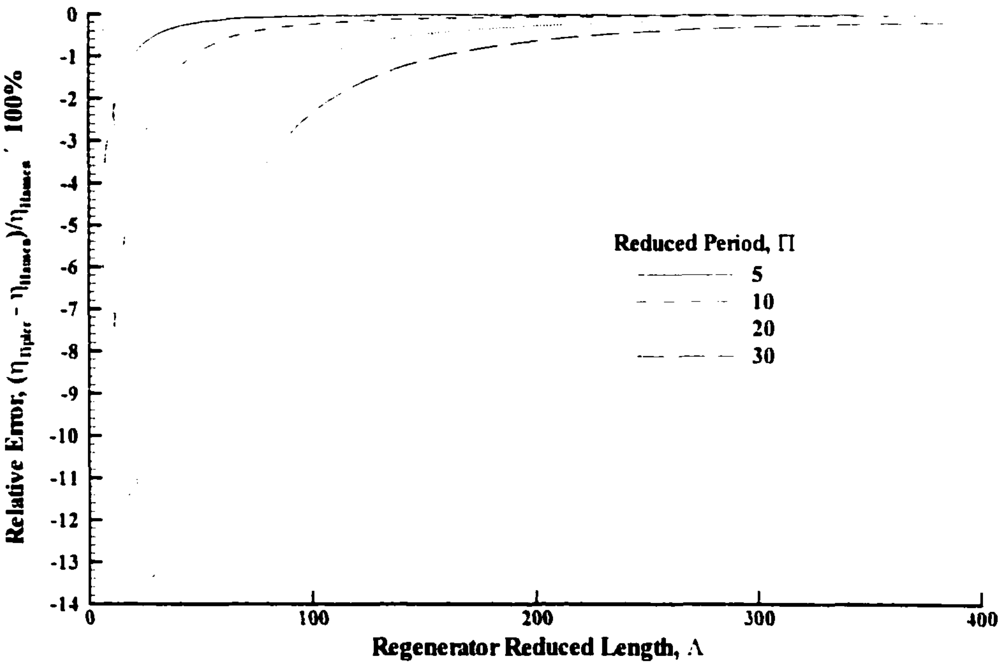

Figure 3.1 Relative error in Tipler's empirical correlation of regenerator thermal ratio compared to Hausen's thermal ratio.

Datskovskii [39] presented a similar empirical correlation for thermal efficiency as:

$$\eta_{th} = \frac{1}{U}\mathrm{Tanh}\left(\frac{F\Pi}{2}\right) \tag{3.2}$$

where:

$$F = \frac{B+1}{B+1+\Lambda} \qquad B = 1 + \frac{U}{2} \tag{3.3}$$

Hausen's results were used to determine the expression for B. The relative error of this expression compared to Hausen's results is shown in Figure 3.2. The magnitude of the relative error of this correlation is smaller than Tipler's correlation at low reduced length and larger at high reduced length.

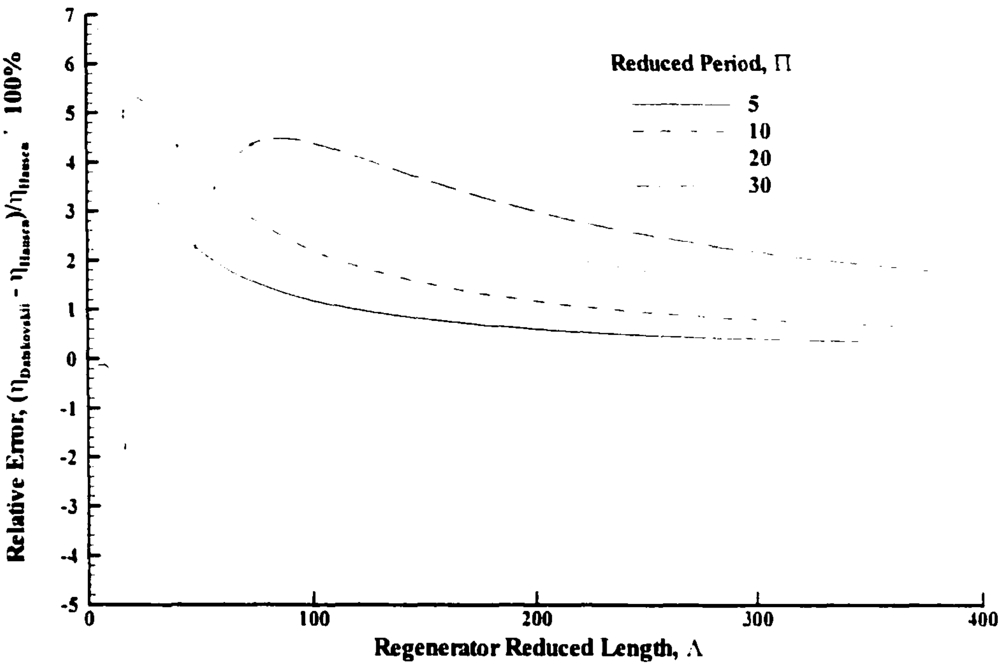

Figure 3.2 Relative error in Datskovskii's empirical correlation of regenerator thermal ratio compared to Hausen's thermal ratio.

The correlations of Tipler and Datskovskii are not readily applicable for cryogenic regenerator design applications due to the large errors exhibited and the simplicity of the underlying thermal model.

3.2.2 Energy Balance Models

With the assumptions of no viscous dissipation in the fluid, and uniform temperature of the constituent solid elements of the regenerator matrix, consideration of the energy balance within a representative volume of the regenerator will yield 2 coupled, partial differential equations over 3 dimensions of space and 1 dimension of time. Further application of the simplifying assumptions will reduce the number of dimensions.

There are two general methods to solve the regenerator energy balance equations which are commonly termed closed and open methods. The closed methods include analytical solutions and directly employ the reversal conditions within the mathematical model to determine the final cyclic-steady-state temperature profile without regard to earlier transient cycles. The open methods simulate the transient behaviour of the regenerator by evaluating the solid and fluid temperatures in successive cycles until cyclic-steady-state is reached.

Generally, for mathematical descriptions of systems, an analytical solution is the preferred method, since it usually provides the least computationally intensive means to the most accurate solution. Unfortunately, an analytical solution is only possible for the regenerator equations for the simplest (linear equation) description of operation, and cannot be used when the physical properties of the matrix and fluid vary with temperature (or other parameters).

3.2.3 Closed Methods

Hausen (1929)

The first analytical solutions to the partial differential equations describing cyclic regenerator operation is credited to Hausen [40] for his Eigen function method. His approach was to regard the temperature fluctuations which arise over a cycle at equilibrium as forced oscillations. The temperature profile is then a sum of the fundamental and harmonic oscillations, where the fundamental oscillation corresponds to the linear variation of temperature in the central portion of the regenerator, and the harmonics correspond to the non-linearities associated with the inlets.

Hausen considered the temperature within a brick element within the regenerator to vary with time. By considering the solid temperature reversal conditions, after some rather complicated manipulations, he determined the particular solutions for the fluid temperature. These solutions, the Eigen functions, are specific non-orthogonal functions, denoted as ϕ_k and ψ_k and contain the product of multiple exponential, trigonometric, and inverse trigonometric terms each having relatively complicated arguments. The gas temperatures can then be represented by the series:

$$T_f = \sum_{k=0}^{n} \alpha_k \phi_k + \sum_{k=1}^{n} \beta_k \psi_k \qquad (3.4)$$

The constants α_k and β_k are determined by the method of least squares by solution of the set of equations $\boldsymbol{Ax} = \boldsymbol{b}$ where the components of the matrices $\boldsymbol{A}$ and $\boldsymbol{b}$ are the results of integral calculations. After determination of α_k and β_k, and the Eigen functions for the solid temperature u_k and v_k, the solid temperature is given by:

$$T_s = \sum_{k=0}^{n} \alpha_k u_k + \sum_{k=1}^{n} \beta_k v_k \tag{3.5}$$

In this method, the advantage of the explicit formulation of the Eigen functions is offset by the complexity of calculating the constants α_k and β_k. Penney [23] cites an undergraduate paper that reports that the method breaks down for large values of reduced period (Π>4). Despite representing an analytical solution, the method is more computationally intensive than other closed schemes.

Hausen also developed the "heat pole method" of solution of the Equations 1.3 and 1.7.2 where he takes advantage of the linearity of the equations to build the final solution as the sum of the particular solutions to the equations after dividing the initial temperature profile in the regenerator into multiple independent sections [19]. The final temperature is determined individually for these sections and subsequently the final results are added together. The separation effectively divides the regenerator length Λ into N equal parts.

Hausen then calculates for each section the "excess" temperature for a blow period, Θ-θ_1, from the dimensionless bed temperature, Θ, and the temperature of the entry gas, θ_1, and denotes these excess temperatures as $f_1, f_2, \ldots f_N$. An individual section of unit height is termed a heat pole corresponding to an initial excess (dimensionless) temperature of Θ-θ_1=1, and outside the section, the excess temperature is 0. He considers first a heat pole at the first section. After a time, the progression of the heat pole through the regenerator develops a temperature distribution within the regenerator over all sections, and the resultant excess temperature is termed the heat pole function and denoted as $\Delta w_1, \Delta w_2, \ldots \Delta w_N$. From the average value of the heat pole function, he determines the influence of each individual section upon the final temperature distribution for each section downstream of the heat pole. The influence of the first heat pole in the first section on the final temperature in the N-sections is then:

$$f_1 \cdot \Delta w_1, f_1 \cdot \Delta w_2, f_1 \cdot \Delta w_3, \ldots, f_1 \cdot \Delta w_N \tag{3.6}$$

A heat pole function is then determined for the second section, and its influence on the downstream sections is determined:

$$0, f_2 \cdot \Delta w_1, f_2 \cdot \Delta w_2, \dots, f_1 \cdot \Delta w_{N-1} \tag{3.7}$$

When all the sections have had their heat pole functions determined, the total solution of excess temperature for a section is the sum of the influences from each heat pole.

$$\begin{array}{rl} \textbf{in the } \mathbf{1^{st}} \textbf{ section:} & \Theta_1 - \theta_1 = f_1 \cdot \Delta w_1 \\ \textbf{in the } \mathbf{2^{nd}} \textbf{ section:} & \Theta_2 - \theta_1 = f_1 \cdot \Delta w_2 + f_2 \cdot \Delta w_1 \\ \textbf{in the } \mathbf{3^{rd}} \textbf{ section:} & \Theta_3 - \theta_1 = f_1 \cdot \Delta w_3 + f_2 \cdot \Delta w_2 + f_3 \cdot \Delta w_1 \\ \textbf{in the } \mathbf{N^{th}} \textbf{ section:} & \Theta_N - \theta_1 = f_1 \cdot \Delta w_N + f_2 \cdot \Delta w_{N-1} + f_3 \cdot \Delta w_{N-2} + f_N \cdot \Delta w_1 \end{array} \tag{3.8}$$

The heat pole functions are determined either graphically by displacing the temperature curve by an amount equal to the section width and subtracting the difference between the original and displaced curves, or by integration of the solid energy balance equation between the limits of the section widths for each section.

An advantage of the heat pole method is that one can directly compute the temperature profile at the instant one is interested in during the blow period, without calculating intermediate temperature profiles up to that instant. The method is also suitable for determining the temperature distribution at the beginning of a period for the cyclic-steady-state condition. Both the Eigen function method and the heat pole method are outlined in greater detail in reference [19].

Iliffe (1948)

Iliffe [41] presents an alternative solution based on Hausen's heat pole method in which the integrals are numerically evaluated employing Simpson's rule. The major disadvantage of this method is ill-conditioning when the ratio of reduced length to reduced period, i.e., $\Lambda/\Pi = 1/U$, increases and is limited to $1/U < 3$ and $\Lambda < 10$ [42]. In particular, the set of equations representing the numerical integration becomes almost singular, and the solution is compromised by truncation errors associated with the integration rule, i.e., Simpson's rule, and accordingly, for a closed solution, the method of Nahavandi and Weinstein [43] is preferred [18].

Nahavandi and Weinstein (1961)

Nahavandi and Weinstein [43] present an analytical solution to the 2-dimensional regenerator equations presented in the form:

$$\frac{\partial^2 t}{\partial \xi \, \partial \eta} + \frac{\partial t}{\partial \eta} + \frac{\partial t}{\partial \xi} = 0 \tag{3.9}$$

where t is the temperature of the matrix, ξ is the dimensionless length for the fluid for the hot blow, and η is the dimensionless time during the hot blow. They solve Equation 3.9 using the method of Laplace transforms. Applying the transformation:

$$\tau_h = T_h \mathbf{exp}^{\xi + \eta} \tag{3.10}$$

where T_h is the temperature of the fluid during the hot blow, Equation 3.9 becomes:

$$\frac{\partial^2 \tau_h}{\partial \xi \, \partial \eta} - \tau_h = 0 \tag{3.11}$$

Letting the Laplace transform of the function $\tau_h(\xi,\eta)$ with respect to the variable ξ be represented by $\tau_h(s,\eta)$ gives:

$$s \frac{\partial \tau_h(s,\eta)}{\partial \eta} - \tau_h(s,\eta) = T_1 \mathbf{exp}^{\eta} \tag{3.12}$$

where T_1 is the initial hot fluid temperature. Equation 3.12 is a linear differential equation with respect to the variable η and can be integrated to give:

$$\tau_h(s,\eta) = c_1 \mathbf{exp}^{\eta/s} + \frac{T_1}{s-1} \mathbf{exp}^{\eta} \tag{3.13}$$

where c_1 is a constant of integration determined by the boundary conditions of the problem. They apply inverse Laplace transforms to each term to give the fluid and solid temperatures during the hot blow as:

$$T_h(\xi,\eta) = 1 - \mathbf{exp}^{-\xi-\eta} \int_0^{\xi} \left[1 - f(\varepsilon)\right] \mathbf{exp}^{\varepsilon} J_0\left(2i\sqrt{\eta(\xi-\varepsilon)}\right) d\varepsilon \tag{3.14}$$

and:

$$t_h = 1 - \exp^{-\eta}\left[1 - f(\xi)\right] + \exp^{-\xi-\eta} \int_0^{\xi} \left[1 - f(\varepsilon)\right] \exp^{\varepsilon} i \sqrt{\frac{\eta}{\xi - \varepsilon}}\, J_1\left(2i\sqrt{\eta(\xi - \varepsilon)}\right) d\varepsilon \qquad (3.15)$$

respectively, where J_0 is the Bessel function of the first kind and zero order, J_1 is the Bessel function of the first kind and first order, and $f(\xi)$ and $f(\varepsilon)$ are unknown functions to be determined from consideration of the reversal conditions. Similarly, the fluid and solid temperatures during the cold blow are given as:

$$T_c(\xi^*, \eta^*) = \exp^{-\xi^*-\eta^*} \int_0^{\xi^*} \left[f^*(\varepsilon)\right] \exp^{\varepsilon} J_0\left(2i\sqrt{\eta^*(\xi^* - \varepsilon)}\right) d\varepsilon \qquad (3.16)$$

and

$$t_c = \exp^{-\eta^*}\left[1 - f^*(\xi^*)\right] - \exp^{-\xi^*-\eta^*} \int_0^{\xi^*} \left[f^*(\varepsilon)\right] \exp^{\varepsilon} i \sqrt{\frac{\eta^*}{\xi^* - \varepsilon}}\, J_1\left(2i\sqrt{\eta(\xi^* - \varepsilon^*)}\right) d\varepsilon \qquad (3.17)$$

respectively, where the asterisks denote the values related to the cold fluid. Expressions for the unknown functions, $f(\xi)$ and $f(\varepsilon)$ are determined from the reversal conditions and are represented by their power series expansions, where the $2n$ coefficients of the power series are determined by $2n$ simultaneous equations representing n points chosen arbitrarily along the regenerator length.

Nahavandi and Weinstein provide an example of the solution procedure assuming that $f(\xi)$ and $f(\varepsilon)$ are represented by second order power series. They present results for values of n up to 7 for various combinations of dimensionless parameters and compare their results with those obtained by finite difference numerical techniques. They conclude that this closed form solution is obtained more rapidly than the finite difference technique.

de Monte (1999)

An analytical solution based on a Lagrange frame of reference is presented by de Monte [44] which considers the cyclic regenerator operation. His solution includes the flushing phase during a blow reversal and is suitable for applications where the time required for a gas particle to pass through the regenerator is approximately equal to the blow time. He expands on the concept of a flushing ratio presented by Organ [45, 46]. The generality is limited by the assumption of infinite thermal capacity of the regenerator matrix.

3.2.4 Open Methods

The open methods represent the regenerator energy balance equations in discrete form, and either directly or iteratively solve the resultant set of algebraic equations. The open methods can be used for the linear formulations of the regenerator equations, and must be used for most non-linear formulations. Non linearities have been catagorised by Kulakowski and Anielewski [47] and further expanded upon by Penney [23] as belonging to one of three groups:

1) Natural,
2) Constructional, and
3) Operational.

Natural non-linearities arise due to temperature dependent physical properties for the fluid and matrix, such as temperature dependent heat capacity or temperature dependent heat transfer coefficient by virtue of the temperature dependence of viscosity and thermal conductivity in its correlation, for example.

Constructional non-linearities arise principally from longitudinal zoning of different materials such as those used in cryogenic applications, where regenerators with separate zones of phosphor-bronze and lead are used to help compensate for the reduced heat capacity of the phosphor-bronze at low temperature. Changes between zones could also include changes in heat transfer area and porosity, for example. Last, non-uniform (but constant) flow due to inlet headers or non-uniform porosity would also be considered constructional non-linearities.

Operational non-linearities are due to changes in the control strategy for the regenerator, such as variable inlet flow rate, temperature, or composition for the fluid.

Some of the closed methods can directly accommodate constructional non-linearities, depending on the formulation, if the reduced length and reduced period are considered functions of position and time. Some closed methods can also accommodate the natural non-linearities, but must be iterated to ensure the physical properties evaluated at the solution temperatures match to some degree of accuracy the physical properties initially assumed. The iteration procedure used with the closed method does not give a transient solution, but rather ensures the correct evaluation of the physical properties corresponding to the ultimate temperature profiles.

Lambertson (1958)

Lambertson [48] presents a finite difference model for calculating the effectiveness of regenerators by considering the metal matrix "stream" in crossflow with each of the gas streams as two separate but dependent exchangers. The concept of crossflow streams derives from the axial flow rotary regenerator for gas turbine applications. Lambertson derives a heat balance on an element and expresses the element "outlet" temperature in terms of the "inlet" temperature and the heat transferred across the element. He solves the resulting equations for each element by successive substitution until cyclic equilibrium is established. He solves the equations on progressively finer grids and extrapolates the results to grid elements of zero area.

Willmott (1964)

Willmott [49] expressed the regenerator energy balance equations in finite difference form and integrated them using the Trapezoidal rule. The technique is equivalent to that presented by Lambertson.

Schmidt and Willmott (1981)

Schmidt and Willmott [18] summarize and critique several open and closed methods for calculation of regenerator temperature profiles and thermal ratio. The models include single blow operation under a variety of simplifying assumptions including infinite fluid thermal heat capacity, negligible or non-negligible internal temperature gradients within the matrix packing elements, as well as varying fluid inlet temperature and matrix geometry considerations. More complex models are presented for cyclic operation including unbalanced operation, radiation heat transfer, and variable inlet fluid flow rate. The calculation methods include acceleration techniques and stability requirements. Schmidt and Willmott also present regenerator optimization techniques and a variety of pressure drop and heat transfer correlations.

3.3 Regenerator Flow Maldistribution

Penney (1987)

Penney [23] undertook a modelling approach to examine the effects of maldistribution of fluid flow through regenerators and compared those results to an experimental rig. He considered the discrepancies between experimental regenerator fluid exit temperatures and those gained from simulations using "classical" or simplified Λ-Π models and suggests that modifications to simulation parameters, most notably the heat transfer coefficient, are unnecessary if maldistribution is incorporated into the thermal model.

Penney offers several flow distribution models, such as linear, quadratic, and exponential variation with radial position, as well as directly measured distributions from an experimental rig. Maldistribution is considered to arise from non-uniformity of void space, such as by random variations and packing effects at walls, and by non-uniformity of initial inlet flow, such as jetting from headers. Penney summarizes several researchers' efforts to obtain a representative flow profile, primarily from packed beds, considering the ratio of bed diameter, *D*, to particle diameter, d_s. He summarizes the essential features of the profiles as:

1) the existence of a maximum of the velocity profile between $d_s/4$ and $3d_s/2$ from the wall;
2) the value of the maximum is usually at least 20% higher than the average velocity;
3) the velocity profile is nearly uniform for $D/d_s \geq 50$;
4) the velocity profile pattern is often similar to that of the voidage profile.

The maldistribution is simulated in Penney's models by considering a division of the original regenerator into a number of equal-area annular sub-regenerators operating in parallel, each with its own proportionate share of uniform fluid flow. He considers any interaction between the sub-regenerators, such as inter-sub-regenerator heat transfer due to thermal gradients from differing temperature profiles developing along each of the regenerators' lengths, to be negligible if the local thermal gradient between regenerators is smaller than the local gradient along the regenerators' lengths. Fluid mixing occurs only at the exits of the regenerator where the net fluid exit temperature is calculated from a consideration of a mass-weighted fluid energy balance summation over the sub-regenerators.

A simulation of the fluid outlet temperatures of the original regenerator with a modified heat transfer coefficient and uniform fluid flow is compared to the sub-regenerators with the unmodified heat transfer coefficient and the proposed flow distribution. Either the heat transfer coefficient is multiplied by an "f-factor", or the flow maldistribution "m*" is modified until a best fit agreement between the simulations is made. Penney also compares the fluid outlet temperatures from the experimental rig with the regenerator simulations of maldistributed flow.

Penney uses a heat transfer correlation for packed beds given by Denton [50] and expressed as:

$$h = 0.72\, C_f G\, Re^{-0.3} \tag{3.18}$$

where C_f is the heat capacity of the heat transfer gas, G is the mass flux per unit free flow area, and Re is the Reynolds number given as:

$$Re = \frac{G D_p}{\mu} \tag{3.19}$$

where D_p is the bed particle diameter and μ is the heat transfer gas viscosity.

Penney defines performance deterioration expressed as a percentage value, *viz*:

$$p = \frac{\eta_{uniform} - \eta_{mal}}{\eta_{uniform}} \times 100 \tag{3.20}$$

where $\eta_{uniform}$ is the thermal ratio of the original regenerator whose behaviour is parameterized by Λ and Π and η_{mal} is the thermal ratio of the maldistributed flow regenerator. He finds that performance deterioration is "relatively small" and will be less than 1% for the typical operation of industrial regenerators ($15 < \Lambda < 25$ and $\Pi = 1$) where the fractional mass flows in each sub-regenerator are given as 0.04, 0.12, 0.20, 0.28, and 0.36 based on a worst-case flow maldistribution of $m^*=1$ for a quadratic fluid velocity profile given as:

$$v(x) = M\left(1 - m^*\right) + 2Mm^*x^2 \tag{3.21}$$

He summarizes that to compensate for the effects of maldistribution by lengthening the regenerator, an increase of approximately 11% is required. Similarly, he finds the performance reduction is equivalent to a 10% reduction in the heat transfer coefficient. He notes that at large lambda the severity of the performance deterioration is decreased, but the degree of compensation required to recover the expected performance is increased.

Penney finds that practical design considerations, such as the use of conical entrance and exit regions to distribute flow over the area of the regenerator bed, will not be particularly effective unless the conical regions have a semi-angle near the "optimal" value of 11° cited by McAdams [51]. This suggestion is based on his observations of the flow within his experimental rig.

Penney's work is a rich resource summarizing heat transfer coefficients obtained by other researchers for various packing geometries, primarily for block and chequerwork packings for high temperature regenerators. He presents a literature review summarizing efforts to measure flow maldistribution and its effects. He also provides a summary and review of various methods of solution of the regenerator energy balance equations.

Chang and Chen (1998)

More recently, Chang and Chen [52] have examined the effect of flow channelling on a regenerator's thermal performance. Using a single-blow apparatus, they measured the gas velocity across the exit and gas exit temperature for stacked screens with different amounts of screen oversize within the regenerator housing. Their temperature measurements were compared to a 1-dimensional, single-blow regenerator model to determine the effective heat transfer coefficient.

Their measured velocity profiles show an increased flow at the outer radius near the regenerator housing, which they note are similar to the results of Jones [53]. They follow the procedure of Jones to conceptually divide the regenerator into two concentric regenerators with homogeneous flow operating in parallel. The submatrices are assumed to have the same screen wire diameters, but different porosity. The ratios of the heat transfer coefficients in the two regions of the inhomogeneous regenerator to that of a well-packed matrix are given based on the ratio of flow velocity and the ratio of the areas of the two regions. The ratio of the measured heat transfer coefficient in the inhomogeneous matrix to that in the homogeneous matrix from the numerical model for equal total flow is then calculated to determine the relative reduction in heat transfer coefficient as a result of the flow channelling.

Results are presented for 3 regenerator configurations, A, B, and C, which differ in the amount of oversize of the screen compared to the regenerator housing, and, as a result of the compaction into the smaller diameter housing, also differ in porosity and hydraulic diameter. The wire screen diameter is held fixed, and is packed into successively smaller diameter housings, such that the screens are larger than the housings by 0.263%, 1.871%, and 2.973%, respectively. The ratios of heat transfer coefficients of the regenerators A, B, and C to that of the well-packed (i.e. uniform) matrix are 0.90, 0.94, and 0.97, respectively. They conclude that flow channelling does reduce the thermal performance of the regenerator, and that using oversized screens is a viable remedial measure to reduce the degree of flow channelling.

3.4 Unbalanced Regenerators

Several researchers have studied the effect of unbalance on the regenerator thermal ratio. The data are typically presented as a function of four dimensionless parameters. Most straight-forward of the possible choices for the four dimensionless parameters is the selection of reduced length and reduced period for both hot and cold blows. That is, the thermal ratio can be presented as:

$$\eta_{th} = fn\left(\Lambda', \Lambda'', \Pi', \Pi''\right) \tag{3.22}$$

It is equally valid to present the thermal ratio as a function of the possible combinations of these parameters, and accordingly, it can be presented as a function of hot and cold reduced lengths, the hot (or cold) utilization, and the unbalance factor, *viz*:

$$\eta_{th} = fn\left(\Lambda', \Lambda'', U', \beta\right) \tag{3.23}$$

Kays and London (1964)

Kays and London [54] present the ineffectiveness curves for a regenerator where the gas heat capacity rates are different for the hot and cold blows. Using the nomenclature of this work, their data are presented as:

$$Ie = fn\left(\Lambda_{min}, \frac{\Lambda_{min}}{\Lambda_{max}}, \frac{\Lambda_{min}}{\Pi}\right) \tag{3.24}$$

where Λ_{min} and Λ_{max} are the minimum and maximum values, respectively, of Λ' and Λ'', $\Pi' = \Pi'' = \Pi$, and is reproduced as Figure 3.3.

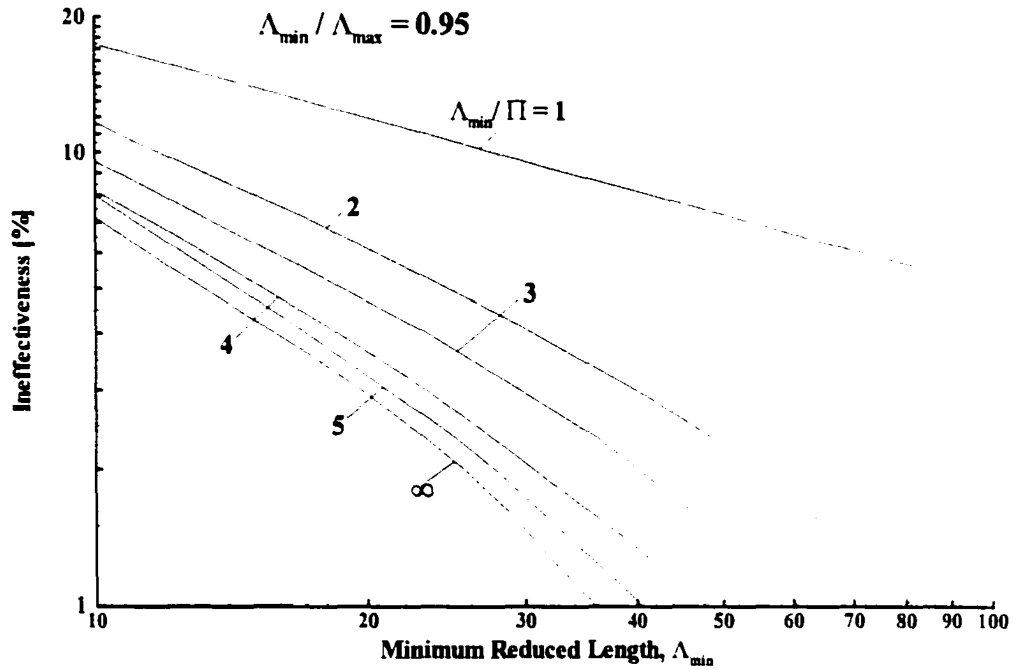

Figure 3.3 Regenerator ineffectiveness as a function of minimum reduced length (after Kays and London [54]).

Since the thermal efficiency is a function of four parameters, it is difficult to clearly represent all possible regenerator combinations on a single chart. Hausen [55] recommended the use of harmonic mean parameters to describe an unbalanced regenerator. The harmonic means are given by:

$$\Lambda_{har} = \frac{2}{1/\Lambda' + 1/\Lambda''} \qquad (3.25)$$

and

$$\Pi_{har} = \frac{2}{1/\Pi' + 1/\Pi''} \qquad (3.26)$$

The thermal ratio of the regenerator in question is then given by the harmonic symmetric balanced regenerator whose thermal ratio is given in Figure 1.9. Using a closed analytical solution, Kern [56] shows that the harmonic mean values suggested by Hausen over-estimate the regenerator's true thermal ratio. Kern suggests that it is more appropriate to use exponential averages given by:

$$\Lambda = \coth\left(\frac{1}{\dfrac{1}{\exp(\Lambda') - 1} + \dfrac{1}{1 - \exp(\Lambda'')}}\right) \qquad (3.27)$$

and

$$\Pi = \coth\left(\frac{1}{\dfrac{1}{\exp(\Pi') - 1} + \dfrac{1}{1 - \exp(\Pi'')}}\right) \qquad (3.28)$$

Mitchell (1982)

Mitchell [24] examines the asymmetrical and unbalanced regenerator and compares results in graphical form with those of several other researchers. His motivation is the optimization of a high temperature regenerator system to achieve a constant exit temperature with time for the cold blow period by combining a time-varying proportion of flow from the regenerator with an external flow. The hot blow proceeds as usual without modifications. The application is for an air supply stream for a blast stove, where a constant exit temperature from the combined regenerator and external flow simplifies the furnace design.

Mitchell points out that a limitation of the methods which correlate an unbalanced and asymmetrical regenerator with a symmetrical and balanced regenerator is that only a single value of thermal ratio is obtained. In practice, the thermal ratios for the hot and cold blow periods can be substantially different, and a method which hides this fact, such as Hausen's and Kern's methods above, will misrepresent the thermal ratio important to the designer. He states that when one stream can be considered a process stream, and one stream a waste stream, a high thermal ratio is only required for the process stream.

Since the thermal behaviour of one stream is dependent on the thermal behaviour of the other stream, being coupled through the regenerator matrix thermal performance, Mitchell's statement above is a bit of a simplification, but this perspective is correct when regarding the regenerator as a black box device. For a GM regenerator, for example, one is not so concerned with the cold blow exhaust gas temperature, since that is expelled from the cooler, but rather with the hot blow gas exit temperature. The lower the hot blow exit temperature, the lower will be the gas temperature, and hence cold head temperature, after gas expansion.

Yang *et al.* (1999)

Both eliminating and enhancing the regenerator unbalance in pulse tube refrigerators has been the focus of several recent papers. Yang *et al.* [57] describe their efforts through simulation and experimentation to reduce the unbalanced flow in a double inlet orifice pulse tube. They find that the second inlet, which connects the warm ends of the pulse tube and regenerator through an orifice valve, allows a net flow from the regenerator through the orifice and into the pulse tube. This gives more mass flow through the regenerator during a cold blow than a hot blow. By addition of another orifice valve, they find that they can minimize the flow imbalance and increase the cooling capacity of their pulse tube apparatus.

Wang *et al.* (1998)

Wang *et al.* [58] also examine unbalanced flow in a single-stage pulse tube cooler. They find that an almost zero, slightly negative flow, i.e. a greater hot blow than cold blow flow, improves the cooling performance. They present the calculated temperature profiles in the regenerator under various unbalanced flow conditions derived from a previous model [59], and recommend that unbalanced flow be minimized. They contrast these results with those for another work describing a lower temperature, two-stage, 4 K pulse tube [60], and note that the direction of unbalanced flow has the opposite effect between the regenerators of the two coolers. For the 4 K, pulse tube, they find optimal performance with a significant unbalance and recommend that unbalance not be zero. From these results, it would appear that the optimal unbalance for pulse tubes is dependent on the system and temperature span reached.

3.5 Regenerators Applied in Refrigeration Cycles

There are many refrigeration cycles that employ passive regenerative heat exchangers, such as the Stirling, reverse Brayton, Solvay, Vuilleumier, Ericsson, Gifford-McMahon (GM) and pulse tube cycles, for example. The active magnetic regenerative refrigerator employs a magnetocaloric material as the regenerator matrix, allowing the regenerator to perform both the cycle work input function and the thermal regeneration function. Recently, an experimental apparatus employing a hybrid cycle has been described by Nellis and Smith, Jr. [61], based on earlier theoretical work [62], where the 2^{nd}-stage regenerator of a GM refrigerator is composed of gadolinium gallium garnet, a magnetocaloric material, which allows the cooling effect to be achieved by gas expansion of the GM cycle or adiabatic demagnetization of the regenerator material, or any combination of the two effects. The success of the hybrid device suggests that the list of regenerator innovations and applications will continue to grow.

3.5.1 Regenerators in GM Systems

For both GM and AMR systems, the primary focus of recent research has been on the development of better regenerator materials and improved system designs to achieve larger cooling capacities and larger temperature spans. For GM systems, several approaches have been taken. One method has been to improve the regenerator effectiveness by increasing the low-temperature heat capacity of the matrix by employing alloys which exhibit a magnetic phase transition at low temperature. The majority of these materials have combined a lanthanide series metal such as neodymium, gadolinium, dysprosium, holmium, erbium, or ytterbium with elements such as nickel, cobalt and aluminum. The magnetic transition temperature, and hence the temperature range in which these materials are most effective, is a function of the elements selected and alloying ratio employed. Examples of these materials exhibiting a heat capacity spike at low temperature are Er_3Ni, $ErNi_{0.9}Co_{0.1}$, $HoCu_2$, and elemental Nd.

Gschneidner, Jr. *et al.* [63] have compared the low temperature heat capacities of Pb, Nd_3Ni, and Er_3Ni to four new materials given as the ternary alloys Er_6Ni_2Sn, Er_6Ni_2Pb and 50:50 Er_6Ni_2Sn/Er_3Ni and the quaternary alloy $Er_6Ni_2(Sn_{0.75}Ga_{0.25})$. They suggest that these new alloys would be superior to Pb and Er_3Ni for regenerative cryocoolers operating down to ~10 K because of their larger heat capacities below 18 K. They label the Er_6Ni_2Pb as the best material of the four studied, citing a low melting point, stability in ambient room temperature conditions, and less brittleness than Er_3Ni.

While these rare-earth intermetallic materials exhibit a larger heat capacity at low temperature compared to Pb, no single material has the highest heat capacity over the usual temperature span of the 2nd-stage regenerator from ~2 K to 40 K. A number of researchers have employed layered beds composed of 2 or more layers of materials in the 2nd-stage regenerator. Hashimoto *et al.* [64] expanded on earlier experimental work by Hashimoto *et al.* [65] and examined the theoretical effectiveness of a regenerator composed of increasing numbers of layers of materials where each material was positioned within the regenerator so its expected temperature range corresponded with its peak heat capacity.

They examined various arrangements of the materials ErNi, Er_3Ni, $Er_{0.9}Yb_{0.1}Ni$, Er_3Co, and $ErNi_{0.8}Co_{0.2}$ and found that the best performance would be obtained using the largest number of layers so that each material operated only in its range of largest heat capacity. They compared their theoretical effectiveness values with the published cooling capacities of GM systems employing the same regenerator constituents and projected a cooling capacity of 1.2 W at 4.2 K from their four-layer design, a 12% improvement over the reported three-layer bed GM capacity. Similar systematic investigations of the optimal distributions of regenerator materials were performed by Lang *et al.* [66], including measurements of the temperature distributions within the regenerators to provide confirmation of the appropriateness of the selection of material distributions.

In conjunction with the replacement of the 2nd-stage regenerator materials, improved fabrication techniques have been employed to reduce flow maldistribution, pressure drop, and regenerator porosity. Chafe and Green report on the performance of embossed neodymium ribbon [67] and chemically etched perforated disks [68,69] in the 2nd-stage of a GM system. The ribbon was produced by rolling Nd wire through two cylindrical rolls, where one roll was embossed with the desired ribbon pattern. Two ribbon patterns were tested for pressure-drop characteristics and cooling performance. One ribbon was superior in both instances to the baseline comparison to spherical Nd powder, while the other ribbon was inferior in both instances. Their work on etched disks demonstrated only slightly higher pressure drop for the disks than for packed spheres. This is despite the fact that the disks had significantly lower porosity of ~10% compared to spheres at ~35% porosity. Using the disks in the 2nd-stage regenerator provided greater than 40% increase in cooling power at 4.5 K compared to the standard production unit containing Nd spheres originally shipped in their test unit. Yaron *et. al.* [70] have produced foils using chemical etching that have a similar geometry to Chafe and Green's embossed ribbon for regenerators and showed increased cooling performance compared to screens in a pulse tube refrigerator.

Others have approached the task of improving the minimum no-load temperature and cooling capacity of GM systems by optimization of the valve timing for the pressure buildup and expansion phases, such as the work by Li *et al.* [71], and by increasing the conductance of the expanded cold gas to the cold head such as by Inaguchi *et al.* [72]. The first technique improves the pressure-volume characteristics of the cycle and the heat transfer within the regenerator and cold space, while the second technique more effectively transfers the cooling capacity of the gas to the cold head load.

Models of the regenerator in GM systems include those cited above where a thermal analysis of the regenerator is performed for various arrangements of regenerator materials, as well as combined thermal and fluid analyses. Wang *et al.* [73] describe a one-dimensional, transient model of a two-stage GM encompassing conservation of mass, momentum, and energy equations for a sinusoidal displacement of the regenerator/displacer. Gas properties are considered a function of temperature and pressure, and properties of the matrix are a function of temperature. Axial conduction is considered negligible and the wall temperatures of the 2nd-stage cold space and cold end heat exchanger are considered constant. Flow through the intake and exhaust valves is determined using a formula for a convergent nozzle with a correction factor. They employ the staggered grid approach for the discretization of the momentum equation on a non-uniform spatial grid. The discretized form of the equations solved are presented and solved using a tri-diagonal matrix algorithm. Results of the calculations show good agreement between the model and their experimental apparatus for the pressure-volume diagram for the 2nd-stage cold space.

3.5.2 Regenerators in AMR Systems

For increasing cooling capacity and temperature span in AMR systems, one area of research has been to increase the magnetocaloric effect and "tune" the Curie temperature of the regenerator materials. Gschneidner *et al.* [74] describe the alloy $Gd_5(Si_xGe_{1-x})_4$ which exhibits what they term a "giant" magnetocaloric effect and a magnetic ordering temperature that is a function of the ratio of silicon to germanium. They note a sudden, sharp difference in behaviour in the material as the silicon fraction exceeds the germanium fraction at x = 0.5, which they attribute to a change in the chemical bonding within the material. Their prediction of the expected magnetocaloric effect was calculated from the maximum entropy change based on their total entropy curves. Giguère *et al.* [75] directly measured the adiabatic temperature change of a sample of $Gd_5Si_2Ge_2$ prepared by Ames Laboratory via arc melting using high purity constituents. They found the magnetocaloric effect lies in the same range as that of Gd and its alloys and attribute the difference in the calculated adiabatic temperature change predicted by Gschneidner *et al.* and their direct measurements to the methodology employed in the prediction. Despite these discrepancies in reported properties, the $Gd_5(Si_xGe_{1-x})_4$ alloys are likely to be useful materials for magnetic regenerators.

Pecharsky and Gschneidner, Jr. [76] summarize the best available materials in the range of ~10 K to ~80 K and describe recent cooling performance results for a linear, dual-bed AMR operating near room temperature using gadolinium as the working material.

3.5.3 Magnetic Regenerator Modelling

Several numerical models of magnetic regenerative systems have been described in the literature. The models include active regenerators performing the work and heat functions and passive regenerators thermally tied to the working magnetic material. The magnetic cycles described include Carnot, Ericcson, reverse Brayton, Stirling, and AMR cycles. Amongst these differences, three key features of the various models can be summarized.

First, two techniques have been employed to account for the magnetocaloric effect of the regenerative material. The first technique can be regarded as a superposition of temperature. Upon application and removal of the applied magnetic field, the adiabatic temperature change of the material is added to the temperature profile of the regenerator bed between blow periods. In effect, a perfectly adiabatic magnetization or demagnetization is achieved and superimposed on temperature profiles calculated using the usual regenerator modelling techniques. The second technique can be regarded as a direct implementation of the magnetization and demagnetization temperature changes. In this case, the regenerator energy balance equations contain terms representing the magnetocaloric effect and the magnetization and heat transfer interaction are solved directly during the thermal solution for the solid. The direct implementation is a better approximation to the porous bed AMR system, since practical limitations on the magnetization process limit magnetization ramp rate and thus the process is not perfectly adiabatic by virtue of heat transfer with the entrained fluid. The direct implementation is slightly more complicated to implement in the numerical model.

Second, the pressure drop within the regenerator is determined either by including a solution of the continuity and momentum equations with the energy equations or by separate calculation based on empirical correlations. The empirical correlations are significantly simpler and are generally employed when the internal regenerator geometry is not uniquely specified, such as in the case of random packed spheres. Some models employ a hybrid scheme where the discretized momentum equations are solved with an additional momentum source term based on an empirical correlation applied to the flow conditions over a small volume. Solution of the continuity and momentum equations is usually included in the low temperature AMR models, $T \leq 20$ K, where the properties of the heat transfer gas, helium, change rapidly.

A third key feature of the various models is the method of discretization of the equations and solution algorithm employed. Typically, finite difference and finite volume formulations are reported in the literature, and an example can be found of a finite element formulation. The model reported in later chapters of this work employs a commercial package using a combined finite element, finite volume formulation. In many cases, the governing equations are clearly defined in the publication but the solution procedure, other than a statement of how the equations generally may be solved, is not given.

Using the above guidelines, several magnetic regenerator models can now be described.

DeGregoria [77] describes two time-dependent one-dimensional models of the active magnetic regenerator. The first model implements the magnetocaloric effect directly, while the second employs the superposition method for equations applicable in the infinite bed mass limit (i.e. zero reduced period). He cites the computational intensiveness of the direct implementation as the motivation for the superposition method. In both models, the heat transfer coefficient is obtained using empirical correlations for packed beds. Variations in properties with temperature for the heat transfer gas and the magnetic material are accounted for. The pumping losses, thermal conduction across the bed, and axial dispersion are taken into account separately. DeGregoria presents results for a $GdNi_2$ regenerator bed operating between ~57 K and ~77 K, including temperature profiles over the cycle and cooling power as a function of heat transfer fluid mass flow for a 7 Tesla applied field change. Gregoria's model was later modified to allow specification of multiple materials which is reported by Schuricht *et al.* [78] showing improved cooling capacity and efficiency compared to a single refrigerant material.

Zhang *et al.* [79] presents a summary of reported work on magnetic refrigeration devices for the temperature ranges of 0.1-1.5, 1.5-4.2, 4.2-20, and 20-77 K, in addition to those in the neighbourhood of 300 K. They also present a computer model of a one-stage reciprocating Carnot cycle magnetic liquefier for helium operating between 15 K and 4.2 K using the material gadolinium gallium garnet. They include effects of eddy currents, seal friction, and conduction in their model. Their results include the separate graphs of net cooling capacity as a function of applied magnetic field, reciprocating frequency, hot sink temperature, eddy current heat, and frictional work. They draw several conclusions from their studies and extend their results to a three-stage hydrogen liquefier system operating between 20 K and 77 K. The same authors present an analysis of the exergy losses of the hydrogen liquefier system in a separate publication [80].

Green *et al.* [81] describe a computer model for a stack of gadolinium pancake ribbons for an AMR cycle with internal regeneration in the magnetic material and external regeneration of the heat transfer fluid in a closed heat transfer fluid circuit. They used a modified commercial finite-element program, NASTRAN [82], to perform a transient thermal analysis between the magnetization and demagnetization steps for three scenarios of field and pancake design to examine the effect of field uniformity and thermal conductance along the pancake stack. Material properties for the gadolinium were obtained from experimental data of the adiabatic temperature change from Benford and

Brown [34]. Noting that the single material restricted the expected temperature span, they further modelled a composite bed composed of pancakes of dysprosium, terbium, and gadolinium in the ratios of 1:2:3, from cold end to hot end, respectively. With the composite regenerator, a 160 K temperature span was predicted. They present results of the corresponding experimental apparatus which achieved a 54 K temperature span from 300 K.

Green and Schroeder [83] later described the implementation details of the NASTRAN model in more detail, in particular their techniques to overcome the NASTRAN's inability to model nonlinear material properties or prescribed temperatures during a transient analysis . To model a complete test run, they employed a sequence of NASTRAN analyses, with the output of one sequence used to describe the input of the next. Each analysis modelled one "stroke" of the cycle, consisting of either a hot blow or a cold blow. In between successive strokes, the adiabatic temperature change was added to the temperature profile of the magnetic material. They used one-dimensional heat conduction elements to model the refrigerant, copper regenerator, chamber walls, and fluid for the model. Heat transfer between the fluid and the refrigerant, copper regenerator, and chamber walls was modelled using surface conduction elements. They compared their simulation results to their corresponding experimental apparatus and found reasonable agreement. The same modelling technique was later applied to a new experimental apparatus designed to provide greater cooling [84].

Carpetis [85] describes a transient, one-dimensional model that directly employs the magnetocaloric effect in the energy balance equations. He solves the equations using a bi-tridiagonal matrix algorithm, for the refrigerants Gd, GdNi, and Er and explores the maximum efficiency and cooling power as a function of heat transfer fluid flow per period. According to his results, the maximum power density and maximum efficiency occur at different optimal fluid flows. Pressure drop losses are not calculated in the model, and are considered externally. Carpetis also presents theoretical performance results for a Gd nanocomposite material, where the magnetic species are in the form of magnetically interacting nanometre-sized clusters of atoms dispersed in a nonmagnetic matrix. He predicts that the nanocomposite material allows superior performance, either by increased temperature span, cooling capacity, or reduced system expense and complexity from a greater response at lower applied fields.

A finite difference numerical model of the thermal operation of a rotary active magnetic refrigerator formed the basis of a Master's thesis by Spearing [86] and its methods and results are employed and extended in this work. The model assumed a pseudo-2-dimensional fluid flow through a porous regenerator ring composed of magnetic refrigerants that rotated through a magnetic field. The pseudo-steady-state energy balance equations for the fluid and the magnetic solid were given in dimensionless form for a radial flow design. The magnetocaloric effect was directly represented in the energy balance equations. The model included the effects of normal and tangential (circumferential and radial) conduction of the solid and fluid, in contrast to the commonly employed assumptions of zero conduction normal to the fluid flow and zero (or finite) conduction tangential to the fluid flow. Also included in the model were electrical eddy current power dissipation and fluid thermal conductivity eddy diffusivity effects. Pressure drop losses were considered externally to the model. Three solution methods and the benefits and drawbacks of each were presented. Limited results for active and passive regenerators were given, and concerns regarding a lack of perfect global energy conservation were left for future work.

The lack of global energy conservation can be traced to some conflicts in the model assumptions and the non-conservative formulation of the differential equations. The largest error in the global energy conservation stems from the incompatibility in the assumption of heat transfer fluid density being a function of local temperature and the fluid flow being pseudo-2-dimensional. The pseudo-2-dimensional fluid flow is described by independent flow in the radial and circumferential directions. The radial flow is due to the hot and cold blow fluid flows and is assumed evenly distributed over the flow region with no accumulation. The circumferential flow is due to entrainment of the fluid within the pores of the matrix material and its velocity is described by the rotation of the solid only.

The incompatibility of these flow assumptions arises when the mass of fluid entrained within the pores is allowed to change as a result of fluid density changes resulting from temperature changes across a hot or cold blow zone during normal operation. Since the circumferential and radial flows are independent and fixed, neither flow can contribute to the accumulation (or reduction) of fluid entrained within the pores. This results in an implicit violation of mass conservation, which in turn results in a violation of global energy conservation.

For large temperature spans, there can be a large change in heat transfer fluid density, and a mass-conservative assumption of constant density may not be appropriate. In this case the simplicity of the pseudo-2-dimensional fluid flow can be maintained, while considering the density variations by implementation of a density profile that is a function of the average temperature circumferentially at a given radius. That is, density will be a function of radius based on the average cycle temperature for the radial position, and will not be a function of circumferential position. The variation in temperature radially will typically be several times the variation in temperature circumferentially, so this approximation maintains the essence of temperature dependent density without violating mass conservation in the simplified flow field.

The non-conservative formulation of the energy balance equations contributes to the global energy imbalance. A non-conservative formulation implies a certain energy flux into and out of a given differential volume. The difficulty arises when the implicit flux out of one volume is not equal to the implicit flux into the adjacent volume. At convergence of the numerical solution, each local conservation equation is satisfied, but the global conservation might not be. Ideally, the energy balance equations should be represented by a conservative formulation; however the non-conservative formulation can be acceptable given sufficient grid resolution for the operating conditions considered.

The number of grid points required for a sufficient global energy balance increases as the reduced length increases and as the utilization factor decreases. Nahavandi and Weinstein [43] point out a similar requirement of their analytical solution procedure for passive regenerators where higher order polynomials are required to describe the matrix temperature distribution at higher reduced length. They attribute this to the asymptotic approach to the thermodynamically limiting temperature requiring higher order curves to represent the actual temperature distribution. Similarly, then, in the case of the numerical solution on a uniform grid, more grid points are required near the boundaries to represent the higher order curve for the higher reduced length and lower utilization regenerator designs. A small error in the representation of the curve at the boundaries, and the resultant error in the fluid exit temperatures, can cause a large error in the global energy balance even though the overall temperature profile and work input are well represented by the model.

3.6 Applications of Unbalanced Regenerators

3.6.1 Boreas Cryocooler

The Boreas Cryocooler is an extension of the GM refrigerator utilizing high pressure ratios and combined counterflow recuperative and regenerative heat exchange in the upper stages and counterflow recuperative heat exchange almost exclusively at the coldest stage [87]. A schematic diagram of the Boreas cryocooler is given in Figure 3.4. Three expansion stages are provided within a concentric heat exchanger. At the upper two stages, the heat exchanger wall and displacer act as a gas gap regenerator. At the lower stages, the low heat capacity of the wall precludes the gap regenerator from achieving effective thermal regeneration. An electromechanical valve is positioned in the cold expansion space of the last stage, connecting the expansion volume to a cold buffer volume. The cold gas in the final stage is cooled recuperatively by the high heat capacity, low pressure gas stream returning from the cold buffer volume. The operation of the cycle is similar to a GM cycle, except that the cold exhaust valve is opened during the expansion phase, allowing a liquid fraction to enter the cold buffer where it is vaporized by the cold head load.

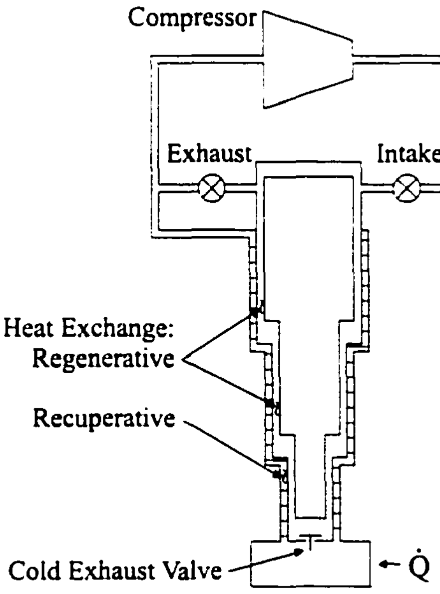

Figure 3.4 Schematic diagram of the Boreas cryocooler.

The design and concept of the Boreas cryocooler are similar to the Bypass GM cryocooler, but the purpose of the bypass stream is different. For the Boreas cryocooler, the bypass stream is provided to overcome the 3^{rd}-stage regenerator limitations imposed by low heat capacity matrix materials at low temperatures. The low pressure helium bypass stream has a high heat capacity and effectively replaces solid-fluid regeneration with fluid-fluid recuperation to precool the gas in the final stage before expansion. The Boreas cryocooler achieves ~1 W cooling at 4.2 K without the use of rare-earth regenerator materials, close tolerances, or Joule-Thomson expansion, but does so at the expense of cooling capacity at higher temperatures, where it provides only ~2.5 W at 150 K [88].

3.6.2 Bypass Active Magnetic Regenerators

Linear and rotary active magnetic regenerative refrigerators employing unequal hot and cold blow fluid flow is the subject of a patent by DeGregoria *et al.* [89]. Exemplary specifications and materials are given for the liquefaction of 0.1 ton per day of hydrogen. The diagrams indicate valving to provide sensible cooling from bypass flow, but do not indicate any provision for a latent cooling component. The description also allows for control of the liquefaction of the process stream by expansion through a J-T valve. One of the authors of this patent has indicated that increased cooling capacity has been achieved with this arrangement, but to date the results have only been discussed at a meeting of the American Physical Society and have not been formally published [90].

Chapter 4

Regenerator Flow Maldistribution

4.1 Maldistribution in Cryogenic Gas Expansion Systems

4.1.1 Penney's Method Extended

Penney's research [23] covered a limited range of reduced length Λ and reduced period Π suitable for operation of regenerators in Cowper stoves. In cryogenic refrigeration applications, a much higher thermal ratio is required of the regenerator, which is accomplished by using regenerators with much higher reduced length.

This increased regenerator thermal performance requirement can be seen from a simplified analysis of the gas expansion in a single-stage GM system, for example. For helium gas expansion from 2 MPa to 0.6 MPa, the change in temperature is on the order of 0.3 times the absolute temperature of the gas, the exact proportionality being somewhat larger near room temperature and decreasing with decreasing temperature. To just maintain a temperature gradient across the regenerator, the minimum thermal ratio required is:

$$\eta_{\min} = \frac{T_H - \dfrac{T_C}{\left(1 - f_{\Delta T}\right)}}{T_H - T_C} \tag{4.1}$$

where T_H and T_C are the regenerator hot and cold end temperatures, and $f_{\Delta T}$ is the gas expansion temperature change proportionality constant. The minimum regenerator thermal ratio required for low temperature and cryogenic systems as a function of cold end (refrigeration) temperature taking $f_{\Delta T}$ as constant at 0.3 and T_H as 300 K is presented in Figure 4.1. For a gas expansion regenerative cycle to provide any useful cooling to a load, and to overcome parasitic losses such as heat leaks into the cold space, the minimum regenerator thermal ratio required is increased.

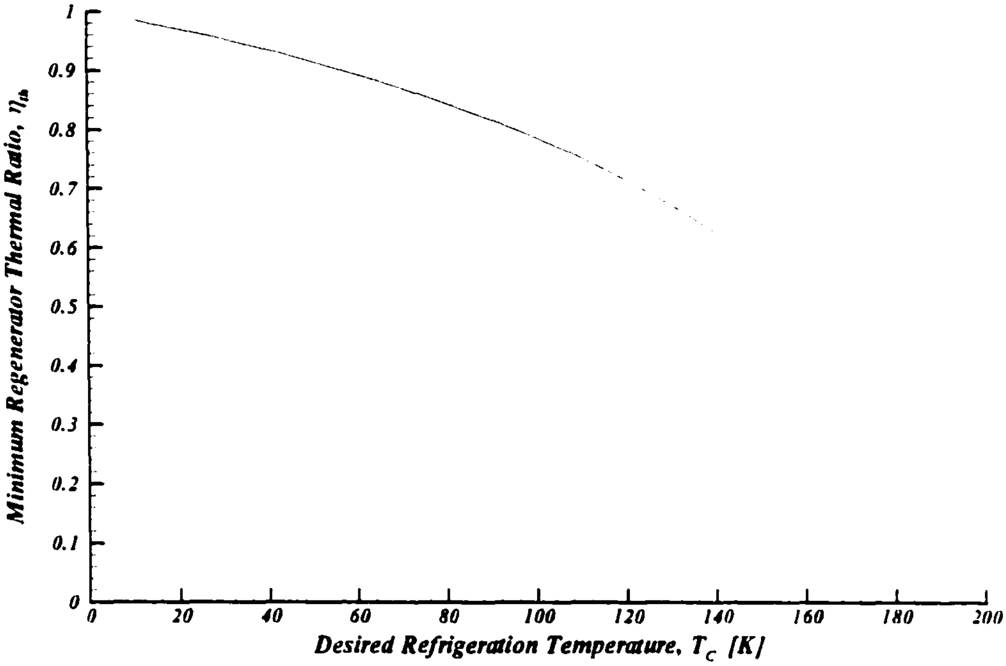

Figure 4.1 Minimum thermal ratio required to maintain regenerator limits between 300 K and T_C from regenerator flow gas expansion having ΔT=0.3T and zero external thermal loads.

Penney's work on the effect of flow maldistribution in reducing the thermal ratio of regenerators can be extended to consider the operation range of cryocooler regenerators having reduced lengths on the order of $50 < \Lambda < 400$ and $0 < \Pi < 30$. The thermal ratio of a regenerator represented by the reduced length Λ and reduced period Π will be reduced by the effect of flow maldistribution. The technique of Penney can be summarized as follows:

Consider a regenerator with reduced length given by:

$$\Lambda = \frac{hA}{\dot{m} C_f} \tag{4.2}$$

where h is the bulk heat transfer coefficient between solid and fluid, A is the uniformly distributed total heat transfer area, $\dot{m}$ is the mass flow rate through the regenerator, and C_f is the fluid heat capacity. Consider also the reduced period given by:

$$\Pi = \frac{hAP}{M_s C_s} \tag{4.3}$$

where P is the blow period, M_s is the total regenerator mass, and C_s is the solid heat capacity. If the heat transfer coefficient is of the form:

$$h \propto \dot{m}^{\beta} \tag{4.4}$$

where β is a constant, and the regenerator is divided into N thermally independent equal-area annular sub-regenerators with the total mass flow divided amongst the sub-regenerators according to:

$$\frac{\dot{m}_i}{\dot{m}} = \frac{\left(1 - m^*\right)}{N} + \frac{\left(2i - 1\right)}{N^2} m^* \tag{4.5}$$

corresponding to a quadratic velocity profile as given in Equation 3.21, then the reduced lengths of the sub-regenerators are given by:

$$\Lambda_i = \left(\frac{N\dot{m}_i}{\dot{m}}\right)^{\beta - 1} \Lambda \tag{4.6}$$

and the reduced periods of the sub-regenerators are given by:

$$\Pi_i = \left(\frac{N\dot{m}_i}{\dot{m}}\right)^{\beta} \Pi \tag{4.7}$$

Using the heat transfer correlation of Equation 3.18, β=0.7, and taking N=5 sub-regenerators, the reduced lengths are given as:

$$\Lambda_i = \left(\frac{5\dot{m}_i}{\dot{m}}\right)^{-0.3} \Lambda \tag{4.8}$$

and the reduced periods are given as:

$$\Pi_i = \left(\frac{5\dot{m}_i}{\dot{m}} \right)^{0.7} \Pi \tag{4.9}$$

The overall thermal ratio of the maldistributed regenerator is the mass-weighted average of the thermal ratios for the sub-regenerators, *viz*:

$$\eta_{th} = \sum_{i=1}^{N} \left(\frac{\dot{m}_i}{\dot{m}} \right) \eta_{th,i} \tag{4.10}$$

Following Penney's technique above for maldistributed regenerator performance with m*=1, the performance of regenerators of interest to cryogenic applications can be evaluated. Figure 4.2 shows the percentage performance deterioration as defined by Equation 3.20 for regenerators operating in the range 5 < Λ < 400 and 0 < Π < 30, which significantly extends the range of reduced length and reduced period presented by Penney.

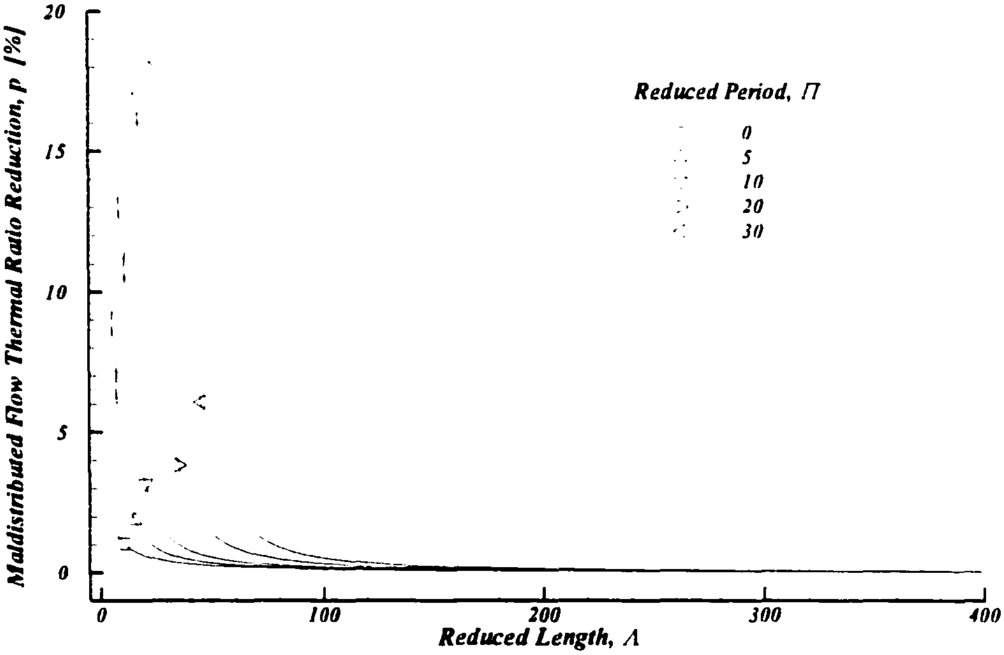

Figure 4.2 Regenerator thermal ratio performance reduction from flow maldistribution as a function of uniform flow reduced length and reduced period.

Figure 4.2 suggests that the deterioration of performance due to flow maldistribution becomes insignificant at a reduced length of approximately $\Lambda=100$, and ultimately asymptotes to zero reduction in performance as reduced length goes to infinity. Further analysis suggests that presenting the performance deterioration in this way, as a percentage decrease in regenerator thermal ratio, is misleading.

4.1.2 Compensating for Maldistribution by Increasing Reduced Length

A better measure of the effect of flow maldistribution is to calculate the required percentage increase in reduced length of the uniform flow regenerator which provides the original uniform flow thermal performance under conditions of maldistributed flow. That is, a regenerator design described by Λ and Π with a thermal ratio of $\eta_{uniform}$ will have a decreased thermal performance under maldistributed flow, η_{mal}. A second regenerator design described by a new reduced length Λ' and the same Π can be found that will have a decreased thermal performance under maldistributed flow, η'_{mal}, such that $\eta'_{mal} = \eta_{uniform}$. What then is the percentage increase in reduced length required to accomplish this?

A procedure can be developed to determine the increase in reduced length required to compensate for maldistributed flow:

1) Calculate the thermal ratio of the original regenerator described by Λ and Π under uniform flow and denote this as $\eta_{uniform}$.
2) Revise the reduced length of the regenerator, so that $\Lambda' = \delta\Lambda$.
3) Calculate the thermal ratio of the revised regenerator under the effect of maldistributed flow and denote this as η'_{mal}.
4) Repeat steps 2 and 3 above until $\eta'_{mal} = \eta_{uniform}$.

Selection of the value by which to revise the reduced length in step 2 above can be accomplished using any sort of optimization or search algorithm.

Figure 4.3 shows the increase in reduced length required to compensate for maldistributed flow for the same maldistribution conditions as previously presented in Figure 4.2. While Figure 4.3 and Figure 4.2 look similar, there are three main differences. First, the peak value of increased length required is shifted to the right compared to the peak value of performance deterioration and falls off to its minimum value more slowly. Second, peak values of increased length required are approximately double the values of performance deterioration, which suggests a much greater degree of intervention required to compensate for the performance deterioration. Third, the increased length required asymptotes at a non-zero value, even for a reduced period of $\Pi=0$, which for the quadratic flow maldistribution with $m^*=1$ is a value of 6.678%. In contrast with the performance reduction presented by Penney, this indicates that the effects of flow maldistribution are significant for all values of Λ and Π.

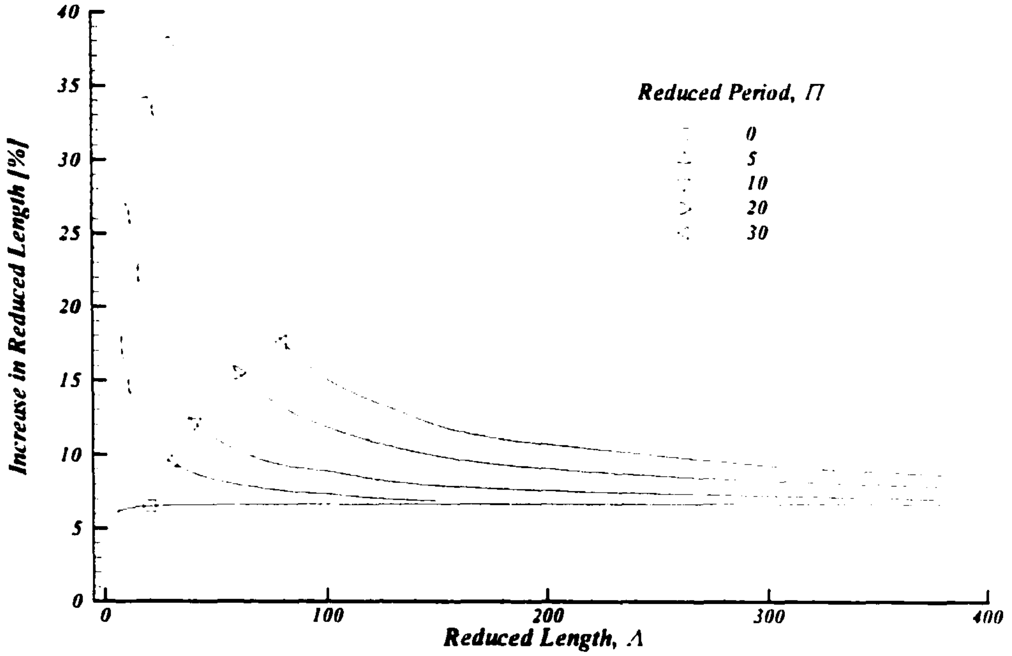

Figure 4.3 Percentage increase in regenerator reduced length required to compensate for effects of maldistributed flow ($m^*=1$) to give equal thermal ratio to uniform flow regenerator.

4.2 Numerical Simulation of Flow within a Regenerator

4.2.1 Motivation

The results of the simulations of idealized Λ-Π regenerators under flow maldistribution suggest that a significant performance reduction can result if the regenerator fluid flow is not evenly distributed across the regenerator. From the opposite perspective, the results suggest that if a given regenerator design suffers from maldistributed flow, then a significant performance improvement can be obtained by reducing the degree of maldistribution. The use of commercially available computational fluid dynamics software packages provide a convenient means by which to study and understand the flow patterns within conventional designs and to develop improved designs.

The distribution of flow within a regenerator is a function of several variables, including packing material type and void distribution, wall effects, inlet and outlet headers, and indirectly the temperature range due to its influence on thermophysical properties of the heat transfer gas. For periodic flow regenerators, the flow distribution is also a function of instantaneous flow rate. A computational fluid dynamics study was undertaken to examine a snapshot in time of the flow distribution within a 1st stage regenerator for a conventional commercial Gifford-McMahon refrigerator and to develop an improved design that minimized flow maldistribution.

4.2.2 Conventional 1st-Stage Gifford-McMahon Regenerator

Figure 4.4 shows a cross-section schematic diagram of a conventional 1st-stage regenerator from a Gifford-McMahon refrigerator. The diagram is approximately to scale, but exact dimensions for the regenerator studied are provided in Table A.1 in Appendix A. Typically, a regenerator core consists of multiple stacks of phosphor-bronze (or copper-bronze) and/or stainless steel wire screens. The screens are individually punched to give circular disks of uniform area and are hand-packed into the regenerator housing. Coarse screens are placed near the hot and cold ends of the regenerator to help provide uniform distribution of flow through the principal stack of fine screens making up the central core. The placement of coarse screens at the hot end of the regenerator also helps to reduce the pressure drop in this region where gas viscosity and velocity through the regenerator is relatively high.

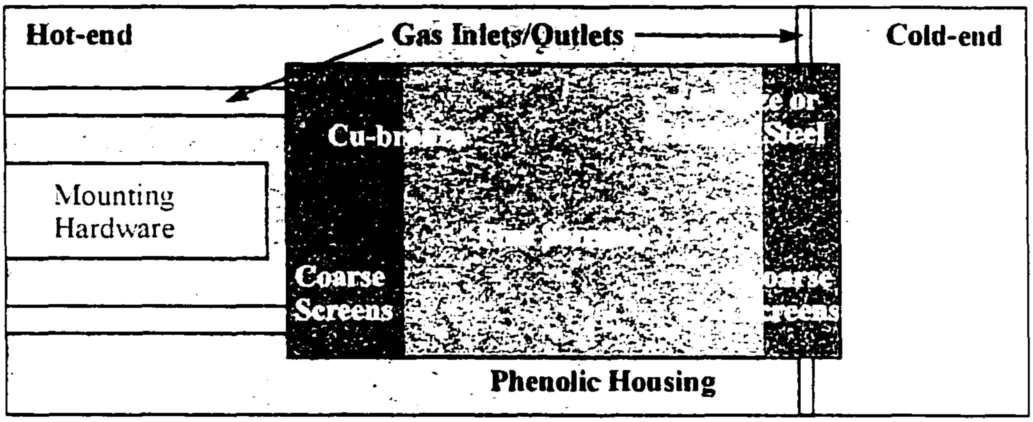

Figure 4.4 Schematic diagram of a conventional GM 1st-stage regenerator seen in cross-section.

The commercially available software package CFX-TASCFlow [91] was used to carry out a full three-dimensional (3-D) fluid flow simulation through the conventional regenerator. The standard release of this package allows solution of the Navier-Stokes equations in porous media in 3-D, with pressure drop through the media modelled using a user-defined momentum source term in the discretized momentum equations. The fluid conservation equations solved by the package expressed in a Cartesian coordinate system in tensor form (with the Einstein summation convention) are:

Conservation of mass:

$$\frac{\partial \rho}{\partial t} + \frac{\partial}{\partial x_j}\left(\rho\, u_j\right) = 0 \tag{4.11}$$

Conservation of momentum:

$$\frac{\partial}{\partial t}\left(\rho\, u_i\right) + \frac{\partial}{\partial x_j}\left(\rho\, u_j u_i\right) = -\frac{\partial P}{\partial x_i} + \frac{\partial \tau_{ij}}{\partial x_j} + S_{ui} \tag{4.12}$$

Conservation of energy:

$$\frac{\partial}{\partial t}\left(\rho\, H_f\right) - \frac{\partial P}{\partial t} + \frac{\partial}{\partial x_j}\left(\rho\, u_j H_f\right) = -\frac{\partial q_j}{\partial x_j} + \frac{\partial}{\partial x_j}\left(u_i \tau_{ij}\right) + S_E \tag{4.13}$$

where u_i represents the velocities in the x_i-coordinate directions, P is the static pressure, H_f is the total enthalpy, ρ is the density, τ_{ij} is the viscous stress tensor, q_j is the molecular energy transport due to conduction, and S_{u_i} and S_E are user-defined additional volumetric momentum and energy source terms. The total enthalpy is defined as:

$$H_f = h + \frac{u_i u_i}{2} \tag{4.14}$$

where h is the static enthalpy of the fluid. The molecular fluxes τ_{ij} and q_j are given by:

$$\tau_{ij} = +\mu\left(\frac{\partial u_i}{\partial x_j} + \frac{\partial u_j}{\partial x_i}\right) + \frac{2}{3}\mu\frac{\partial u_l}{\partial x_l}\delta_{ij} \tag{4.15}$$

and:

$$q_j = -k_f\frac{\partial T_f}{\partial x_j} \tag{4.16}$$

where μ is the dynamic viscosity, and k_f is the thermal conductivity.

TASCFlow repeatedly solves these transient conservation equations, and if a steady-state solution is desired, the equations are successively solved until a sufficient number of time steps or convergence level as set by the user determines that steady-state has been reached. The selection of a suitable time step to achieve accuracy in the transient solution and/or rapid and stable convergence for a steady-state solution depends on the flow being modelled. The initial convergence and stability can vary considerably based on the initial flow conditions set by the user at the start of the simulation.

For the GM regenerator studies, the momentum source term was modelled to represent a local pressure drop corresponding to the relation:

$$\Delta P = \frac{1}{2}f\cdot N\left(\frac{1-\alpha^2}{\alpha^2}\right)\rho V_b^2 \tag{4.17}$$

where f is the friction factor, N is the number of screens, α is the screen porosity, ρ is the fluid density, and V_b is the bulk velocity. The friction factor is given by a non-linear curve fit to the graphical data presented by Kays and London [54]. A linear variation of temperature along the regenerator bed from 295 K to 35 K was used to determine local transport properties of the gas. Each control volume used local flow conditions to determine an appropriate momentum source term, which assumed isotropic conditions within the screen material.

Typical results of computer simulation of the 3-D flow through the conventional regenerator for a 45° model section can be seen in Figure 4.5. With reference to the nomenclature and orientation shown in Figure 4.4, Figure 4.5 shows the gas flow streaklines for a fixed helium mass flow through the regenerator of 16 g/s from the hot end to the cold end. This flow roughly corresponds to the peak flow through the regenerator during the intake phase for a GM refrigerator operating at 2.4 Hz with gas supplied by a 4.6 kW helium gas compressor.

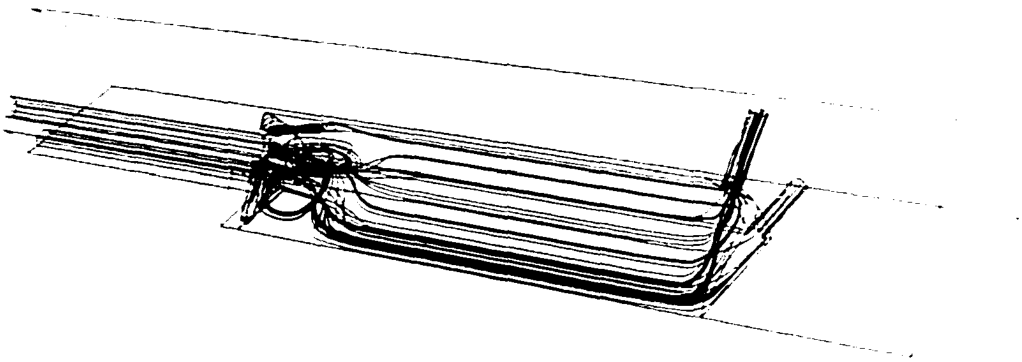

Figure 4.5 Helium fluid flow streaklines from inlet to outlet in a 45° model section of a conventional 1st-stage GM regenerator showing recirculation eddies near the inlet region.

Large recirculation eddies can be seen in the hot-end coarse screen region; this suggests that simplified 1-D momentum and energy models will overestimate the regenerator effectiveness because they will inherently ignore the detrimental heat transport associated with the eddies. The ratio of the total fluid free-flow cross-sectional area of the stacked screen region (i.e. the area available for fluid flow after subtracting the area blocked by the screen wire material itself), is approximately 7.2 times larger than the total free flow area of the hot end gas fill tubes. As a result, gas exiting the fill tubes and entering the coarse mesh screen region sees a sudden expansion and gas jetting results.

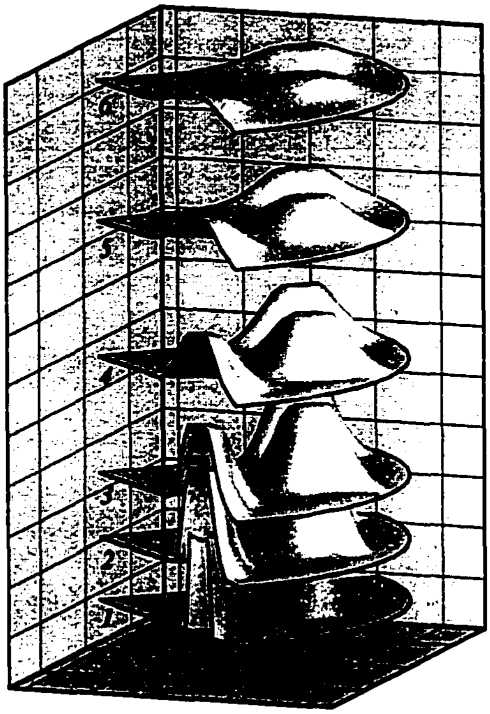

Figure 4.6 Representation of gas speed within the first 20% of the length of a conventional GM regenerator.

The gas jetting is evident in Figure 4.6 which plots a series of relief surfaces representing the gas speed as a function of position within the first 20% of the regenerator length from the exit of the hot end gas fill tubes and entrance of the coarse screen region. The lowermost surface, numbered 1 in the diagram, is the surface closest to the hot end gas fill tubes. Each surface is plotted according to the relation:

$$height = x + speed \times scale \qquad (4.18)$$

where x corresponds to the distance of each plane region under consideration from the start of the coarse screen region normalized relative to the total regenerator bed length, ***speed*** is the helium gas speed at the plane, and ***scale*** is a constant scaling factor equal to a height of 1 bed length for a speed of 1340 m/s. The scaling factor is derived from the maximum velocity in the bed and an arbitrary height factor that shows the trend in speed without unduly cluttering the figure. The maximum speed within the regenerator is approximately 67 m/s. Each plane on which the relief surface is then imposed is a 90° pie-shaped wedge that would result if the cylindrical regenerator were quartered lengthwise with the cutting planes intersecting the hot end fill tubes.

Two important features of the gas flow in the regenerator entrance region are evident. First, there is considerable disparity in gas velocity across each cutting plane. Second, the disparity is still evident even after 20% of the regenerator length. The non-uniformity in gas flow leads to non-uniform utilization, which has previously been shown to be detrimental to regenerator performance. The degree of non-uniformity of flow is qualitatively evident from the figure.

A quantitative comparison of the flow maldistribution of the conventional regenerator is presented in Table 4.1. The table lists the regenerator planes corresponding to the indices of Figure 4.6. The ideal uniform speed for the plane is the gas speed that would result if the total mass flow were uniformly distributed over the entire available flow area. The uniform speed decreases with increasing penetration into the regenerator due to the effect of increasing gas density due to the assumed temperature gradient. That the maximum speed shown at plane 2 is higher than at plane 1 is an artifact of the method by which the CFD code calculates the average speed over a control volume, which for plane 1 straddles a 55% porosity region and a 100% porosity region. For each plane, the maximum speed is significantly higher than the ideal uniform flow speed.

Table 4.1 Comparison of the maximum gas speed and ideal uniform flow speed within the conventional GM regenerator in the first 20% of the regenerator length.

Plane Index	Position, x % Regenerator	Maximum Speed [m/s]	Uniform Speed [m/s]
1	0	54.0	5.8
2	2.44	54.4	5.7
3	4.96	44.0	5.6
4	9.60	30.5	5.3
5	15.05	19.8	5.1
6	20.50	12.1	4.8

4.2.3 Modified 1st-Stage Gifford-McMahon Regenerator

Figure 4.7 shows a schematic diagram of a non-uniform cross-section regenerator. The diagram is approximately to scale, but exact dimensions for the regenerator studied are provided in Table A.2 in Appendix A. Fine and coarse annular-shaped screens make up the main body of the regenerator.

arranged with coarse screens at the hot end, fine screens in the middle, and medium-coarse screens at the cold end. The main body forms a frustrum of a right circular cone, and has a solid phenolic central core that excludes flow. A small frustrum of a right circular cone is placed adjacent to the main regenerator body in each inlet/outlet at the hot end. Lead spheres are packed in the annular space between the cold end screens and the cold end gas outlets/inlets.

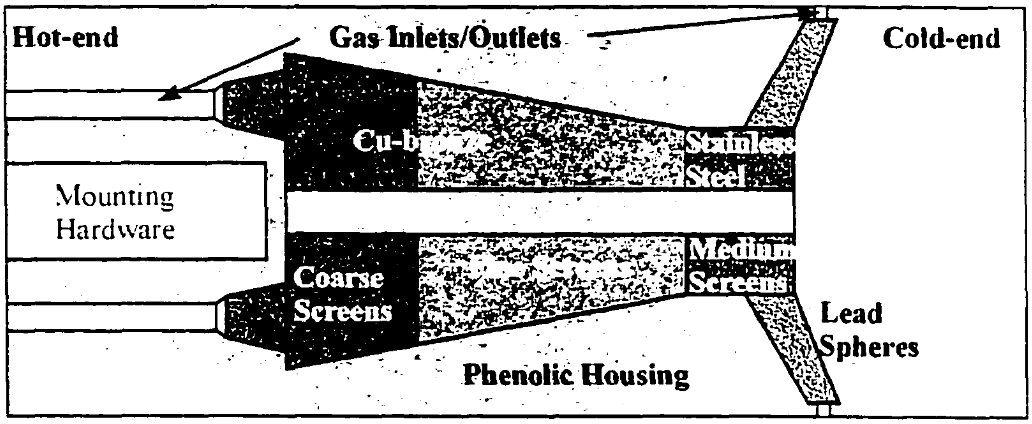

Figure 4.7 Schematic diagram of a conical taper GM 1st-stage regenerator as seen in cross-section.

Figure 4.8 shows streaklines on a 45° model section for the same inlet flow conditions as the uniform cross-section regenerator. The non-uniform cross-section forms a linear taper in screen outer diameter and serves to streamline the flow and eliminate recirculation eddies. The tapered design compensates for the thermal dependence of the transport properties of the circulation gas, allowing a lower pressure drop in the screens due to a lower gas velocity at the hot end of the regenerator and a higher heat transfer coefficient due to higher gas velocity at the cold end. Along their length, the tapered screens allow a more uniform flow impedance and heat transfer coefficient, thereby better utilizing the maximum potential performance of each screen.

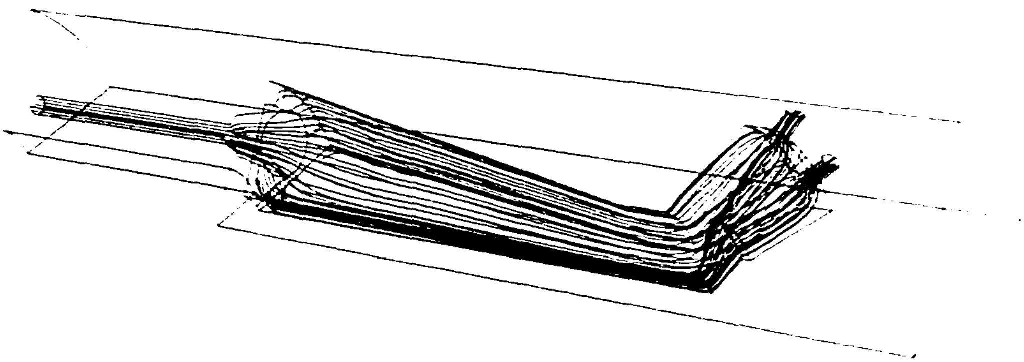

Figure 4.8 Helium fluid flow streaklines from inlet to outlet in a 45° model section of a conical 1st-stage GM regenerator showing smooth flow without recirculation throughout the entire regenerator matrix.

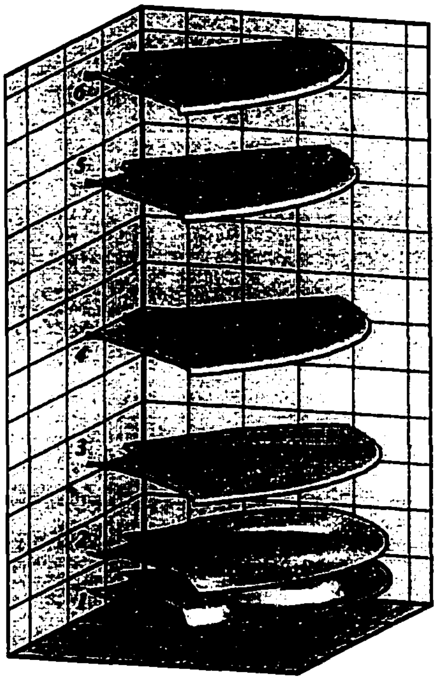

Figure 4.9 Representation of gas speed within the first 20% of the active conical region of a non-uniform area GM regenerator.

The improved uniformity of the flow in the tapered design can be seen in Figure 4.9, which is drawn using the same sectioning and surface relief scaling as Figure 4.6. The tapered regions at the ends of the hot inlet tubes serve to substantially reduce the jetting effect and maximum gas speed within the main body of the regenerator, as can be seen by the broader and lower relief surfaces. The jetting is reduced because of two factors. First, at the entrance to the main body of the regenerator, the flow area is a factor of approximately 2.5 times the flow area of the exit of the conical region of the hot inlet tubes, and by the conical shape of the exit, the flow is smoothly diverging as it enters the larger flow area. While the cross-sectional area of the main regenerator body is initially larger than the conventional regenerator, the relative expansion exiting the hot inlet tubes is smaller by a factor of almost 3. Second, the acceleration of the flow required as the porosity decreases is confined to a region within the hot inlet tubes shaped to inhibit recirculation eddies.

A quantitative comparison of the flow maldistribution of the conical regenerator is presented in Table 4.2. The maximum speed in the first 22% of the regenerator is consistently lower than the conventional regenerator, and the ratio of the maximum speed to the ideal uniform gas flow speed is very close to unity after 10% of the regenerator length. This gives a nearly uniform plug flow for the conical regenerator over most of its length. For the conical regenerator, the ideal speed is a function of the decreasing flow area as well as the increasing gas density.

Table 4.2 Comparison of the maximum gas speed and ideal uniform flow speed within the first 22% of the active conical region of a non-uniform area GM regenerator.

Plane Index	Position, x % Regenerator	Maximum Speed [m/s]	Uniform Speed [m/s]
1	0	9.5	3.6
2	1.61	7.8	3.6
3	5.39	5.4	3.6
4	10.88	4.0	3.7
5	17.43	3.8	3.8
6	22.00	3.9	3.8

4.3 Conventional and Modified Regenerator Performance

4.3.1 Comparison of Experimental Results

In collaboration with other researchers, a regenerator having the conical geometry of Figure 4.7 was constructed and tested in a GM refrigerator. A complete report of the construction techniques and performance of the conical regenerator and comparison with the conventional regenerator in a single-stage GM and as the 1st-stage of a two-stage GM refrigerator has been published elsewhere [92]. A brief summary of the results is presented here.

Tests using the one-stage apparatus consisted of measurement of the no-load minimum temperature for a range of operating frequencies and temperature under a modest load of 25 W at 2.4 Hz, for both the conical and conventional regenerators. Tests on the two-stage apparatus consisted of measurement of the no-load minimum temperatures for the 1st and 2nd-stages, and 1st and 2nd-stage temperatures under a combination of loads to both stages using a 2nd-stage regenerator filled with lead spheres. No-load tests were conducted across a spectrum of operating frequencies, while load tests were performed solely at 1.5 Hz.

The no-load tests on the single-stage apparatus revealed a frequency dependence of the 1st-stage temperature, as can be seen in Figure 4.10. The conical regenerator has a stronger frequency-dependent no-load minimum temperature than does the conventional regenerator. Between 1 Hz and 2.44 Hz, the conical regenerator has a lower no-load minimum temperature than does the conventional regenerator.

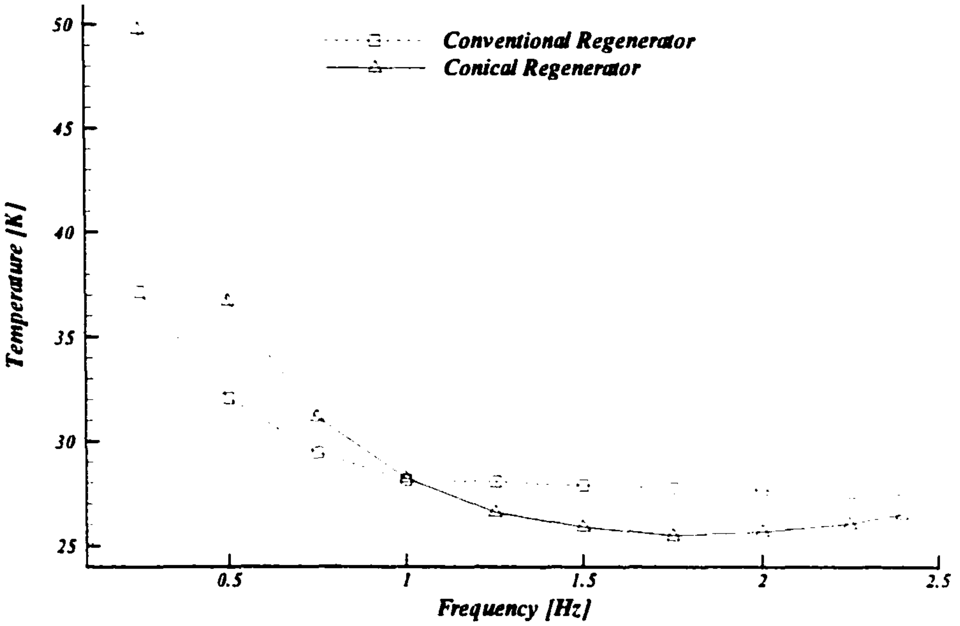

Figure 4.10 Comparison of the frequency dependent no-load minimum temperatures of the conventional and conical regenerators in the single-stage GM refrigerator.

The no-load tests on the two-stage arrangement revealed a frequency dependence of both the 1st and 2nd-stage temperatures. Results of these tests are shown in Figure 4.11. Other researchers have reported a similar optimum frequency of operation for attaining the lowest no-load temperatures [93]. At all frequencies, the conical 1st-stage regenerator permitted a lower no-load minimum temperature on the 2nd-stage than did the conventional regenerator. The conical regenerator also exhibited a lower 1st-stage temperature than the conventional regenerator at most frequencies tested. Peak cooling performance is achieved at approximately 1.5 Hz for both the 1st and 2nd-stages for the conical regenerator.

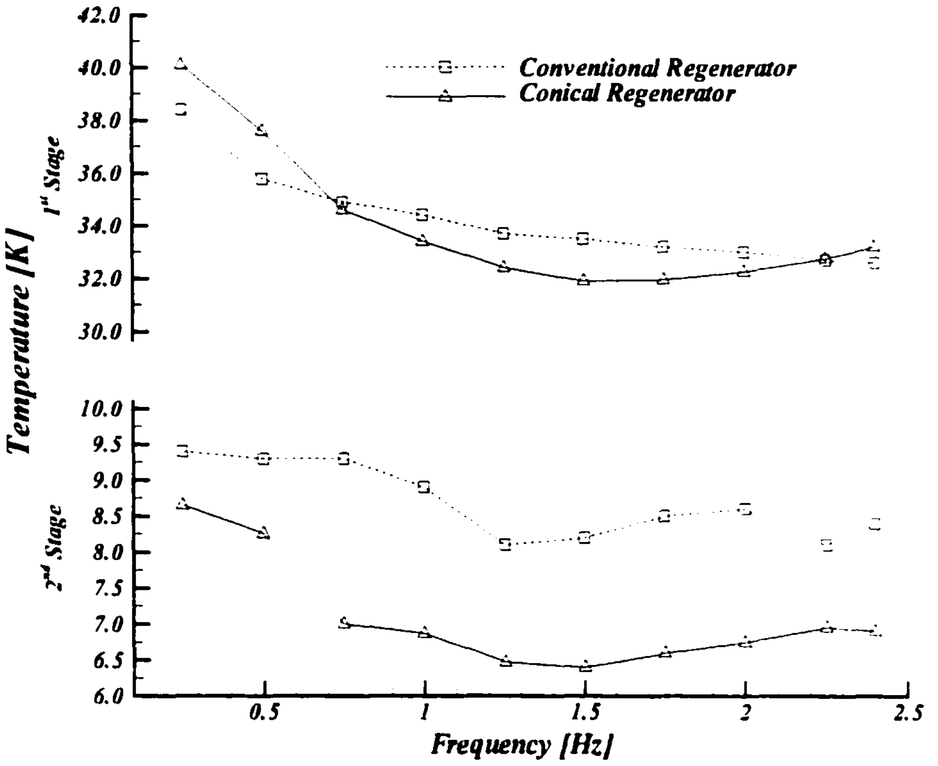

Figure 4.11 Comparison of the 1^{st} and 2^{nd}-stage no-load minimum temperatures as a function of operation frequency for the conventional and conical regenerators in the two-stage GM refrigerator.

Under load, the conical regenerator gave mixed results compared to the conventional regenerator. Figure 4.12 displays the cooling performance curves using the conical and conventional regenerators for the 1^{st}-stage, with the conventional lead regenerator for the 2^{nd}-stage. Applied heat loads were identical for both regenerators tested. In the figure, loads for the conventional regenerator can be found on the corresponding points of the curves for the conical regenerator. For most loads, the conical 1^{st}-stage allowed a lower 2^{nd}-stage temperature. Only at low 1^{st}-stage loads did the conical 1^{st}-stage also consistently provide a lower 1^{st}-stage temperature.

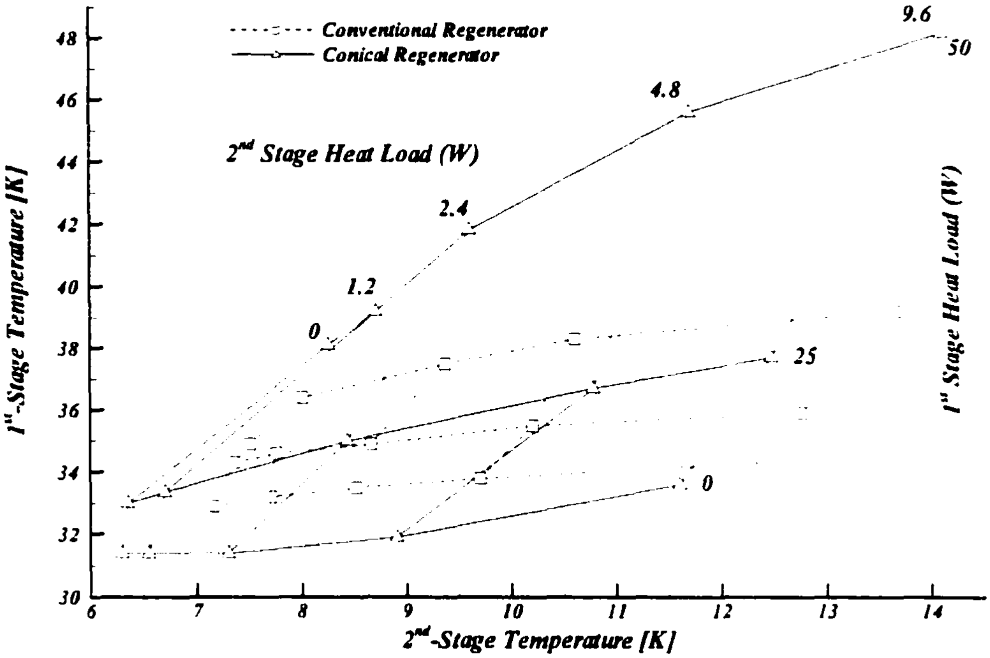

Figure 4.12 Comparison of the cooling performance curves for the conventional and conical regenerators in the two-stage GM refrigerator.

While the results presented in Figures 4.10, 4.11, and 4.12, as well as results presented in the original reference and not summarized here, show improved performance in most circumstances for the conical regenerator, they do not provide any direct proof that the improved performance is specifically as a result of improved flow distribution within the regenerator. The studies required to demonstrate beyond the numerical level that design changes such as those used for the conical regenerator are responsible for improved performance in commercial refrigerators are beyond the scope of this work.

Chapter 5

Refrigeration and Liquefaction Principles

5.1 Liquefaction of Gases

The liquefaction process generally consists of two steps, namely, sensible cooling of the gas to the desired saturation temperature, and latent cooling of the saturated gas to condense it to a liquid product. The details to accomplish these two steps are specific to the liquefaction process employed, and consequently can vary considerably. In some cycles, such as the Linde, Claude, Heylandt, and Collins cycles, the gas to be liquefied can also be the working fluid of the device providing the refrigeration effect. In other cycles, such as the classical cascade and mixed refrigerant cycles, the gas to be liquefied is kept entirely separate from the working fluid except for heat exchange. Other details include whether the cycle employed provides cooling at discrete temperature levels or across varying temperatures. Many excellent texts are available, for example, those of Bejan [94], Timmerhaus and Flynn [95], and Walker [17, 26], which describe in detail the thermodynamic and cycle considerations for these refrigeration and liquefaction cycles.

Of interest in this work is the case where the gas to be liquefied is supplied at the desired saturation pressure and is only in thermal contact with the refrigeration device. The refrigeration device removes the gas sensible and latent heat in frictionless heat exchangers to form a liquid product and is assumed to be operating at steady-state. Issues such as gas contaminants and multi-component mixtures, ortho-para conversion for hydrogen, or transient effects during start-up are not considered.

5.1.1 Refrigerator Versus Liquefier

When a cycle provides cooling at discrete temperature levels, it is generally referred to as a refrigeration cycle. When the cycle provides cooling across varying temperatures, it is generally referred to as either a refrigeration cycle or as a liquefaction cycle, depending on the application to which it is applied. This can cause some uncertainty of what to name the cycle when a refrigeration cycle is used for gas liquefaction, or less commonly when a liquefaction cycle is used for refrigeration. In this work, the terms refrigerator and liquefier will correspond to the application, unless specifically noted otherwise, and the term refrigeration device will generically apply to both refrigerator and liquefier.

5.2 Ideal Performance

5.2.1 Carnot Cycle

Often it is desirable to compare the performance of a given refrigeration device to some ideal device. It is a corollary of the Second Law of Thermodynamics that no cycle can be more efficient than a reversible cycle operating between the same temperature limits; also, any two *reversible* cycles receiving heat at one particular temperature and rejecting it at another particular temperature must have identical values of thermal efficiency. Thus, it is often useful to compare the thermal efficiency of the cycle being considered with the thermal efficiency of a reversible cycle operating between the same two temperatures.

For a refrigeration device that interacts thermally with the hot and cold reservoir temperatures of T_H and T_C, respectively, the ideal cycle used for comparison is the Carnot cycle. Figure 5.1 shows a temperature-entropy diagram of the Carnot refrigeration cycle which is defined by two isothermal and two isentropic processes.

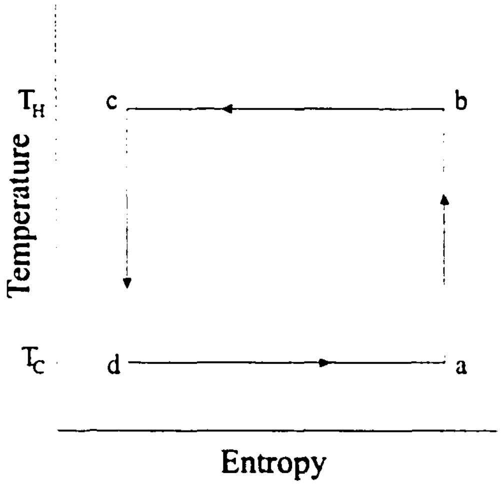

Figure 5.1 Temperature-entropy diagram of the Carnot refrigeration cycle.

The measure of performance for any device can be stated broadly as the ratio of the desired effect to the effort required to achieve that effect. For a power cycle, this ratio is commonly termed the thermal efficiency and ranges in value from 0 to 1. For a refrigeration cycle, this ratio can take on values greater than 1, and to avoid confusion, a distinct name is given. For a refrigeration device, the ratio is given the name "coefficient of performance," COP, and is given by:

$$COP = \frac{\textit{refrigeration effect (rate)}}{\textit{net work input (rate)}} = \frac{\dot{Q}_C}{\dot{W}} \tag{5.1}$$

where $\dot{W}$ is the rate of work input, and $\dot{Q}_C$ is the rate of heat removed at the lower temperature and rejected at the higher temperature. The COP can be calculated in terms of the total heat and work for a fixed mass system, or equivalently as the heat and work rates as given above. For the Carnot cycle, the coefficient of performance is given by:

$$COP_{t,Carnot} \equiv \eta_C = \frac{\dot{Q}_C}{\dot{Q}_H - \dot{Q}_C} = \frac{T_C}{T_H - T_C} \tag{5.2}$$

where $\dot{Q}_H$ is the heat rejection rate at the upper temperature level, T_H.

5.2.2 Cold Gas Refrigerator

When the cold load is absorbed at varying temperature, instead of at constant temperature as in the Carnot cycle, it is more appropriate to make a comparison to a reversible cold-gas refrigeration (CGR) cycle. This cycle consists of two adiabatic processes, one constant temperature process, and one variable temperature process, usually taken to be a constant pressure process. The reversible cold-gas cycle is shown in Figure 5.2.

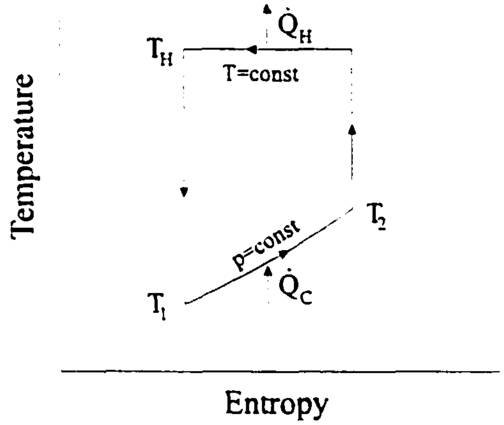

Figure 5.2 Temperature-entropy diagram of the reversible cold-gas refrigeration cycle.

Applying the basic definition for the coefficient of performance and substituting the appropriate thermodynamic quantities gives:

$$COP_{t,CGR} \equiv \eta_{CGR} = \frac{\dfrac{\dot{Q}_C}{\dot{m}}}{\dfrac{\dot{Q}_H}{\dot{m}} - \dfrac{\dot{Q}_C}{\dot{m}}} = \frac{h_2 - h_1}{T_H(s_2 - s_1) - (h_2 - h_1)} \tag{5.3}$$

where s and h are the refrigeration gas entropy and enthalpy, respectively, and the subscripts 1 and 2 correspond to the conditions at temperatures T_1 and T_2, respectively.

To compare the performance of real refrigerators to the ideal refrigerator, the performance criterion known as the figure of merit is often employed. The figure of merit, *FOM*, is defined as:

$$FOM = \frac{COP}{COP_t} \tag{5.4}$$

where COP is the coefficient of performance of the real refrigerator and COP_t is the coefficient of performance of the thermodynamically ideal system. The selection of the ideal system on which to base the comparison should match the non-ideal system. That is, the Carnot cycle should be selected when the refrigeration effect is provided at a fixed temperature, and the CGR cycle should be selected when the refrigeration effect is provided across a temperature span. The FOM can range from 0 to 1, where the closer the approach to unity, the closer the system under consideration is approaching an ideal system.

5.2.3 Ideal Liquefier

When the purpose of the refrigeration process is to provide liquefaction, comparison with the ideal liquefier is most appropriate. The ideal liquefier is an open-system process and consists of reversible isothermal compression followed by reversible isentropic expansion. Figure 5.3 shows the temperature-entropy diagram for the reversible liquefaction process. In practice, for many gases, the pressures required before isentropic expansion are well beyond current compression equipment, but ideally, it is assumed that the high pressure can be obtained so that expansion will result in complete liquefaction of the gas.

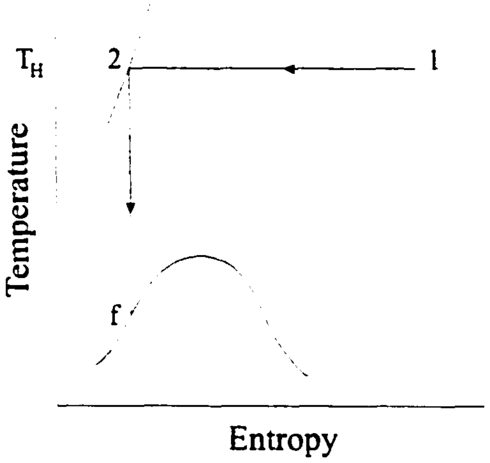

Figure 5.3 Temperature-entropy diagram of the ideal liquefaction process.

In the ideal liquefier, the work rate required for compression of the gas is given by:

$$\frac{\dot{W}_{comp}}{\dot{m}_f} = h_2 - h_1 + \dot{Q}_{comp} \tag{5.5}$$

where $\dot{W}_{comp}$ is the compressor input power (work rate), $\dot{m}_f$ is the mass flow rate of the gas, $\dot{Q}_{comp}$ is the heat rejection rate during isothermal compression, and the subscripts 1 and 2 refer to the initial and compressed states at T_H, respectively. The heat rejection rate during compression is given by:

$$\begin{aligned}\frac{\dot{Q}_{comp}}{\dot{m}_f} &= T_H(s_1 - s_2)\\ &= T_H(s_1 - s_f)\end{aligned} \tag{5.6}$$

where s is the entropy of the gas, and the subscript f refers to the saturated liquid state. The work produced during the isentropic expansion is given by:

$$\frac{\dot{W}_{exp}}{\dot{m}_f} = h_2 - h_f \tag{5.7}$$

where $\dot{W}_{exp}$ is the output power of the gas expander, and h_f is the enthalpy of the saturated liquid. The output power of the gas expander is used to offset the input power, so the ideal work rate per unit mass liquefied is given as:

$$\frac{\dot{W}_t}{\dot{m}_f} = T_H\left(s_1 - s_f\right) - \left(h_1 - h_f\right) \qquad (5.8)$$

The measure of performance commonly used for liquefiers is also known as the figure of merit; however, the FOM for liquefiers is normally defined as:

$$FOM = \frac{\left(-\dot{W}_t/\dot{m}_f\right)}{\left(-\dot{W}/\dot{m}_f\right)} \qquad (5.9)$$

where $\dot{W}_t/\dot{m}_f$ is the work of compression per unit mass liquefied for the ideal liquefaction cycle and $\dot{W}/\dot{m}_f$ is the work of compression per unit mass liquefied for the actual cycle. Again, the closer the FOM approaches unity, the closer the system under consideration is approaching an ideal system.

5.3 Comparison of the Ideal Cycles Applied to Gas Liquefaction

5.3.1 Latent and Sensible Cooling Requirements

Any of the ideal refrigerator, ideal cold gas refrigerator, or the ideal liquefier can in principle be used to liquefy a process gas; however, only the latter is well suited to the task. For example, a single-stage ideal refrigerator must remove both the sensible and latent heat of the process gas at the saturation temperature. The ideal refrigerator is well suited to remove the required latent heat component, since the refrigeration provided and the refrigeration required are at constant temperature. The ideal refrigerator is not well suited to efficiently remove the sensible heat component. For different process gases with progressively lower saturation temperatures, there is an increasing mismatch between the refrigeration required by the gas and the refrigeration supplied by the ideal refrigerator because of an increase in the sensible cooling requirements from ambient relative to the latent cooling requirements at the saturation temperature.

The sensible heat that must be removed to liquefy a process gas is given by the difference in vapour enthalpy between the initial conditions and the saturation temperature. Assuming that the initial conditions are $T = T_H$, the ambient warm temperature, and $P = P_{sat}$, the desired saturation pressure corresponding to the desired saturation temperature, T_{sat}, the sensible heat component is given by:

$$\Delta h_{g(T_H - T_{sat})} = h_g\Big|_{(T_H, P_{sat})} - h_g\Big|_{(T_{sat}, P_{sat})} \tag{5.10}$$

where h_g is the enthalpy of the vapour phase of the process gas to be evaluated at the subscripted conditions. Similarly, the latent heat that must be removed is given by the difference in the enthalpies of the vapour and liquid states at the saturation pressure, and is given by:

$$\Delta h_{fg(T_{sat})} = h_g\Big|_{(T_{sat}, P_{sat})} - h_f\Big|_{(T_{sat}, P_{sat})} \tag{5.11}$$

In this work, the enthalpy ratio, h_R, is defined as the ratio of latent heat $\Delta h_{fg(T_{sat})}$ to the sensible heat $\Delta h_{g(T_H - T_{sat})}$ cooling requirements of a gas process stream being cooled from ambient temperature and liquefied at constant pressure corresponding to the saturation pressure. That is, the enthalpy ratio is defined as:

$$h_R = \frac{\Delta h_{fg(T_{sat})}}{\Delta h_{g(T_H - T_{sat})}} \tag{5.12}$$

Figure 5.4 shows the enthalpy ratio, h_R, for a number of gases taking ambient temperature to be 300 K. The curves extend from the gas triple point to critical point conditions, with each legend symbol drawn at the fluid's normal boiling point at atmospheric pressure. The curves have the same general form, extending from an enthalpy ratio of zero at the maximum saturation temperature to some maximum enthalpy ratio at an intermediate saturation temperature, except for ethane which appears somewhat anomalous. The curves will have a minimum enthalpy ratio of zero when the latent heat component is zero, which occurs for all gases at the critical point. Ethane's critical point is above 300 K, and consequently, on this graph, where the sensible heat component is measured relative to 300 K, the latent heat remains non-zero while the sensible heat approaches zero, giving an infinite value for h_R near 300 K. If the curves were drawn relative to a temperature above ethane's critical point temperature, the apparent anomaly would be absent.

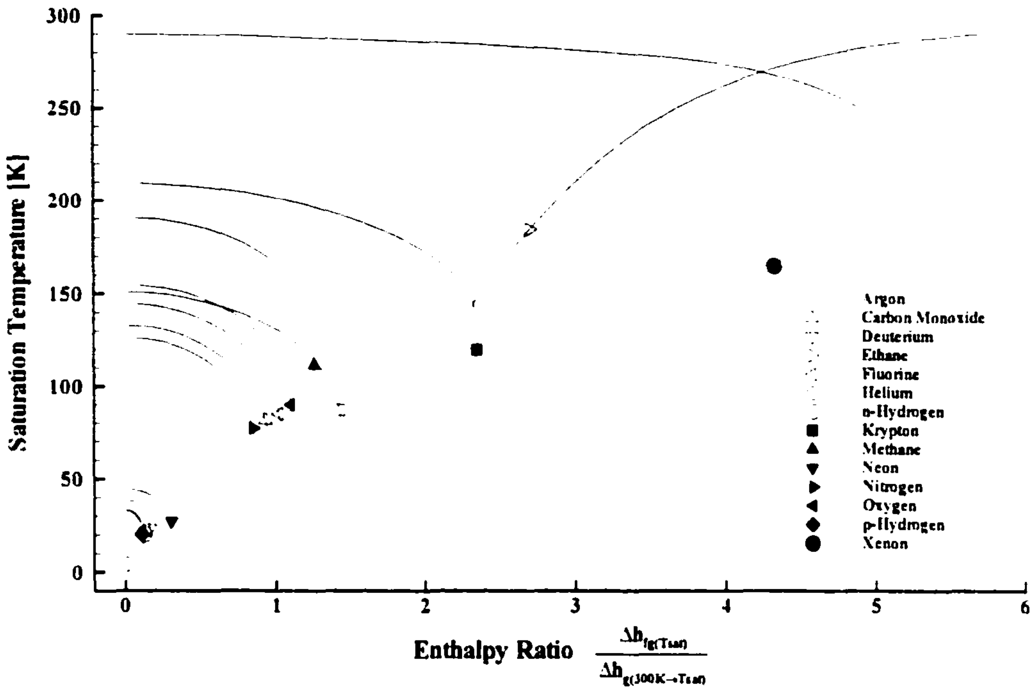

Figure 5.4 Saturation temperature from triple point to critical point saturation pressures vs. the ratio of latent heat to sensible heat, h_R, for a number of gases.

5.3.2 Figure of Merit

Comparing the curves for helium and krypton, for example, it is apparent that a helium liquefier must provide most of its cooling as sensible cooling, and very little as latent cooling, while a liquefier for krypton for much of the saturation range must provide a significant portion of its cooling as latent cooling. A comparison of the ratio of liquefaction yield for an ideal refrigerator to the liquefaction yield of an ideal liquefier for equal input power gives an idea of the mismatch of the ideal refrigerator to the cooling requirements for liquefaction. Using this definition, a figure of merit for this comparison can be defined as:

$$FOM_{R:L} = \frac{\left(\dot{W}_t / \dot{m}_f\right)_{ideal\ liquefier}}{\left(\dot{W} / \dot{m}_f\right)_{refrigerator,\ ideal}} \qquad (5.13)$$

where $\left(\dot{W}_t/\dot{m}_f\right)_{ideal\ liquefier}$ is the input power per unit mass liquefied for the ideal liquefier and is given by Equation 5.8, and $\left(\dot{W}/\dot{m}_f\right)_{refrigerator,\ ideal}$ is the input power per unit mass liquefied using an ideal refrigerator for the liquefaction process, and is given by:

$$\left(\dot{W}/\dot{m}_f\right)_{refrigerator,\ ideal} = \frac{T_H - T_{sat}}{T_{sat}}\left(\Delta h_{g(T_H - T_{sat})} + \Delta h_{fg(T_{sat})}\right) \qquad (5.14)$$

The larger the deviation below unity for the figure of merit, the more poorly suited is the ideal refrigerator to the task of liquefaction.

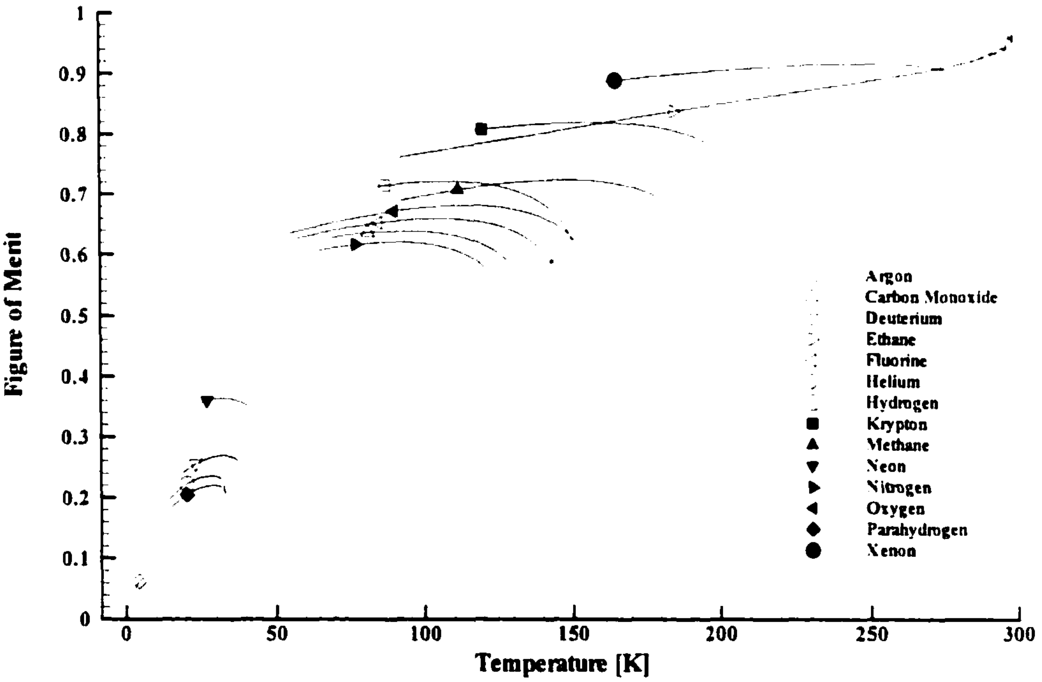

Figure 5.5 Ratio of ideal refrigerator to ideal liquefier liquefaction yield for equal input power, $FOM_{R:L}$, as a function of saturation temperature from the triple point to the critical point for a number of gases cooled from 300 K.

Figure 5.5 shows the figure of merit, $FOM_{R:L}$, as function of saturation temperature for the same gases previously shown in Figure 5.4. Legend symbols are drawn at each fluid's normal boiling point at atmospheric pressure. Once again, the curve for ethane seems somewhat anomalous, but its distinctiveness is an artifact of the ambient temperature selection relative to the critical point temperature. The oscillations in ethane's curve near its upper limit are due to round-off errors in the evaluation of gas properties.

There are several valid interpretations of Figure 5.5. The figure shows that generally as the saturation temperature decreases amongst the various gases, the ideal refrigerator shows decreasing performance relative to the ideal liquefier. For optimal efficiency, it therefore becomes increasingly important at lower temperatures to configure the refrigeration device for the task of liquefaction rather than just for refrigeration. Another interpretation is that if a non-ideal refrigeration device designed as a refrigerator is reconfigured to provide some sensible cooling at the expense of the latent cooling, a net increase in overall efficiency is possible. This last statement is made more obvious by the separation of the sensible and latent cooling components.

5.3.3 Separation of Sensible and Latent Cooling Requirements

Consider the removal of the sensible heat load $\Delta h_{g(T_H - T_{sat})}$ in a precooling process. The sensible load can be removed by an ideal refrigerator removing heat at the saturation temperature and will have a Carnot coefficient of performance, η_C, given by Equation 5.2. The sensible load can also be removed by a reversible cold gas refrigerator, and will have a coefficient of performance, η_{CGR}, given by Equation 5.3, which will always exceed the coefficient of performance for the ideal refrigerator.

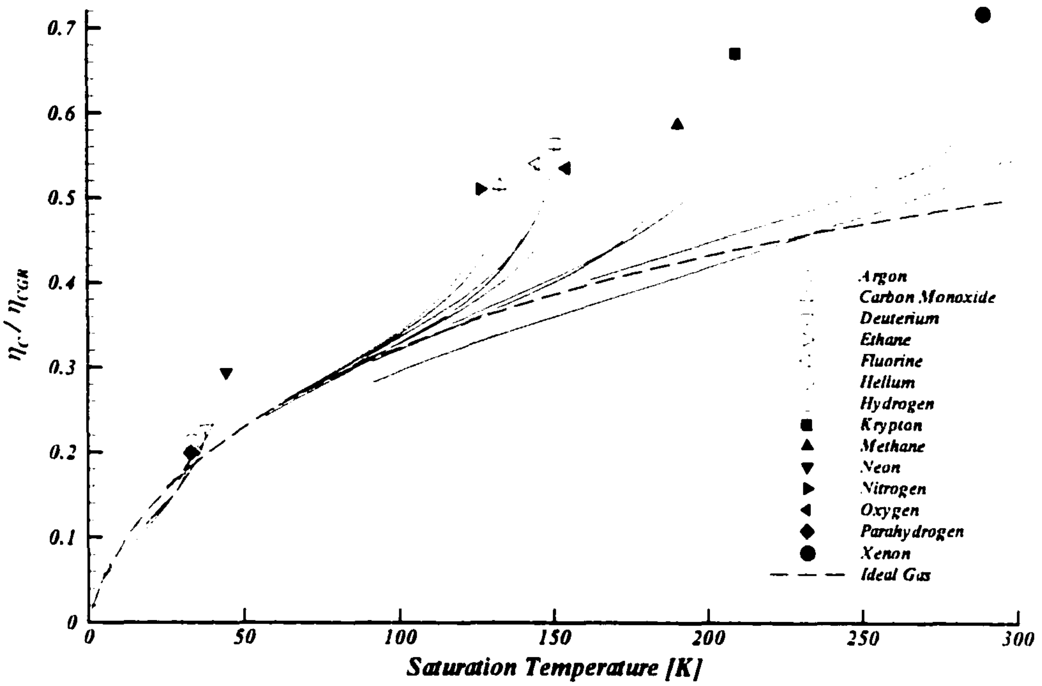

Figure 5.6 Ratio of the ideal refrigerator coefficient of performance to the cold-gas refrigerator coefficient of performance, η_C/η_{CGR}, as a function of saturation temperature for the sensible cooling requirements from 300 K to T_{sat} for a number of gases.

The superiority of the cold gas refrigerator over the ideal refrigerator when applied to precooling a process gas is shown in Figure 5.6 where the ratio η_C/η_{CGR} is plotted as a function of the saturation temperature according to the expression:

$$\frac{\eta_C}{\eta_{CGR}} = \frac{T_{sat}}{T_H - T_{sat}} \, \frac{T_H \Delta s_{g(T_H - T_{sat})} - \Delta h_{g(T_H - T_{sat})}}{\Delta h_{g(T_H - T_{sat})}} \qquad (5.15)$$

where $\Delta h_{g(T_H - T_{sat})}$ is the sensible heat load of the gas from ambient $T_H = 300\,K$ to the saturation temperature, T_{sat}, and $\Delta s_{g(T_H - T_{sat})}$ is the entropy change of the gas from ambient to the saturation temperature. Legend symbols are located at the gas critical point temperatures. When the gas being cooled is an ideal gas, and taking $\tau = T_H/T_{sat}$, Equation 5.15 can be expressed as:

$$\frac{\eta_C}{\eta_{CGR}} = \frac{\frac{\tau}{\tau - 1}\ln\tau - 1}{\tau - 1} \tag{5.16}$$

and is also plotted in Figure 5.6 for comparison. For nitrogen at 77 K, for example, $\eta_C \approx 0.29\eta_{CGR}$, so that only a non-ideal precooling process whose efficiency is lower than $0.29\eta_{CGR}$ requires more power than an ideal refrigerator producing all the refrigeration at the condensation point. When the enthalpy ratio, h_R, is less than 1, the sensible cooling requirement is larger than the latent cooling requirement, and a significant reduction in power consumption required for liquefaction is possible by precooling with a cold-gas refrigerator because of its higher efficiency. A final interpretation of Figure 5.4 is that when the goal of the refrigeration device is liquefaction, it is not sensible to eke out a few percent improvement in efficiency of a refrigerator that supplies its cooling at the saturation temperature only, when a much larger improvement in efficiency is possible by modifying or augmenting the refrigeration process to additionally supply sensible cooling from ambient to the saturation temperature.

5.4 Unbalanced, Asymmetrical Regenerator Liquefiers

Traditionally, regenerative cycles have been operated using balanced and symmetrical regenerators, or at least, as close to balanced and symmetrical conditions as the practicalities of the refrigeration equipment permits. When the goal is refrigeration at a fixed temperature, this design criterion makes sense. A simple thought experiment can demonstrate why this is so.

Consider a non-ideal regenerator that operates between the limits of T_H and T_C and is at cyclic-steady-state. Cold gas that enters the cold end of the regenerator during the cold blow can at best cool the regenerator matrix near the entrance to the cold gas temperature, T_C. As more gas flows into the regenerator, the thermal penetration depth increases, increasing the proportion of matrix material at the cold temperature. When the cycle reverses, and warm gas flows into the regenerator, the warm gas is cooled and exits at some average cold temperature above T_C. So far, this operation is typical.

Now consider that for the next cold blow, an extra supply of cold gas is available. The thermal penetration depth is now increased. Consider that so much cold gas is available, that the entire regenerator is now at T_C. If the hot blow flow conditions are not modified, then the gas now exiting the cold end must be colder than during the cyclic-steady-state conditions when no extra cold gas had been available, simply because the entire regenerator now has a much larger thermal range to accept heat from the hot blow before warming up to the cyclic-steady-state profile.

There would be no threshold value of supplemental cold blow gas that would be required to next cause a decrease in the hot blow exit temperature, and therefore, any supplemental cold blow gas will reduce the average hot blow exit temperature compared to the balanced case. In the absence of extra cold blow gas, maximizing the cold blow is equivalent to not minimizing it; i.e. ensuring balanced flow.

When the application for a regenerative cycle is liquefaction, the design criterion of balanced and symmetrical regenerator operation might not provide the optimum performance for the complete application. It is possible to suffer a reduction in internal efficiency of the refrigeration device as a result of unbalanced and asymmetrical operation which is more than offset by the increase in efficiency of the external liquefaction process.

5.4.1 Bypass Regenerator

It was conceived that the Gifford-McMahon and Active Magnetic Regenerative cycles described previously can be modified to operate with different values of balance and symmetry from their typical operation by diverting a portion of the hot blow stream exiting the cold end into an external heat exchanger. The diverted stream bypasses the usual path through the regenerator, and hence, the operation can be termed a bypass regenerator. A bypass flow arrangement for a GM cycle is shown in Figure 5.7, and that for an AMR cycle is shown in Figure 5.8.

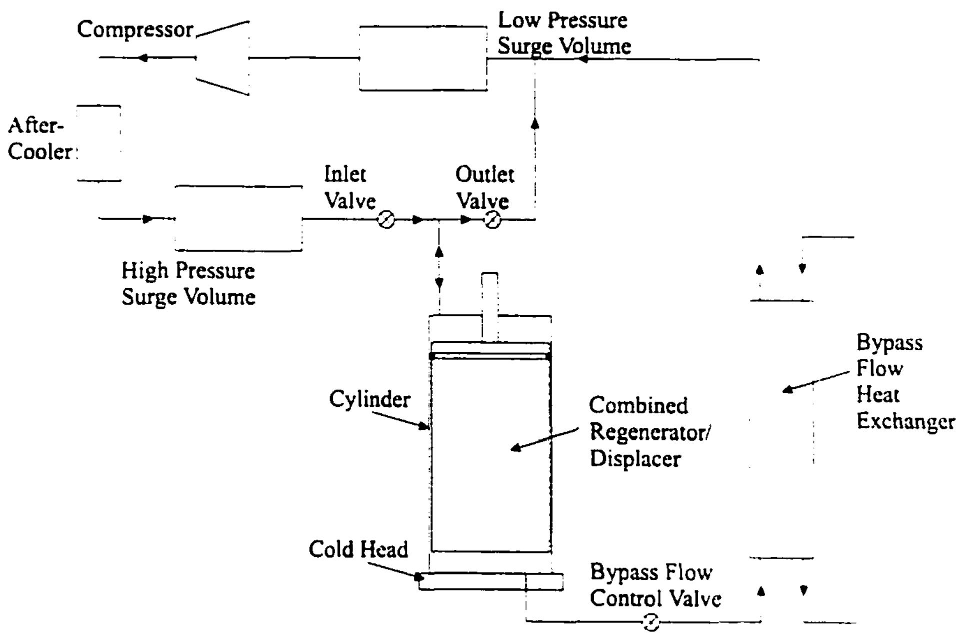

Figure 5.7 Schematic diagram of a single-stage Gifford-McMahon refrigerator modified for bypass regenerator operation.

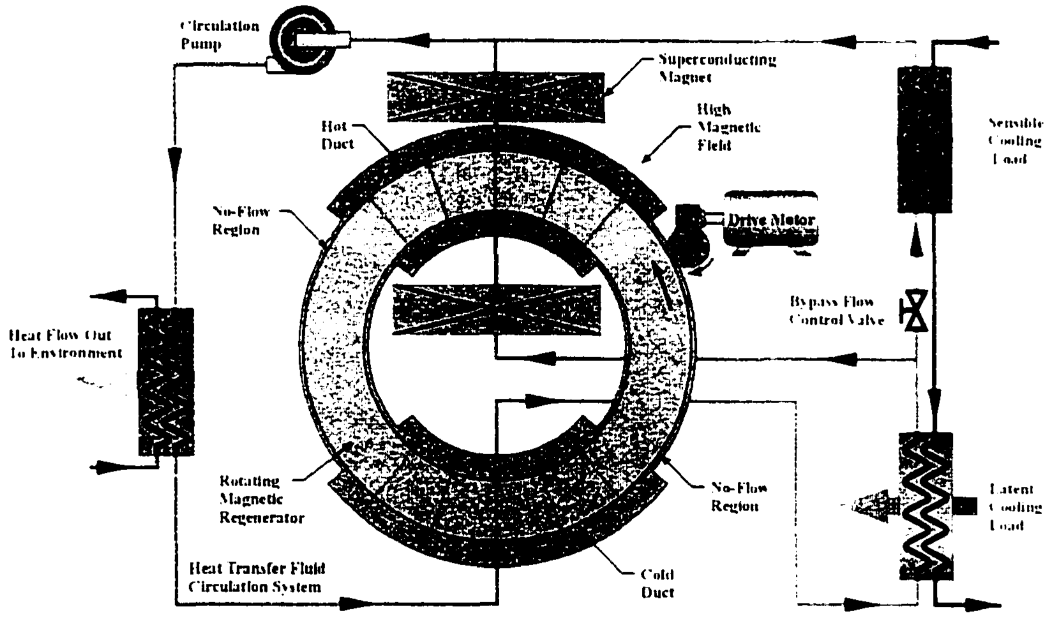

Figure 5.8 Schematic diagram of a single-stage AMR refrigerator modified for bypass regenerator operation.

The bypass flow control valves shown in Figure 5.7 and Figure 5.8 are used to control the proportion of flow that is diverted to the sensible cooling load heat exchangers. If the bypass valves are closed, then the refrigeration devices perform as previously described, without any distinct sensible cooling capability. As the bypass valves are gradually opened, an increasing proportion of the regenerator flow is diverted to the bypass heat exchanger.

5.5 Effect of Bypass Flow on GM Systems

5.5.1 Thermal Performance

It has been shown previously that when the goal of a refrigeration device is liquefaction, providing both a sensible cooling capacity and a latent cooling capacity is more efficient than providing a latent cooling capacity only, except in cases where the sensible cooling component is provided by a particularly inefficient process. Generally, then, the effect of bypass flow is to improve the liquefaction capability of the cooling capacity.

The effects of the bypass flow on the regenerator and net cooling capacity of the refrigeration device are as yet undetermined. For the bypass regenerator schemes to be effective, the product of any reduction in the net cooling capacity multiplied by the increase in the liquefaction capacity must be greater than unity. The degree of effectiveness of the bypass flow is specific to the operating conditions and the gas being liquefied.

5.5.2 Effect of Unbalance on the Thermal Ratio

Over the range $150 \leq \Lambda_{min} \leq 250$; $10 \leq \Pi \leq 30$, for an unbalanced regenerator with $\Pi' = \Pi''$, solving the Hausen regenerator equations, Equation 1.12 and Equation 1.13, shows that the hot blow thermal ratio can be approximated by:

$$\eta'_{th} \approx \beta \tag{5.17}$$

When $0.4 \leq \beta \leq 0.97$, this error is within ±0.5%, where the error is defined as:

$$\%\,Error = \frac{\beta - \eta_{th}'}{\eta_{th}'} \times 100\% \qquad (5.18)$$

with the largest deviation at the upper limit of the range. For $\beta > 0.97$, the approximation is accurate within +1.5%; however, small deviations in the value for thermal ratio near unity give rise to significant differences in the gas exit temperatures and lowest temperature obtainable upon adiabatic expansion, as indicated previously by Figure 4.1. As a result of this approximate equality, Figure 4.1 could also be used to determine the ideal minimum unbalance ratio (representing the maximum flow capacity imbalance) that could be tolerated in a GM to achieve a given cold head temperature by regarding the dependent variable as the unbalance factor.

5.5.3 Effect of Unbalance on the GM Cold Head Minimum Temperature

At the upper limit of thermal ratio, Figure 4.1 suggests that temperatures of approximately 25 K can be achieved with a regenerator having a thermal ratio of 0.96, if the system is adiabatic and the cold gas expansion results in a decrease of temperature by 0.3 times the absolute gas temperature before expansion. This is too idealized to accurately predict the GM cold head temperature as a function of unbalance ratio, since it ignores various sources of heat leak into the cold space.

For a reasonable estimate of the GM minimum temperature as a function of unbalance, some assumptions and definitions need to be made. With increasing unbalance, i.e., decreasing values of β, the achievable minimum cryocooler temperature increases, and hence temperature span decreases. A temperature span efficiency with unbalance ratio can be defined as:

$$\eta_{T_{span}} = \frac{T_H - T_{C,\beta}}{T_H - T_{C,\beta=1}} \qquad (5.19)$$

for

$$T_{C,\beta} = \frac{T_H\left(1 - \eta_{th,\beta}'\right)\left(1 - \Delta T_{R,net}\right)}{1 - \eta_{th,\beta}'\left(1 - \Delta T_{R,net}\right)} \qquad (5.20)$$

where $T_{C,\beta}$ is the minimum cold head temperature achievable with the unbalance ratio β and net gas expansion cooling proportional to $\Delta T_{R,net}$ times absolute temperature, T, and $\eta'_{th,\beta}$ is the regenerator thermal ratio for the hot blow with regenerator unbalance ratio β. The temperature span efficiency is the ratio of the maximum temperature span with an unbalanced regenerator to the maximum temperature span of the balanced regenerator for a fixed adiabatic expansion cooling proportionality constant $\Delta T_{R,net}$. $\eta'_{th,\beta=1}$ is the hot blow thermal ratio for the balanced, symmetric regenerator.

Over the range $150 \leq \Lambda_{min} \leq 250$; $10 \leq \Pi \leq 30$, the temperature span efficiency is a weak function of reduced length Λ_{min} and reduced period Π, and a strong function of the adiabatic expansion proportionality constant $\Delta T_{R,net}$. Figure 5.9 shows the temperature span efficiency for various values of Λ_{min}, Π, and $\Delta T_{R,net}$ as a function of regenerator unbalance ratio, β. For each regenerator, the temperature span efficiency decreases as the degree of unbalance increases (i.e., β decreases), and as the net adiabatic expansion coefficient decreases.

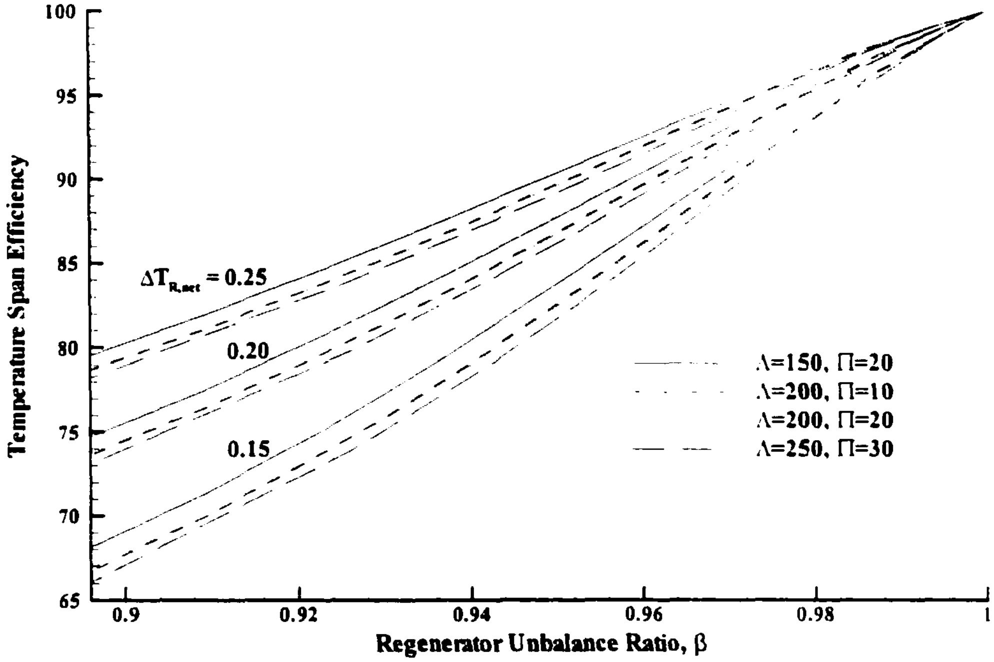

Figure 5.9 Regenerator temperature span efficiency as a function of unbalance ratio for various values of Λ_{min}, Π, and $\Delta T_{R,net}$.

Figure 5.10 shows the corresponding Bypass GM minimum cold head temperature as a function of bypass flow ratio, $1-\beta$, for an adiabatic expansion proportionality constant $\Delta T_{R,net} = 0.15$. For a GM regenerator spanning 300 K to ~20 K, the assumptions of the simple Λ-Π regenerator model, and the assumption of a constant value for $\Delta T_{R,net}$ are rather suspect, and the predicted cold head temperature shown should be considered as a guide only.

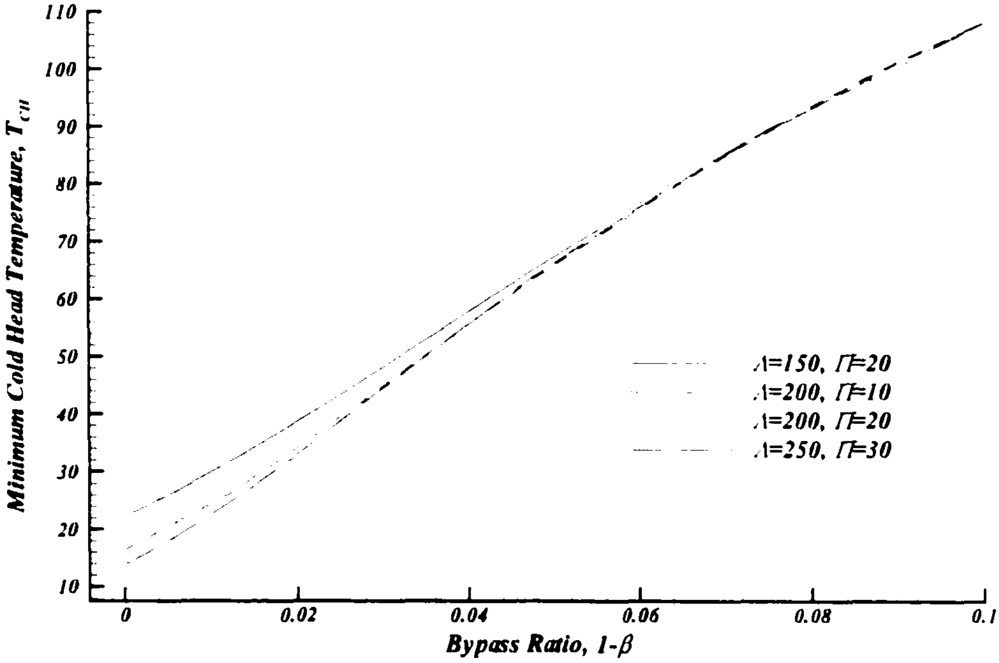

Figure 5.10 Predicted Bypass GM minimum cold head temperature as a function of bypass ratio.

When the regenerator must span a large temperature difference and multiple materials are used to maximize the solid heat capacity of the matrix, the optimal distribution of the matrix materials is a function of the unbalance because of its effect on the temperature profile within the regenerator. Schematic diagrams of the temporal and spatial temperature distributions within a symmetric balanced regenerator were given as Figure 1.2 and Figure 1.3. Figure 5.11 shows the matrix spatial temperature distributions at the moments of gas reversal for a symmetric balanced regenerator of reduced length $\Lambda = 100$ and reduced period $\Pi = 20$, and an asymmetric unbalanced regenerator of reduced length $\Lambda' = \Lambda_{\min} = 100$, reduced period $\Pi = 20$, and unbalance factor $\beta = 0.95$. The solid curves correspond to the symmetric balanced case and the dotted curves to the asymmetric unbalanced case, with the upper curves representing the end of the hot blow period and the lower curves representing the end of the cold blow period. As the unbalance increases, the average temperature within the regenerator matrix increases.

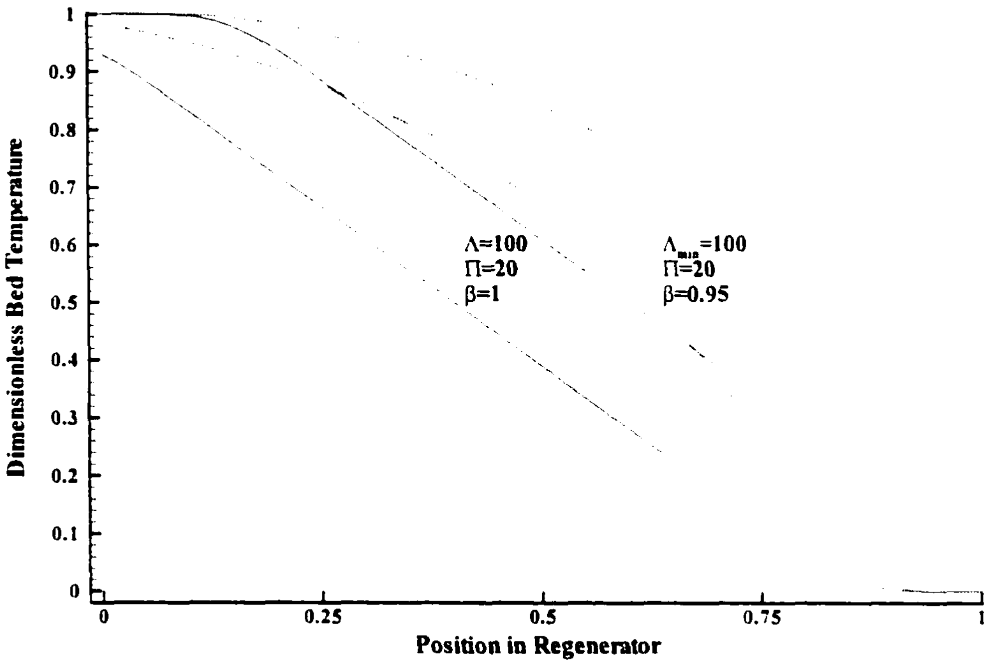

Figure 5.11 Comparison of dimensionless temperature profiles within balanced symmetric and unbalanced asymmetric regenerators.

5.6 Bypass AMR Regenerator

Without bypass flow, the regenerator of the AMR is unbalanced and asymmetrical due to the temperature and field dependence of the magnetic regenerator material and the usual selection of equal blow periods. Equation 2.8 shows that the operation can be made nominally balanced and symmetrical when bypass flow is permitted by allowing a heat transfer fluid flow imbalance during the hot and cold blow periods to compensate for the matrix material heat capacity imbalance from the applied magnetic field during the cold blow period.

A numerical model of the thermal operation of a rotary active magnetic regenerative refrigerator formed the basis of a Master's thesis by Spearing [86] and a modified version of that model serves as the basis for the theoretical results presented here. The lack of global energy conservation in the original model was addressed by a mass conservative formulation of density variation based on the average circumferential temperature at a given radial position, and selection of grid resolution sufficient for the flow conditions being considered for the results presented here.

5.6.1 Bypass AMR Simulations

Using the Spearing Master's AMR model, with fluid density constant circumferentially, and variable radially, and sufficient resolution for the fluxes considered so the non-conservative formulation does not introduce significant error, a study of typical bypass operation of an AMR was undertaken. The key operating conditions of the model are summarized in Table 5.1 and represent the operating conditions for the AMR's described in this section. A complete model input file is given in Appendix B. The system represented by the model was presented in Figure 2.10 in the case of equal hot and cold blow flow, and Figure 5.8 for the bypass flow cases.

Table 5.1 Summary of key parameters of the bypass AMR simulations.

Matrix Material	Packed bed of gadolinium spheres, 100×10^{-6} m diameter, 40% porosity
Matrix: R_{INNER}, R_{OUTER}, Thickness [m]	0.2725, 0.3275, 0.05
Flow Angle: Hot Blow, Cold Blow [°]	100, 100
No Flow Angle (Each Reversal) [°]	80
Maximum Fields [Tesla]	4, 5
Frequency of Rotation [Hz]	4
Heat Transfer Gas	Helium @ 5 MPa
Inlet Temperatures: T_H, T_C [K]	275, 225
Flow Rate: Hot Blow, Cold Blow [kg/s]	0.5, variable

In all cases presented here, the global energy balance represented by the sum of the heat out minus work in minus heat in all divided by the heat out is within 0.15%. That is, the error in the global energy balance is given by:

$$\left|\%Error\right| = \left|\frac{\dot{Q}_{out} - \dot{Q}_{in} - \dot{W}_{in}}{\dot{Q}_{out}} \times 100\%\right| < 0.15\% \qquad (5.21)$$

The global energy balance errors were approximately 10 times lower than this limit for the majority of the results presented here.

Figure 5.12 shows the temperature profile within the AMR matrix material for the parameters given in Table 5.1, with a maximum field of 4 Tesla and equal flow rate of heat transfer gas during the hot and cold blows. Temperature is represented by elevation above a schematic of the regenerator bed and flow ducts. The hot blow region is shown in the foreground and the cold blow region is in the background, with no-flow regions on each side separating the hot and cold blow sections. Boundary lines drawn on the surface of the temperature plot denote the divisions between the flow regions. The high magnetic field region is shown by the ellipse which covers the cold blow section. For the perspective of this figure (and following figures), the regenerator ring rotates counter-clockwise. To clarify the trend across the radius of the plot, the inner radius has been drawn to a value of approximately one-half the outer radius.

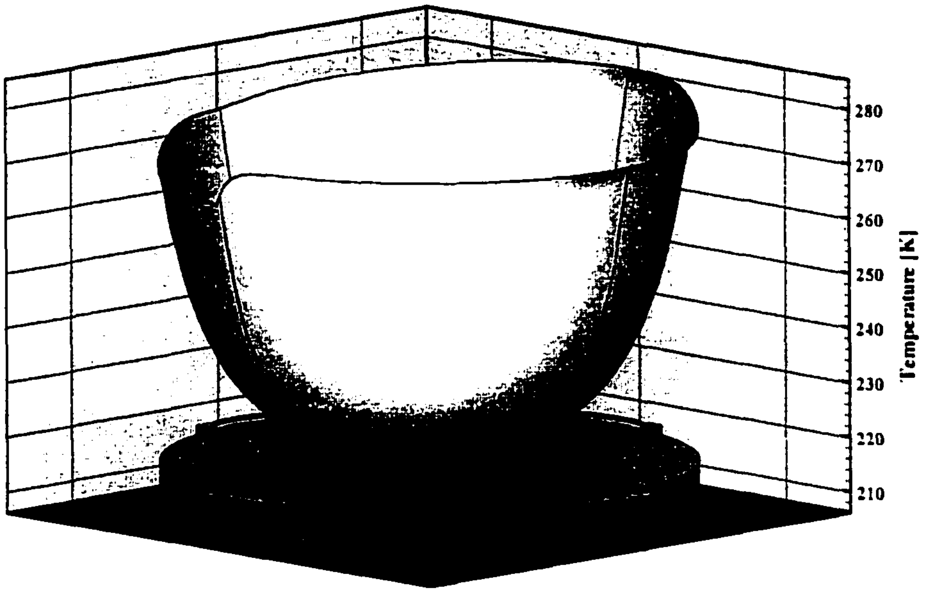

Figure 5.12 Solid temperature profile for an AMR with equal heat transfer fluid flow for hot and cold blow periods.

The temperature profile of the standard, equal flow AMR can generally be described as "bowl-shaped," due primarily to the regenerator unbalance between the hot and cold blows. The unbalance can be seen in Figure 5.13 which plots the utilization as a function of regenerator position, where the reduced length and reduced period values used to calculate the utilization are based on local conditions within the regenerator. Direct comparison of the hot and cold region utilization factors is possible because the hot and cold blow periods (angular widths) are equal. Unequal blow periods would require comparison of the integral of the utilizations over the flow area. The utilization is higher in the high field region, corresponding to the cold blow, compared to the utilization in the hot blow region.

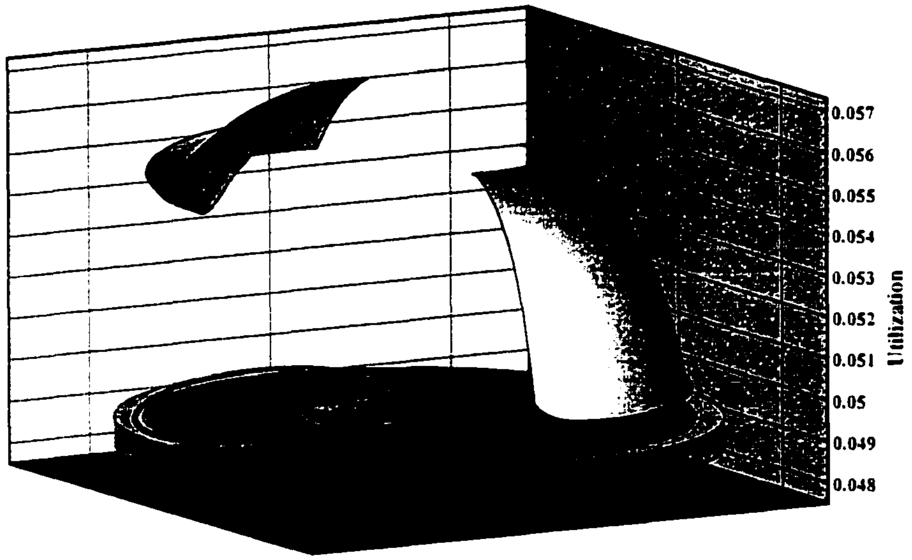

Figure 5.13 Utilization factor for an AMR with equal heat transfer fluid flow for hot and cold blow periods.

As bypass flow is extracted from the system, causing a flow imbalance between the hot and cold blows with the hot blow having a greater mass flow, the temperature profile within the regenerator gradually changes from concave to nearly linear to convex. At some critical value of bypass flow, dependent on the matrix material, temperature span, magnetic field, and heat transfer fluid flow rate, the average exit temperature of the cold heat transfer fluid from the hot blow stream exactly equals the cold blow inlet temperature. Beyond this value of bypass flow, the temperature span from T_H to T_C cannot be supported by the refrigeration supplied by the AMR regenerator material under the given operating conditions. In effect, there is too much flow extracted from the system and insufficient cold blow regeneration to support the temperature span of the regenerator.

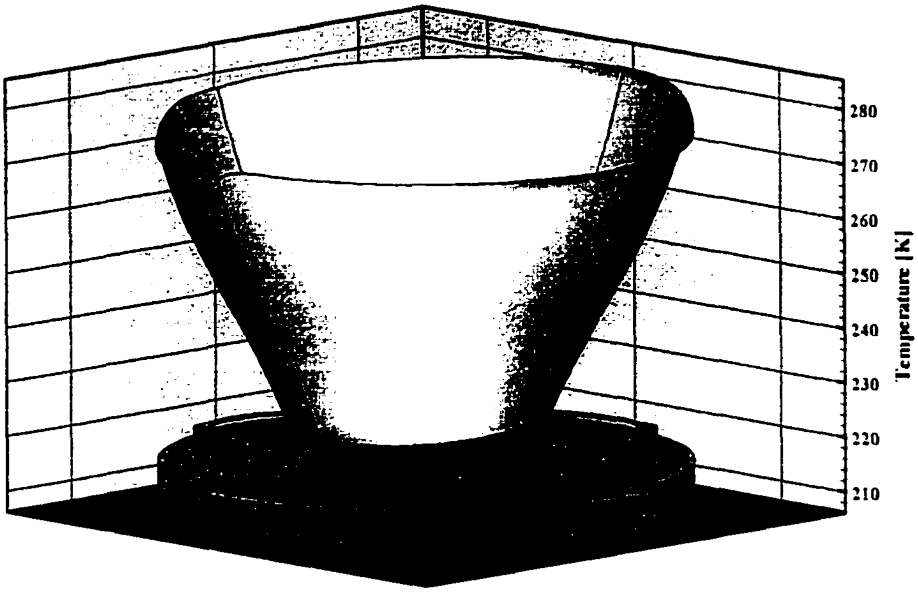

Figure 5.14 Solid temperature profile of a bypass AMR with 4% bypass flow.

Figure 5.14 shows the temperature profile within the regenerator when the cold blow stream flow rate is 96% of the hot blow stream flow rate, where the 4% imbalance is diverted for the bypass stream. The figure is drawn with the same orientation as the temperature profile of Figure 5.12. Note that the ratio of net cold blow flow (i.e. total flow minus the bypass flow) to total flow is not equal to the unbalance factor, β, because of the stricter definition for the utilization factor for AMR's which does not assume constant matrix material properties. The temperature profile is nearly linear across the regenerator bed, with the maximum and minimum temperatures each greater than the corresponding temperatures of the equal flow regenerator. The average heat transfer fluid rejection temperature is correspondingly higher than the equal flow regenerator, which in a practical device would facilitate heat rejection from the system where the rejection temperature is only modestly higher than the hot blow inlet temperature due to the limited temperature change of the magnetic material upon adiabatic magnetization.

The nearly linear temperature profile of the 4% bypass flow AMR regenerator is due primarily to the nearly equal utilization factors for the device. Figure 5.15 shows the utilization using the same orientation as the equal flow AMR utilization profile of Figure 5.13. For the equal flow AMR, the volume-integrated utilization factor is approximately 4.3% higher in the cold blow region than in the hot blow region. In the 4% bypass AMR, the volume integrated utilization factor is approximately 1.2% higher in the cold blow region than in the hot blow region. In addition, both the hot blow region and cold blow region volume integrated utilization factors are lower in the 4% bypass AMR than the corresponding regions of the equal flow AMR, by approximately 1.8% and 4.8%, respectively.

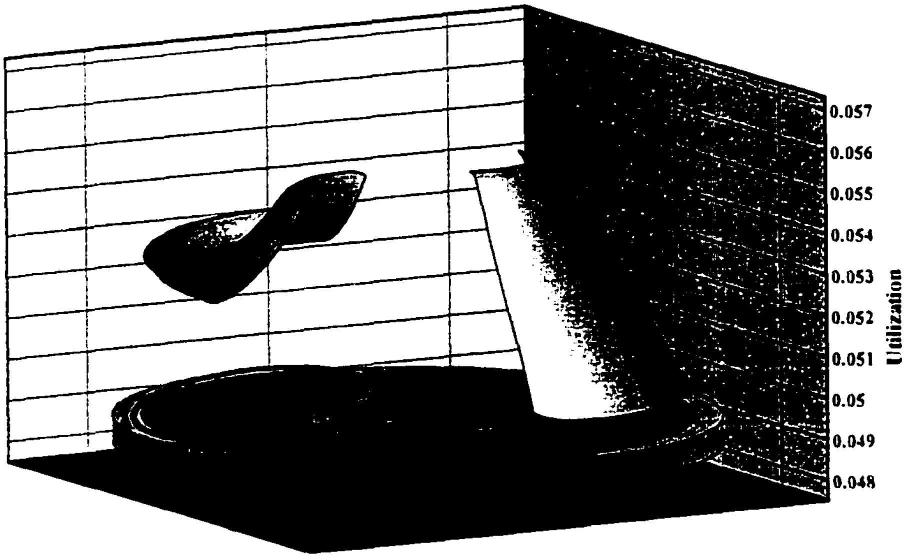

Figure 5.15 Utilization factor of a bypass AMR with 4% bypass flow.

As the bypass flow approaches the maximum permissible while maintaining the temperature span of the AMR, the temperature profile becomes convex, as shown in Figure 5.16. This figure helps to make obvious another trend in the temperature profiles as the degree of flow imbalance is increased. For equal flow for hot and cold blows, the largest temperature variation over the cycle is within the material at the outer rim of the matrix. This variation is evident in the large temperature rise at the start of the hot blow region, where the matrix is rapidly warmed to the hot blow inlet temperature. At the start of the cold blow, the matrix material is only slightly warmer than the cold blow inlet temperature. For the 4% bypass flow, the temperature variation at the inner and outer rims of the matrix are nearly equal. For the 8% bypass flow, the largest cycle variation in temperature occurs at the inner rim, and very little occurs at the outer rim.

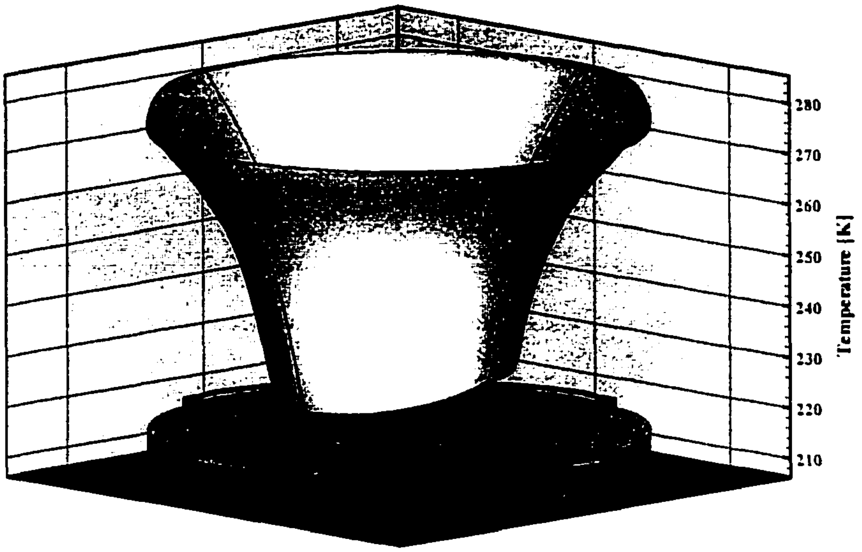

Figure 5.16 Solid temperature profile of a bypass AMR with 8% bypass flow.

5.6.2 Effect of Bypass Flow on the Magnetic Work Rate

The ratio of bypass flow has a significant effect on the distribution of work within the regenerator. The pseudo-steady-state work rate for the regenerator is given by the integral over the volume of the magnetization power per unit volume, *viz*:

$$\dot{W}_{in} = -\omega\mu_0 \int_{vol} H \frac{dM}{d\theta} dV \qquad (5.22)$$

where ω is the angular rotation frequency of the regenerator. If the temperature, and hence the magnetization, does not change over the cold blow region for a given infinitesimal volume, then that volume provides no net refrigeration over the cycle. For the AMR, this leads to a conflict with the traditional requirements for regenerators. On the one hand, the ideal regenerator is characterized by an infinite thermal mass that does not change temperature despite heat transfer fluid flow. On the other hand, the AMR regenerator does not provide useful refrigeration unless the temperature, and hence the magnetization, is changed as a result of fluid flow. This conflict leads to an optimal fluid flow that balances these requirements, both in terms of total flow, and the ratio of bypass flow.

Figure 5.17 shows the magnetization power per unit volume for the AMR without bypass flow. The positive peak and negative valley on either side of the magnetic field region show the inherent work recovery of the rotary system. The work recovery is apparent mechanically as a net rotational torque on the regenerator ring. The temperature change in the cold blow region causes a change in magnetization, which is responsible for the net torque of the system. If the temperature did not change over the cold blow region, there would be zero net torque (assuming no electrical eddy currents or magnetic hysteresis) and zero cooling power.

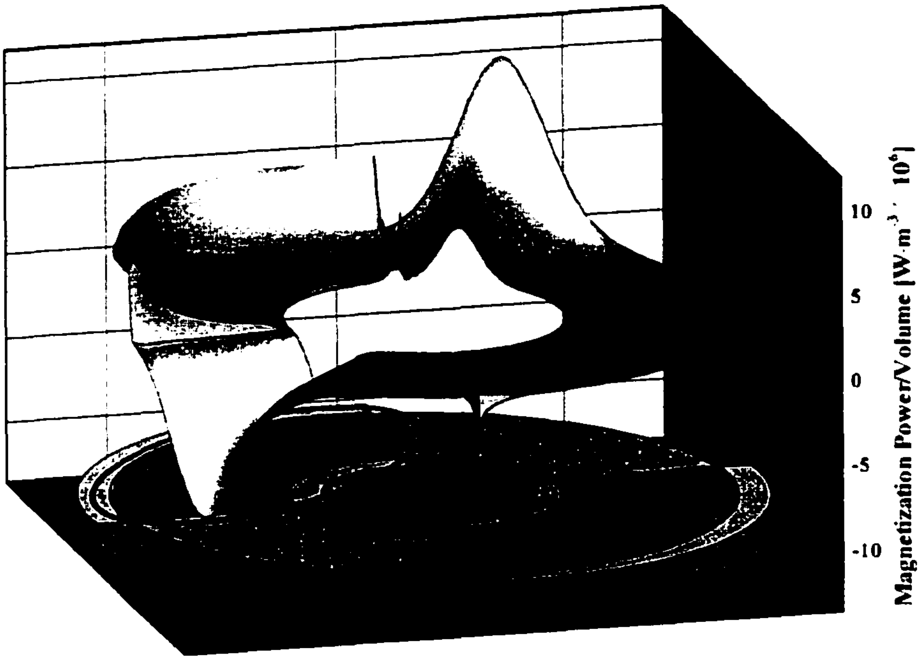

Figure 5.17 Magnetization power per unit volume for an AMR without bypass flow.

Integrating the regenerator pseudo-steady-state magnetization power per unit volume over the volume yields the total work rate. Integration is carried out over the three dimensions of the ring-shaped volume, namely, the thickness, the angular displacement, and the radial thickness. If the integral is performed over the first two dimensions, namely the thickness (dz) and the angular displacement (r·dθ), a line integral that represents the net cycle work for a given radial position results. That is, a plot of the function $\dot{W}'(r)$, taken from the integral:

$$\dot{W}_m = \int_r \dot{W}' \, dr \tag{5.23}$$

where $\dot{W}''$ is the work rate per circular shell area of the regenerator, will yield a curve that shows the contribution of each concentric shell of regenerator matrix material. When the contribution is small, that portion of regenerator does not contribute significantly to the overall refrigeration effect. If the refrigeration contribution is small, then that segment may be having a negative impact on the overall performance of the AMR, since the segment will still be contributing to the cost of the device through increased material and magnet costs, increased structural requirements, and increased entropy production from imperfect heat transfer over the volume.

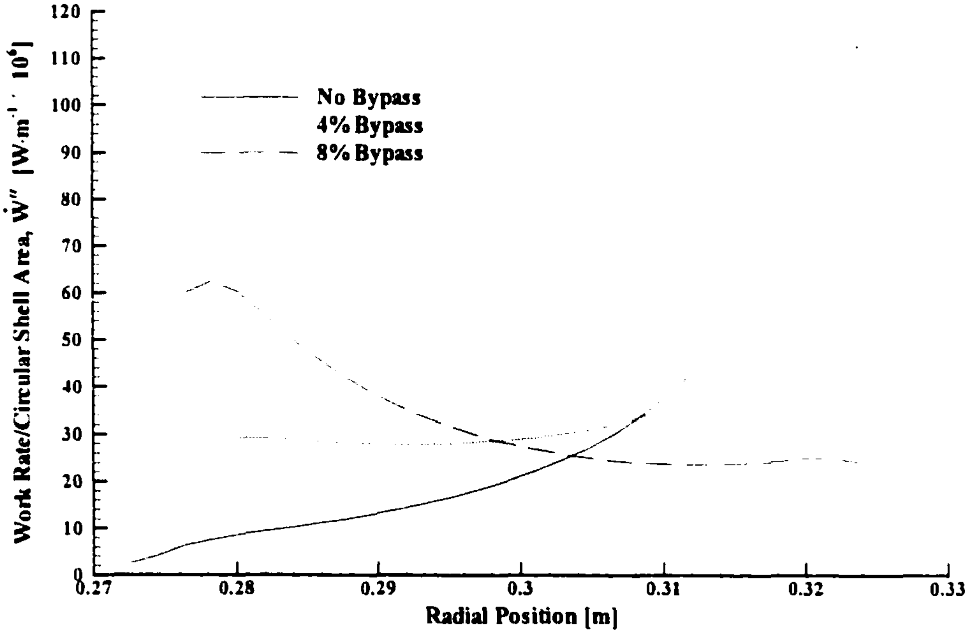

Figure 5.18 Comparison of the distribution of radial work input rate between standard and bypass AMR's.

Figure 5.18 shows a plot of the work rate per circular shell area of the regenerator as a function of radial position for the three AMR flow cases presented above. The total work rate for each AMR is equal to the area under the respective curve. For the standard AMR with zero bypass flow, the majority of the refrigeration is provided by material at the outer radius of the AMR ring. The 4% bypass flow AMR has a bias of work at the outer radius, but has an almost even distribution of work input across the regenerator. The 8% bypass flow AMR has the majority of the work input at the inner radius. Despite the largest magnetocaloric effect occurring at the outer radii where the material is warmer and closer to the Curie point, the work input can be "tuned" using bypass flow. This could be especially important in a multi-material AMR having a larger temperature span if one material has a significantly different magnetocaloric effect compared to the other constituent materials. The bypass might provide a means to bias the work input to or from this disparate material.

5.6.3 Latent and Sensible Load Matching

As the proportion of bypass flow is increased, there is an increasing proportion of cooling provided as sensible cooling, and any ratio of latent cooling to sensible cooling is attainable by suitable selection of the bypass ratio. For this work, for the bypass AMR, the latent cooling is calculated as the cooling capacity of the hot blow stream between the limits of the average exit temperature of the stream and the inlet temperature of the cold blow stream. That is, the latent cooling capacity is defined as:

$$\dot{Q}_C = \left(\dot{m}C_f\right)_{hot}\left(T_C - \bar{T}'_{f,o}\right) \tag{5.24}$$

The sensible cooling is defined as the cooling capacity of the bypass stream between the limits of the cold blow inlet temperature and the hot blow inlet temperature. That is, the sensible cooling capacity is defined as:

$$\dot{Q}_B = \left(\dot{m}_B C_f\right)\left(T_H - T_C\right) \tag{5.25}$$

where $\dot{m}_B$ is the mass flow rate of the bypass stream, and C_f is taken as the average heat capacity of the heat transfer fluid over the temperature limits considered. The upper temperature limit is somewhat arbitrary, in that any heat transferred into the bypass stream above the hot blow inlet temperature will ultimately be rejected along with the cold blow outlet stream, which is also above the hot blow inlet temperature, in the heat rejection exchanger. For the liquefaction capacity calculations, the upper limit of the bypass heat exchanger is taken as 280 K, which lies between the hot blow inlet temperature and the cold blow exit temperature.

Figure 5.19 shows the total latent cooling and the ratio of latent cooling to sensible cooling as the proportion of AMR bypass flow is varied for the conditions previously presented in Table 5.1 for a 4 Tesla applied field. The datapoints for the ratio of cooling capacities at the extrema of zero bypass flow and maximum bypass flow are excluded from this figure, being infinite and zero, respectively. The latent cooling at zero bypass flow is 7730 W. The sensible cooling increases linearly with bypass flow rate, since the temperature limits of the bypass flow are fixed. At a bypass ratio of 10%, the sensible cooling capacity is 13066 W and the latent cooling capacity is 285.5 W. The latent cooling is zero at approximately 10.22% bypass.

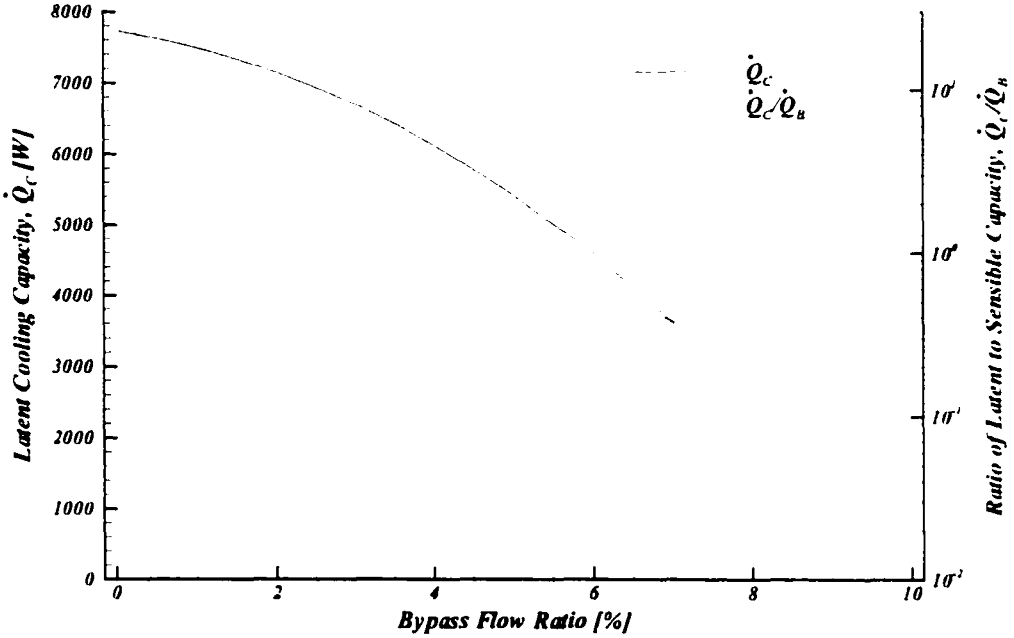

Figure 5.19 Bypass AMR latent cooling capacity and ratio of latent to sensible cooling capacity as a function of bypass flow ratio.

5.6.4 Total Equivalent Cooling Capacity

The work input rate for the AMR is nearly constant across a broad range of bypass flow. Across the range of zero to 10% bypass flow, the lowest work input rate is just under 4% lower than the highest work input rate. If the bypass cooling load exergy is ideally converted to an equivalent cooling load at T_C, then a total refrigeration coefficient of performance can be defined as:

$$COP_{Q_{EQ}} = \frac{\dot{Q}_C + \dot{Q}_{B,EQ}}{\dot{W}_{in}} \tag{5.26}$$

where

$$\dot{Q}_{B,EQ} = \dot{m}_B C_f T_C \left[\frac{T_H}{T_H - T_C}\ln\left(\frac{T_H}{T_C}\right) - 1\right] \tag{5.27}$$

Figure 5.20 plots the equivalent cooling load coefficient of performance as a function of bypass ratio for the AMR operating under a 4 Tesla field and, for comparison, a 5 Tesla field. The higher field allows a higher peak COP value and also shifts the peak to higher values of bypass flow. Since the input power is nearly constant over the range of bypass flow, the increase in the COP is primarily due to an increase in the total cooling capacity.

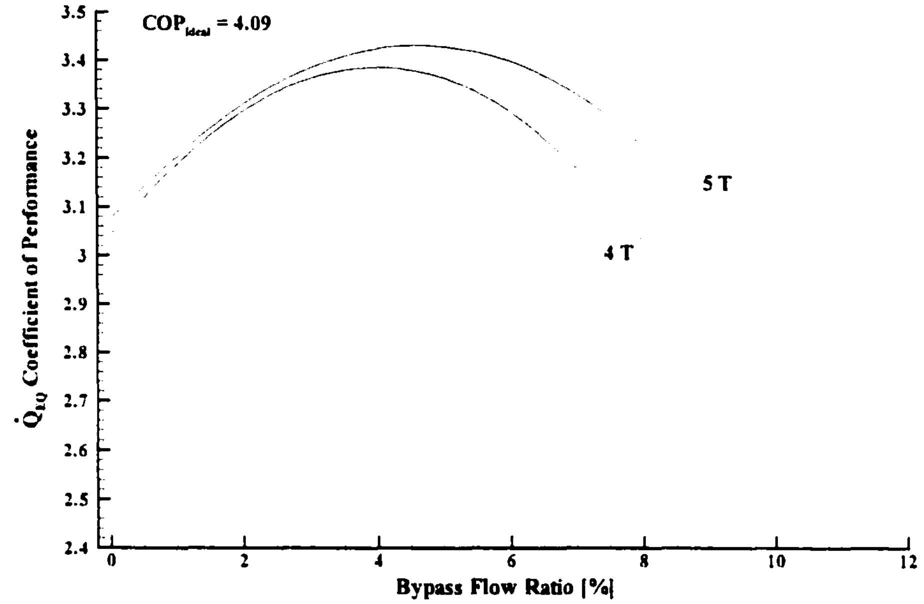

Figure 5.20 AMR equivalent cooling load coefficient of performance as a function of bypass flow ratio for applied fields of 4 Tesla and 5 Tesla.

The coefficient of performance can also be plotted as a function of the ratio of latent to sensible cooling capacity, as shown in Figure 5.21. This figure shows that the optimal liquefaction operation point would coincide with a latent to sensible cooling requirement of approximately 1.25. At the saturation temperature of 225 K and starting with process gas at 300 K, Figure 5.4 shows the latent to sensible cooling requirements of ethane and krypton are 3.22 and 5.02, respectively. When the process gas starting temperature is lower, the enthalpy ratios are higher for a given saturation temperature. Even though these ratios are greater than the optimal enthalpy ratio for the peak equivalent cooling load COP, the liquefaction capacity of the AMR is enhanced by the bypass flow.

The gas liquefaction capacity of the AMR with and without bypass flow can be determined given some assumptions and definitions.

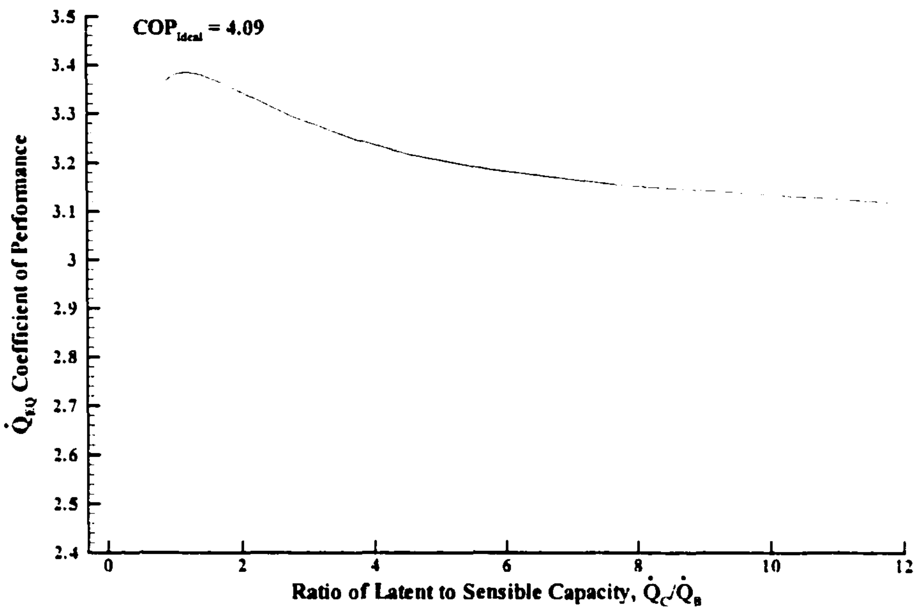

Figure 5.21 AMR equivalent cooling load coefficient of performance as a function of latent to sensible cooling capacity ratio for an applied field of 4 Tesla.

5.6.5 Case Study:

Effect of Bypass Flow on the Liquefaction of Ethane at 225 K

For the AMR without bypass flow, it is assumed that process gas at $T_H = 280\,K$ is introduced into a frictionless heat exchanger placed between the hot blow exit and the cold blow inlet and the process mass flow adjusted such that the sensible heat and latent heat absorbed in the exchanger corresponds to the available cooling, $\dot{Q}_C$, from the AMR. The inlet temperature of the process gas is selected to correspond with the approximate rejection temperature of the AMR for the given operating conditions. The analysis and results are similar regardless of the initial temperature of the process gas, with slightly higher efficiency predicted as the process gas inlet temperature rises. The liquified process gas exits the exchanger at $T_C = 225\,K$. With these assumptions, the AMR without bypass flow can liquefy a process stream with a mass flow rate given by:

$$\dot{m}_P = \frac{\dot{Q}_C}{\left(h_g\big|_{(T_H,P_{sat})} - h_f\big|_{(T_C,P_{sat})}\right)_P} \tag{5.28}$$

where the subscript P refers to the process stream, h is the stream enthalpy, and the subscripts g and f refer to the vapour and liquid states, respectively at the subscripted temperature and pressure conditions. The condensation process is considered ideal in that all available cooling in the condensing heat exchanger is utilized.

For the AMR with bypass flow, it is assumed that process gas at $T_H = 280\ K$ is first introduced into a frictionless counterflow heat exchanger with the countercurrent gas flow supplied by the bypass gas at T_C. From the counterflow heat exchanger, the process gas is then further cooled and liquefied in a heat exchanger between the hot blow exit at $\bar{T}'_{f,o}$ and the cold blow inlet at T_C. The process gas exit temperature from the counterflow heat exchanger is a function of the heat exchanger effectiveness, defined as:

$$\varepsilon = \frac{\textit{heat actually transferred}}{\textit{maximum heat available for transfer}} \tag{5.29}$$

The performance analysis is greatly simplified if the heat exchanger gases are assumed to have constant heat capacity, and the heat exchanger effectiveness can then be expressed as:

$$\varepsilon = \frac{C_h\left(T_{h_1} - T_{h_2}\right)}{C_{\min}\left(T_{h_1} - T_{c_1}\right)} = \frac{C_c\left(T_{c_2} - T_{c_1}\right)}{C_{\min}\left(T_{h_1} - T_{c_1}\right)} \tag{5.30}$$

where C_h is the product $\left(\dot{m}C_f\right)_h$ for the hot inlet stream (i.e. process stream), C_c is the product $\left(\dot{m}C_f\right)_c$ for the cold inlet stream (i.e. bypass stream), $C_{\min}$ is the minimum of C_h and C_c, T_{h_1} is the hot inlet stream inlet temperature, T_{h_2} is the hot inlet stream outlet temperature, T_{c_1} is the cold inlet stream inlet temperature, and T_{c_2} is the cold inlet stream outlet temperature. In terms of the notation of the AMR, $T_{h_1} \equiv T_H$

and $T_{c_1} \equiv T_C$. The bypass gas exit temperature, the process gas exit temperature, and the process gas flow rate are now unknowns to be solved once the heat exchanger effectiveness and AMR latent cooling capacity are specified according to:

$$T_{c_2} = T_{c_1} + \varepsilon\left(T_{h_1} - T_{c_1}\right) \tag{5.31}$$

and

$$T_{h_2} = \frac{\dot{Q}_C T_{h_1} - C_c\left(T_{c_2} - T_{c_1}\right)\left[\left(\frac{h_{fg}}{C_f}\right)_P - T_C\right]}{\dot{Q}_C + C_c\left(T_{c_2} - T_{c_1}\right)} \tag{5.32}$$

if $C_{\min} = C_c$, or are specified according to:

$$T_{h_2} = T_{h_1} - \varepsilon\left(T_{h_1} - T_{c_1}\right) \tag{5.33}$$

and

$$T_{c_2} = T_{c_1} + \frac{\dot{Q}_C\left(T_{h_1} - T_{h_2}\right)}{C_c\left[\left(\frac{h_{fg}}{C_f}\right)_P + T_{h_2} - T_C\right]} \tag{5.34}$$

if $C_{\min} = C_h$, where in either case the latent cooling load is applied to the process gas liquefaction according to:

$$\dot{Q}_C = \dot{m}_P\left[\left(h_{fg}\right)_P + \left(C_f\right)_P\left(T_{h_2} - T_C\right)\right] \tag{5.35}$$

where the subscript P refers to the process gas, $\dot{m}_P$ is the mass flow rate, $\left(h_{fg}\right)_P$ is the latent heat of condensation, and $\left(C_f\right)_P$ is the heat capacity. For a given bypass heat exchanger, it is first assumed that $C_{\min} = C_c$ and Equations 5.31 and 5.32 are solved in sequence. Equation 5.35 is then solved for the process stream mass flow rate, $\dot{m}_p$, and the assumption that $C_{min} = C_c$ is checked. If $C_{min} \neq C_c$, then the first results for T_{c_2} and T_{h_2} are discarded and instead Equations 5.33 and 5.34 are solved in sequence, followed by Equation 5.35 to determine the process mass flow rate, i.e. the quantity of process gas that can be liquefied with the given cooling loads available.

In this analysis, all the latent cooling capacity, $\dot{Q}_C$, is applied to the liquefaction process, whereas some of the bypass cooling load, $\dot{Q}_B$, may be discarded according to the energy balance in the bypass heat exchanger and the limitations of the latent cooling capacity. This procedure is repeatedly performed on the 4 Tesla AMR simulation results to examine a range of bypass heat exchanger effectiveness from $\epsilon = 0.01$ to $\epsilon = 1.00$, and a bypass flow ratio from 0% to 3.5% for the liquefaction of the process gas ethane at a saturation temperature of 225 K. The enthalpy ratio is 4.43 for this process gas under these operating conditions. The results are calculated as a figure of merit, where the liquefaction capacity is normalized to an ideal liquefier having the same input work rate as the particular AMR operating conditions under consideration, and are presented in Figure 5.22.

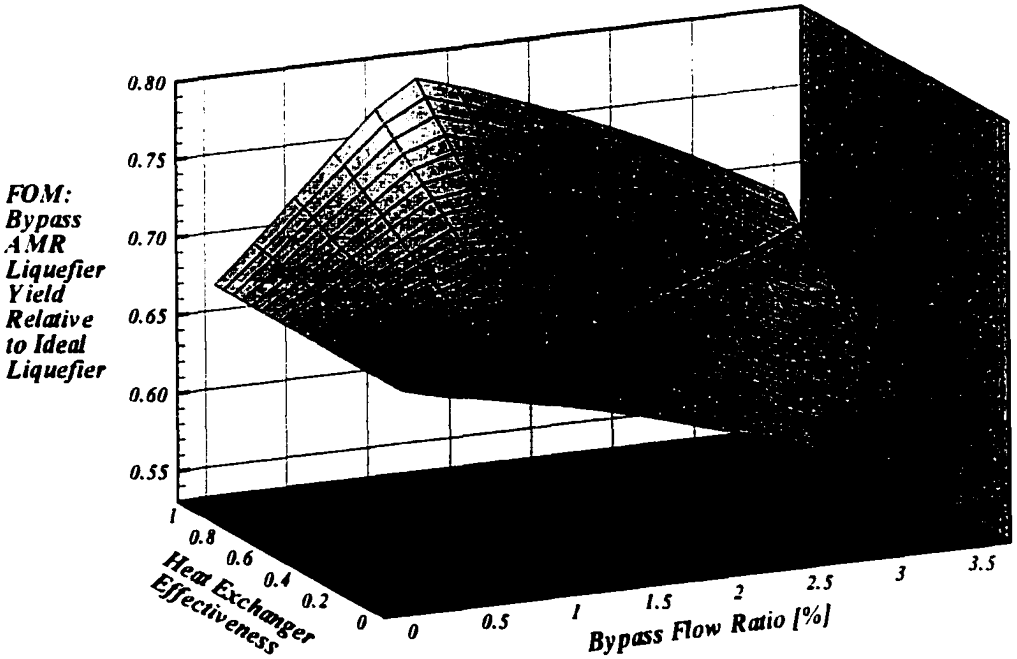

Figure 5.22 Ratio of the liquefaction capacity of ethane at 225 K of the 4 Tesla bypass AMR to an ideal liquefier as a function of the bypass AMR sensible cooling heat exchanger effectiveness and bypass flow ratio.

At zero bypass flow ratio, the AMR liquefier yield is independent of the bypass heat exchanger effectiveness because the bypass heat exchanger is not used. The entire liquefaction sensible and latent cooling load is accepted at T_C using the latent cooling capacity. The FOM along this line, and along the thick dividing line drawn across the surface, is approximately 0.67. Above the dividing line, the combination of heat exchanger effectiveness and bypass flow ratio gives an FOM greater than 0.67. For these configurations, the bypass flow arrangement gives a higher liquefaction yield than the standard AMR without bypass flow.

The maximum value of FOM of 0.79 occurs at a bypass ratio of approximately 1.25% and a heat exchanger effectiveness of unity. For this operation point, the bypass flow has provided a 17.5% increase in liquid ethane yield over the AMR without bypass flow for the same input power. Below the dividing line, the yield is lower than the AMR without bypass flow and would not normally be selected as the preferred operation point. For these operation points, a significant portion of the available cooling capacity is unused, either as a result of ineffective heat transfer in the bypass exchanger (low ϵ), or as a result of insufficient cooling capacity in the condensing heat exchanger relative to the capacity of the bypass heat exchanger (low $\dot{Q}_C/\dot{Q}_B$ compared to h_R).

The increased liquefaction rate with the bypass flow is achieved by "internal" and "external" improvements of the liquefier system. As the bypass flow is increased, the AMR itself operates more efficiently, as evident in Figure 5.20 which shows a maximum in the efficiency and total refrigeration capacity (since the input power is nearly constant) at a bypass ratio of approximately 4%. At a bypass ratio of 1.25%, where the ratio of latent to sensible cooling capacity is approximately 4.54, the total refrigeration capacity is larger by a factor of approximately 1.057 compared to zero bypass ratio. This improvement can be classified as an internal improvement, since it results in a more efficient conversion of input power to total refrigeration without regard to how that refrigeration capacity is used.

For ethane cooled from 280 K and liquefied at 225 K, the ideal refrigerator liquefaction yield is only 90.1% of the ideal liquefier yield. Inverting the relation, the ideal liquefier capacity is larger by a factor of 1.110 compared to the ideal refrigerator. Providing pre-cooling to the gas before condensation can be considered an external improvement, since it is an improvement to the gas liquefaction application without consideration of the source of the cooling.

The total increase in yield for the bypass AMR is the product of the factors by which the internal and external improvements increase the yield, which is 1.173, or an increase of 17.3%. The slight discrepancy in the yield increase, 17.3% calculated here compared to 17.5% indicated in Figure 5.22, is due to the net effect of the error introduced by assuming constant heat capacity in the bypass heat exchanger, the imperfect match of latent and sensible cooling capacities to the process gas requirements, and setting the upper limit of cooling capacity of the bypass exchanger as 280 K for the liquefaction calculations, rather than 275 K which was used for the equivalent cooling load COP calculations.

Chapter 6

Simulation of Active Magnetic Regenerators Using CFX-TASCFlow

6.1 Introduction

6.1.1 Problem with Existing Models

The rotary active magnetic regenerative refrigerator computer numerical model by Spearing [86] employed a simplified pseudo-2-dimensional fluid flow within the regenerator. The pseudo-2-dimensional fluid flow is described by independent flow in the radial and circumferential directions. The radial flow is due to the hot and cold blow fluid flows and is assumed evenly distributed over the flow region with no accumulation. The circumferential flow is due to entrainment of the fluid within the pores of the matrix material and its velocity is described by the rotation of the solid only.

The incompatibility of these flow assumptions arises when the mass of fluid entrained within the pores is allowed to change as a result of fluid density changes from temperature changes across a hot or cold blow zone during normal operation. Since the circumferential and radial flows are independent and fixed, neither flow can contribute to the accumulation (or reduction) of fluid entrained within the pores. This results in an implicit violation of mass conservation, which in turn results in a violation of global energy conservation. The error introduced by the density-induced mass conservation violation increases as the entrained fluid flow increases relative to the forced mass flow from the hot and cold blow flows, i.e., generally at increasing reduced length and decreasing reduced period.

For large temperature spans, there can be a large change in heat transfer fluid density, and a mass-conservative assumption of constant density may not be appropriate. In this case the simplicity of the pseudo-2-dimensional fluid flow can be maintained, while considering the density variations, by implementation of a density profile that is a function of the average temperature circumferentially at a given radius. That is, density will be a function of radius based on the average cycle temperature for the radial position, and will not be a function of circumferential position. The variation in temperature radially will typically be several times the variation in temperature circumferentially, so this approximation maintains the essence of temperature dependent density without violating mass conservation in the simplified flow field.

6.2 Rotary Regenerator Fluids Simulation Using CFX-TASCFlow

6.2.1 Conservation of Fluid Mass and Momentum

Whether an assumption of constant density or average circumferential density is employed, of interest is the validity of a pseudo-2-dimensional fluid flow field representing the likely flow pattern within a rotary AMR. A computational fluid dynamics model using CFX-TASCFlow was developed to examine this issue. The equations solved by the package expressing the conservation of mass, momentum, and energy for the system have been outlined previously as Equations 4.11, 4.12, and 4.13, respectively.

6.2.2 Momentum Source Term

For the AMR regenerator studies, the regenerator bed was considered to consist of a packed bed of spherical particles, and a corresponding momentum source term was modelled to represent a local pressure drop per unit length corresponding to the Ergun equation [96] as:

$$\frac{dP}{dx_i} = -\frac{150\mu(1-\alpha)^2 u_i}{D_p^2\,\alpha^3} - \frac{1.75\rho_f(1-\alpha)|\bar{v}|u_i}{D_p\,\alpha^3} \qquad (6.1)$$

where μ is the fluid viscosity, α is the bed porosity, D_p is the packing particle diameter, ρ_f is the fluid density, and u_i is the component of the fluid velocity $\bar{v}$ in the x_i coordinate direction.

When the regenerator bed was considered to rotate, the momentum source term was determined using the relative fluid velocity calculated as the difference between the absolute velocity of the bed and the absolute velocity of the fluid. This imparted momentum to the fluid in the direction of the solid rotation, while not affecting the momentum in the radial direction compared to calculations without bed rotation. This allowed the representation of a rotating bed using a stationary computational grid.

6.2.3 Scope of Model and Methodology

The packed particle bed regenerator ring was modelled without any accompanying container. In a practical device, some container would be necessary to contain the particles (unless the particles are sintered or bonded in some way), however, the details of container design were omitted to simplify the problem. Further simplifications included the omission of any radially oriented flow barriers or other clearances and seals which would be required to limit circumferential flow in excess of the entrained flow. Such flows outside the desired flow path through the regenerator would cause a thermal short-circuit and degraded performance in a practical device.

A transient, two-dimensional model, using three nodal planes in the axial direction was created. The upper and lower nodal planes were assigned symmetry boundary conditions. The nodes of the middle nodal plane defined the centres of control volumes. This follows the recommended procedure for this software to create what is effectively a two-dimensional model with no variation in the third (axial) direction within the framework of the three-dimensional code.

Three different scenarios were modelled for the flow inlet and outlet duct regions. In the first scenario, the duct regions were considered to be fully open, 100% porous regions. In the second scenario, the duct regions were considered to be fully open for half the duct, then 65% porous for half the duct adjacent to the regenerator ring. Figure 6.1 shows a schematic diagram of this arrangement. In the third scenario, the duct regions were removed and the fluid boundary conditions were applied at the same surface location as that defining the solid boundary.

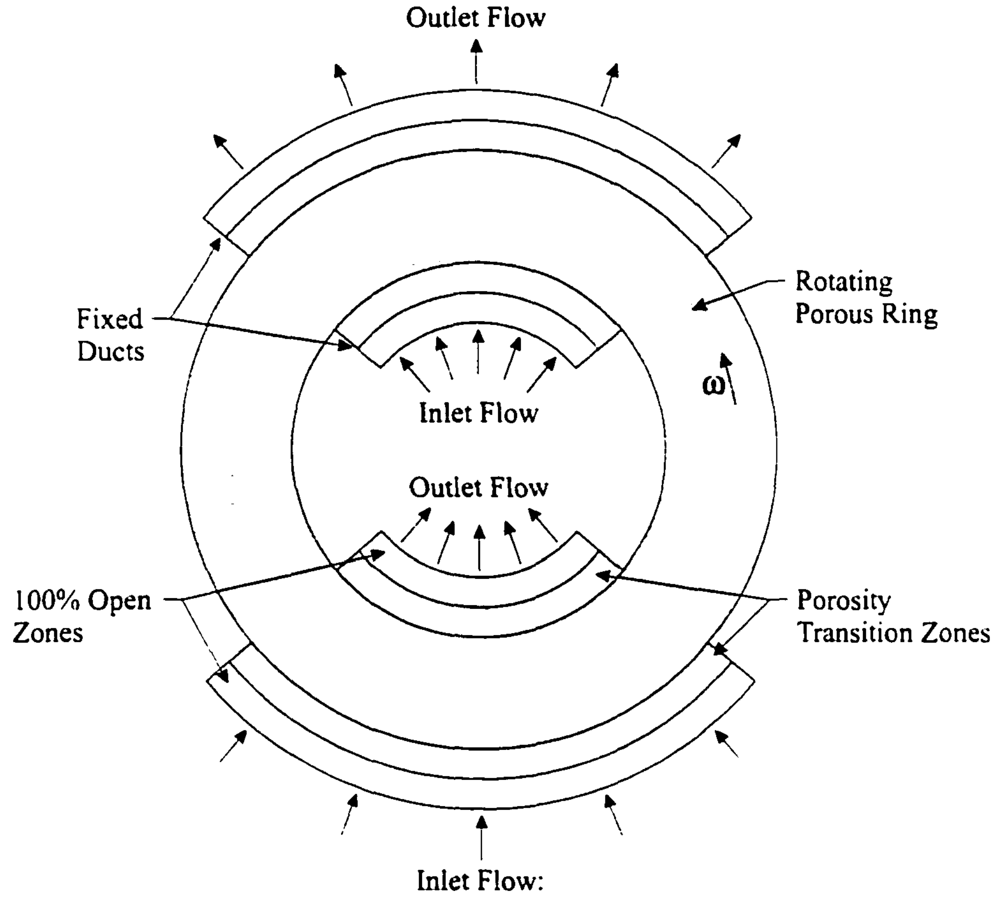

Figure 6.1 Schematic representation of the AMR model with flow ducts for the computational fluid dynamics flow studies.

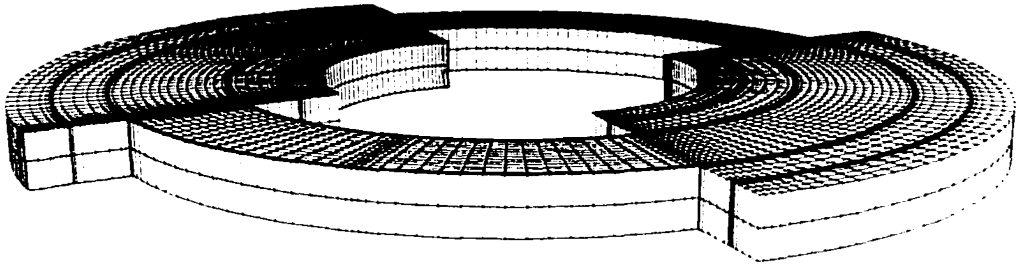

Figure 6.2 General representation of the computational grid used in the AMR flow simulations.

A schematic diagram of a representative grid used in the flow simulations showing node concentration at the boundaries in regions of rapidly changing fluid flow conditions is given in Figure 6.2. The grid shows the arrangement of three nodal planes in the axial direction. The duct regions abut the regenerator packed bed region. The grid is constructed in one piece with the angular regions between the ducts defined as block-off regions excluded from the computations. The grid was formed as a closed C-shaped region with the connecting faces specified as a rotationally periodic boundary. Nodes were distributed using semi-isogeometric interpolation. In the figure, boundaries between the 100% porous and 65% porous regions of the ducts, as well as between the duct regions and the regenerator ring are discernable by the node concentrations. Nodes are also concentrated across the regenerator near the angular limits of the ducts. The regenerator ring was specified as 40% porous.

Initial grids used an axial dimension that formed approximately cubic control volumes for the majority of the control volumes, and in regions of node concentration, the aspect ratio of the longest dimension to the smallest dimension was less than 100, consistent with the recommended grid design guidelines given in the TASCFlow user documentation. For the solution procedure of this code, large aspect ratios tend to preferentially reduce errors in the directions of the shorter dimensions, which for a general three-dimensional flow case can lead to slow convergence in the long dimension.

For the two-dimensional solution on the three-dimensional grid of the AMR, this grid design guideline is not appropriate. In solving the mass and momentum equations, the small axial dimension and associated round-off errors caused false gradients in the axial direction and subsequent flux terms that had a magnitude comparable to the fluxes from forced and entrained flow. The random nature of the round-off error caused solution instability. Stability, convergence rate, and absolute level of convergence were significantly improved by increasing the axial dimension. The absolute convergence increased by two to three orders of magnitude, depending on the model, where the convergence was measured as a residual error in the conservation equations. Aspect ratios for the majority of nodes were on the order of 100, with those for the refined grid regions exceeding 1000.

6.2.4 Boundary Conditions

The boundary conditions applied at the inlets were constant, uniform specified mass flow normal to the inlet face. The circulation fluid was defined as helium with a constant density of 11 $kg \cdot m^{-3}$. The boundary conditions applied to the outlets were static pressure set to be constant over the outlet with pressure equal to zero. Setting an average pressure over the outlet proved unstable, likely due to the large pressure gradient in the regenerator ring relative to the duct region. A relatively small change in flow conditions in the regenerator ring would cause a large local change in pressure at the boundary between the regenerator and the duct relative to the total pressure drop in the duct region.

These inlet and outlet boundary conditions do not match the AMR heat transfer fluid circulation conditions, but instead correspond approximately to independent pumps for the hot and cold blow regions. This simplification was required to prevent pumping from the hot blow inlet to the cold blow outlet through the regenerator ring in the absence of radial walls within the regenerator ring that would normally prevent this flow.

The outer boundary of the fluid region was specified as a no-slip wall in the duct region, and a rotating wall with the same angular velocity at the regenerator solid along the inner and outer regenerator regions not covered by the ducts. These walls were also specified as no-slip for some modelling scenarios, with little effect on the overall flow pattern for the grid resolution possible with the available computer equipment. Any real rotary regenerator would have a gap between the rotating regenerator and the stationary, no-slip walls of the AMR housing, which could be a vast area of research in itself for proper seal design.

The flow was specified as incompressible with constant density. Under some flow conditions, the model would contain a mix of laminar and turbulent conditions, but the code only provides for specification of one or the other of these conditions throughout the entire domain. In the porous media where the flow was strongly influenced by the momentum source term, the solution was insensitive to selection of laminar or turbulent conditions, so laminar conditions, which take less time and computer resources to solve, were primarily specified.

The presence of the duct regions improved convergence when the axial dimension was small, and had little influence when the axial dimension was large. The more gradual transition of porosity from fully open in the duct to 65% open in the duct to 40% open in the regenerator ring helped to reduce numerical overshoot (evident as velocities in excess of those expected due to the reduction of area) at the porous region boundaries from the sudden contraction (or expansion) of available flow area compared to models where the transition porous regions were absent. Numerical stability and convergence was poorest at these boundary regions, and in particular at the "corners" at the angular limits of the ducts and just inside the regenerator ring. At these locations, there was a sharp transition from low pressure drop within the duct to relatively high pressure drop with transverse (circumferential) acceleration of the fluid within the regenerator ring. The problem areas also included the transition regions moving from the regenerator ring to the ducts towards the outlets.

6.3 Rotary Regenerator Flow Simulation Results

6.3.1 Basic Flow Pattern

The path through space that massless particles would follow if they were entrained within the fluid flowing through the AMR is shown in Figure 6.3. The streaklines are coloured from blue to magenta by time of flight from the inlet. The regenerator orientation, rotation direction, and inlets and outlets are identical to those shown in Figure 6.1. The ratio of radial fluid velocity at the outer radius (assuming uniformly distributed flow over the inlet area) to circumferential velocity at the outer radius of the regenerator ring is approximately 0.47.

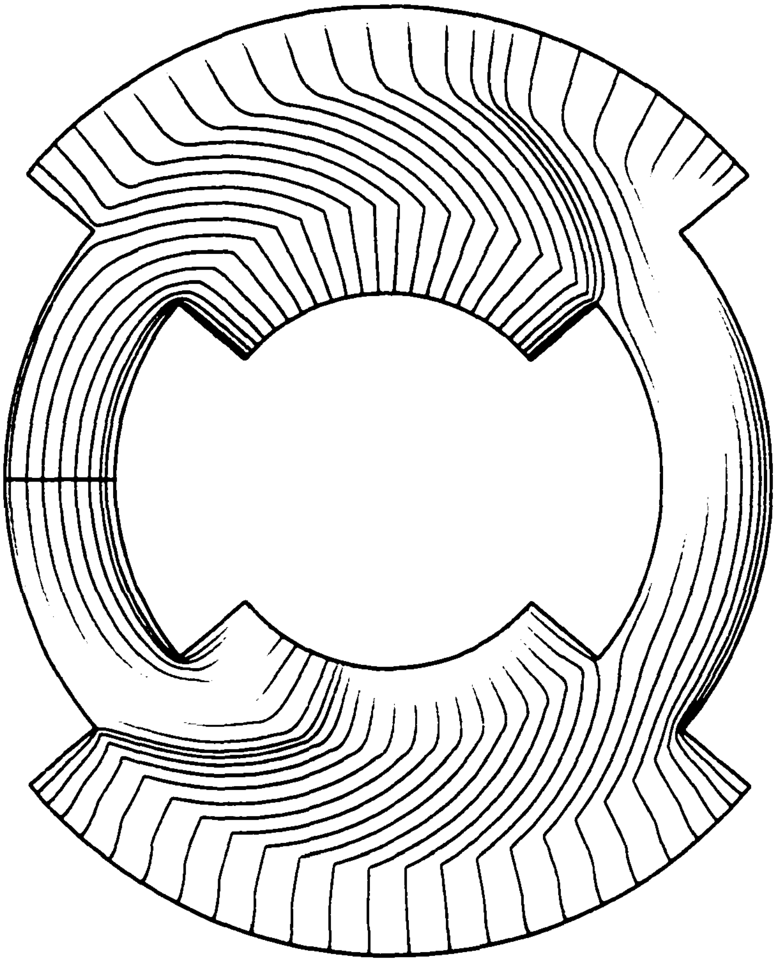

Figure 6.3 Fluid flow streaklines for an AMR rotating counter-clockwise having a fluid to ring relative velocity ratio at the outer rim of 0.47.

Generally, the fluid enters the regenerator at the inlet side and passes toward the outlet side while being entrained in the rotating regenerator. For fluid that enters the regenerator towards the end of the duct region, relative to the rotation direction of the regenerator, there is not sufficient time to reach the opposite duct. The fluid is then carried around within the regenerator to the opposite blow region, where it is the first fluid to be expelled. As the ratio of circumferential velocity of the ring to radial velocity of the fluid increases, an increasing proportion of fluid is carried around to be expelled at the opposite blow ducts.

No fluid from a hot or cold blow directly reaches the corresponding hot or cold blow outlet duct, but instead is expelled in the opposite blow region outlet duct when the ratio of circumferential velocity to radial velocity exceeds the ratio of circumferential duct length to regenerator bed length, i.e., when:

$$\frac{R_o \omega}{V_r} > \frac{R_o \phi}{R_o - R_i} \tag{6.2}$$

where R_o and R_i are the inner and outer radii of the regenerator ring, respectively, V_r is the radial velocity at the outer radius of the regenerator ring, ϕ is the angular width of the duct region, and ω is the angular rotation rate. This assumes that the inner and outer ducts have equal angular width and no relative angular offset, the porosity of the matrix is constant, and the density of the fluid is constant. The exact value of the velocity ratio when these conditions are not met would be geometry, temperature, and heat transfer fluid dependent.

6.3.2 Fluid Velocity Decomposition

The fluid velocity calculated in TASCFlow in Cartesian components can be mapped into radial and circumferential components. The circumferential component can be represented as either a circumferential velocity or as an angular rotation rate, where the latter representation removes the effect of the changing velocity due to changing radial position across the regenerator ring. These components can be compared to the Spearing model pseudo-2-dimensional fluid flow assumption described earlier.

Figure 6.4 shows a relief surface where elevation represents the decomposed Cartesian velocity components into an angular rotation rate of the fluid within the regenerator ring. For this model, the duct regions were removed and the fluid boundary conditions applied at the surface of the ring, but other aspects of the model such as the boundary conditions and relative velocities of fluid and solid correspond with those previously described. The regenerator rotates at 10 radians/s. A schematic of the regenerator with duct regions is plotted below the surface to aid in visualization. The hot blow region is shown on the right-hand side in the foreground, while the cold blow region is shown on the left-hand side in the background, and is highlighted by an ellipse surrounding the region on the schematic.

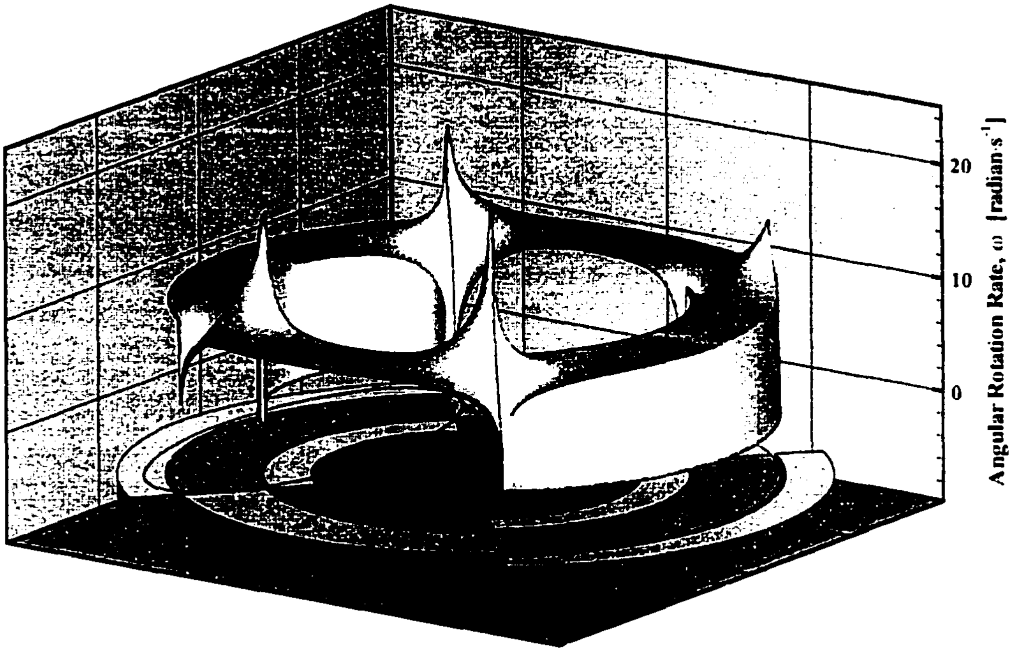

Figure 6.4 Surface representing the local angular rotation rate of the fluid within an AMR rotating at 10 radian·s^{-1}.

Along the hot and cold blow inlet regions, the surface appears "skirted," having a zero angular rotation rate. This is a result of the fluid boundary conditions of specified mass flow normal to the surface being applied at the same surface as the regenerator ring. The flow has no angular velocity component until it penetrates into the ring and is acted upon by the momentum source terms to accelerate it to travel with the regenerator ring. For most of the regenerator ring, the fluid angular velocity is nearly identical to the regenerator angular velocity.

There are peaks and valleys in the surface at the angular limits of the blow regions which correspond to local acceleration or deceleration associated with flow tending to diverge from the inlet regions into the ring and converge to the outlet regions. In areas where the fluid diverging or converging corresponds to the same direction as the regenerator rotation direction, there is a peak in angular velocity. Negative valleys correspond to competition between the converging or diverging flow and the rotation direction. If the flow identically followed the pseudo-two-dimensional flow assumption, then the angular rotation rate would map to a surface of constant elevation. The most significant difference between the assumption and the flow simulation is the flow in the regions at the angular limits of the blow regions.

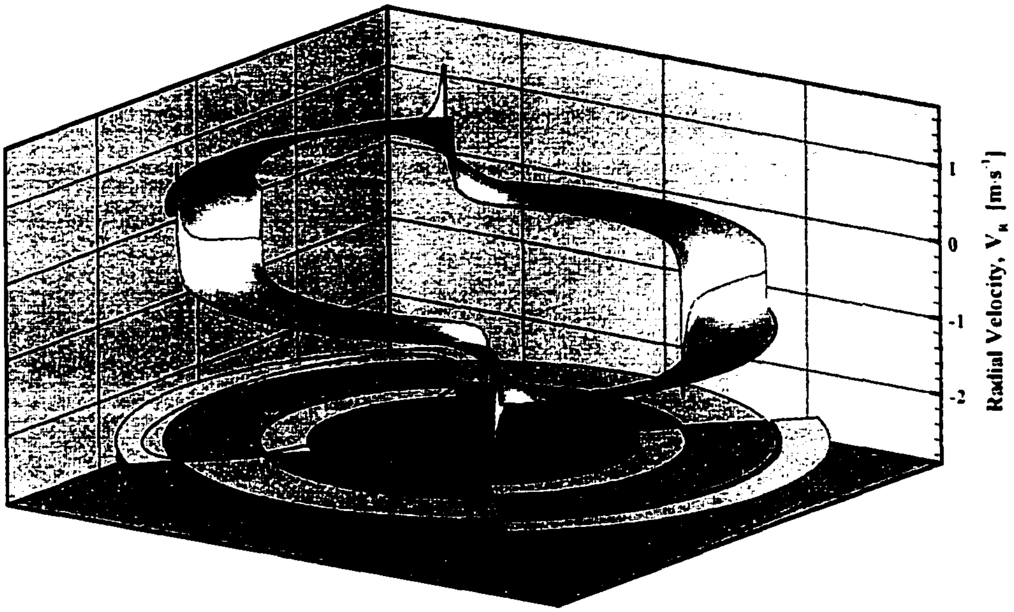

Figure 6.5 Surface representing the local radial velocity of the fluid within an AMR rotating at 10 radian·s^{-1}.

A relief surface showing the radial component of velocity is shown in Figure 6.5. In the majority of the no-flow regions between hot and cold blow regions, the radial velocity component is almost identically zero. For the no-flow region between the hot blow inlet and the cold blow outlet, there is a small positive radial velocity, while for the no-flow region between the cold blow inlet and the hot blow outlet, there is a small negative radial velocity. The magnitude of these no-flow region velocities is on the order of 1% of the velocity of the forced flow in the hot and cold blow regions.

Over the majority of the hot blow region, the radial velocity magnitude is approximately uniform but gradually increases radially inward corresponding to the reduction in flow area associated with the reduction in radial position. Similarly, over the cold blow region, the velocity magnitude is approximately uniform but gradually decreases radially outward corresponding to the increase in flow area with radial position. At the angular limits of the hot and cold blow regions, a step change in radial velocity as assumed by the pseudo-two-dimensional flow assumption is not observed. In these boundary regions, the radial flow makes a gradual change in magnitude consistent with the flow diverging from the inlet regions and converging towards the outlet regions.

6.4 Regenerator Thermal Modelling in CFX-TASCFlow

6.4.1 Conservation of Energy

The rotary regenerator fluid dynamics models showed that the simplified pseudo-two-dimensional flow approximation accurately represented the flow over the majority of the regenerator. These models also showed that there were distinct differences in the flow pattern particularly at the angular limits of the hot and cold blow regions. Of interest was whether these differences might have an unexpectedly large effect on the thermal performance of either the passive or active magnetic rotary regenerator.

A regenerator thermal model was defined within the capabilities of the standard release of the TASCFlow code by adding an second computational grid to represent the solid portion of the porous bed. The second grid was identical to the first grid over the regenerator ring region but was not physically attached to the first grid. Figure 6.6 gives a schematic representation of this arrangement, where the upper grid corresponds to the grid used to solve the fluid mass, momentum, and energy conservation equations and the lower grid the solid energy conservation equation only.

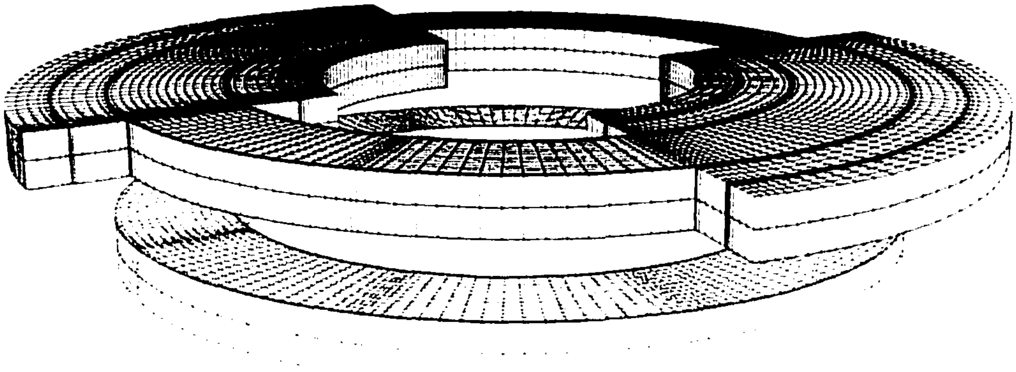

Figure 6.6 Representation of the fluid (upper) and solid (lower) unattached grids allowing representation of conjugate heat transfer over a volume using the standard release of TASCFlow.

Ordinarily, in TASCFlow, a control volume defined as a porous region is considered to have an isotropic solid and fluid region which do not violate assumptions about representing a continuum. The solid is assumed to play no part in thermal interactions and is given the same temperature as the fluid within the volume. A separate solid conjugate heat transfer region can be defined that ordinarily is placed adjacent to a fluid region and the code computes the heat transfer that would result at the solid-fluid interface, as well as within the non-porous solid.

The additional, unattached grid allowed representation of a solid fraction over the volume, rather than just at a solid-fluid interface surface, that was thermally coupled to the fluid but not equated to the fluid temperature. The solid region was non-porous, but porosity could be mimicked by appropriate scaling of terms in the energy equations. The solid-fluid coupling was achieved through the used of source terms in the energy equations.

Within the solid conjugate heat transfer region, TASCFlow solves the diffusion equation, given as:

$$\frac{\partial(\rho_s C_s T_s)}{\partial t} = \frac{\partial}{\partial x_j}\left(k_s \frac{\partial T_s}{\partial x_j}\right) + S_T \qquad (6.3)$$

where ρ_s is the solid density, C_s is the solid heat capacity, T_s is the solid temperature, k_s is the solid conductivity, and S_T is a volumetric energy source term. For the unattached grid, this equation has no intrinsic coupling to the fluid energy equation. For the rotating solid media, it also has no representation of the solid advection. To represent the required solid energy equation for a regenerator, these terms were added using the volumetric source term.

6.4.2 Energy Source Terms and Solid-Fluid Coupling

The volumetric source terms employed in the discretized equations were determined by linearization of the conjugate heat transfer and advection sources using a Taylor series expansion. If some source, S, is a function of the desired unknown variable ϕ, then a Taylor series expansion of S about ϕ is given by:

$$S = S^0 + \left(\frac{dS}{d\phi}\right)^0 (\phi - \phi^0) \qquad (6.4)$$

where the superscript represents a known value at the current iteration time step. This expression can be separated into two parts such that one part contains the component of the source which varies linearly in ϕ, and one part contains constants and known values from the current time step, *viz*:

$$S = S_C + S_P\phi \tag{6.5}$$

A comparison of Equations 6.4 and 6.5 gives the active coefficient, $S_P = \left(\frac{dS}{d\phi}\right)^0$, which is evaluated using known values at the current time step. This formulation of the source term improves convergence by using the known dependence of S on ϕ during solution, and is a linearization because it expresses S as a linear function of ϕ. A complete discussion of the importance of careful source term linearization in numerical simulations is given in the TASCFlow user manuals [91] and other numerical modelling texts [97].

In TASCFlow, the user source term and active coefficient are required in residual form, which respectively gives:

$$S_{USER} = S_C + S_P\phi^0 \tag{6.6}$$

and

$$A_{USER} = S_P \tag{6.7}$$

Considering the above linearization procedure, the solid advection was represented by a source term based on a counter-clockwise direction of rotation defined as:

$$S_\omega = -\omega\rho_s C_s \frac{\partial T_s}{\partial \theta} \tag{6.8}$$

The corresponding active coefficient for solid advection, expressed in residual form, was defined as:

$$A_\omega = \frac{\partial S_\omega}{\partial \theta} \cdot \frac{\partial \theta}{\partial T_s} = \frac{-\omega \rho_s C_s \dfrac{\partial T_s^2}{\partial^2 \theta}}{\dfrac{\partial T_s}{\partial \theta}} \tag{6.9}$$

When the denominator of the solid advection active coefficient was equal to zero, the coefficient was defined as zero. The solid heat capacity variation with position is zero for constant heat capacity material, and for passive regenerators negligible compared to the temperature gradient term.

The coupling between the solid and the fluid was achieved by complementary volumetric source terms for the solid and fluid energy equations. The conjugate heat transfer source term for the solid was determined as:

$$S_{CHT,s} = \frac{hA'''\left(T_f - T_s\right)}{\left(1 - \alpha\right)} \tag{6.10}$$

and for the fluid was determined as:

$$S_{CHT,f} = hA'''\left(T_s - T_f\right) \tag{6.11}$$

where h is the bulk heat transfer coefficient based on local flow conditions, A''' is the heat transfer surface area per unit volume, T_f is the fluid temperature, and α is the porosity. The solid equation has a porosity factor which corrects for the intrinsic solid grid definition as a non-porous region. The solid advection source term also has this correction factor in the denominator, but in the expression for S_ω it is exactly cancelled by the same factor in the numerator. The corresponding active coefficients for these source terms were defined as:

$$A_{CHT,s} = \frac{hA'''}{\left(1 - \alpha\right)} \tag{6.12}$$

and

$$A_{CHT,f} = \frac{hA'''}{C_f} \tag{6.13}$$

respectively, where C_f is the fluid heat capacity. The fluid heat capacity enters the expression for the active coefficient for the fluid source term, and not the solid source term, because TASCFlow solves an enthalpy equation for the fluid, and a temperature equation for the solid. For the fluid, the active coefficient is determined by the derivative of source term with respect to enthalpy, and thus applying the chain rule to the source term gives:

$$\begin{aligned} \frac{dS_{CHT,f}}{dH_f} &= \frac{dS_{CHT,f}}{dT_f} \cdot \frac{dT_f}{dH_f} \\ &= \frac{dS_{CHT,f}}{dT_f} \cdot \frac{1}{C_f} \end{aligned} \tag{6.14}$$

The heat transfer coefficient was calculated using volume averaged fluid properties and was based on the relative velocity between the solid and fluid. Where the relative velocity between the fluid and solid was "sufficiently large," the heat transfer coefficient was calculated as [95]:

$$h = 0.255\, C_f\, G\left(\alpha\, Re\right)^{-1/3} Pr^{-2/3} \tag{6.15}$$

where C_f is the fluid heat capacity, $G = \rho_f \left|\vec{v}\right|$ is the relative local fluid mass flow rate per unit free flow area, $Re = D_p G/\mu$ is the Reynolds number, where D_p is the particle diameter and μ is the fluid viscosity, $Pr = C_f \mu / k_f$ is the Prandtl number, and k_f is the fluid thermal conductivity. The relative velocity between the solid and the fluid is calculated in the same manner as that employed in the momentum source term for the fluid momentum equation. The heat transfer coefficient calculated from Equation 6.15 was compared to the heat transfer coefficient of a single sphere in an infinite fluid medium:

$$h = \frac{Nu \cdot k_f}{D_p} \tag{6.16}$$

where Nu is the Nusselt number taken equal to 2. If the latter heat transfer coefficient was greater, then it was used instead of Equation 6.15. Studies on the Spearing Master's AMRR model show that the solution is strongly influenced by the selection of heat transfer coefficient in the hot and cold blow regions because of its influence on reduced length and reduced period, whereas in the no-flow regions over the range $1 \leq Nu \leq 3$, the solution is insensitive to the exact value of Nusselt number because of rapid approach of the fluid to the solid temperature and little heat transfer after that point.

The heat transfer surface area per unit volume for a packed bed of spherical particles is given by:

$$A''' = \frac{6(1-\alpha)}{D_p} \qquad (6.17)$$

Additional boundary conditions are required to fully describe the passive rotary regenerator model when the energy equations are solved. For both the solid and fluid, the upper and lower nodal planes were assigned thermal symmetry boundary conditions following the procedure used previously for the mass and momentum equations solution for the fluid. Adiabatic walls were specified at the outer and inner radius for solid, and in wall regions between the hot and cold blow inlets and outlets for the fluid. The hot blow inlet temperature was specified as 273 K and the cold blow inlet temperature was specified as 200 K.

6.4.3 Energy Equation Solution

No attempt was made to solve the energy equations until a converged solution of the mass and momentum equations was obtained. Upon convergence of the mass and momentum equations, the fluid flow solution was held fixed and only the energy equations were then solved. Initial models described passive regenerators only with fluid thermal and transport properties evaluated at the average of the fluid inlet stream temperatures.

In the standard release of the TASCFlow code, the linearized coefficients of the discretized solid and fluid energy balance equations are assembled, then each equation set is solved separately. That is, there is no active coupling between the solid and fluid energy equations during solution. The source terms form a weak form of coupling between the two energy equations, because the sources are based on values from a previous iteration. In regenerator simulations, this weak coupling prevents the attainment of a steady-state solution in a reasonable time because very small time steps must be used to maintain stability.

Figure 6.7 shows the reduction in the common logarithm of the root mean squared (RMS) conservation equation residuals as a function of iteration number for the fluid and the solid for a typical simulation having a time step just small enough to ensure solution stability. The equations are generally considered to be converged at an RMS residual level below approximately 10^{-6}. The frequency of the oscillations in the RMS residuals corresponds to twice the AMR rotation rate for the selected time step per iteration. One complete regenerator thermal cycle, corresponding to one revolution, is completed in 833 iterations. An animation of a relief plot of the solid and fluid temperatures over the 2500 iterations showed the progression of a thermal wave around the regenerator ring having a magnitude of approximately 2 K superimposed on an essentially linear temperature profile between the hot and cold inlet temperature limits. The peaks in the RMS residual correspond to the arrival of the thermal wave at the hot and cold blow regions.

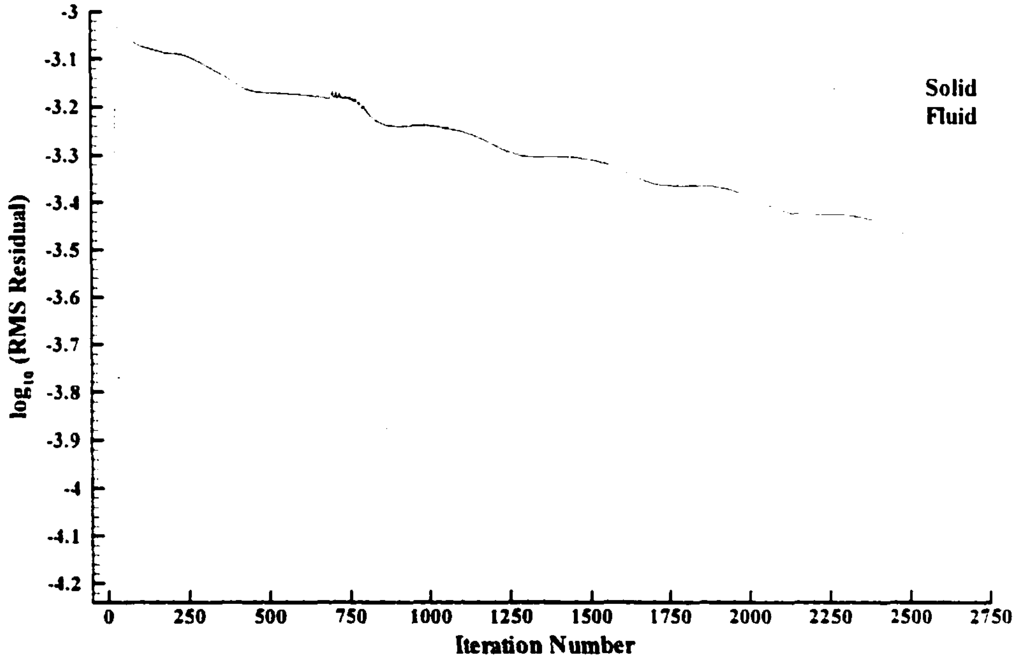

Figure 6.7 Typical error residual reduction as a function of iteration number for the dual-grid TASCFlow rotary regenerator simulation.

In regenerators, the conjugate heat transfer source terms are comparable in magnitude to the advection terms. In TASCFlow, they are lagged source terms calculated based on a large coefficient multiplied by a small temperature difference between the solid and the fluid. If the time step is too large, the solid temperature solution and the fluid temperature solution at a node generally diverge somewhat giving a temperature difference that is relatively large, say on the order of 2-3 times what the "correct" temperature difference would be. The error is quite small relative to the temperature span of the regenerator, but very large relative to the subsequent conjugate heat transfer calculation.

If it is assumed that the error lies in the determination of the solid temperature, then the subsequent calculation of the solid advection source term, which is also weakly coupled since the active coefficient does not directly link adjacent nodes, will be in error by the same relative magnitude as the conjugate heat transfer term. The net source term for the solid is then the sum of two large numbers, comparable in magnitude, which are the dominant terms of the solid energy balance equation. The solution diverges with increasing solid temperature oscillations about the expected temperature with the fluid lagging slightly.

Generally, it was found that the stability and the maximum permissible time step could be increased as the utilization factor of the regenerator was increased. The gain for any regenerators of interest and the possible reduction in solution time was not significant.

If the solid advection term was set to zero, which represents no rotation of the solid, then the solution was relatively stable and converged with reasonable values of time step. Unfortunately, the regenerative action is lost in this arrangement as the solid assumes the fluid inlet temperatures in the respective hot and cold blow regions, with a diffusion-dominated profile between them.

6.4.4 Energy Source Terms and Coupling, Revisited

The instability can be traced to the derivation of the source term active coefficients. The derivation assumes that the source term is a function of only one variable corresponding to the variable of interest for the energy equation at that control volume only. That is, the active coefficient for the conjugate heat transfer in the solid equation is derived assuming that the fluid temperature is constant, and vice-versa (or equivalently that the solid and fluid temperatures are independent). Similarly, the active coefficient for the solid advection term is not actively applied to both of the solid nodes coupled by the advection term. For the conjugate heat transfer term for the fluid, a Taylor series expansion that recognizes the source term as a function of both the solid and fluid temperatures gives:

$$\begin{aligned} S(T_f, T_s) &= S(T_f, T_s)^0 + \left(\frac{\partial S}{\partial T_f}\right)^0 \left(T_f - T_f^0\right) + \left(\frac{\partial S}{\partial T_s}\right)^0 \left(T_s - T_s^0\right) \\ &= hA'''\left(T_s^0 - T_f^0\right) - hA'''\left(T_f - T_f^0\right) + hA'''\left(T_s - T_s^0\right) \\ &= hA'''\left(T_s - T_f\right) \end{aligned} \tag{6.18}$$

The implication of this result is that to effectively code the conjugate heat transfer term for optimal stability and convergence, an active coefficient, $A_{CHT,f}$, is required for the fluid enthalpy variable, as determined previously, and an active coefficient, $A_{CHT,s}$, is also required for the solid temperature variable. The lagged source term, $S_{CHT,f}$, based on the previous values of solid and fluid temperature remains unchanged. A similar result arises from any source term that is based on the difference of two variables. The solid advection source term is based on the derivative of temperature, which can be discretized as the temperature difference between adjacent solid nodes multiplied by a scaling factor containing solid density, heat capacity, rotation rate and spacing between the nodes.

The standard release of TASCFlow does not allow for the specification of an active coefficient for a variable outside the usual conservation equation. That is, an active coefficient for the solid for a volumetric source term cannot be specified when solving the fluid energy equation and vice-versa. This causes difficulties for the conjugate heat transfer term. Further, the active coefficient can only be applied to the variable corresponding to the current node under consideration, and cannot be applied to adjacent nodes within the same linearized conservation equation. This causes difficulties for the solid advection term.

6.5 Thermal Modelling Using a Custom TASCFlow Release

6.5.1 Features of the Custom Release

The lack of sufficient coupling between the solid and fluid energy equations in the standard release of TASCFlow prevented solution of the energy equations describing regenerator behaviour. To increase the coupling, a contract was arranged whereby AEA-ASC Advanced Scientific Computing, the authors of TASCFlow [91], modified their proprietary code to actively couple the solid and fluid energy equations. The porous solid was represented directly, so that the second separate grid was no longer required. Last, the code was modified to allow for storage space for variables associated specifically with magnetic regenerators. Other aspects of the code, such as the Incomplete Lower Upper (ILU) factorization used to solve the equations, availability of additional user momentum and energy source terms, etc., were unchanged.

6.5.2 Convergence

After significant modifications to remove initial bugs and simplify functionality, results from the custom code were encouraging, showing excellent stability with large time steps and rapid convergence. Figure 6.8 shows the reduction in the common logarithm of the root mean squared (RMS) conservation equation residuals as a function of iteration number for the fluid and the solid for a typical simulation using the custom code release. After several initial iterations with a small time step (not shown in the figure), the time step was increased so that one iteration represented approximately 10^9 complete thermal cycles. Approximately 5 iterations using a small time step plus 20 additional iterations using a large time step were required to reach convergence.

Comparison of Figures 6.7 and 6.8 shows that the custom release with active coupling between the solid and fluid equations resulted in an improvement in convergence rate from approximately 10,000 iterations per decade reduction in the error residual to approximately 4 iterations per decade.

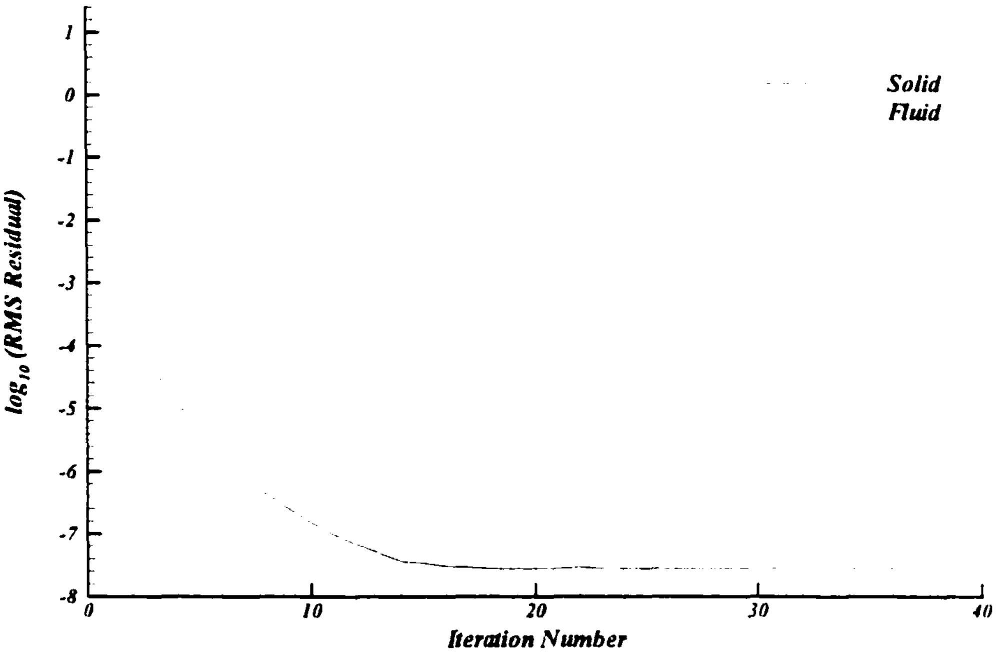

Figure 6.8 Typical error residual reduction as a function of iteration number for the custom TASCFlow release rotary regenerator simulation.

The custom release allowed independent control of the conjugate heat transfer term and the solid advection term. As such, it was possible to effectively turn off one or the other actively coupled source term and substitute the weakly coupled source term used previously in the dual grid scheme to explore the stability of each term alone. It was found that the only stable and convergent arrangement with reasonable time steps was obtained when active coupling for both terms was applied.

6.5.3 Thermal Solution

Considerable effort was expended in the examination of the thermal solutions from the custom code release, first to verify and correct the representation of the regenerator conservation equations, and second, to examine some unexpected results. Figure 6.9 shows a relief surface of the temperature profile within the solid matrix of a regenerator of reduced length Λ = 300 and reduced period Π = 10 as calculated in TASCFlow. The hot blow region is shown in the foreground with the inlet at the outer radius. The cold blow region is shown in the background highlighted with an ellipse, with the inlet at the inner radius. Inlet temperatures for the hot and cold blows are 273 K and 200 K, respectively. Lines drawn along the surface denote the boundaries between the forced blow regions and "no-flow" regions.

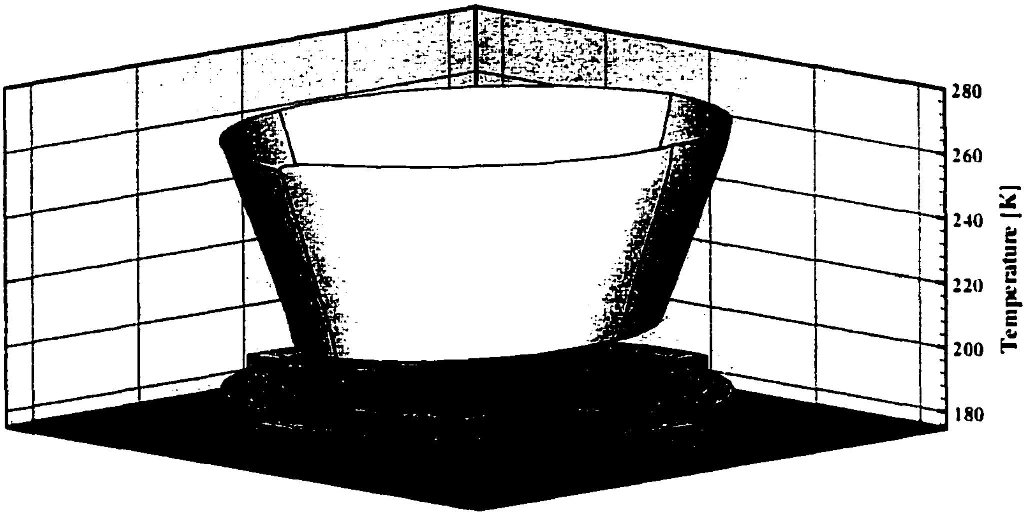

Figure 6.9 Temperature profile of a passive regenerator of reduced length $\Lambda = 300$ and reduced period $\Pi = 10$ as calculated in the custom TASCFlow release on a non-uniform grid.

A cursory examination suggests that the temperature profile is reasonable, being essentially linear across the regenerator between the limits of the hot and cold blow inlet temperatures. The magnitude of the solid-fluid temperature difference within the hot and cold blow regions is nearly uniform, ranging from about 0.19 K to 0.22 K, excluding the volumes along the region boundaries. This closely approximates the expected temperature difference of approximately 0.24 K based on the temperature span and reduced length from the relation:

$$\Delta T_{sf} = \frac{T_H - T_C}{\Lambda} \tag{6.19}$$

where ΔT_{sf} is the magnitude of the temperature difference, T_H is the hot blow inlet temperature, T_C is the cold blow inlet temperature, and Λ is the reduced length.

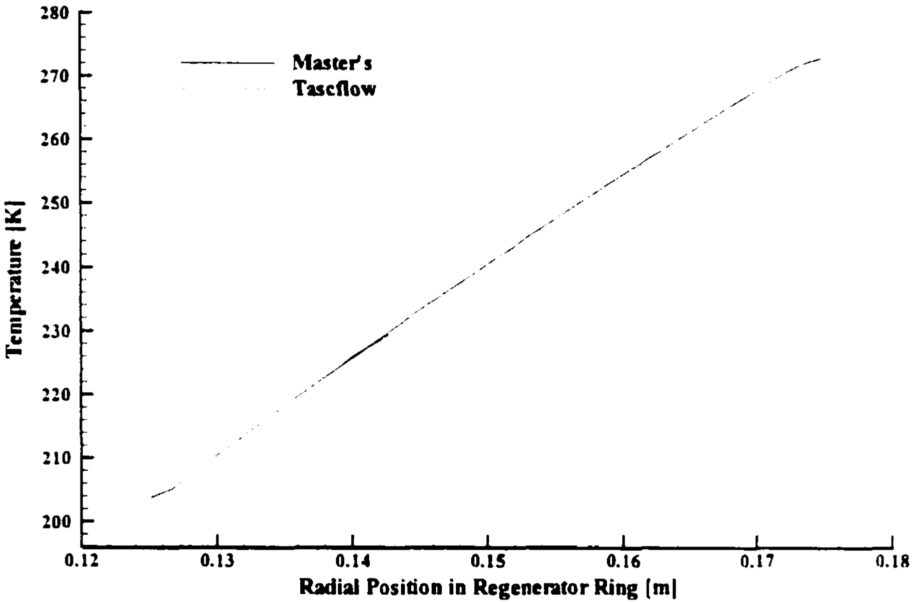

Figure 6.10 Comparison of the solid temperature versus radial position within the passive regenerator ring as solved by the Spearing Master's thesis model and by the custom TASCFlow release.

A close examination of the temperature profiles that develop across the regenerator ring by the end of blow periods show an unphysical behaviour. Figure 6.10 shows the solid temperature profile radially across the regenerator ring at the end of the hot blow period as calculated using the Spearing Master's model and the custom TASCFlow release. The TASCFlow profile has a "knee" near the hot blow inlet side, and compared to the Master's profile has a higher temperature at the hot blow exit side and generally a smaller gradient.

The "knee" develops over the course of the hot blow period, where the material adjacent to the hot blow inlet warms more than the material within the regenerator interior. Figure 6.11 shows this behaviour with equally spaced snapshots of the temperature profile versus radial position over the course of the hot blow period. The unphysical aspect of this behaviour is that the regenerator utilization does not vary with the penetration into the regenerator, and therefore, the inlet region and the interior region should see identical relative warming. A similar development of a knee in the cold inlet region occurs over the course of the cold blow period.

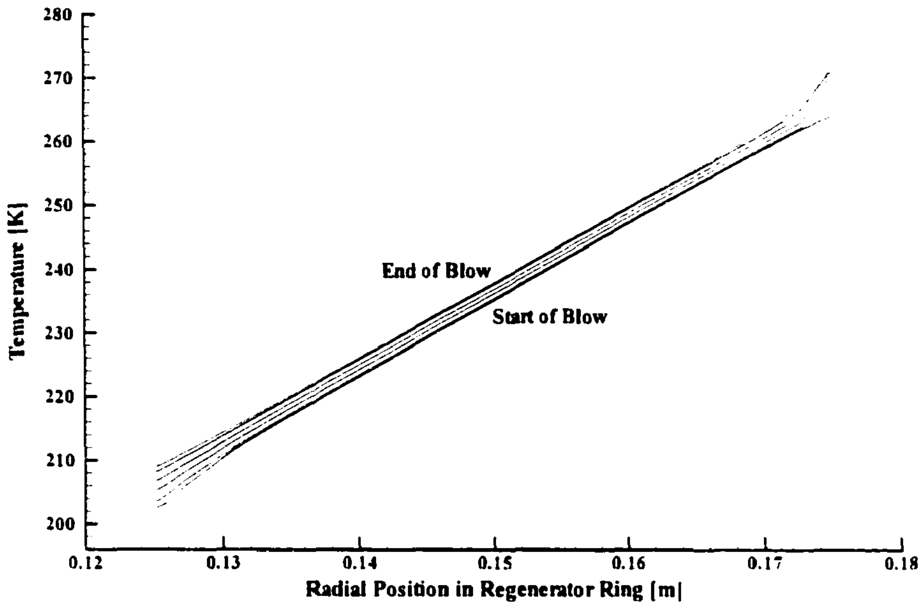

Figure 6.11 Equally spaced snapshots of the hot blow temperature profile versus radial position for the custom TASCFlow release.

6.5.4 Thermal Solution Grid Dependency

The source of the knee was traced to the radial variation in the grid node spacing. Figure 6.12 shows the effect of different node spacing schemes on the solid temperature profile across the regenerator bed at the end of the hot blow period. Four different grid node spacing schemes are shown having various proportions of uniform spacing (U), contracting spacing (C), and expanding spacing (E). For example, the notation E50:C50 indicates that for the first 50% of the nodes across the regenerator bed, the nodes are spaced at increasing intervals, and for the second 50% of the nodes, the nodes are spaced at decreasing intervals. In the expanding and contracting regions, the ratio of the spacing between successive nodes is constant.

The temperature profile indicated by the open triangle is based on uniform grid node spacing and is almost perfectly linear. The temperature profiles indicated by the solid square and solid diamond symbols are based on grids that are "opposite," where one expands, the other contracts. The temperature profile indicated by the open circle accentuates the effect of the grid spacing by having only expanding or contracting regions and no uniform spacing regions.

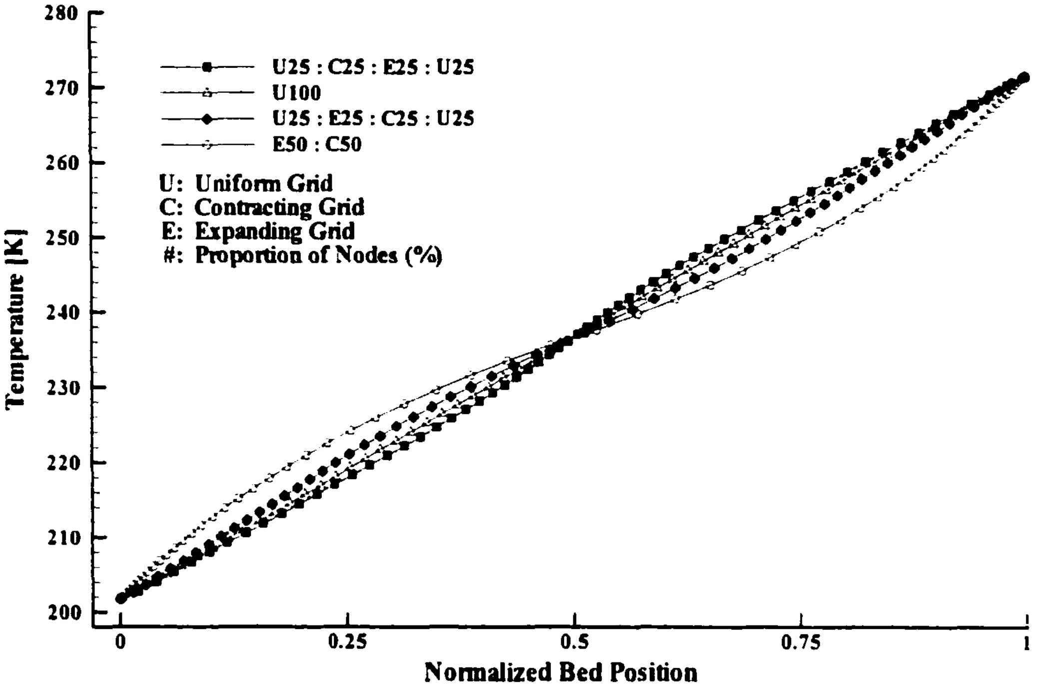

Figure 6.12 Comparison of the temperature profile across the regenerator bed at the end of the hot blow for different grid node spacing schemes.

A comparison of the temperature profiles indicated by the solid square and solid diamond legend symbols shows that expanding and contracting grids have opposite effects on the local gradient. In the portion of the grid with uniform spacing, the temperature gradient is very nearly constant. The local gradient is a variable function of the grid spacing in the expanding or contracting grid only. A contracting grid in the direction of decreasing temperature tends to decrease the value of the temperature gradient (i.e., make it more negative). An expanding grid in the direction of decreasing temperature tends to increase the value of the temperature gradient (i.e., make it more positive).

The temperature profile is unchanged with grid refinement if the refined grid has the same relative expansion ratios between successive nodes. That is, doubling the number of nodes but leaving the grid node spacing scheme unchanged does not alter the resultant solution. Similarly, if the number of nodes of a uniformly spaced grid is increased until the grid resolution is identical to the finest spacing of a non-uniformly spaced grid, the temperature profile is still linear. This indicates that the solution on the non-uniform grid is not due to improved resolution of important thermal effects at some point within the regenerator compared to a uniformly spaced grid having the same number of nodes.

Interestingly, the effect of grid expansion and contraction increases with decreasing utilization factor, making the effect particularly pronounced for regenerators of high reduced length and low reduced period, corresponding to those of interest for AMR's and other high-performance regenerator systems.

6.5.5 Source of the Thermal Solution Grid Dependency

Despite the extensive scrutiny of the energy conservation equations implemented within the TASCFlow release, no error responsible for this behaviour could be found, either by this author or by the experts who originally wrote the software and its custom modifications. The possible explanations for the grid dependency that were ruled out included:

- Selection of the transient solution time step;
- Gross coding errors, such as missing or incorrect coefficients;
- Missing or incorrect representation of flux terms;
- Inappropriate interior node interpolation scheme (for flux values within each control volume boundary);
- Incorrect assembly of the energy equation matrix coefficients;
- Degree of convergence during the ILU factorization procedure;
- Degree of convergence of the overall solution;
- Circular versus linear geometry on a Cartesian grid;
- Use of single versus double precision.

Possible explanations for the grid-dependent solutions that could not be ruled out included:

- Incompatibility of solving enthalpy and temperature equations together due to the disparity of relative magnitudes of the matrix coefficients;
- Small errors associated with the fluid mass and momentum equations on the non-uniform grid biasing the energy conservation equations;
- Small errors in the calculation of the solid advection term biasing the energy conservation equations.

6.5.6 Implementation Issues

The close scrutiny of the custom TASCFlow release did reveal several implementation issues which, if the grid dependency issue is solved, could still adversely affect the accuracy of the passive and active regenerator simulations. These issues are:

- The definition of a control volume is face-centred, with some properties for the control volume calculated as average values over the volume and others calculated individually for each control volume octant.
- Block-off regions pass through grid nodes which can subsequently lead to the control volumes for the porous solid encompassing mixed velocity specifications.
- The Cartesian representation of the rotary regenerator leads to incorrect interpolation of the surface velocity vectors, which leads to incorrect evaluation of the boundary fluxes for the solid advection.

6.5.7 Control Volume Definition

There are two common techniques for defining the control volume and discretization grid for finite difference or finite volume equations. The first is face-centred volumes, while the second is node-centred volumes. In the first technique, one defines the locations of the grid nodes, then locates the faces of the control volumes midway between the nodes. In the second technique, the locations of the control volume faces are defined, then the grid nodes are placed midway between the faces. Figure 6.13 shows schematically the two grid arrangements for 2-dimensions, with nodes defined by the intersection of the solid lines, and faces defined by the dashed lines. The arrangement is similar for 3-dimensions. TASCFlow employs face-centred control volumes.

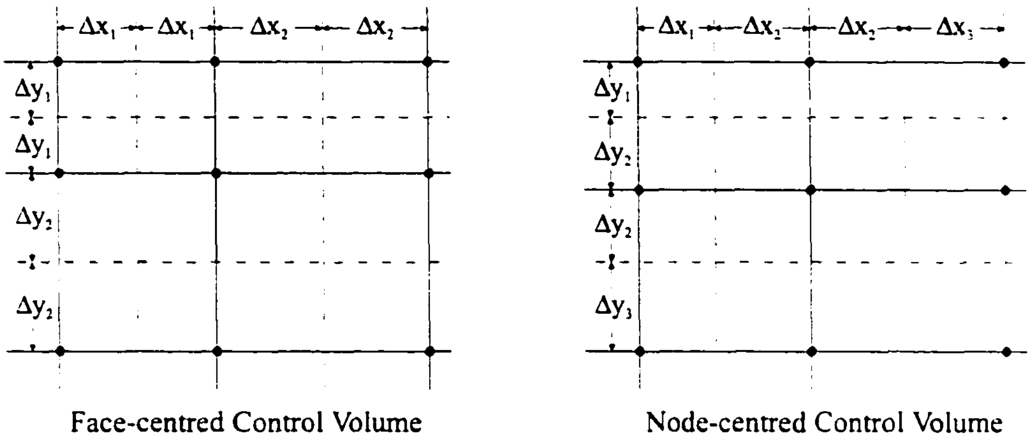

Figure 6.13 Comparison of face-centred control volume and node-centred control volume definitions.

Errors associated with the control volume implementation are evident in regenerator cases where there is a material or porosity change at a nodal boundary. The conservation of mass and momentum is calculated by consideration of the flow within each octant, but the total flux is based on the average porosity over the entire control volume. The porosity discontinuity at the node is replaced by a volume-averaged porosity. Similarly, density of the solid is based on a volume average, so the solid advection term can be based on some composite blend of multiple materials with multiple densities. Both of these effects introduce errors into the solution. The influence on the solution of these errors would normally be minimized by minimizing the control volume at material or porosity boundaries compared to surrounding volumes; however, this would require non-uniform grids, which have already been shown to have considerable error.

6.5.8 Grid Block-Off

Errors associated with block-off regions arise when the block-off abuts a rotating and a stationary region, such as the non-participatory circumferential regions between the flow inlet and outlet duct regions. Consider the intersection where one quadrant of the control volume is removed. This arrangement for the rotary regenerator with ducts is shown in Figure 6.14 where shading indicates the control volume and cross-hatching denotes the block-off region.

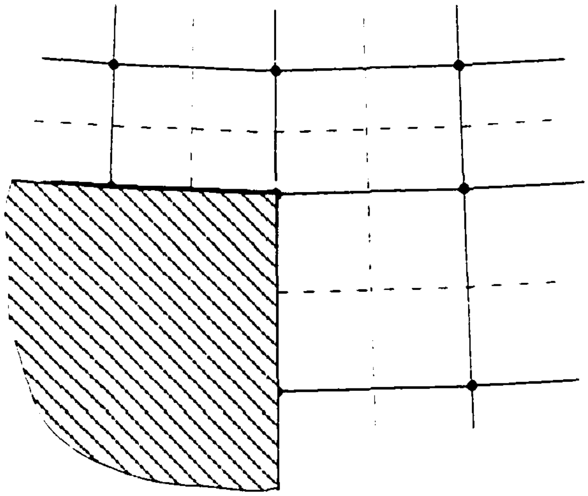

Figure 6.14 TASCFlow control volume definition at the intersection of duct, regenerator ring, and block-off regions.

The node at the centre of the control volume is defined to be part of the regenerator ring, and therefore is rotating. All three quadrants are assigned the rotation rate of the central node, and therefore, the quadrant within the duct is implicitly defined as rotating, despite being explicitly defined by the boundary conditions entered by the user to be separate from the regenerator ring and non-rotating. The solid mass conservation equation, which is implicitly defined by a mass conservative velocity specification of the nodes, is then effectively violated as the regenerator passes either into or out of a duct region. Mathematically, it's as if the solid suddenly expands (is created) as the solid passes the start of the duct region and contracts (is destroyed) as the solid passes the end of the duct region.

The effect of the mass violation can be minimized by grid refinement at the boundary between the regenerator and the duct. It can be eliminated by removing the duct regions, or by including a clearance gap between the regenerator ring and the duct regions. Adequate resolution for any reasonably sized clearance gap would require grid refinement or significant computer memory and computational resources. Any local grid refinement will result in errors due to the non-uniform grid.

6.5.9 Cartesian Grid Representation

The rotary regenerator geometry is best represented using a Polar grid definition, however, only a Cartesian grid representation is available in TASCFlow. Each node of the rotating regenerator has a Cartesian velocity vector determined by mapping the angular velocity to equivalent Cartesian components. Assuming solid body rotation about the z-axis, the Cartesian velocity components of a node located at the coordinate pair (x,y) are:

$$\begin{aligned} u &= -\omega y \\ v &= +\omega x \end{aligned} \tag{6.20}$$

in the x-axis and y-axis directions, respectively, where ω is the angular rotation rate. When the angular boundaries of the control volume are defined by radial lines (the projection of which intersect at the axis of rotation), the u,v components of velocity at the node do not describe the u,v components of velocity of the boundary face due to the angular separation between the node and the face. If the grid is described by nodes with equal angular spacing, $\Delta\theta$, then the solid advection at the control volume angular boundaries, based on the component of velocity normal to the boundary face, will be under-represented by a factor of $\sqrt{\frac{1+\cos(\Delta\theta)}{2}}$. As the angular spacing tends to zero (i.e., an infinite number of nodes circumferentially), this factor tends to unity.

If the angular spacing is constant, then this artifact of the Cartesian representation under-represents the solid advection by a small amount which would be equivalent to specifying a slightly slower angular rotation rate. If the angular spacing varies, then the net flux into the control volume is not equal to the net flux out of the control volume, which violates mass conservation for the porous solid, even for a mass-conservative nodal velocity specification. Additionally, there is always a finite velocity component in the radial direction, implying that the solid is expanding radially, or that there is a net solid flux radially, which violates the specification of the porous solid region as a rigid body. This last effect was evident in non-zero solid boundary energy fluxes reported by the code despite the solid boundary being specified as an adiabatic boundary condition.

6.6 Active Magnetic Regenerator Simulation

Despite the unresolved issues of grid dependency and non-conservative representation of the solid advection, it was still possible to solve the AMR energy conservation equations, albeit with unknown accuracy. To minimize the grid dependency issues, a grid having uniform spacing in both the radial and circumferential directions was constructed. The heat capacity of the solid was defined to be a function of each local control volume's nodal temperature and applied magnetic field. A source term representing the magnetic interaction for each control volume based on local nodal temperature and applied field for a counter-clockwise rotation was defined as:

$$S_H = -\mu_0 \omega T_s \left(\frac{\partial M}{\partial T} \right)_H \frac{dH}{d\theta} \tag{6.21}$$

where μ_0 is the permeability of free space, ω is the angular rotation rate, $\left(\frac{\partial M}{\partial T} \right)_H$ is the change in magnetization with temperature at constant field, and $\frac{dH}{d\theta}$ is the change in field with angular position.

The corresponding active term was defined as:

$$A_H = -\mu_0 \omega \frac{dH}{d\theta} \left[\left(\frac{\partial M}{\partial T} \right)_H + T_s \left(\frac{\partial^2 M}{\partial T^2} \right)_H \right] \tag{6.22}$$

The working material was defined to be gadolinium where the material properties were calculated using a molecular field model approximation. The material was assumed to be magnetically soft, having no hysteresis or crystallographic orientation effects. Induced electrical eddy currents were considered to be negligible and were not modelled.

A normalized, symmetrical magnetic field was defined analytically by a Chebyshev rational expression as a function of angular position only, and is shown in Figure 6.15. FORTRAN source code to generate this profile is provided in Appendix C. For a given AMR model, the normalized field was scaled to the maximum field value, and oriented so the minimum and maximum field values corresponded to the centres of the hot and cold blow regions, respectively.

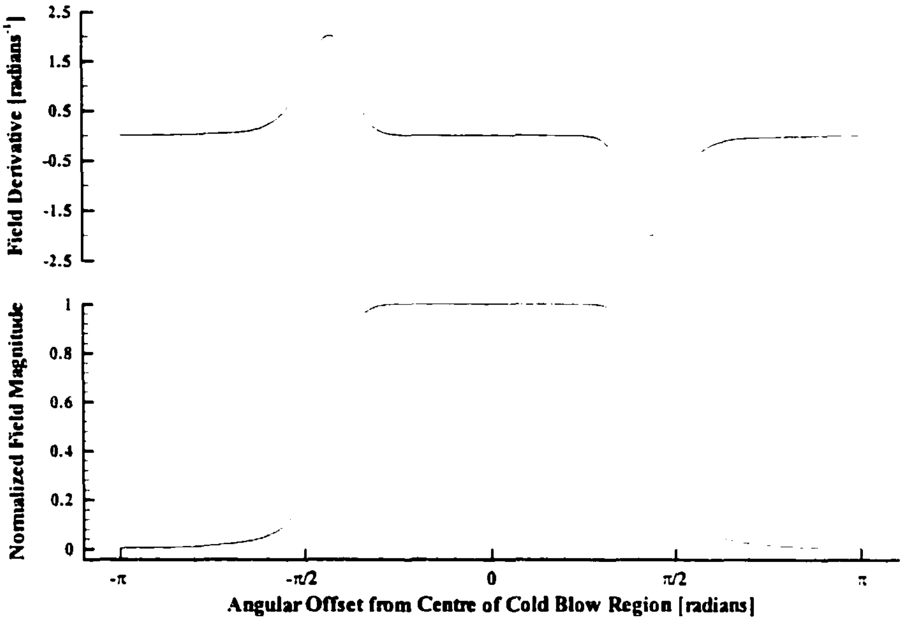

Figure 6.15 Normalized magnetic field profile and its derivative used in the custom TASCFlow release AMR simulations.

A relief surface representing the solid matrix temperature profile as a function of position calculated by the custom TASCFlow release for a 5 Tesla applied field is shown in Figure 6.16. The hot blow region is shown in the foreground, while the cold blow region is shown in the background with the high magnetic field region denoted by the ellipse. The regenerator rotates counter-clockwise. There is a region of the ring having a temperature in excess of 400 K. This region corresponds to the increasing field region having an angular offset of approximately -π/2 in Figure 6.15.

The development of the temperature spike is due to a thermal runaway effect, initially induced by error in the solution. Starting with a profile very closes to the expected "correct" solution, the magnetic interaction source term gives a temperature profile that overestimates the magnetocaloric effect. The slightly higher temperature gives a slightly lower value for the property $\left(\frac{\partial M}{\partial T}\right)_H$, but the net product of higher temperature and lower $\left(\frac{\partial M}{\partial T}\right)_H$ is a larger source term for the magnetic interaction for the next iteration. The temperature profile in this region grows until limited by the effects of conduction and solid-fluid heat transfer. The sharp boundaries in the solid temperature spike is due on the initial side to the large magnetocaloric effect at low field, and due to solid-fluid heat transfer from the cold blow on the terminal side.

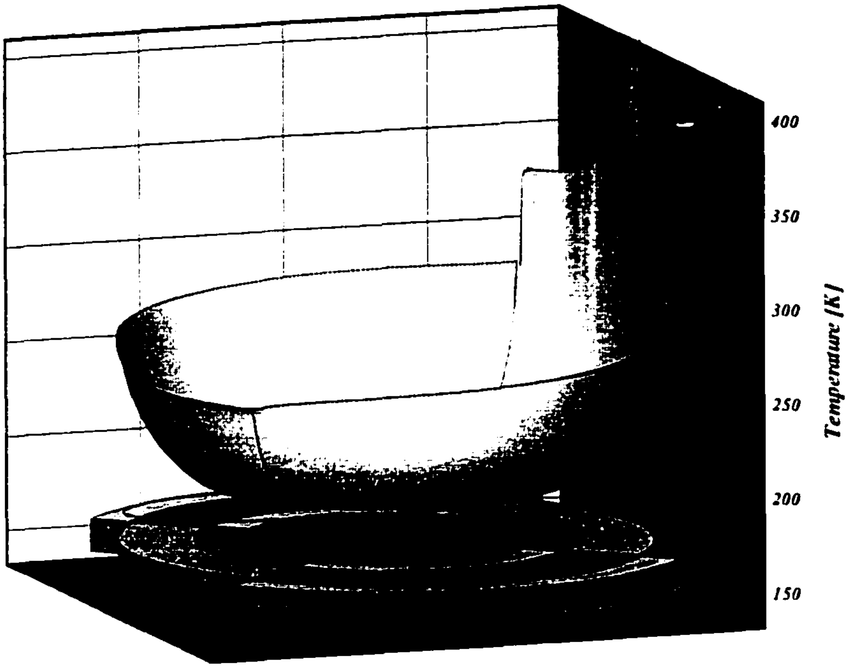

Figure 6.16 Solid matrix temperature profile of a gadolinium regenerator operating between inlet temperatures of 200 K and 273 K under a 5 Tesla applied field as calculated using the custom TASCFlow release.

The source term and material property routines were re-coded to limit the effect of thermal runaway in the solution, but the resultant solutions nonetheless overestimated the magnetocaloric effect, with the solution held to whatever temperature limit was imposed.

It is not readily visible in Figure 6.16, but the magnetocaloric effect is also overestimated during demagnetization. At the end of the cold blow region, the solid matrix temperature at the outer radius is approximately 271.7 K. Upon demagnetization, the temperature drops to approximately 256.5 K; a decrease of 15.2 K. The expected adiabatic demagnetization for gadolinium at this temperature for a change in field from 5 T to 0 T is approximately 7.7 K.

It was postulated that with the observed magnetocaloric effect approximately twice that expected that there may have been a coding error in the implementation of the source term which neglected to account for porosity of the solid. The magnetic interaction source term would then be overstated by a factor of $1/(1-\alpha)$. A quick check, performed by scaling the magnetic source term to correct for porosity, thereby reducing the source term by 40% for this simulation, resulted in an approximately 10% reduction in the observed magnetocaloric effect, and no significant reduction of the gross over-estimation of the magnetocaloric effect during magnetization.

A comparison of the source terms calculated using the TASCFlow code and the Spearing Master's AMR code for the same model revealed at most a 9% difference between the two source terms. The largest differences were observed in the regions of magnetization and demagnetization. This suggests that small differences in the source term, either through error in calculating the term or through the subsequent errors in the solution procedure can have a significant effect on the final temperature profile in TASCFlow.

Other possibilities included subtle errors introduced as a result of the discretized representation of the governing equations, in particular different assumptions inherent in the determination of boundary fluxes versus the control volume quantities, and possible circumferential grid/temperature dependencies when a significant gradient exists, such as during magnetization and demagnetization. Ultimately, despite close scrutiny, no definitive explanation could be found for the incorrect temperature profiles under application of applied magnetic fields.

6.7 Conclusion

A rotary active magnetic regenerator model created within a commercial computational fluid dynamics package revealed that over the majority of the regenerator, a simplified pseudo-2-dimensional flow profile with independent radial and circumferential flow components is a close approximation to the flow profile determined by solution of the Navier-Stokes equations. There are substantial differences between the two flow profiles at the boundaries between the forced flow and no-flow regions. At these boundaries, there is a dispersion of flow from the forced flow regions into the surrounding no-flow regions, which reconverges at the fluid outlets.

The solution of the rotary regenerator energy equations using a standard, uncoupled solver is impractical, since stability issues associated with the lack of coupling between the solid and the fluid in the case of conjugate heat transfer, and between adjacent solid control volumes in the case of solid advection, prevent solution in a reasonable time frame. Significantly improved stability and convergence can be obtained by use of a fully coupled solver. Convergence rate improved by a factor of approximately 2500 in the CFX-TASCFlow package used in this study that employs an incomplete upper-lower factorization solution procedure.

A commercial computational fluid dynamics package is theoretically capable of solution of the conservation of mass, momentum, and energy equations necessary to describe passive and active magnetic regenerators. The CFD package used in this study revealed implementation issues that must be considered for the solution of rotary regenerators. It is likely impossible to determine the exactness of the regenerator thermal solutions without access to the complete source code for the CFD package employed, which may be difficult to obtain considering the proprietary nature of commercial packages.

Future studies of passive and active magnetic regenerators will require a carefully designed implementation of the energy equations that is accurate and self-consistent. Discretization issues, such as the representation of the solid entropy change in terms of an enthalpy flux based on a heat capacity advection term and volumetric magnetic work based on a volumetric magnetization change, need careful attention to ensure that the physical properties of the solid are not misrepresented. Interpolation of physical properties on a non-uniform grid may lead to an implicit violation of the Second Law of Thermodynamics through an inconsistent representation of the solid properties at the flux surfaces compared to the interior volumes. Using Cartesian grids to describe rotary regenerator geometry may exacerbate the problem of ensuring self-consistency of physical properties and mass-conservation for the solid rotation, and therefore polar grids may be required.

Despite the specific implementation difficulties encountered with the CFD package within this work, the goal of creating a viable regenerator model within a commercial CFD package is possible and worthy of future effort. The general nature of the commercial package allows for a rapid geometrical model development which is important for an understanding of the intricacies of a proper fluid seal design both within the regenerator itself and between a moving regenerator and its housing. This understanding will be critical to design and build high performance magnetic regenerative refrigerators with minimal thermal short circuits from undesired fluid flow paths.

Chapter 7

Bypass Gifford-McMahon Experimental Apparatus

7.1 Introduction

Previous chapters of this work describe the results of theoretical calculations that indicate that unbalanced and asymmetrical regenerative cooling systems can, if properly configured, provide improved gas liquefaction capacity over single-stage, balanced, symmetrical regenerative systems. The unbalanced, asymmetrical system's provision of sensible cooling in addition to latent cooling significantly reduces the ideal input power required to liquefy a given mass flow rate of gas, even though the unbalance itself can decrease the liquefier's gross cooling power. This chapter describes an experimental apparatus that was constructed to verify the theoretical results of the Bypass Gifford-McMahon (GM) liquefier concept presented in Figure 5.7 in Chapter 5.

7.2 Bypass GM Apparatus

7.2.1 Cycle Schematic

A simplified schematic of the apparatus used to study GM cryocooler operation with bypass regenerator flow is given in Figure 7.1. Operation of the cycle with bypass flow is almost identical to a conventional GM cycle, having no modification of the usual valve timing for pressure buildup and pressure release, and no modification of the regenerator/ displacer motion. The bypass apparatus has a check valve mounted in the cold head which during the pressure buildup phase allows a portion of the regenerated cold gas to be diverted to an external stream. The external stream is fed to a cold buffer volume which acts as a capacitance element to smooth the periodic flow of gas from the cold head into a steady flow through the bypass heat exchanger. In the bypass heat exchanger, a counter-current process gas is cooled by the bypass stream. The proportion of the flow diverted from the cold head is controlled by the bypass metering valve at room temperature at the exit of the bypass heat exchanger. Once through the metering valve, the bypass gas joins the usual low pressure gas stream.

Some additional components are required to compensate for the temperature-dependent density of the cycle working gas. The Bypass GM apparatus forms a closed cycle containing a fixed mass of helium gas. After cooldown, the density of the gas within the cold buffer volume is increased, and therefore the cold volume can contain a large fraction of the total system gas charge. The gas accumulation in the cold buffer tends to reduce the overall system pressures. A warm buffer containing additional gas returns the system to pressures consistent with those of the standard GM cycle, and can also act as a surge volume for the compressor return line.

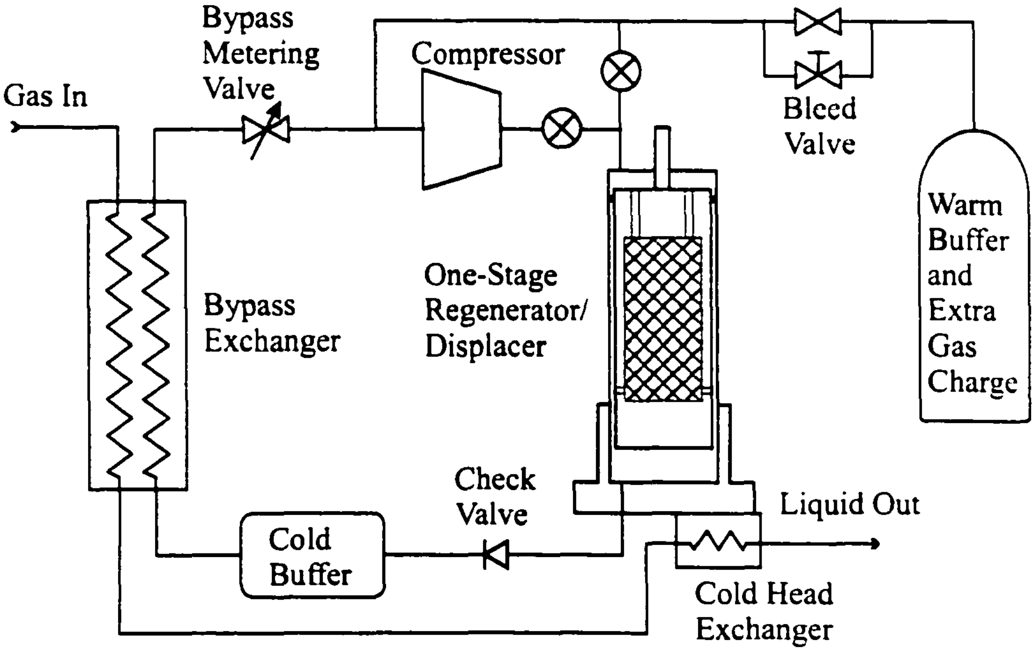

Figure 7.1 Schematic diagram of the Bypass Gifford-McMahon cycle.

If the bypass metering valve is closed, then once the cold buffer volume reaches the maximum cold head pressure, bypass flow from the cold head stops and the system behaves as if it were a simple GM system accepting a load at the cold head only. Opening the bypass valve allows a stream of cold gas to flow through the bypass heat exchanger, thereby providing cooling between ambient and nominally the cold head temperature, in addition to the cooling load at the cold head. In this mode, the gas flow through the regenerator during the hot blow is larger than the return gas flow during the cold blow, and the regenerator operation is then asymmetric and unbalanced.

The bypass gas diverted from the cold head is nominally at the cold head temperature, but could be cooler than, equal to, or warmer than the cold head temperature depending on the specific valving used to divert the bypass gas. In Figure 7.1, a passive check valve is shown which allows the high pressure helium charge, which has not undergone expansion, to be diverted. Because it has not undergone expansion, the gas is warmer than the cold head temperature. If the bypass gas is below the inversion temperature, insertion of a JT valve after the check valve could be used to reduce the bypass gas pressure and its temperature. Alternatively, an active valve could be used to divert gas during some part of the expansion phase of the GM cycle, rather than the charge phase, which could provide gas warmer or cooler than the cold head temperature, depending on the exact timing of the valve. The check valve plus JT valve combination, or the active valve arrangement, would provide greater efficiency, since the work of compression of the helium gas would be converted to useful cooling, rather than wasted through the bypass metering valve. One drawback of these alternatives would be slightly greater system complexity. Another drawback is that the maximum inversion temperature for helium is 40 K, which tends to limit the range of cycle operation for which the JT valve would be beneficial.

Three cycles were identified to distinguish the possible cooling modes of the Bypass GM apparatus. If there is no bypass flow, and accordingly, a load is only applied at the cold head, then this mode of operation shall be termed the Standard GM cycle. If the cold head heat exchanger is not used, or equivalently, there is no load applied to the cold head, and bypass gas is drawn from the cold head expansion space to supply cooling to the bypass heat exchanger load, then this mode of operation shall be termed the Bypass GM cycle. If both the bypass and cold head heat exchangers are used, then this mode of operation shall be termed the Combined GM cycle.

7.2.2 Experimental Apparatus

A single-stage GM cryocooler system using the conical regenerator described in Chapter 4 was modified to test the operating characteristics of the bypass GM system. The bypass flow was achieved through the use of a check valve mounted directly in the cold head that allowed gas flow when the pressure differential between the cold head expansion space and the buffer volume exceeded ~20 kPa. Mounted on the end of the check valve was a screen filter containing zeolite adsorbent to adsorb any trace condensibles. Texts on recuperative heat exchangers [95] indicate that any condensible impurities in the gas within a DC flow refrigeration system tend to accumulate at the coldest surface. Hall [98] has found this to be true of AC regenerative (pulse tube) systems as well. From the buffer volume, the flow was directed through a series of heaters in place of the bypass counterflow heat exchanger which warmed the gas to room temperature. The bypass flow rate was controlled using a 20-turn precision metering valve. An electric heater provided a load to the cold head in place of the cold head condensing exchanger.

The system was instrumented to determine the bypass mass flow rate, as well as the total system flow rate using mass flow meters. Temperatures were recorded for the cold head, the cold buffer volume exit temperature (bypass heater inlet), and the bypass heater exit using platinum resistance thermometers (PRT's). The bypass pressure and the compressor return pressure were recorded using silicon bridge diaphragm transducers. A piezoelectric pressure transducer was flush-mounted in the cold head expansion volume to sense the pressure fluctuations of the expansion space. The cold head pressure transducer signal was conditioned using a custom designed charge amplifier circuit, given as Figure D.1 in Appendix D.

A magnet mounted in the regenerator cold end provided excitation to a Hall probe mounted on the cold head yielding a timing signal for the regenerator/displacer reaching bottom dead centre. The displacer motion is harmonic, so position of the displacer only requires knowledge of the minimum and maximum displacement and the operation frequency, plus a synchronization signal. This arrangement is simpler and less intrusive than a linear voltage displacement transducer (LVDT) such as used by Inaguchi *et al.* [72] or laser displacement sensor such as used by Kurihara *et. al.* [99] for measuring displacer position. The position information used together with the cold head pressure signal output allowed the generation of pressure-volume diagrams.

All electronic pressure gauges, flow meters, and PRT's were monitored using a computer data acquisition system running on a Power Macintosh PC. Analogue signals were conditioned through National Instruments [100] SCXI (Signal Conditioning eXtensions for Instrumentation) modules model 1102 and 1100 in a SCXI-1000 chassis and converted to digital signals within the PC using a PCI-MIO16XE50 multifunction I/O board.

The digital signals were monitored using a custom LabView interface program. LabView by National Instruments allows graphical programming of complex data input and output functions, real time control functions, and real time monitoring and graphing functions. Signals from the Bypass GM apparatus were plotted in real time, including on-the-fly calculation of pressure-volume data from the cold head expansion space. Data representing time-averaged samples were recorded to disk at regular periodic intervals within the program. Data "snapshots" representing a timed log of instantaneous values with minimal data processing were also recorded for data at steady-state conditions.

A schematic of the experimental apparatus is given in Figure 7.2 and the corresponding photo of the room temperature components of the apparatus is given in Figure 7.3. System components and suppliers are specified in Table E.1 in Appendix E.

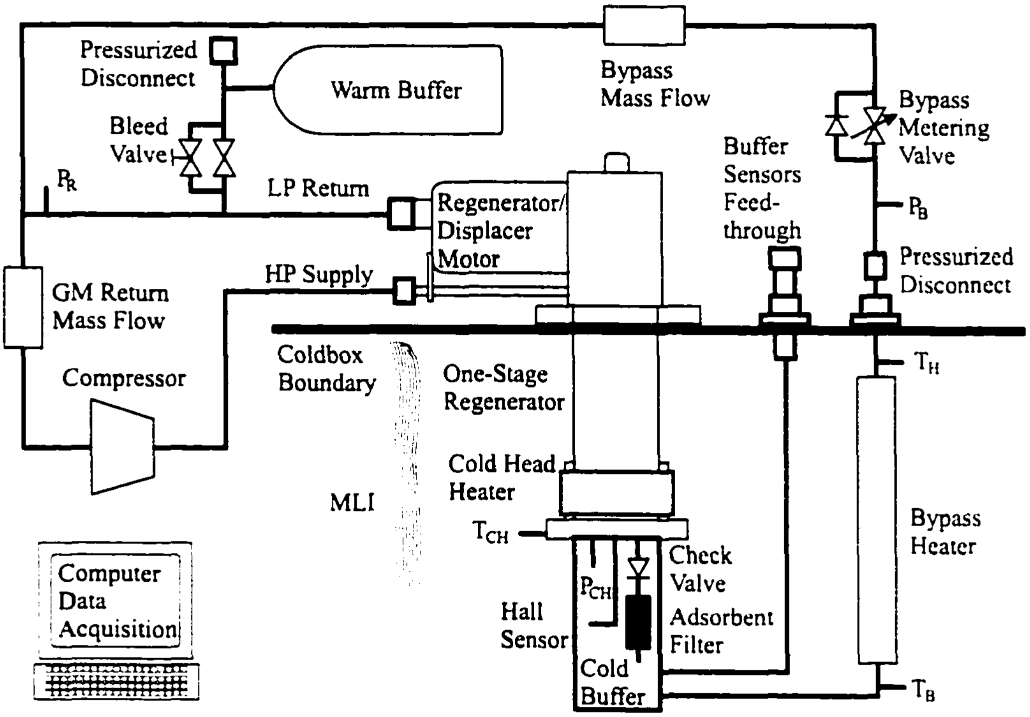

Figure 7.2 Schematic diagram of the Bypass GM test apparatus showing key system components and instrumentation.

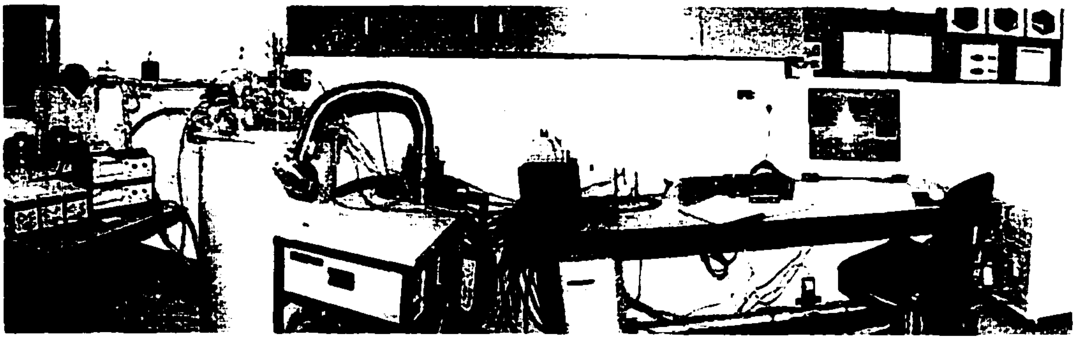

Figure 7.3 Photo of the Bypass GM experimental apparatus showing room-temperature components and data acquisition system.

7.3 Key Elements of the Apparatus Design

7.3.1 Cold Head and Cold Buffer

The cold head cylinder, which houses the regenerator/displacer, features a removable cold head flange. The seal between the cylinder and the flange is provided by an indium wire seal. The buffer volume was originally designed to mount to the cold head flange using a second indium seal, but it was found that the process of mounting the buffer volume to the flange tended to compromise the existing seal between the flange and the cylinder. A second arrangement, with the flange sandwiched between the cylinder and the buffer while the buffer was bolted directly to the cylinder, proved successful. The indium seals proved leak tight to 32 K under both static and dynamic pressure loads, but were only effectively leak tight under static loads below 32 K. Below 32 K, the helium leak rate to the vacuum space was approximately 10^{-7} standard cm^3 per second.

The primary reason for designing a buffer volume that bolts directly to the cold head flange was to reduce the chance for leaks into the vacuum space. Both the piezoelectric pressure transducer and the check valve need to penetrate into the cold head expansion space, while the zeolite filter needs to be placed between the check valve and the buffer volume. It was deemed likely that one indium seal around the buffer volume which then enclosed all the other components, rather than separate seals for each of the pressure transducer, check valve (which is a two piece unit with a teflon seal between the two halves), zeolite adsorbent filter, and buffer volume, would be less problematic.

A photo of the cold head flange mounted in the end of the cold head cylinder is given in Figure 7.4. Visible in the left centre of the photo is the Hall probe where the Hall probe integrated circuit chip is mounted on the end of a white nylon bolt. In the right centre is the piezoelectric transducer. In the background is the check valve and mounted to the check valve is the zeolite filter. The cold buffer volume mounts over and contains these components.

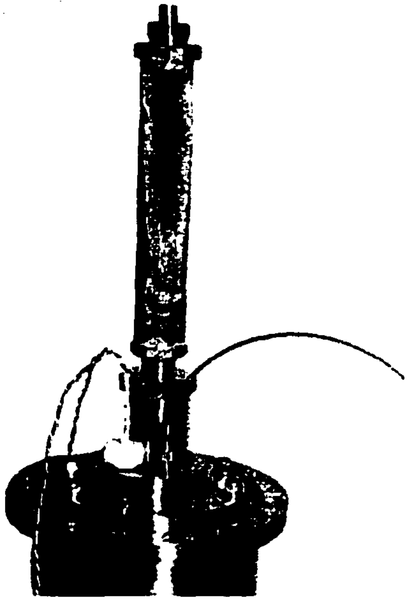

Figure 7.4 Photo of the cold head flange with Hall probe, piezoelectric pressure transducer, check valve, and zeolite adsorbent filter components mounted.

The buffer volume arrangement also satisfied the two requirements of operating the pressure transducer electronics. First, the transducer electronics needed to be directly connected to the piezoelectric transducer, and not through an electrical feedthrough which would bleed the charge from the transducer and degrade or eliminate the transducer signal; and second, the electronics needed to be kept under pressure, as opposed to under vacuum, where the surrounding gas could provide some convective cooling. The feedthrough for the transducer electronics output and the Hall probe signal were at room temperature, where a buna-N O-ring provided the seal.

Finally, the buffer volume satisfied the requirements of smoothing the bypass flow by acting as a capacitive element. Total active volume of the buffer was 450 cm^3. The bypass flow and cold buffer can be viewed in a similar manner to a capacitor filter arrangement for a half-wave rectifier circuit. The pressure swing in the cold buffer can be approximated using the relationship for an ideal gas and the assumptions that the pressure ripple is small, the charging time is small, and that the pressure is nearly constant. The ideal gas equation is:

$$P_B V_B = m_B \Re T_B \tag{7.1}$$

where P_B is the cold buffer volume pressure, V_B is the volume of the cold buffer, m_B is the mass of helium within the cold buffer, $\Re$ is the gas constant for helium, and T_B is the buffer volume temperature. The change in the mass contained in the buffer volume can be related to the change in the buffer pressure as:

$$\Delta P_B V_B = \Delta m_B \Re\, T_B \tag{7.2}$$

Noting that if the charge time is small relative to the discharge time, and assuming that the mass flow out of the volume is nearly constant, then:

$$\Delta m_B = \dot{m}_B \tau_{GM} \tag{7.3}$$

where $\dot{m}_B$ is the mass flow rate from the buffer volume and τ_{GM} is the period of the GM cycle. Setting Equation 7.2 and Equation 7.3 equal, the buffer volume pressure swing can be expressed as:

$$\Delta P_B = \frac{\dot{m}_B \tau_{GM} \Re\, T_B}{V_B} \tag{7.4}$$

The expected pressure swing rises linearly from approximately 60 $\frac{kPa}{g/s}$ at 25 K to 240 $\frac{kPa}{g/s}$ at 100 K. Bypass mass flows were not expected to exceed 0.15 g/s at 100 K, thus giving a worst case pressure swing of approximately 36 kPa, which is well within acceptable limits and the assumptions in the above pressure swing derivation.

7.3.2 Warm Buffer Volume and Make-up Gas

Because the Bypass GM test apparatus is a closed system, as the average gas temperature decreases during cooldown, the average system pressure also decreases. The warm buffer was sized so that during operation of the cold head the change in mass within the cold buffer volume due to the increased pressure (compared to the compressor off state) and decreased temperature would be exactly compensated by the decrease in mass within the warm buffer due to the decrease in the return line pressure (compared to the compressor off state). This would bring the operation pressures in line with those experienced by the conventional GM system lacking the bypass buffer arrangement.

The design point selected for balancing the buffer masses was at a cold head temperature of approximately 35 K. Below this temperature, more gas would be transferred to the cold buffer volume than would be removed from the hot buffer, with the excess gas coming from other portions of the system, such as the compressor high and low pressure buffer volumes and the compressor supplies lines, for example. At cold head temperatures above 35 K, the system pressure would rise above the pressure that would be experienced by the conventional GM system. In this system, the warm buffer gas could not be added for tests with cold head temperatures above approximately 40 K without the compressor high pressure supply line safety valve tripping.

The warm buffer volume was separated from the return line by a 25.4 mm diameter ball valve. A 5-turn metering valve and a small shut-off valve were mounted in parallel to the large ball valve and were used to slowly bleed the buffer volume gas into the return line. When the return line and buffer volume pressures were equalized, the large ball valve was opened allowing a minimum flow impedance between the volume and the return line.

7.3.3 Bypass Heater

The bypass heaters warmed the bypass gas to approximately 300 K and indirectly provided a secondary measure of gas flow rate using the known input power, temperature difference, and heat capacity of the bypass gas. Two different bypass heater designs were tested (though only the second design was used in gathering the data presented in this work).

The first design consisted of fibreglass insulated 28 AWG nichrome wire wrapped around a helical section of 6.35 mm diameter, 0.711 mm wall stainless steel tubing through which the bypass gas flowed. The stainless tubing was prepared by removing the surface polish with 120 grit emery cloth and thoroughly cleaning with acetone. The heater wire was measured out to give 4 heating zones based on maximum wire current and power supply considerations. Maximum wattage for the 4 zones in order of increasing distance from the cold buffer volume were 600, 350, 250, and 100 W, respectively.

The heater wire was bonded and potted to the stainless tubing with Stycast 2850 epoxy. To improve the surface reflectivity properties and to provide a surface more easily cleaned of contaminants from handling, etc., the heater was given a tightly stretched wrap of aluminized Mylar superinsulation. For the higher bypass flow rates, this heater worked very well. At the lower flow rates, the laminar flow heat transfer coefficient was too low tending to allow the unit to overheat before achieving the required heat transfer. Further, the heater was sluggish to respond to changes in heater setting at the low flow rates.

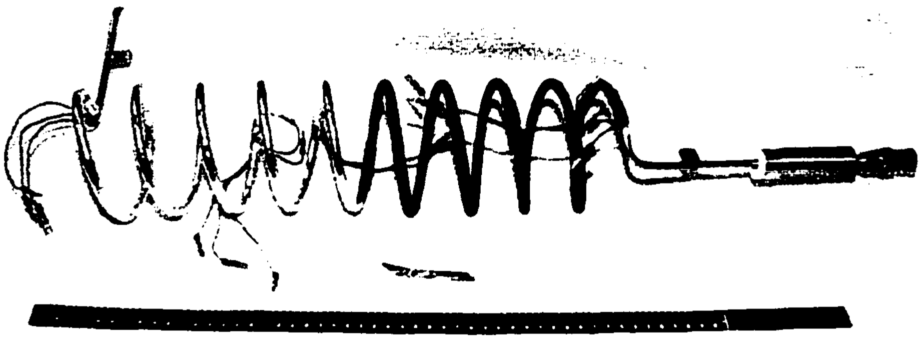

Figure 7.5 Photo of the first heater design consisting of fibreglass coated nichrome wire wrapped.around and epoxied to stainless steel tubing, then wrapped with aluminized mylar superinsulation.

Figure 7.5 shows a close-up photograph of the nearly completed nichrome wire-wrapped heater after partial wrapping of mylar insulation. Brass tabs visible above and below the heater section are mounting tabs for temperature sensors. The pressurized disconnect fitting and cold box feedthrough shell are visible on the right side of the photo. The many individual wires extending off the heater allow separate energizing of each wire in each heater zone.

The second heater design consisted of two cartridge heaters mounted in series with two 3.175 mm diameter, 0.711 mm wall thickness stainless steel tubes wrapped helically in parallel around the cartridges. The cartridge heaters were soldered to the tubing by pre-tinning both the cartridge heaters and tubing separately, wrapping the tubing on a mandril of slightly smaller diameter than the cartridge heaters, then inserting the cartridge heaters into the pre-formed coils. Energizing the cartridge heaters themselves then provided the necessary heat to melt the solder on the snugly fitting mating surfaces, thus bonding the two surfaces together. Extra solder was then added to better pot the tubing to the cartridge heaters. This second design also tended to overheat at the low flow rates, though not so severely as the first design. This heater was less responsive than the first design, being sluggish at both the lower and moderate bypass flow rates.

Figure 7.6 shows a close-up of the completed tubing-wrapped cartridge heater. Brass tabs visible above and below the heater section are mounting tabs for temperature sensors. Each cartridge heater can be separately energized.

Figure 7.6 Photo of the second heater design consisting of stainless tubing wrapped around and soldered to cartridge heaters.

7.3.4 Bypass Metering Valve

The bypass metering valve used in the apparatus had a maximum flow coefficient of $C_V = 0.024$. The valve was not a zero-flow shut-off valve, so a ball valve was mounted in series with the metering valve. The shut-off ball valve provided a convenient means of temporarily stopping bypass flow without having to tamper with the metering valve setting. A check-valve with adjustable cracking pressure was mounted in parallel to the metering and shut-off valves to guard against potential overpressures in the cold buffer and bypass line in the event of power failure or other unexpected event. If, for example, the bypass valve were closed, and the compressor then turned off or power was lost, the accumulated gas in the cold buffer volume could warm causing a large pressure rise in the bypass lines, eventually resulting in rupture. If the rupture occurred within the vacuum space of the cold box, the damage could be extensive. The bypass valve was set to open at a pressure differential of 2 MPa. The bypass and shut-off valves were left open during shut-down to prevent any overpressures.

7.3.5 Insulation

All cold surfaces were enveloped with close-fitting, shaped, blankets of fabric-backed aluminized Mylar superinsulation. The blankets consisted of 24 to 26 layers of insulation loosely wrapped around pre-forms of the appropriate shapes and sizes, then the blankets were removed from the forms and sewn together with cotton thread. Care was taken to avoid "short circuits" in the insulation at joints and corners by ensuring that there were no sharp bends, compressions, or inner insulation layers directly in thermal contact with outer layers. Care was also taken to limit contact points between the insulation and the cold surfaces. Joints and seams were made with aluminized polyester tape.

7.3.6 Coldbox Vacuum

The cold components of the Bypass GM apparatus were isolated in an aluminum vacuum chamber to reduce conduction and convection heat leaks. Vacuum was maintained using a turbo-molecular pump backed by a roughing pump. With inherent leaks and outgassing present with the apparatus, the vacuum system could maintain typical vacuum at better than 7×10^{-6} Torr measured at the farthest point from the vacuum pump.

7.3.7 Mass Flow Measurement

Mass flow was measured for both the bypass flow line and the GM return line using electronic mass flow meters that detected the true mass flow rate. In these units, a portion of the gas flow passes through a precision manufactured sensing tube. A constant heat rate is applied to the tube. The temperature is measured both upstream and downstream of the tube heater, and the differential temperature is proportional to the mass flow rate. The flow rate was determined as the average of the sampled flow rate as recorded by the data acquisition equipment.

7.3.8 Temperature Measurement

Platinum Resistance Thermometers, or PRT's, were used for all temperature measurements even through they are not normally employed in applications below approximately 30 K due to a nearly constant resistance and therefore reduced sensitivity at these temperatures. Commonly, the Callendar-Van Dusen equation is used to approximate the PRT resistance as a function of temperature, and is given by:

$$R_T = R_0\left[1 + AT + BT^2 + C(T - 100)^3\right] \tag{7.5}$$

where R_T is the resistance of the PRT at temperature T measured in degrees Celsius, and A, B and C are the Callendar-Van Dusen coefficients shown in Table 7.1. For temperatures above 0° Celsius, the coefficient C equals zero. If you pass a known current through the PRT, and measure the voltage across the PRT, together this will provide the resistance, which can be converted to a corresponding temperature. To determine temperatures below 0° Celsius, the Callendar-Van Dusen equation is a somewhat messy cubic to be solved. For temperatures below 40 K, or -233.15° Celsius, there is substantial deviation in the equation from observed resistance, and in fact, the Callendar-Van Dusen equation predicts zero resistance at approximately 26.3 K.

Table 7.1 Callendar-Van Dusen coefficients corresponding to common platinum resistance thermometer standards.

Standard	A	B	C
DIN 43760	3.9080×10^{-3}	-5.8019×10^{-7}	-4.2735×10^{-12}
American	3.9692×10^{-3}	-5.8495×10^{-7}	-4.2325×10^{-12}
ITS-90	3.9848×10^{-3}	-5.8700×10^{-7}	-4.0000×10^{-12}

Using typical values of PRT resistance as a function of temperature obtained from the PRT manufacturer's calibrated tests, an improved equation giving temperature as a function of calculated resistance based on applied current and measured voltage was obtained. The manufacturer's resistance-temperature data was presented in two charts using integer temperature values in Kelvin and

Centigrade scales. The first chart gave temperature-resistance values in 1 K increments from 30 K to 400 K. The second chart gave values in 1° Celsius increments from -250° Celsius to 0° Celsius. The improved temperature-resistance equation is:

$$T = a + bR_T + cR_T^2 + \frac{d}{R_T} \tag{7.6}$$

where T is the temperature in Kelvin, R_T is the resistance in Ohms given by Ohm's Law from the applied current and measured voltage across the PRT, and a, b, c and d are the coefficients listed in Table 7.2.

Table 7.2 Coefficients for an improved temperature-resistance correlation for DIN 43760 Standard, 100 Ω PRT's.

Coefficient	Value
a	32.744261557800
b	2.243129790765
c	0.001633948835
d	-37.890903626670

The improved temperature-resistance equation is valid from 325 K to 23 K for DIN 43760 Standard PRT's with a resistance of 100 Ω at 0° Celsius. Below 50 K, the curve fit is accurate to the manufacturer's calibrated data to with ±0.3 K. Below 30 K, the curve fit is accurate to the manufacturer's data to ±0.1 K. Over the range of validity, the error, ϵ_T, between the calibration temperature and the calculated temperature is bounded by $-0.41 < \epsilon_T < 0.46$ K. For this work, it is assumed that the PRT's used to instrument the Bypass apparatus follow this curve fit given that individual calibration at room temperature and liquid nitrogen temperature corresponded within 0.2 K and 0.5 K, respectively.

Chapter 8

Bypass Gifford-McMahon Cycle Experimental Procedure and Results

8.1 Procedure

Six distinct sets of experiments were performed to verify the theoretical superiority derived herein of the bypass regenerative liquefier system over the balanced flow system by measuring the cooling load performance and operational characteristics of the Standard GM cycle, Bypass GM cycle, and Combined GM cycle using the Bypass GM apparatus. These experiments were:

1) Cold head cooling load, $\dot{Q}_{CH}$, versus cold head temperature, T_{CH}.
2) Cold head cooling load, $\dot{Q}_{CH}$, versus cold head temperature, T_{CH}, with extra gas charge from opening the connection to the warm buffer volume.
3) Bypass cooling load, $\dot{Q}_B$, versus cold head temperature, T_{CH}.
4) Bypass cooling load, $\dot{Q}_B$, versus cold head temperature, T_{CH}, with extra gas charge from opening the connection to the warm buffer volume.
5) Combined cold head cooling load $\dot{Q}_{CH}$, and bypass cooling load, $\dot{Q}_B$, versus cold head temperature, T_{CH}.

6) Pressure-Volume diagrams of the cold head expansion space under the cooling loads listed above.

Experiments 1 and 2 tested the operation of the apparatus as a Standard GM cycle cryocooler. Experiments 3, and 4 tested operation of the apparatus as a Bypass GM cycle cryocooler providing only bypass cooling. Experiment 5 tested operation of the apparatus as a Combined GM cycle cryocooler providing both bypass and cold head cooling. Experiment 6 tested whether operation of the unit under bypass and combined cooling loads significantly altered the pressure-volume relationship in the cold head expansion space compared to operation as a Standard GM cycle.

For all experiments, the coldbox vacuum was maintained better than 2×10^{-5} Torr, and when the cold head temperature was above 32 K, typical vacuum was better than 7×10^{-6} Torr. Steady state was considered established when the measured temperatures did not change by more than 0.2 K within a 20 minute period, and an asymptotic temperature approach had been demonstrated. In most cases, the change near steady state was less than 0.2 K, but in some cases this could not be achieved due to long time frame temperature oscillations near steady state of approximately ±0.3 K. These oscillations may have been due to the Bypass GM apparatus itself (such as due to performance changes in the regenerator due to condensible gases blocking flow channels) but seemed better correlated to the room ventilation system (which likely affected the power supplies' settings for the cold head and bypass heaters). In cases where temperature oscillations greater than 0.2 K were observed, steady state conditions were considered to be the state points centred about the limits of the oscillations.

For the bypass and the combined load experiments, the bypass flow rate was set with the bypass metering valve and the bypass heater power was manually adjusted until the heater exit temperature was approximately 300 K at steady-state as defined above.

8.2 Results

8.2.1 Experiments 1 and 2:

Operation of the Bypass Apparatus as a Standard GM Cryocooler

With the bypass metering valve and the warm buffer valves closed, the Bypass apparatus was allowed to cool from room temperature to its minimum no-load temperature. A typical cooldown curve is shown in Figure 8.1. The initial cooldown rate is approximately 7 K/minute, reaches a "knee" in the cooling curve at 40 K and further cooling is at approximately 0.1 K/minute after the knee reaching 24.0 K after 140 minutes from the start of the cooldown. A cold head temperature of 23.2 K was the lowest observed, after 3.5 hours of operation with a small bypass flow to cool the cold buffer volume followed by 30 minutes of operation without bypass flow.

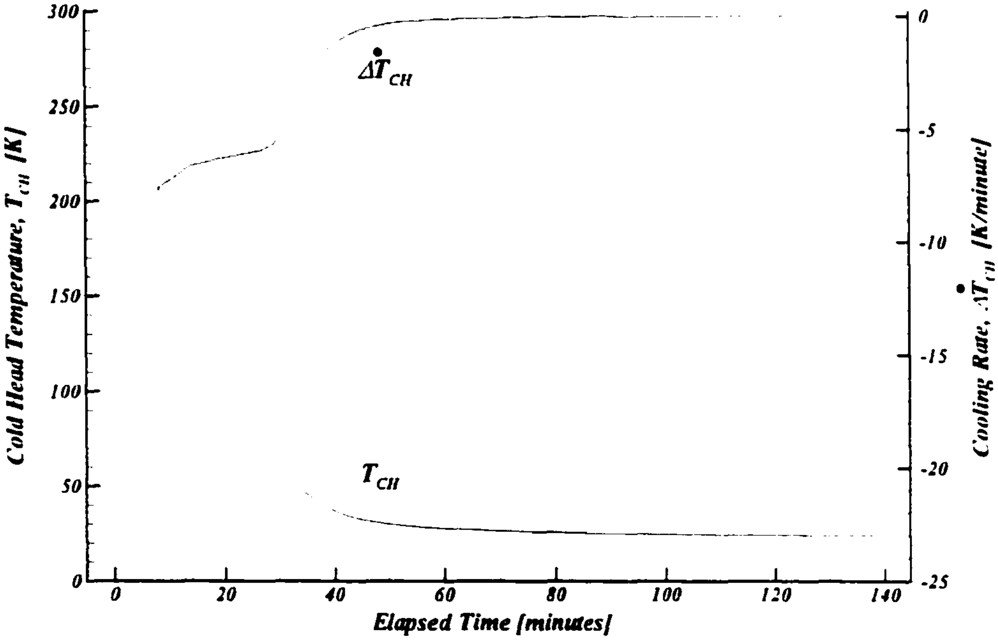

Figure 8.1 Cold head temperature and cold head temperature rate of change as a function of elapsed time for the Bypass GM apparatus under Standard GM cycle operation.

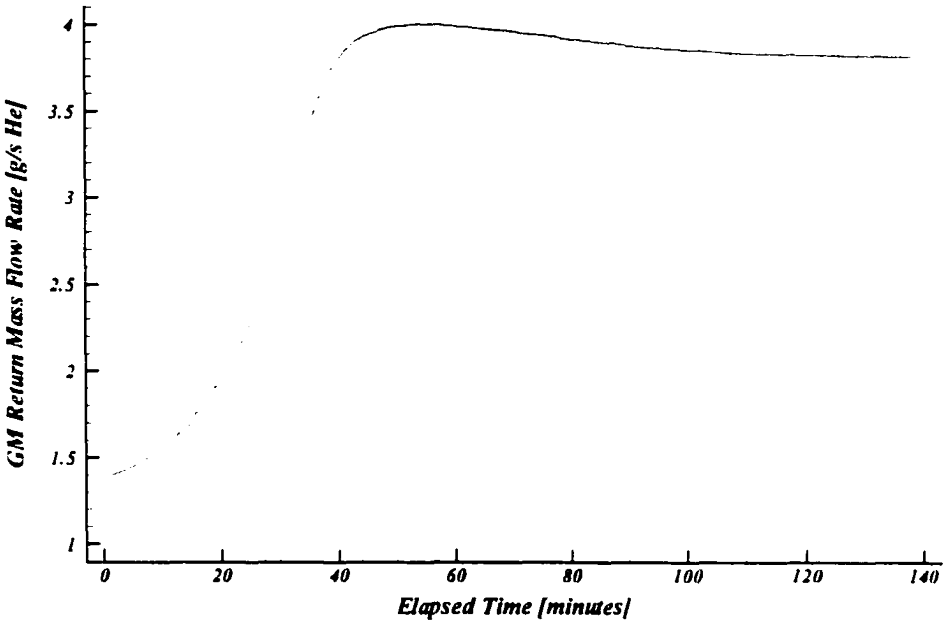

Figure 8.2 GM compressor return line mass flow rate as a function of elapsed time during initial cooldown of the Bypass GM apparatus under Standard GM cycle operation.

During a cooldown, the total mass flow measured through the GM return line steadily increases as shown in Figure 8.2. As the temperature of the cold head and cold head expansion space decreases, so does the average temperature within the regenerator, and therefore the average temperature within the void volume of the regenerator. The helium gas that then fills the regenerator and cold head expansion space, being progressively colder, has a progressively higher density, and therefore a greater mass fills and leaves the fixed volume with each cycle. Near the minimum no-load temperature, a peak flow is reached, which is then decreased by the effects of a drop in system pressure as the cold buffer volume cools and accumulates gas from the rest of the system. Note that the "knee" in the cooldown curve of Figure 8.1 occurs at the same time as the rapid rise in the mass flow curve of Figure 8.2, suggesting that the increased mass flow through the regenerator, and the resulting decrease in regenerator efficiency, has a strong influence on the cooling rate.

After reaching the minimum no-load temperature, electrical loads were applied to the cold head heater. After steady state was achieved for a given cooling load, the system operation points, namely cold head, cold buffer volume, and heater exit temperatures, cold buffer volume and GM return pressures, and bypass flow and GM return flow rates, were recorded. A pressure-volume diagram was generated using the cold head pressure sensor and the Hall probe synchronization signals.

Cold head loads for the operation with and without use of the warm buffer volume were 0, 2, 4, 10.4, 25, 50, and 75 W. A load of 100 W was also applied only in the case of the operation without the warm buffer because of limitations to the compressor system supply line pressure safety release at the warmer temperatures of the cold head. Some loads were tested twice to verify that the steady-state temperature achieved during an increase in the cold head load was the same as the temperature achieved during a decrease in the cold head load. The operation points were found to be independent of the cooling load path taken, except for the cold buffer volume temperature which does not give a valid measurement when there is no bypass flow.

At the completion of the experiments without the warm buffer, the cold head load was removed and the system was allowed to cool back down to its minimum no-load temperature. The warm buffer volume was then bled into the system, which gradually increased the average system pressure. When the warm buffer volume had reached the return line pressure, a ball valve was opened to directly connect the warm buffer volume with the compressor return line and each cooling load was tested in turn.

Figure 8.3 shows the heat load map for the Standard GM cycle, giving cold head temperature as a function of applied cold head heater load for operation with and without the warm buffer volume. For loads below 10.4 W, slightly better performance is achieved without the extra gas from the warm buffer. Above 10.4 W, performance is better using the warm buffer gas. The differences in performance with and without the warm buffer gas are small, being a maximum difference of -0.8 K at the lowest temperatures and +1.8 K at the higher temperatures.

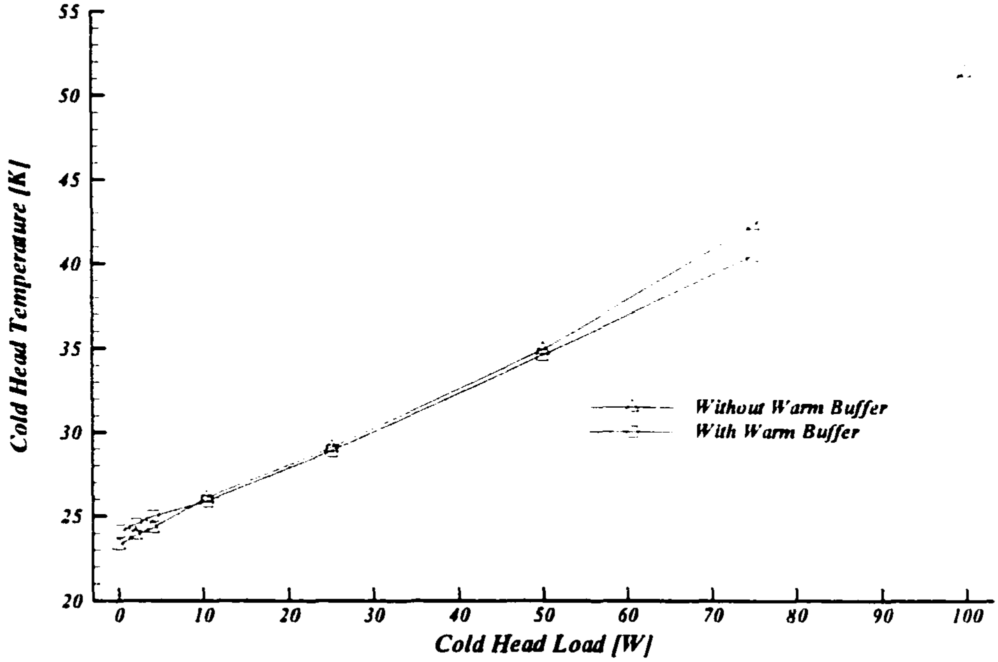

Figure 8.3 Cold head temperature as a function of applied cold head cooling load for Standard GM cycle operation, with and without use of the warm buffer and make-up gas.

8.2.2 Experiments 3 and 4:

Operation of the Bypass Apparatus as a Bypass Only GM Cryocooler

With the bypass metering valve and the warm buffer valves closed, the Bypass GM apparatus was allowed to cool from room temperature to its minimum no-load temperature. The bypass metering valve was progressively opened and the bypass heater load manually adjusted to warm the bypass gas to approximately 300 K. Figure 8.4 shows the bypass mass flow rate as a function of the number of valve turns for the Bypass GM apparatus (with no cooling load on the cold head). The experiments with the additional warm buffer gas were limited by pressure limits imposed by the compressor safety release valve as the system pressure rose with increasing cold head temperature.

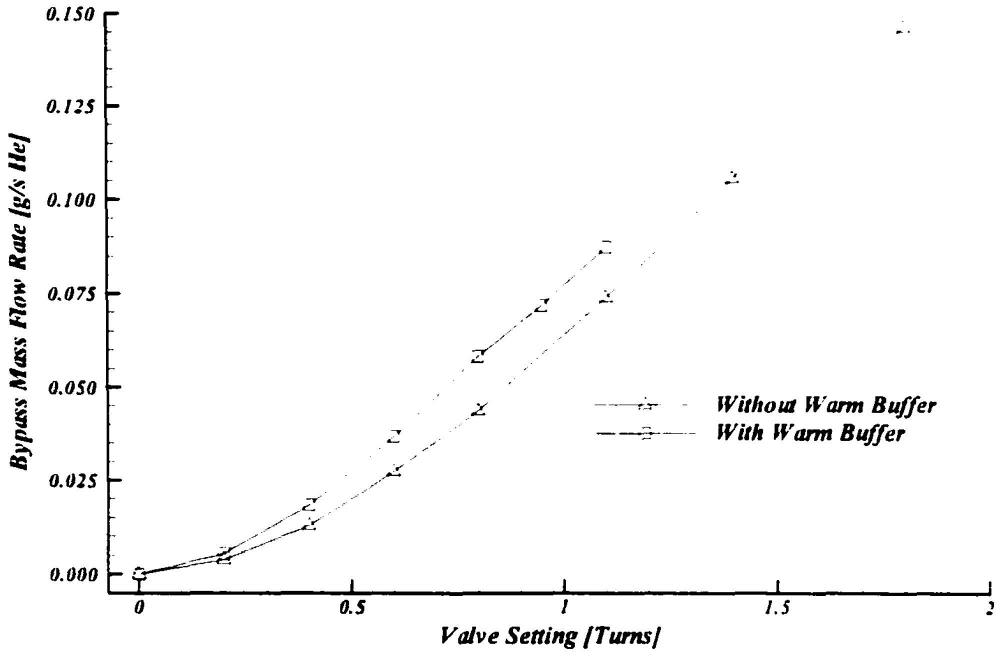

Figure 8.4 Measured Bypass GM apparatus bypass mass flow rate as a function of the number of valve turns, with and without use of the warm buffer and make-up gas.

For the bypass flow experiments, the bypass heat load is not an independent variable *per se*. Once the bypass flow rate is set by the valve turns, the cold head and the bypass flow temperatures come to steady state. On the approach to steady state, the system pressures change to some degree, which in turn affects the bypass flow rate. At the low bypass flow rates, the pressure and flow rate changes are small, but at the higher flow rates, a feedback effect causes a significant change in flow rate from the initial setting.

The feedback loop is in part due to the peculiarities of a fixed mass, fixed volume system using a gas with large changes in density with temperature over the range of operation. A warming cold head and cold buffer causes a decrease in flow into the regenerator and a decrease in the storage of gas in the cold head and cold buffer due to gas density changes. The gas displaced from the cold regions then causes an increase in the average system pressure and pressure ratio. The increased pressure differential across the bypass metering valve causes an increased bypass flow. With the decreased regenerator flow and increased bypass flow, the bypass flow becomes a larger percentage of the total regenerator flow, causing a greater hot and cold blow flow imbalance in the regenerator. The increasing regenerator imbalance lowers the regenerator efficiency which corresponds to an increase in the cold end exit temperature. The increased exit temperature from the regenerator causes an increase in the cold head and cold buffer temperatures, which completes the feedback loop.

Once the system has reached steady-state, the bypass heat load is fixed by the cold buffer volume exit temperature and the heater exit temperature. The bypass heater exit temperature was selected to be nominally 300 K. A bypass heater exit temperature ranging from 285 K to 315 K was deemed acceptable, so long as the temperature satisfied steady-state requirements. All bypass heat loads presented have been scaled as if the exit temperature were exactly 300 K by assuming that the bypass gas flow had a constant heat capacity of 5.2 kJ/kg/K from the buffer exit temperature to 300 K. The cold buffer volume exit temperature and the cold head temperature as a function of bypass mass flow rate are given in Figure 8.5.

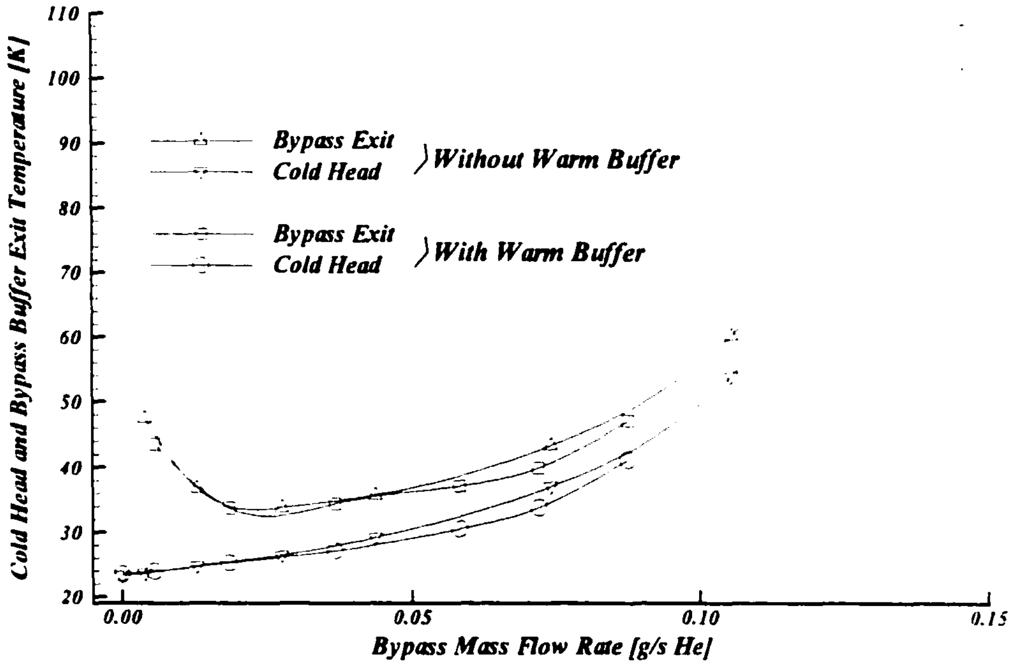

Figure 8.5 Cold head temperature and cold buffer exit temperature as a function of bypass mass flow rate, with and without use of the warm buffer and make-up gas.

At zero bypass flow rates, the bypass exit temperature, which is measured at the entrance to the bypass heater, is independent of the cold head temperature, and at low flow rates, is artificially high. At low flow rates where the heat transfer coefficient is low, the bypass heater must have a larger temperature difference to achieve the required heat transfer to the bypass gas than at the higher flow rates. Because of the temperature sensor's proximity to the heater and distance from the cold buffer volume, the sensor reads artificially high. Turning off the heater for short periods caused a reduction in the heater inlet temperature indicating the nature of the error. A second warming effect, due to the sensor's isolation and the distance from the cold head, was the radiant heat load and/or sensor self-heating. This effect could be demonstrated by increasing the mass flow through the bypass heater for periods short enough to cool the sensor but not affect the cold head temperature appreciably. No correction to the data was made for these effects.

A heat load map can be generated for the Bypass GM cycle. The bypass load is defined as:

$$\dot{Q}_B = \dot{m}_B C_f \left(T_H - T_B\right) \tag{8.1}$$

where $\dot{m}_B$ is the bypass mass flow rate, C_f is the heat capacity of the bypass gas taken as constant at 5.2 kJ/kg/K, T_H is the bypass heater exit temperature taken as 300 K, and T_B is the bypass cold buffer volume exit temperature measured at the entrance to the bypass heater.

Figure 8.6 shows the cold head and bypass temperatures as a function of the bypass load with and without the warm buffer volume. The increase in cold head temperature is nearly linear until a cooling load of 100 W, then rises sharply. In this region the feedback mechanism discussed above is quite pronounced. Further, as the buffer exit temperature rises, the bypass load, which is proportional to the temperature difference from 300 K assuming constant heat capacity and flow rate, decreases. At some point of increased flow rate, the product of heat capacity, flow rate, and temperature difference would reach a maximum, beyond which increased flow would result in decreased bypass load.

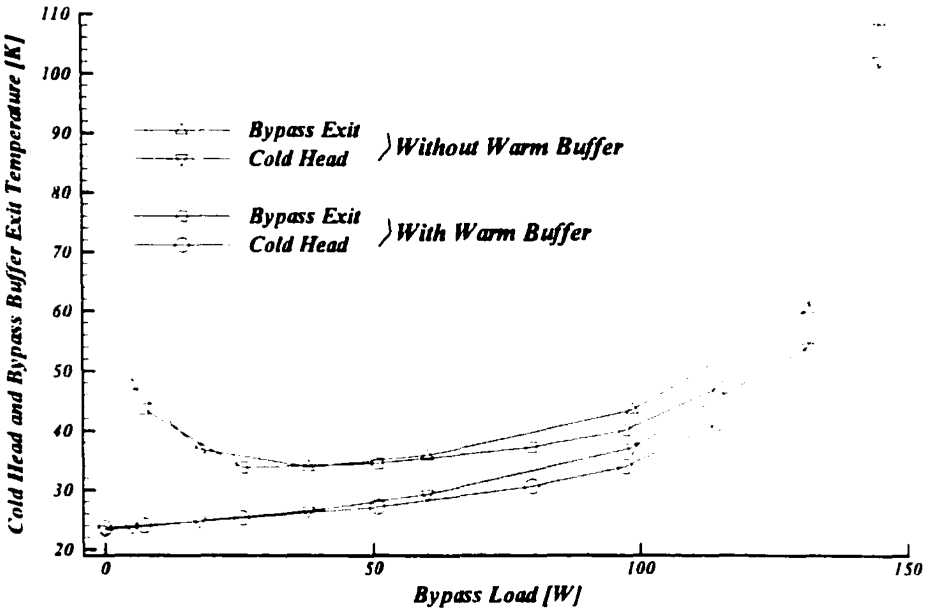

Figure 8.6 Cold head temperature and cold buffer exit temperature versus bypass cooling load, with and without use of the warm buffer and make-up gas.

8.2.3 Experiment 5:

Operation of the Bypass Apparatus as a Combined GM Cryocooler

With the bypass metering valve and the warm buffer valves closed, the Bypass GM apparatus was allowed to cool from room temperature to its minimum no-load temperature. The bypass metering valve was progressively opened and the bypass heater load manually adjusted to warm the bypass gas to approximately 300 K, while simultaneously a cooling load was applied to the cold head heater. All experiments reported in this section were performed without the warm buffer to avoid the limitations imposed by the compressor safety valve at higher cold head temperatures and system pressures.

Figure 8.7 presents a family of curves showing cold head temperature as a function of the bypass load for different values of cold head load. Also shown are three datapoints for distinct load conditions. For the zero cold head load conditions, some data at the higher bypass rates have been omitted from the figure for clarity but were nonetheless previously presented in Figure 8.6. Omitting values for the zero bypass flow, where the buffer exit temperature is not valid, Figure 8.8 presents a similar family of load curves for the buffer exit temperature.

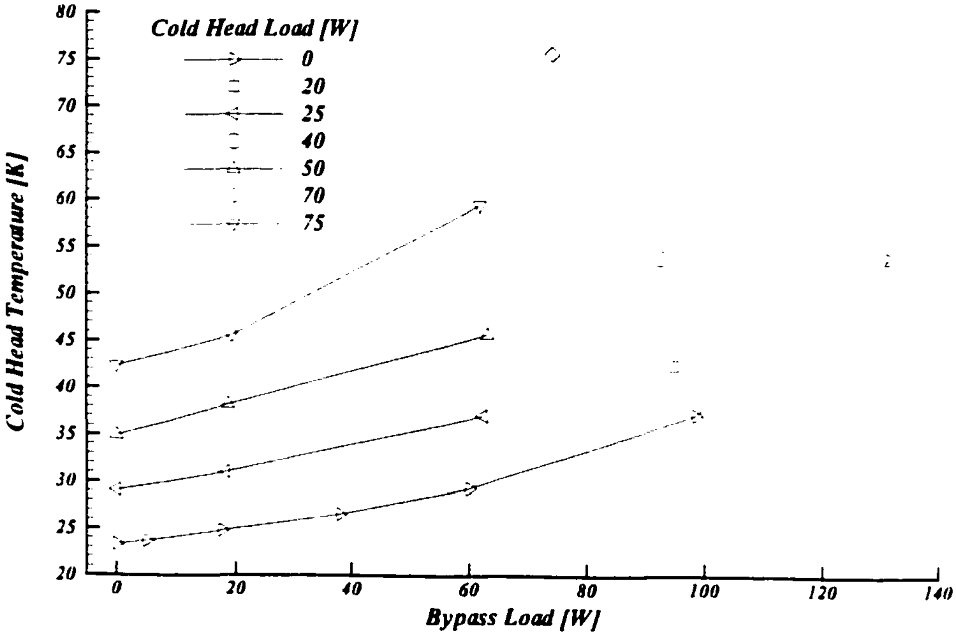

Figure 8.7 Cold head temperature versus bypass and cold head cooling loads for the Combined GM cycle.

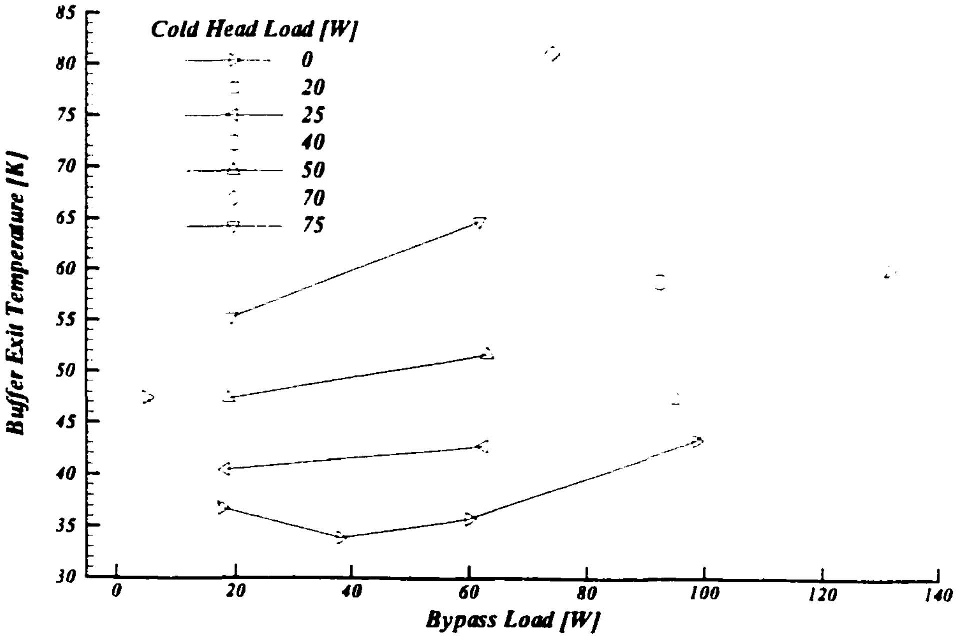

Figure 8.8 Cold buffer exit temperature versus bypass and cold head cooling loads for the Combined GM cycle.

8.3 Comparison of the Cooling Performance of the Standard GM, Bypass GM, and Combined GM Cycles

8.3.1 Basis of Comparison

A quick glance at Figures 8.3 and 8.6 might suggest that the Bypass GM cycle is always superior to the Standard GM cycle since for a given cold head temperature the bypass load, $\dot{Q}_B$, exceeds the cold head load, $\dot{Q}_{CH}$. It must be recalled, however, that the Bypass GM cycle provides its cooling over a large temperature span, whereas the Standard GM cycle provides all its cooling at the cold head temperature. Direct comparison of the applied cooling loads $\dot{Q}_B$ and $\dot{Q}_{CH}$ is not valid to determine superiority. A valid comparison must consider the performance in the intended mode of operation.

8.3.2 Comparison of Performance as a Refrigerator

Comparison of performance of the Standard GM cycle, Bypass GM cycle, and Combined GM cycle as a refrigerator considers that all cooling loads can be ideally converted in some black box device to a single cooling load at the cold head temperature. In the case of the Standard GM cycle, the black box does nothing because all cooling is already provided at the cold head temperature. In the case of the Bypass GM and Combined GM cycles, the black box is allowed to communicate thermally with the cold head, the bypass stream and a thermal reservoir at the environmental temperature. It is also allowed to communicate with a mechanical pressure reservoir at the GM return pressure. The environmental temperature is taken as 300 K, while the GM return pressure is that recorded for each of the experiments. The black box is assumed to contain some ideal refrigerator that can convert the thermal and pressure difference of the cold buffer exit bypass stream with the reservoir to a single cooling load which is added to any cooling load already available at the cold head. The conversion process is shown schematically in Figure 8.9.

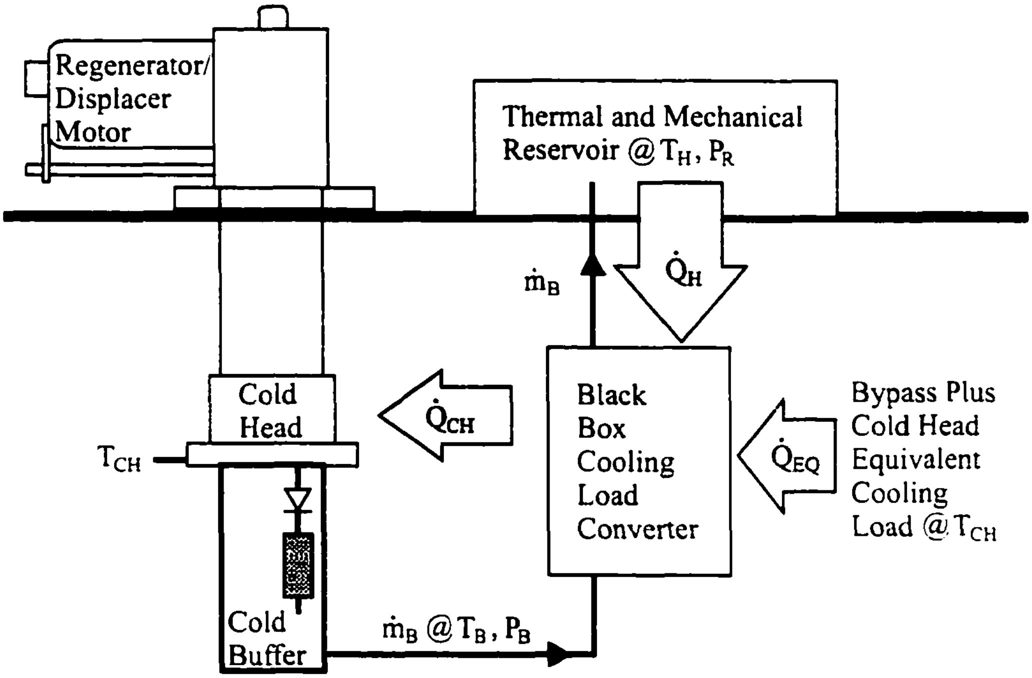

Figure 8.9 Black box converter concept to compare Standard GM, Bypass GM, and Combined GM performance of the Bypass GM apparatus when operating as a refrigerator.

An exergy balance on the black box cooling load converter reveals that the bypass load plus cold head cooling load could be ideally converted to an equivalent cooling load, $\dot{Q}_{EQ}$, at the cold head temperature, T_{CH}, given by:

$$\dot{Q}_{EQ} = \dot{Q}_{CH} + \frac{T_{CH}}{T_H - T_{CH}} \dot{m}_B \left[\left(h - T_H s\right)_{in} - \left(h - T_H s\right)_{out} \right] \tag{8.2}$$

where h is the specific enthalpy and s is the specific entropy of the bypass gas. The subscript *in* refers to the pressure and temperature condition at the exit of the cold buffer volume (and/or entrance to the bypass heater). The subscript *out* refers to the temperature and pressure of the thermal and mechanical reservoir, here taken to be the corrected temperature at the exit of the bypass heater and the pressure of the GM return line. When the bypass flow is zero, the second term in Equation 8.2 is zero, and the equivalent cooling load is simply equal to the cold head load. For zero bypass flow, $\dot{Q}_H$ shown in Figure 8.9 is zero. With bypass flow, $\dot{Q}_H$ as shown in the figure is positive and is given by:

$$\dot{Q}_H = \dot{Q}_B - \frac{T_{CH}}{T_H - T_{CH}} \dot{m}_B \left[\left(h - T_H s\right)_{in} - \left(h - T_H s\right)_{out} \right] \tag{8.3}$$

It should be noted that $\dot{Q}_H$ is a theoretical load that would be transferred to the black box cooling load converter, and is not a load applied to the Bypass GM apparatus. Similarly, $\dot{Q}_{EQ}$ is not a load applied to the apparatus, except in the case of zero bypass flow where $\dot{Q}_{EQ} = \dot{Q}_{CH}$.

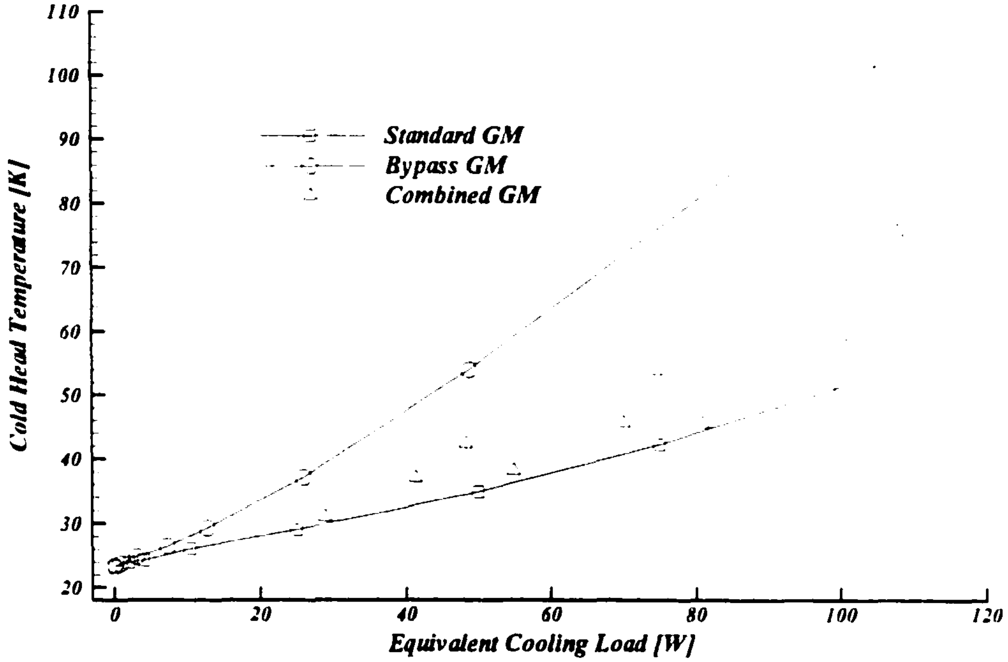

Figure 8.10 Cold head temperature as a function of equivalent refrigerator operation cold head load for the Standard GM, Bypass GM, and Combined GM cycles.

Figure 8.10 presents the performance of the Standard GM cycle, the Bypass GM cycle, and the Combined GM cycle when viewed as a refrigerator using Equation 8.2 to determine the equivalent cooling load that could be supplied at the cold head temperature. For all equivalent loads, the operation of the bypass apparatus as a Standard GM cycle provides the lowest cold head temperature, and the operation as a Bypass GM cycle provides the highest cold head temperature. This indicates that if cooling at a single temperature is desired of the bypass apparatus, the Standard GM cycle allows the largest cooling load at the desired cold head temperature compared to the Bypass GM and Combined GM cycles, even with ideal conversion of the bypass cooling loads to an additional cooling load at the cold head temperature. Any real conversion device in place of the ideal black box cooling load converter would provide still poorer performance for these cycles.

8.3.3 Comparison of Performance as a Liquefier

Comparison of performance of the Standard GM cycle and the Combined GM cycle as a liquefier considers that process gas is to be liquefied at the saturation pressure, P_{sat}, corresponding to the cold head saturation temperature $T_{sat} = T_{CH}$. Comparison of performance of the Bypass GM cycle considers that process gas is to be liquefied at some saturation point above the cold buffer exit temperature, T_B, where the saturation temperature is selected to match the available bypass cooling. A second comparison of the Bypass GM cycle is made by extrapolation of the operating conditions to give an expected cooling capacity corresponding to a bypass temperature at the critical point of the process gas.

For the Standard GM cycle, it is assumed that process gas at $T_H = 300K$ is introduced into a frictionless heat exchanger attached to the cold head and the mass flow adjusted such that the sensible heat and latent heat absorbed at the cold head at T_{CH} corresponds to the interpolated cooling load, $\dot{Q}_{CH}$, as determined by the cooling load curve. Gas exiting the cold head heat exchanger is at T_{CH}. The cold head can liquefy a process stream with a mass flow rate given by:

$$\dot{m}_P = \frac{\dot{Q}_{CH}}{\left(h_g\big|_{(T_H,P_{sat})} - h_f\big|_{(T_{CH},P_{sat})}\right)_P} \tag{8.4}$$

where the subscript P refers to the process stream, h is the stream enthalpy, and the subscripts g and f refer to the vapour and liquid states, respectively at the subscripted temperature and pressure conditions. The Standard GM cycle cooling load curve is interpolated to give an estimate of the cooling load $\dot{Q}_{CH}$ available at T_{CH}, where T_{CH} is selected to correspond to specific data points from the Combined GM cycle experimental results in order to directly compare liquefaction capacity at corresponding saturation pressures and temperatures.

For the Combined GM cycle, the same procedure outlined in Section 5.6.4 to determine the AMR liquefaction capacity is used, with slight differences in notation and temperature limits corresponding to the Bypass GM apparatus notation and temperature limits developed in this chapter. It is assumed that process gas at $T_H = 300K$ is first introduced into a frictionless counterflow heat exchanger with the countercurrent gas flow supplied by the bypass gas at T_B. From the counterflow heat exchanger, the process gas is then further cooled and liquefied at the cold head heat exchanger at T_{CH}.

In terms of the notation of the Bypass GM apparatus, the inlet temperatures of the bypass stream heat exchanger are taken as $T_{h_1} \equiv T_H$ and $T_{c_1} \equiv T_B$ to calculate effectiveness from Equation 5.30. The bypass gas exit temperature (previously assumed to be warmed to the thermal and mechanical reservoir temperature for the Bypass GM cycle analysis but now considered variable), the process gas exit temperature, and the process gas flow rate are now unknowns to be solved once the heat exchanger effectiveness and cold head cooling power are specified according to Equations 5.31 through 5.35 taking $T_{CH} \equiv T_C$, and $Q_{CH} \equiv Q_C$.

In this analysis, all the cold head cooling load, $\dot{Q}_{CH}$, is applied to the liquefaction process, whereas some of the bypass cooling load, $\dot{Q}_B$, may be discarded according to the energy balance in the bypass heat exchanger and the limitations of the cold head cooling capacity. This procedure reflects the fact that as the cold head cooling load at T_{CH} diminishes to zero, and the cold buffer exit temperature remains above T_{CH}, no liquefaction of the process stream can take place at $T_{sat} = T_{CH}$ regardless of the cooling load available from the bypass stream (without some additional black box load converter). Some liquefaction to a temperature at or above T_B would be possible for an appropriate saturation pressure of the process gas.

For the Bypass GM cycle, an analysis of the performance as a liquefier requires arbitrary selection of a saturation temperature, T_{sat}, at or above the cold buffer exit temperature, T_B, as well as specification of the bypass heat exchanger effectiveness. "Liquefaction" at the condition $T_{sat} = T_B$ can only be achieved if T_B corresponds exactly to the critical point of the process gas, at which condition there is no distinction between gas and liquid states. This operation point could, in principle, be achieved with the Bypass GM apparatus by adjustment of the bypass flow rate until the desired conditions are met. If the selected saturation temperature (and hence pressure) is at the critical point, then the cooling power of the bypass stream is most efficiently used, since the bypass stream provides sensible cooling, which is the only cooling requirement of a gas at its critical pressure.

If the selected saturation temperature is away from the critical point and above but close to the cold buffer exit temperature, then the capacity to liquefy the process gas stream is limited by the relatively small temperature difference (and hence small cooling power) available from the bypass stream between T_{sat} and T_B. The large cooling power from T_H to T_B goes largely unused.

If the selected saturation temperature is away from the critical point and well above the buffer exit temperature, then the capacity to liquefy the process gas is limited by the efficiency of requiring the cooler to reach a temperature well below T_{sat} for a load at T_{sat}. That is, it would not be efficient to require the cold head to reach a temperature as low as 20 K, for example, if the minimum temperature requirement of the cooling load were only 100 K.

With the above considerations in mind, two gases to be liquefied and two liquefaction scenarios have been selected for comparison. Considering the temperatures reached by the Bypass GM apparatus, the gases to be liquefied are neon and normal deuterium. The first liquefaction scenario is that the saturation temperature is selected such that the cooling available from the cold buffer exit temperature, T_B, to the saturation temperature, T_{sat}, is exactly sufficient to liquefy the quantity of gas that can be cooled from the ambient temperature, T_H, down to T_{sat}, considering that all heat exchangers have an effectiveness of unity. Algebraically, the saturation temperature is selected so that:

$$\frac{\left(\dot{m}C_f\right)_C\left(T_{sat} - T_B\right)}{\left(\dot{m}C_f\right)_C\left(T_H - T_{sat}\right)} = \frac{\left(\dot{m}h_{fg}\big|_{(T_{sat},P_{sat})}\right)_P}{\left[\dot{m}\left(h_g\big|_{(T_H,P_{sat})} - h_g\big|_{(T_{sat},P_{sat})}\right)\right]_P} \qquad (8.5)$$

where the subscript C refers to the cold buffer bypass stream, the subscript P refers to the process gas stream, namely neon or normal deuterium, h_{fg} is the latent heat of condensation evaluated at the subscripted temperature and pressure conditions, and h_g is the enthalpy of the vapour state evaluated at the subscripted conditions. Under these conditions, the numerators of the left and right sides of Equation 8.5 are equal, as are the denominators. The maximum process stream liquefaction rate is then given by either of:

$$\dot{m}_P = \frac{\left(\dot{m}C_f\right)_C\left(T_{sat} - T_B\right)}{\left(h_{fg}\big|_{(T_{sat},P_{sat})}\right)_P} \tag{8.6}$$

or

$$\dot{m}_P = \frac{\left(\dot{m}C_f\right)_C\left(T_H - T_{sat}\right)}{\left(h_g\big|_{(T_H,P_{sat})} - h_g\big|_{(T_{sat},P_{sat})}\right)_P} \tag{8.7}$$

8.4 Liquefaction Yields

8.4.1 Liquefaction Yield for the Bypass GM Cycle

An examination of the cooling curve for the Bypass GM cycle reveals that it is possible to liquify some quantity of process gas having a saturation temperature above 33.9 K. Based on the temperatures reached by the Bypass GM apparatus during the experiments, of particular interest are the gases neon and normal deuterium. For these gases, four of the bypass flow operation points could be used to liquefy neon, while three of these four reach a low enough temperature to liquefy deuterium. The relevant bypass flow conditions and "optimal" gas liquefaction conditions based on Equations 8.6 and 8.7 are summarized in Table 8.1. The cold buffer exit temperatures and bypass flow rates are shown with greater accuracy than the measurement accuracy for process state calculation purposes only.

Table 8.1 Bypass GM cycle operation flow states and corresponding optimal liquefaction states of deuterium and neon.

Flow Case	Bypass GM Cycle Operation		Optimal Liquefaction Condition	
	Cold Buffer Exit Temperature [K]	Bypass Mass Flow [g/s He]	Deuterium	Neon
1	36.767	0.0129	T_{sat} = 38.29 K P_{sat} = 1.6613 MPa	T_{sat} = 44.405 K P_{sat} = 2.6493 MPa
2	33.901	0.0274	T_{sat} = 38.19 K P_{sat} = 1.6479 MPa	T_{sat} = 44.320 K P_{sat} = 2.6210 MPa
3	35.837	0.0437	T_{sat} = 38.262 K P_{sat} = 1.6580 MPa	T_{sat} = 44.380 K P_{sat} = 2.6410 MPa
4	43.409	0.0739		T_{sat} = 44.4916 K P_{sat} = 2.67862 MPa

The potential liquefaction yields for the Bypass GM cycle and the Standard GM cycle are presented in Table 8.2 for deuterium and in Table 8.3 for neon for each viable flow case of Table 8.1. The yield for the Bypass GM cycle has two entries to reflect the calculated yields based on each of Equations 8.6 and 8.7, with any differences between the two entries due to round off error and process gas thermal property accuracy. The yield for the Standard GM cycle has a single entry based on the interpolated cooling capacity at the selected saturation temperature. Again, the Bypass GM apparatus operation data are shown with greater than measured accuracy to demonstrate the analysis procedure.

For the selected optimal deuterium liquefaction conditions, in all cases the Standard GM cycle provides a greater yield than the Bypass GM cycle. For flow case 3, where the majority of the cooling requirement is sensible cooling, the yields are almost equal for the two cycles, with the Bypass GM cycle having approximately 98% of the yield of the Standard GM cycle. Interpolating the Bypass GM cycle and Standard GM cycle cooling curves to the critical point of deuterium suggests that the Bypass GM cycle could achieve at best about 18.3% greater liquefaction by matching the sensible cooling demand to the available cooling with the latent cooling requirement eliminated.

Table 8.2 Comparison of deuterium liquefaction yields under Bypass GM cycle and Standard GM cycle operation.

Deuterium		Gas Cooling Requirements	Bypass Capacity		Cold Head Capacity @ T_{sat}	
Flow Case	Load Category	Enthalpy [J/g]	Cooling Load [W]	Yield [g/s]	Cooling Load [W]	Yield [g/s]
1	Latent	11.785	0.1019	0.00865	61.582	0.03007
	Sensible	2034.385	17.5147	0.00861		
2	Latent	32.792	0.6107	0.01862	61.244	0.02990
	Sensible	2021.149	37.2790	0.01844		
3	Latent	18.458	0.5510	0.02985	61.487	0.03002
	Sensible	2029.697	59.4801	0.02930		

Table 8.3 Comparison of neon liquefaction yields under Bypass GM cycle and Standard GM cycle operation.

Neon		Gas Cooling Requirements	Bypass Capacity		Cold Head Capacity @ T_{sat}	
Flow Case	Load Category	Enthalpy [J/g]	Cooling Load [W]	Yield [g/s]	Cooling Load [W]	Yield [g/s]
1	Latent	9.098	0.5112	0.05618	80.893	0.25722
	Sensible	305.396	17.1054	0.05601		
2	Latent	12.406	1.4836	0.11959	80.659	0.25520
	Sensible	303.663	36.4062	0.11989		
3	Latent	10.216	1.9413	0.19004	80.824	0.25656
	Sensible	304.812	58.0898	0.19058		
4	Latent	1.307	0.4161	0.31840	81.131	0.26113
	Sensible	309.384	98.2176	0.31746		

For the selected optimal neon liquefaction conditions, only flow case 4 provides a higher yield for the Bypass GM cycle than the Standard GM cycle. In this case, almost the entire cooling requirement is sensible cooling, allowing the Bypass GM cycle to provide approximately 22% greater yield than the

Standard GM cycle. Interpolating the Bypass GM cycle and Standard GM cycle cooling curves to the critical point of neon suggests that the Bypass GM cycle could achieve at best about 24.4% greater liquefaction by matching the sensible cooling demand to the available cooling with the latent cooling requirement eliminated.

8.4.2 Liquefaction Yield for the Combined GM Cycle

While the Bypass GM cycle was somewhat restricted in the gases that could be liquefied by the temperature of the cold buffer exit being above that of the cold head, this is not true of the Combined GM cycle. An examination of the cooling curve for the Combined GM cycle reveals that it is possible to liquify some quantity of process gas having a saturation temperature above the minimum cold head temperature of 23.2 K. At this temperature, the only cryogenic gas that cannot be liquefied is helium (and the liquefaction ranges of normal and parahydrogen as well as deuterium, are restricted.).

Table 8.4 lists the Combined GM cycle operation data and the corresponding "optimal" liquefaction conditions selected by the available saturation temperatures. This "optimal" condition is in contrast to the Bypass GM cycle data where the optimum was based on balancing sensible and latent cooling loads. Empty boxes in the table indicate that the gas cannot be liquefied at that saturation temperature because the temperature is above the critical point of the gas (parahydrogen, normal hydrogen, deuterium, and neon), or below the triple point of the gas (oxygen, fluorine, nitrogen, and carbon monoxide). The saturation pressure superscript notation for oxygen and fluorine indicates the number of zeros between the decimal and the significant digits.

Table 8.4 Combined GM cycle operation flow states and corresponding optimal liquefaction states of various gases.

Flow Case	Combined GM Cycle Operation				Optimal Liquefaction Condition, P_{sat} [MPa]							
	T_{sat} and Cold Head Temperature [K]	Cold Head Load [W]	Cold Buffer Exit Temperature [K]	Bypass Mass Flow [g/s He]	p-Hydrogen	n-Hydrogen	Deuterium	Neon	Oxygen	Fluorine	Nitrogen	Carbon Monoxide
1	30.984	25	40.538	0.0135	0.9591	0.9439	0.5707	0.2822				
2	36.960	25	42.860	0.0467			1.4302	0.9094				
3	38.188	50	47.428	0.0143			1.6476	1.1095				
4	42.388	20	47.645	0.0722				2.0396				
5	45.597	75	55.315	0.0152								
6	45.729	50	51.792	0.0490								
7	53.532	40	59.040	0.0738								
8	59.532	75	64.856	0.0506					0.0[illegible]644	0.0[illegible]132		
9	75.757	70	81.331	0.0652					0.0164	0.0303	0.0836	0.0489

For the Combined GM cycle, the process gas is cooled by the bypass gas flow in the bypass heat exchanger. Depending on the bypass heat exchanger effectiveness, and the relative capacity rates of the bypass and process gas, at best the process gas can be cooled to the cold buffer exit temperature. For the gases listed in Table 8.4, the liquefaction temperature is below the cold buffer exit temperature, so the cold head load includes both the latent heat of condensation as well as the sensible cooling from the bypass heat exchanger process stream exit temperature to the saturation temperature. When the bypass heat exchanger has an effectiveness of unity, and the process stream represents the minimum capacity rate, then the process stream will reach the cold buffer exit temperature. For a bypass heat exchanger effectiveness less than unity, or if the bypass stream has the lower capacity rate, then the process stream exit temperature will be above the cold buffer exit temperature.

The Combined GM cycle liquefaction yield for each of the gases in Table 8.4 can be calculated as a function of the bypass heat exchanger effectiveness. The liquefaction yield for deuterium for flow case 2 is presented in Figure 8.11. This curve has several interesting features.

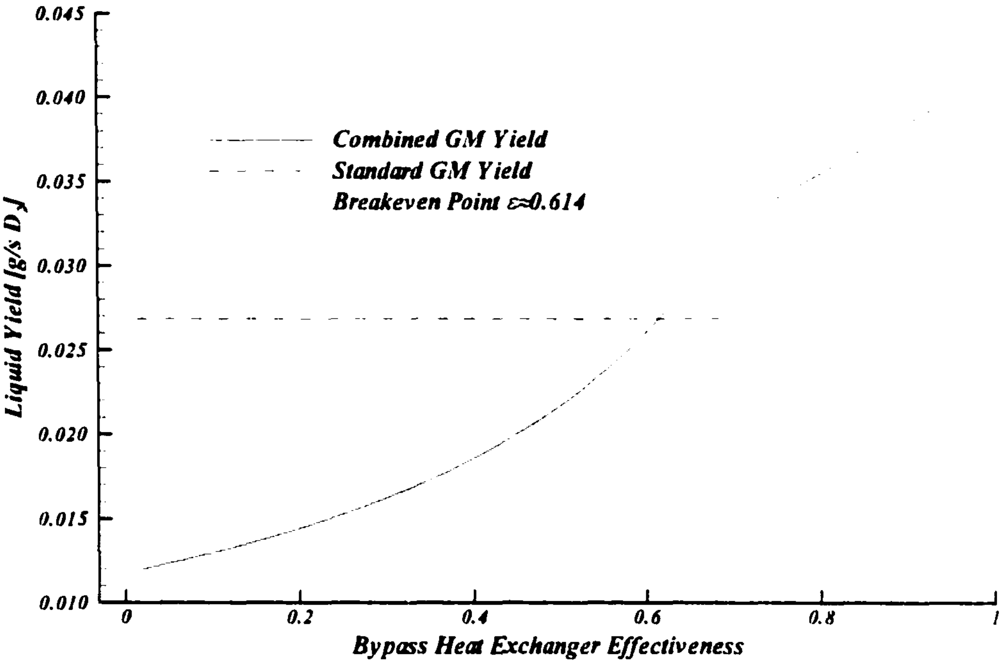

Figure 8.11 Interpolated Standard GM cycle and Combined GM cycle deuterium liquefaction yields for the conditions of flow case 2 as a function of bypass heat exchanger effectiveness.

First, the yield for the Standard GM cycle is independent of the bypass heat exchanger effectiveness, since in that configuration the bypass heat exchanger is not used. Therefore, as long as a bypass heat exchanger having an effectiveness $\varepsilon \geq 0.614$ is used, the Combined GM cycle will produce a greater yield than the Standard GM cycle.

Second, if the bypass heat exchanger effectiveness is unity, the Combined GM cycle has a deuterium yield of approximately 0.0413 g/s, compared to the Standard GM cycle yield of 0.0269 g/s. For this operation point, the Combined GM cycle could potentially give a 54% greater yield than the Standard GM cycle.

Third, the Combined GM cycle yield curve has a "knee" at an effectiveness of approximately $\varepsilon = 0.697$. Above the knee, the yield is limited by the cooling capacity of the bypass stream. That is, for the selected saturation temperature, the ratio of available cold head to bypass cooling capacity exceeds the ratio of the "latent" to sensible cooling requirements of the process stream. Here, "latent" includes some sensible cooling to bridge the temperature gap between the bypass heat exchanger process gas exit temperature and the saturation temperature. Algebraically, in the notation developed previously, this is,

$$\frac{\dot{Q}_{CH}}{\dot{Q}_B} > \frac{\left[\dot{m}\left(h_g\big|_{(T_{h_2},P_{sat})} - h_f\big|_{(T_{sat},P_{sat})}\right)\right]_P}{\left[\dot{m}\left(h_g\big|_{(T_H,P_{sat})} - h_g\big|_{(T_{h_2},P_{sat})}\right)\right]_P} \tag{8.8}$$

Above the knee, the yield could be further increased by rebalancing the ratio of cold head cooling capacity to bypass cooling capacity to better reflect the requirements of the process stream. Ideally, the knee would occur at an effectiveness of exactly unity, if the operating or gas conditions would permit. Reducing the cold head capacity while keeping the bypass capacity constant would tend to shift the curve to the right, reducing the yield. Increasing the bypass capacity while keeping the cold head capacity constant will move the knee to the right and up, increasing the yield. Together, the net effect is to increase the yield when the cooling capacities are properly balanced.

Generally, from a given operation point, increasing the bypass flow increases the sensible cooling component but also raises the cold head temperature. The cold head temperature can be lowered, and the relative proportion of sensible cooling further increased by reducing the cold head load. Flow cases 5 and 6, just above a temperature convenient for liquefaction of neon, demonstrate the potential for load balancing. Both cases have approximately the same cold head temperature, but have vastly different cold head to bypass cooling load ratios of 3.88 and 0.79, respectively.

Below the knee, the yield is limited by the ability of the bypass heat exchanger to transfer the heat from the process stream to the bypass stream. The bypass heat exchanger provides some precooling of the process stream towards the liquefaction temperature of the cold head, but a large percentage of the available cooling capacity of the bypass stream is unused. For this flow case for deuterium, at the knee, just over 30% of the bypass stream cooling capacity is unused while at the breakeven point indicated in Figure 8.11, over 50% is unused.

If the Combined GM cycle liquefaction yield as a function of bypass heat exchanger effectiveness is divided by the constant value of the Standard GM cycle liquefaction yield for the given saturation temperature, the result is a normalized yield ratio curve having the same shape as the Combined GM cycle yield curve. This procedure allows the various gases and liquefaction conditions listed in Table 8.4 to be charted together without loss of resolution and detail that would occur if presented using the large range of absolute liquefaction rates.

Figure 8.12 presents the ratio of Combined GM cycle liquefaction yield to Standard GM cycle liquefaction yield as a function of bypass heat exchanger effectiveness for the gases parahydrogen, normal hydrogen, deuterium, and neon for flow cases 1 to 4. Figure 8.13 presents the yield ratio for the gases oxygen, fluorine, nitrogen, and carbon monoxide for flow cases 8 and 9. The curves are presented in separate figures for clarity considering the large number of curves to be displayed.

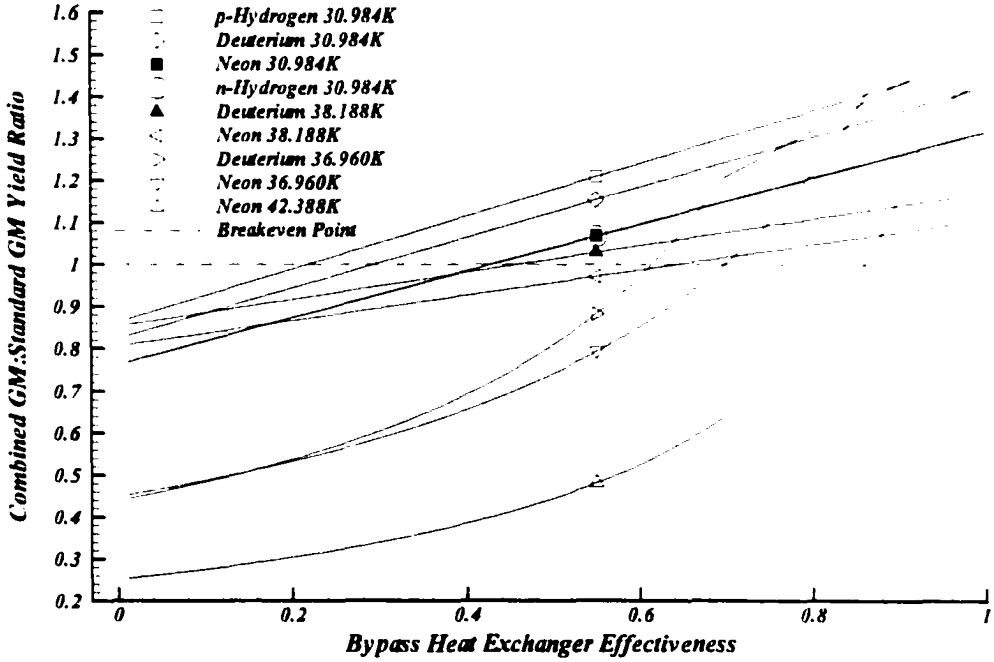

Figure 8.12 Ratio of Combined GM cycle liquefaction yield to Standard GM cycle liquefaction yield for flow cases 1 through 4.

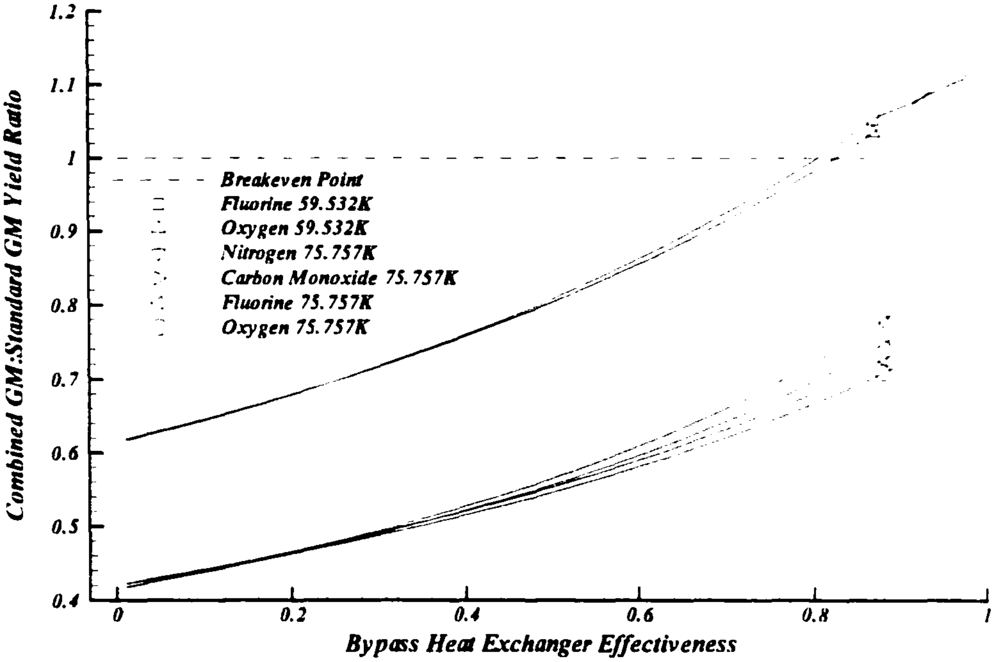

Figure 8.13 Ratio of Combined GM cycle liquefaction yield to Standard GM cycle liquefaction yield for flow cases 8 and 9.

For each of the gases and saturation temperatures presented in Figure 8.12, the yield ratio exceeds a value of 1 for some minimum value of bypass heat exchanger effectiveness, indicating the Combined GM cycle's capacity to liquefy a greater quantity of process gas than the Standard GM cycle. Not all curves exhibit the "knee" previously described, which is due to the particular cycle operation and gas liquefaction conditions for the gases considered. For those curves without a knee, the liquefaction rate is limited by the available bypass gas flow rate and would benefit by a rebalancing of the bypass and cold head cooling capacities.

For parahydrogen at a saturation temperature of 30.984 K, a bypass heat exchanger effectiveness of only $\varepsilon \geq 0.22$ will allow a greater yield from the Combined GM cycle than the Standard GM cycle. This is a very low value for effectiveness and would correspondingly be a relatively inexpensive heat exchanger.

For each of the gases with a saturation temperature of 59.532 K presented in Figure 8.13, the yield ratio exceeds a value of 1 for some minimum value of bypass heat exchanger effectiveness. For each of the gases with a saturation temperature of 75.757 K, no value of heat exchanger effectiveness provides a greater yield for the Combined GM cycle than the Standard GM cycle.

There are at least three possible reasons why the Combined GM cycle liquefaction capacity is below that of the Standard GM cycle for the saturation temperature of 75.757 K. First, the cooling capacity of the Combined GM cycle is known from the measured operation data of the Bypass apparatus, whereas the Standard GM cycle cooling capacity is extrapolated from the cold head load cooling curve. It may be that the Standard GM cycle would also exhibit a relative decline in cooling capacity at 75.757 K, as is evident in the Combined GM cycle, which is not accounted for in the extrapolated cooling capacity. Second, the Combined GM cycle could be operating beyond its useful range of bypass cooling capacity. There is a sharp decline in the rate at which cooling capacity increases with increasing bypass flow near the selected operation point. Third, the ratio of absolute yield of these two operation points for the Combined GM cycle and Standard GM cycle might not be a fair basis of comparison, in that the cooling capacity per unit power input might be substantially different.

8.4.3 Cycle Input Power

The input power required to operate the Bypass GM apparatus consists of the helium gas compressor power and regenerator displacer motor power. The compressor power is a function of the compression ratio, the mass flow rate, and the compressor efficiency. It is assumed that the displacer motor power is negligible compared to the compressor power.

No direct power measurements were made of the Bypass apparatus compressor, but an idea of the ideal input power required for the various operation points can be obtained by assuming that the compressor is isothermal and that the helium behaves as an ideal gas. For an ideal gas in an isothermal compressor, the work required to compress a unit mass of gas is given by:

$$W = P_1 \upsilon_1 \ln\left(\frac{P_2}{P_1}\right) \tag{8.9}$$

where P_1 is the initial pressure, υ_1 is the initial specific volume, and P_2 is the final pressure. The ideal compressor input power for the Bypass apparatus is then:

$$\dot{W} = \dot{m}_R P_R \upsilon_R \ln\left(\frac{P_B}{P_R}\right) \tag{8.10}$$

where the subscript R refers to the compressor return line, the subscript B refers to the bypass pressure and to a close approximation the supply pressure, and $\dot{m}$ is the mass flow rate through the compressor.

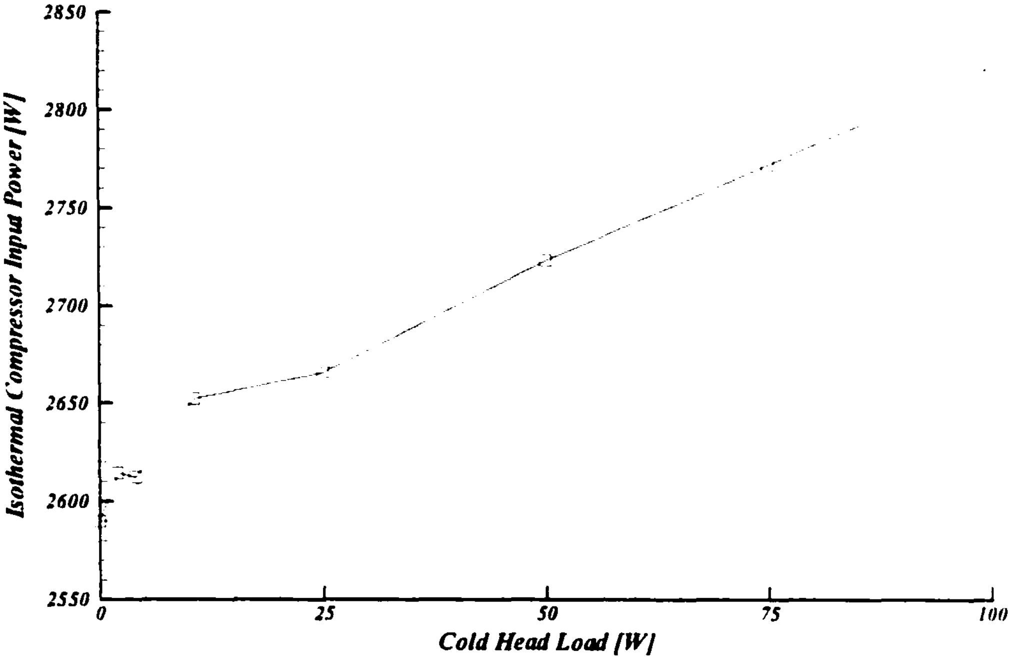

Figure 8.14 Isothermal compressor input power as a function of cold head load for the Standard GM cycle operation.

The isothermal compressor input power as a function of cold head load for the Standard GM cycle operation is presented in Figure 8.14. The input power is nearly a linear function of the cold head load, particularly at the higher loads. Extrapolating the Standard GM cycle input power for the extrapolated cold head load for the saturation temperature of 75.757 K of flow case 9 gives an input power of approximately 2956 W. Direct evaluation of the input power for the Combined GM cycle operation for flow case 9 gives a significantly lower input power of approximately 2186 W. Similarly, flow case 8 gives an input power of 2867 W and 2584 W for the Standard GM cycle and Combined GM cycle operation, respectively.

8.4.4 Effect on Yield of Equalizing Input Power

Figure 8.15 shows the Combined GM cycle to Standard GM cycle yield ratio after scaling the Combined GM cycle yield to reflect an equal compressor input power. After scaling, the Combined GM cycle yield exceeds the Standard GM cycle yield for some value of bypass heat exchanger effectiveness for all gases for flow cases 8 and 9. In all flow cases of Table 8.4, the directly calculated compressor input power of the Combined GM cycle is less than the interpolated (or extrapolated) compressor input power for the Standard GM cycle operating at the given saturation temperature, with the difference between the two increasing as the saturation temperature increases.

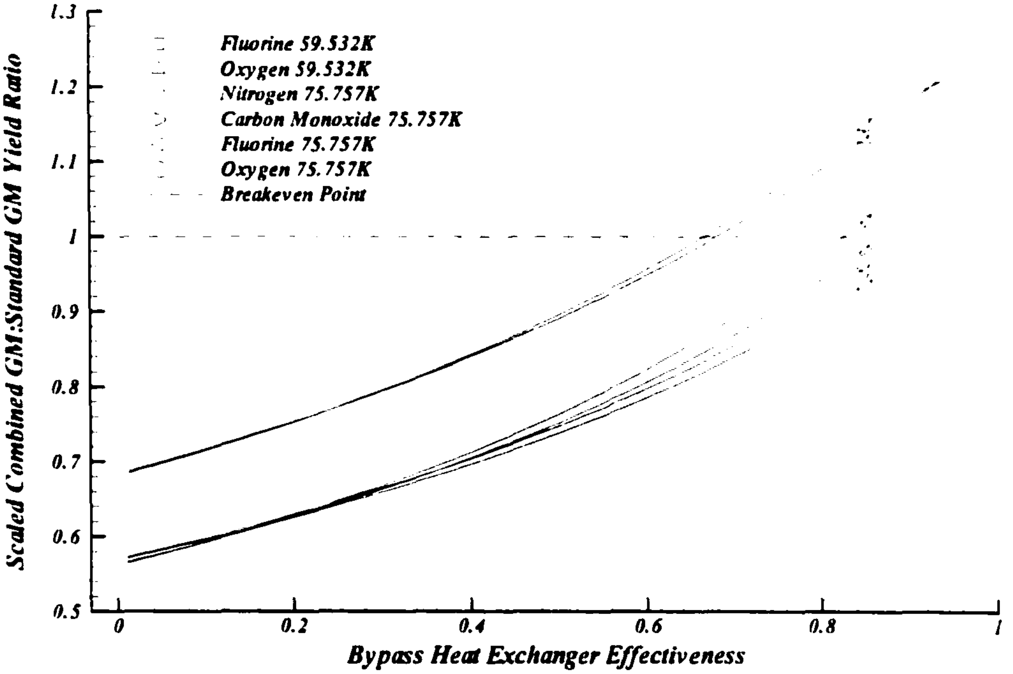

Figure 8.15 Ratio of Combined GM cycle liquefaction yield to Standard GM cycle liquefaction yield for flow cases 8 and 9 after scaling for equal ideal compressor input power.

8.5 Effect of Bypass Flow on the GM Cycle

8.5.1 Experiment 6:

Investigation of the Pressure-Volume Diagrams for the Bypass Apparatus

Plotting the pressure-volume (PV) diagram for a GM cycle gives insight into the performance of the device. For an ideal GM cycle, the PV diagram is rectangular, as shown previously in Figure 2.3 in Chapter 2. Practical limitations of the mechanical components change the shape of the PV diagram and reduce the maximum possible work.

The most significant mechanical limitations of the Bypass GM apparatus and their effects on the PV diagram of its cycle can be listed. First, the charge and discharge of the cycle gas takes a finite time, and occurs through valves with a non-zero pressure drop. This tends to constrict the pressure excursions of the cold head cylinder below the maximum and above the minimum pressures of the compressor supply and return lines. As the pressure drop through the valves increases, and as the time that the valves are open decreases, the degree of constriction of the pressure excursions increases. This effect in and of itself would not necessarily lead to a non-rectangular shape of the PV diagram (if infinite time to charge and discharge were allowed), but will when considered with the displacer/regenerator limitations.

A second limitation is imposed by the displacer/regenerator which is usually driven with a harmonic motion to limit forces exerted on the drive mechanisms and to limit mechanical noise. The harmonic motion does not leave sufficient time for fully charging and discharging the cycle gas at the limits of the displacer/regenerator motion. As a result, the valve timing is typically set advanced so that the cold head cylinder is charging or discharging while the cold head expansion space is not yet at its minimum or maximum, respectively. This tends to rotate the rectangular PV diagram counter-clockwise, and decrease the average maximum pressure and increase the average minimum pressure.

A third limitation is the pressure drop through the regenerator. Sudden pressure swings are damped as the resulting mass flow accelerates and begins moving through the regenerator. This effect, combined with the above two effects, tends to round out the sharp corners and straight lines of the theoretical diagram.

In this study, it was of interest to see if the Bypass GM cycle PV diagram was significantly different from the Standard GM cycle diagram, either in shape or pressure excursion, or some other unexpected manner.

8.5.2 Pressure Transducer

The piezoelectric pressure transducer mounted in the cold head expansion space provided a charge output that was proportional to pressure. The charge output was amplified with a custom high impedance charge amplifier circuit given in Figure D.1 in Appendix D. Together, the pressure transducer and the charge amplifier circuit make up the cold head pressure sensor. The output from the charge amplifier is linear with charge input to the circuit; however, the output from the pressure transducer is temperature dependent.

Three indirect techniques were employed to calibrate the cold head pressure sensor given time and fiscal restraints for a direct calibration. First, PV diagrams and system operation values (temperatures, pressures, mass flows, etc.) were recorded each minute during initial cooldown of the Bypass GM apparatus. In this mode, the pressure of the cold buffer volume, which was recorded by the silicon bridge diaphragm transducer at room temperature, was very nearly the maximum pressure of the cold head expansion space. Slight discrepancies exist because the check valve separating these spaces had a finite cracking pressure and very small, temperature dependent reverse flow leak. Both effects tend to reduce the cold buffer volume pressure to a value below the maximum pressure of the cold head; however, the small reverse flow of the check valve allowed the cold buffer volume pressure to be reduced without bypass gas flow as the maximum pressure in the cold head decreased.

The minimum pressure of the expansion space was assumed to be the pressure of the compressor return line, which, considering its measurement location, was slightly lower than the minimum pressure of the expansion space. It is assumed that both the high pressure and low pressure measurements are in error by the same amount, and that if not, the net error is small relative to the pressure excursion of the cold head expansion space.

The pressure difference between the cold buffer volume and the compressor return line was calculated for each PV diagram recording, and denoted ΔP_{CH}. The peak-to-peak pressure sensor voltage was calculated for each recording and denoted ΔV_S. To determine the net scaled response, S_p, of the cold head pressure sensor, the ratio of ΔV_S to ΔP_{CH} was taken as a function of the cold head temperature. The response is nearly constant from 300 K to 80 K, then drops off rapidly with decreasing temperature. Figure 8.16 gives the pressure sensor response S_p as a function of cold head temperature.

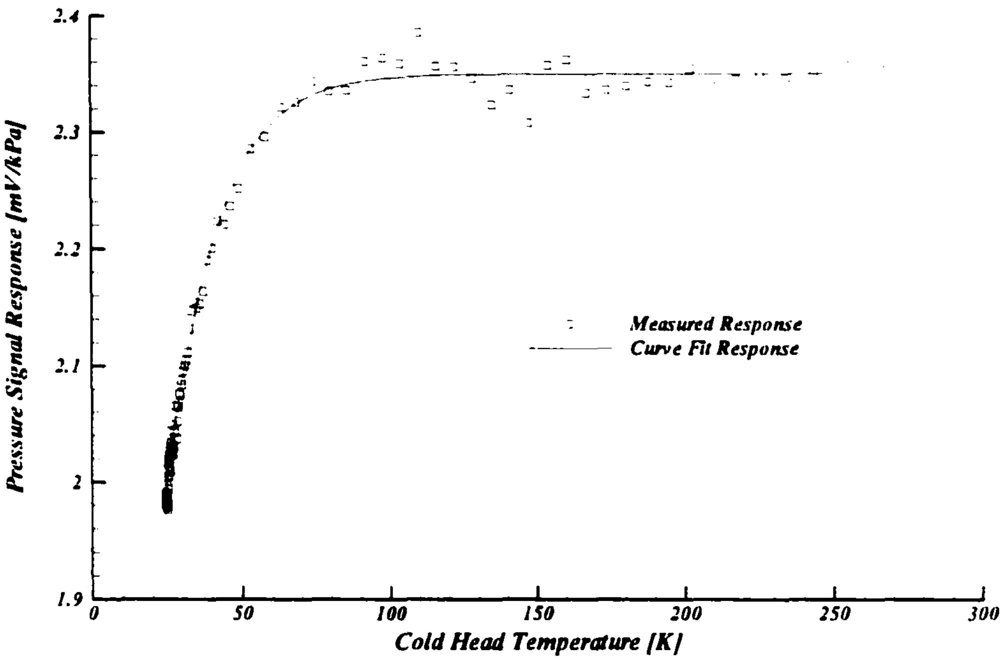

Figure 8.16 Measured and curve fit cold head pressure sensor response as a function of cold head temperature.

The response can be fit to a curve given by:

$$S_p = a + \frac{b}{T_{CH}} + \frac{c}{T_{CH}^2} + \frac{d}{T_{CH}^3} + \frac{e}{T_{CH}^4} + \frac{f}{T_{CH}^5} \tag{8.11}$$

where S_p is the change in output voltage of the cold head pressure sensor for a unit change in cold head pressure in units of mV/kPa, T_{CH} is the temperature of the cold head in Kelvin, and a, b, c, d, e, and f are the coefficients listed in Table 8.5.

Table 8.5 Coefficients for temperature dependent cold head piezoelectric pressure sensor voltage response to changes in pressure in units of mV/kPa.

Coefficient	Value
a	$2.3657210093 \times 10^{0}$
b	$-8.3861893241 \times 10^{0}$
c	$1.5970975655 \times 10^{3}$
d	$-1.2510152270 \times 10^{5}$
e	$3.3137802035 \times 10^{6}$
f	$-2.9920735698 \times 10^{7}$

The second technique to determine the pressure sensor response was almost identical to the first technique, differing only in the data used to determine the response. In the first technique, the PV diagram data was obtained during transient operation of the GM, so it was postulated that the cold buffer volume pressure might not be representative of the maximum cold head pressure, due to the vagaries of the leak rate of the check valve. In the second technique, the PV diagram data was taken from the data recorded at steady-state operation points.

The predicted curve fit response of the cold head pressure sensor based on the cold head temperature of the steady-state points is within 2% of the measured response. In the range of approximately 30 to 60 K, the curve fit tends to overestimate the response, suggesting that the curve fit based on the transient cooldown data does have an error associated with the maximum cold head pressure decreasing faster than the average cold buffer pressure. Below 30 K, the curve fit tends to underestimate the response by up to 2%.

The third technique to determine the pressure sensor response was to compare the pressure sensor response with and without the warm buffer volume make-up gas for conditions at steady-state. When the warm buffer volume gas was added, the system pressure rose. It was assumed that the change in system pressures would correspond to a proportionate change in cold head pressures. Any pressure losses in the charge and discharge valves would only be very slightly affected, since the mass flow into and out of the cold head is only modestly changed, so any error from this source would tend to cancel out between the two sets of readings with and without make-up gas. If the error due to the valve losses was significant, this third technique should predict a sensor response substantially different from the previous two techniques, especially at the lowest temperatures where the mass flow through the valves is largest.

In this calibration technique, the response was calculated as the ratio of the change in peak-to-peak voltage to the change in pressure differential. That is, the response was calculated as:

$$S_P = \frac{\Delta V_{S_1} - \Delta V_{S_2}}{\Delta P_{CH_1} - \Delta P_{CH_2}} \tag{8.12}$$

where the subscripts 1 and 2 refer to the condition before and after the addition of make-up gas, respectively and voltage and pressure notations are as previously described. Make-up gas was added when the cold head reached its minimum temperature during two separate test runs for which PV data was recorded. The pertinent data are presented in Table 8.6. The net response from the combination of the separate responses is consistent with the previous two techniques employed to determine sensor response. Taking the average value of S_P from the curve fit of Equation 8.11 for states 1 and 2 and comparing that to the combined value of S_P, suggests that the curve fit underestimates the pressure sensor response by 1.3% and 4.4% for cases 1 and 2, respectively, for these temperatures.

Table 8.6 Cold head pressure sensor calibration data from the addition of warm buffer make-up gas to the compressor system.

Case	State	T_{CH} [K]	ΔV_S [mV]	ΔP_{CH} [kPa]	$S_P = \frac{\Delta V_S}{\Delta P_{CH}}$ [mV/kPa]	Curve Fit S_P [mV/kPa]
1	1	24.3	2494.81	1237.734	2.0156	1.9807
	2	24.1	2805.32	1392.761	2.0142	1.9730
	Combined		310.51	155.027	2.0029	
2	1	23.6	2486.42	1272.703	1.9537	1.9576
	2	23.8	2848.97	1449.504	1.9655	1.9629
	Combined		362.55	176.801	2.0506	

The close agreement amongst the three techniques suggests that the curve fit sensor response is a reasonable approximation to a directly calibrated sensor response. For this reason, all PV diagrams have been scaled according to this curve. The pressure sensor voltage output has been converted to a pressure output according to:

$$P_{CH} = P_B + \frac{V_S - V_{S_{MAX}}}{S_P} \tag{8.13}$$

where $V_{S_{MAX}}$ is the maximum voltage from the pressure sensor and S_P is calculated from Equation 8.11 at the temperature of the cold head. This scales the maximum pressure in the cold head to the pressure of the cold buffer volume. The minimum pressure in the cold head is determined by the recorded sensor voltage and the curve fit calibration scaling for the cold head temperature, and the compressor return line pressure is ignored. In some cases this leads to a calculated cold head pressure slightly below the return line pressure, which is physically unlikely. In all cases the discrepancy in minimum pressure is small relative to the overall pressure levels.

8.5.3 Initial Cooldown

During the initial cooldown, with the bypass metering valve closed, PV diagrams were recorded once per minute. From a cold head temperature of 300 K down to 100 K, the PV diagrams are substantially unchanged. Below 100 K, as the maximum system pressure begins to drop due to increasing average gas density in the system, the rate at which the cold head increases to its maximum value and decreases to its minimum value declines. Figure 8.17 shows four sample PV diagrams recorded during the initial cooldown, with the cold head temperature noted for each diagram. Note that the changes in maximum pressure are approximately equal for these selected diagrams, yet the changes in cold head temperature are quite unequal.

With decreasing system pressure, the cold head reaches its pressure extrema earlier in its cycle. Figure 8.18 shows the temperature dependent phase shift of the maximum and minimum cold head pressures relative to the extrema of the first recorded PV diagram at a cold head temperature of 282 K. The relative phase shift is given in degrees, with a complete PV cycle taking 360 degrees.

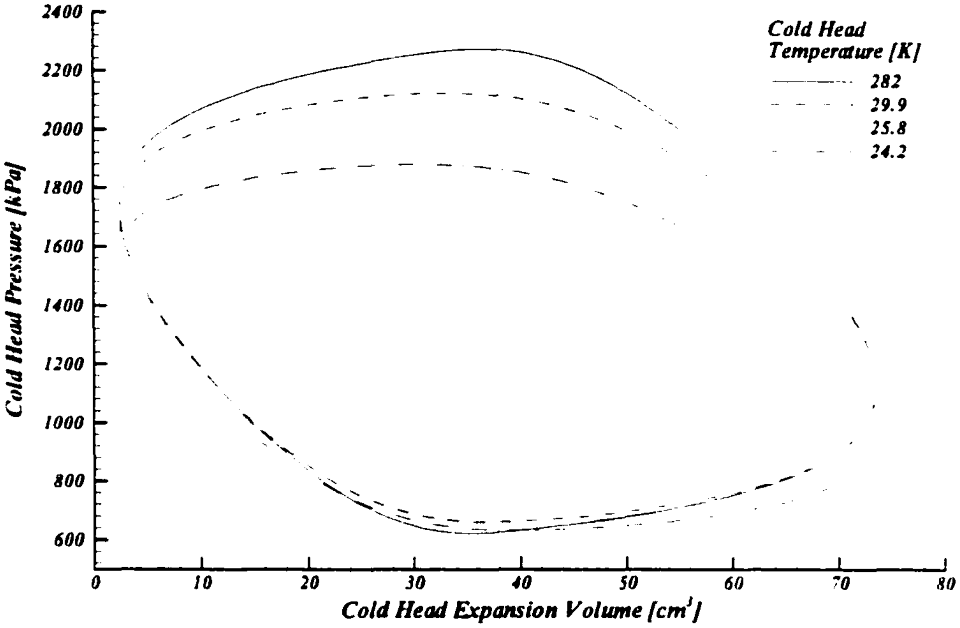

Figure 8.17 Cold head expansion space pressure-volume diagrams recorded during initial cooldown of the Bypass GM apparatus.

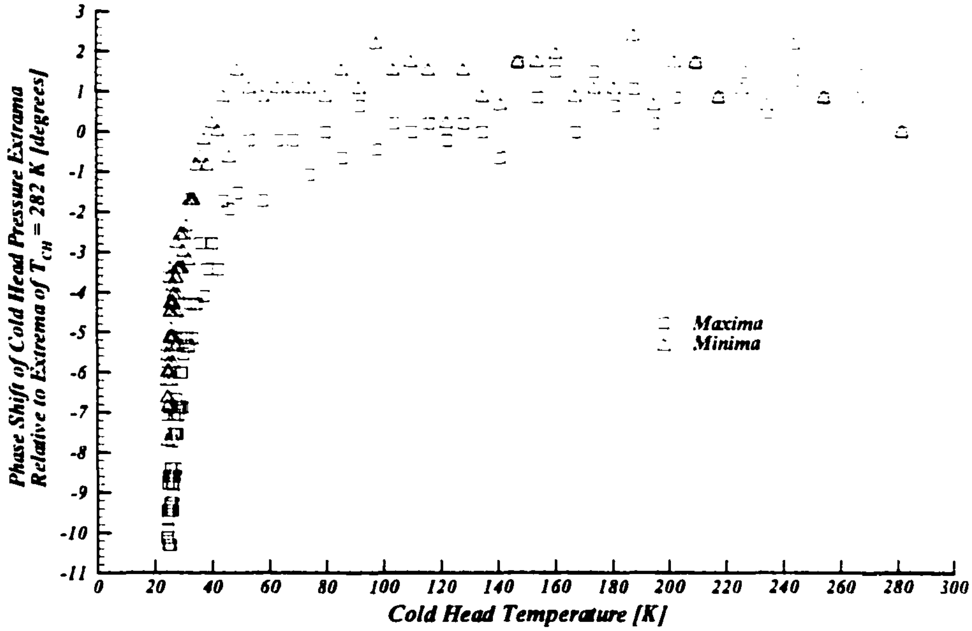

Figure 8.18 Temperature dependent phase shift of cold head pressure extrema relative to pressure extrema of PV diagram recorded at 282 K during initial cooldown.

The area enclosed within the PV diagram represents the work done by the gas on the displacer. For an ideal gas and adiabatic conditions, the area is equal to the change in enthalpy of the gas and represents the net available refrigeration per cycle [26]. The work per cycle multiplied by the operation frequency yields the work rate. Because the basic shape of the PV diagram is not substantially changed during cooldown, the PV work rate is strongly correlated to the cold head pressure swing, ΔP_{CH}.

Figure 8.19 shows the PV work rate, $\dot{W}_{PV}$, and cold head pressure swing, ΔP_{CH}, as a function of elapsed time during initial cooldown. In this figure, the numerical range of $\dot{W}_{PV}$ and ΔP_{CH} differing by exactly a factor of 10 is a purely coincidental artifact of the units selected. A comparison of this figure with Figure 8.1 suggests that the decreased pressure swing may have a strong influence on the cooldown rate of the cold head, in addition to the mass flow effect previously noted. Both curves exhibit "knees" at an elapsed time of approximately 30 minutes.

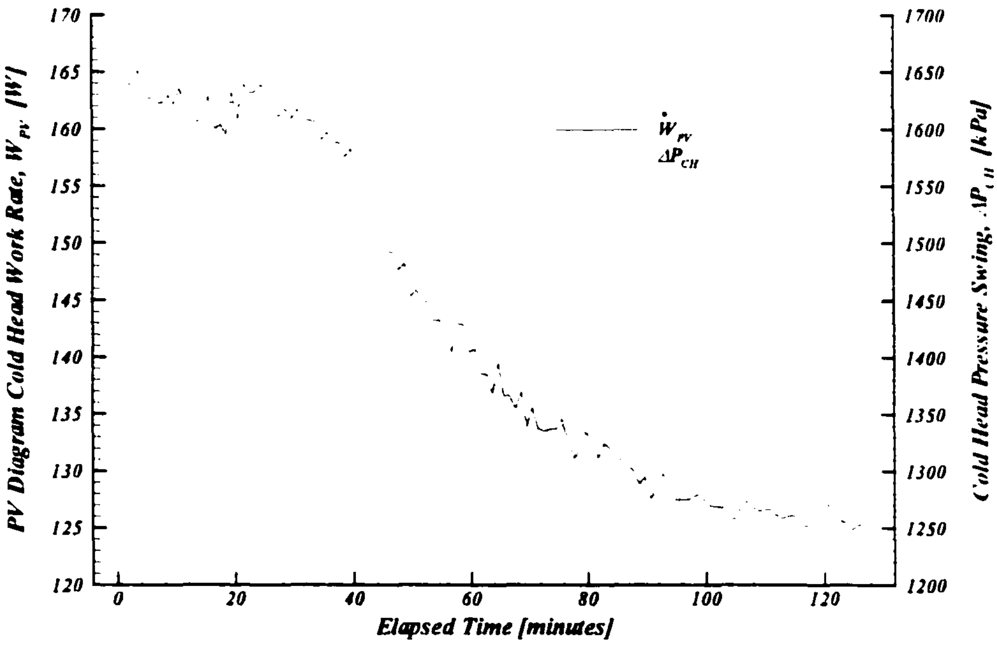

Figure 8.19 PV diagram cold head work rate and cold head pressure swing as a function of elapsed time during initial cooldown.

8.5.4 Warm Buffer Volume Plus Make-up Gas

Both Figure 8.3 and Figure 8.6 showing cold head temperature as a function of applied cooling load, either cold head load or bypass load respectively, show generally increased cooling capacity for a given cold head temperature with the warm buffer volume open and its make-up gas added to the system. In the first case of applied cold head load only, at loads below approximately 10 W, the warm buffer volume and make-up gas do not improve the cooling capacity, but rather decrease it slightly. For the second case of bypass cooling load only, at loads below approximately 40 K, performance curves with and without the warm buffer and make-up gas are almost indistinguishable.

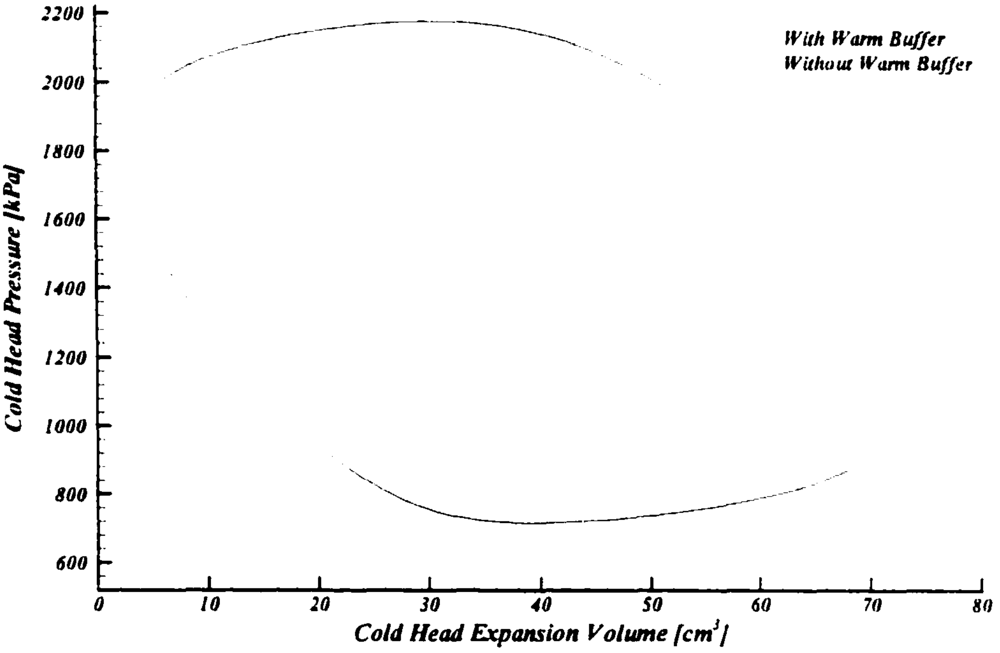

Figure 8.20 Comparison of the PV diagrams at a minimum no-load temperature of 23.6 K with and without the use of the warm buffer volume and make-up gas.

Figure 8.20 shows the PV diagrams for zero applied load with zero bypass mass flow with and without use of the warm buffer volume and make-up gas. For both cases, the cold head temperature is at steady-state at 23.6 K. The maximum and minimum cold head pressures increase as a result of the addition of the make-up gas thereby increasing the net pressure swing, ΔP_{CH}, by approximately 220 kPa. Interestingly, the ratio of maximum to minimum pressure, PR_{CH}, is virtually unchanged.

increasing from 2.94 without the warm buffer to 2.98 with the warm buffer. The PV work rate is increased significantly from 124.8 W to 145.7 W, an increase of almost 17%.

While the increased PV work rate might suggest that a significantly lower no-load minimum cold head temperature could be achieved, this was not observed. A possible reason for this behaviour is that the net increased PV work rate could be entirely used to offset increased losses in the regenerator due to the increased mass flow through the regenerator at the higher gas pressure and density. As the mass flow increases, the effectiveness of the regenerator decreases, resulting in a higher temperature of the cold head gas before expansion. As the warmer gas then expands, it expands to a slightly higher temperature than did the lower pressure and colder gas without the warm buffer. The expanded gas would then have slightly higher cooling capacity, but at a slightly higher temperature, which when combined with the radiation and other parasitic loads on the cold head (which are basically unchanged) results in no net decrease in the cold head temperature.

8.5.5 Standard GM Cycle versus Combined GM Cycle Operation

Previously it was noted that for a given cold head temperature, operation of the Standard GM cycle had a higher isothermal compressor power requirement than did operation as a Combined GM cycle. This higher compressor input power does not, however, yield an increased PV work rate at the cold head. Operation data for a Standard GM cycle and Combined GM cycle having essentially equal cold head temperatures is summarized in Table 8.7.

Table 8.7 Comparison of operation data for a Standard GM cycle and a Combined GM cycle with approximately the same cold head temperature.

Operation Mode	T_{CH} [K]	P_{MAX} [kPa]	P_{MIN} [kPa]	ΔP_{CH} [kPa]	PR_{CH}	$\dot{Q}_C$ [W]	$\dot{m}_B$ [g/s He]	$\dot{Q}_B$ [W]	$\dot{W}_{PV}$ [W]
Standard	42.3	2088.7	639.3	1449.4	3.27	75	0.0	0.0	146.8
Combined	42.4	2081.4	624.8	1456.6	3.33	20	0.0722	94.7	148.6

The PV diagrams corresponding to the operation points summarized in Table 8.7 are shown in Figure 8.21. Two features of these diagrams are notable. First, the overall shape of the PV diagram is not significantly influenced by the extraction of bypass gas from the cold head expansion space. The bypass flow rate in the Combined GM cycle case cited above is approximately 2.1% of the total GM return line flow rate, and approximately 7% of the flow that could charge and discharge from the cold head pressure swing in a volume equal to the maximum cold head expansion space at constant temperature of the bypass temperature. Second, the area enclosed by each diagram, and hence the PV work, is almost identical, but the Combined GM cycle has a slightly larger PV work (and PV work rate) primarily due to a slightly lower minimum pressure.

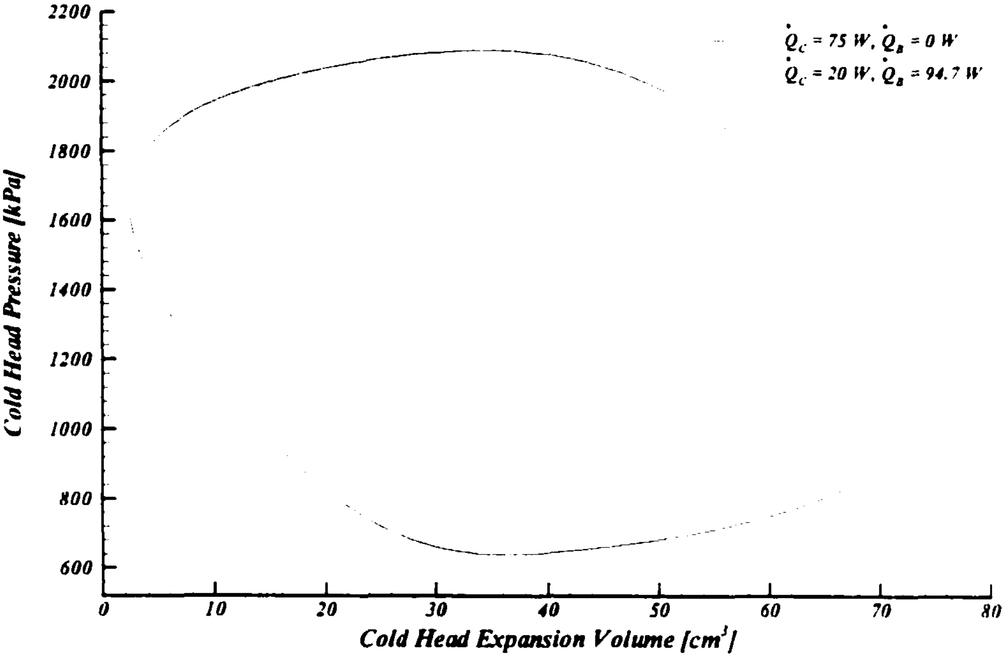

Figure 8.21 Comparison of PV diagrams for a Standard GM cycle and a Bypass GM cycle presented in Table 8.7 having approximately equal cold head temperatures.

8.5.6 Valve Timing

The PV diagrams presented in this work show a significant deviation from the ideal, perfectly rectangular, PV diagram for the GM cycle. The valve timing has a significant influence on the shape of the PV diagram. Using the pressure extrema of the PV diagram as a guide to the valve timing, and taking bottom dead centre as 0 degrees, the high pressure valve opens at approximately 270 degrees and the low pressure valve opens at approximately 85 degrees. Other commercial GM units would likely have different valve timing.

If the action of charging and discharging of the helium gas can be assumed independent of the displacer position, then the PV work rate could be enlarged by changing the valve timing. Consider the PV diagram for the Standard GM cycle operation point presented in Table 8.7. If the displacer motion as a function of time is assumed to remain unchanged, and the cold head pressure as a function of time is assumed to remain unchanged except for a phase shift, then the area enclosed by the PV diagram can be increased. Figure 8.22 shows the resulting PV diagrams for various phase shifts of the pressure function which equally delay the opening of the high and low pressure valves until later in the cycle while keeping constant the duration that the valves are open.

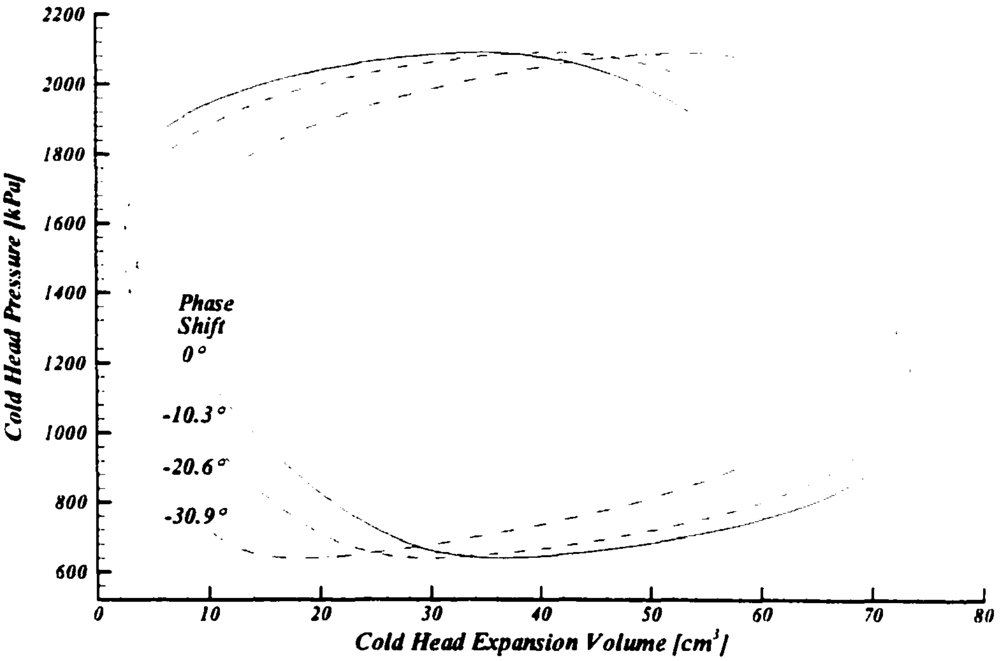

Figure 8.22 Modified PV diagrams for the Standard GM flow case presented in Table 8.7 having theoretical phase shifts of 0, -10.3, -20.6, and -36.9 degrees in valve cycle timing relative to existing timing.

The PV work rate for a phase shift from 0 degrees to -36.9 degrees is presented in Figure 8.23, showing a maximum work rate at a shift of approximately -18.5 degrees. The optimal valve cycle phase shift is a function of cold head temperature, increasing at lower temperatures. The PV work rate as a function of pressure phase shift shows a broad maximum, indicating that a shift of between approximately -15 and -25 degrees would provide close to the expected maximum work rate at all temperatures.

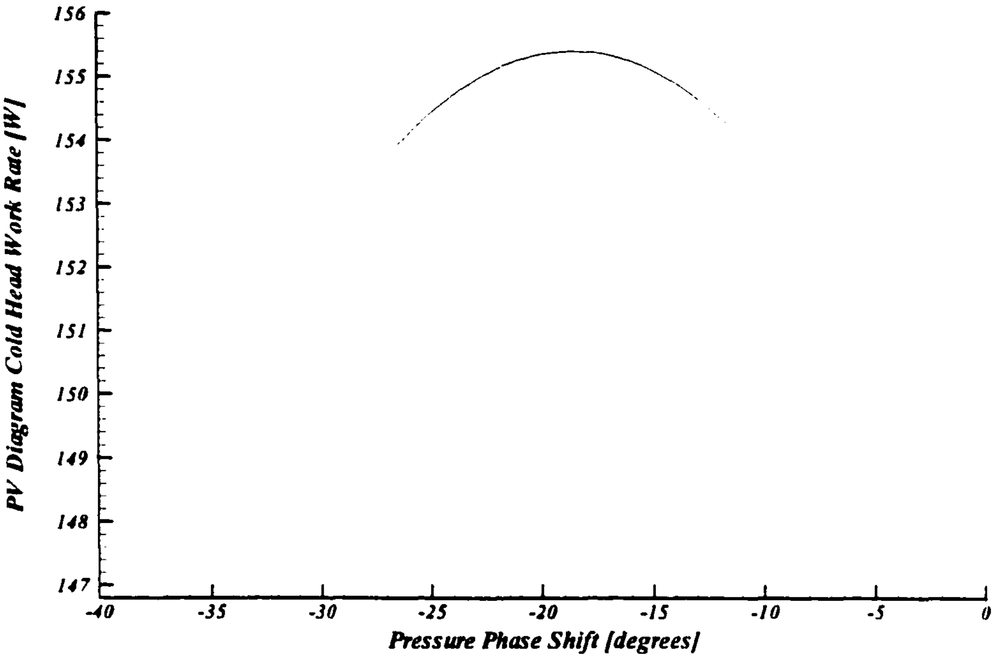

Figure 8.23 Expected Standard GM cycle PV work rate for a phase shift in valve timing from 0° to -36.9° relative to existing timing.

8.6 Summary and Conclusions

A GM cryocooler was modified to operate with an asymmetric and unbalanced regenerator by diverting a stream of gas from the cold head expansion space. Significant sensible cooling loads could be provided by the bypass stream. Using an exchanger exit temperature of 300 K, bypass loads from 0 W to 100 W for a bypass stream cold buffer volume exit temperature of ~25 K to ~40 K resulted in an approximately linear rise in the cold head temperature. Bypass loads beyond 100 W resulted in a rapid rise in cold head temperature, making the practical limit of the bypass load approximately 130 W between ~50 K and 300 K for this apparatus.

When only latent cooling was required, operation as a Standard GM cycle provided the largest equivalent cooling power for the same cold head temperature. Under Standard GM cycle operation, the cold head temperature rose approximately linearly from 0 W at ~24 K to 75 W at ~42 K. The ideal compressor input power is higher for the Standard GM cycle than the Combined GM cycle and the Bypass GM cycle for the same cold head temperature, and the relative advantage of the

Standard GM cycle would likely be reduced, though not eliminated, if a correction was made for equal input power.

Operation as a Combined GM cycle, where a portion of the load is provided as sensible cooling from the bypass gas stream and a portion is provided as latent cooling from a cold head load, is best for applications requiring a combination of sensible and latent cooling, such as liquefaction of gases. For these applications, the Combined GM cycle can provide significantly higher yields, particularly as the sensible heat component increases for gases with lower normal boiling point temperatures. For example, without correction for equal input power, operation of the Bypass GM apparatus as a Standard GM cycle can provide approximately 0.93 litres per hour of liquid deuterium at ~37 K, whereas operation as a Combined GM cycle can provide approximately 1.43 litres per hour. With a correction for equal input power, the Combined GM cycle yield would be further increased relative to the Standard GM cycle. Alternatively, from the perspective of power consumption costs, operation of the Bypass GM apparatus as a Combined GM cycle represents at least a 35% reduction in power required to produce a desired deuterium liquid yield rate at ~37 K compared to the Standard GM cycle.

The pressure-volume plots taken during operation of the Bypass GM apparatus under the various modes of operation revealed that diversion of the bypass gas does not significantly alter the shape of the PV diagram, or the PV work. For a given device, PV work is most strongly influenced by mechanical considerations such as valve and displacer timing and operational considerations such as maximum and minimum cycle pressures. The Bypass apparatus used in this study could have its valve timing modified to increase its cold head PV work and thereby its cooling power, without increasing the maximum and minimum pressure levels.

Chapter 9

Conclusions and Recommendations

9.1 Conclusions

Several new mechanisms for improving the gas liquefaction performance of Gifford-McMahon (GM) and active magnetic regenerative (AMR) cryocoolers were demonstrated using both theoretical and experimental studies. Specifically designing for unbalanced regenerative operation as a means of improving overall liquefaction capacity, which is counter to conventional wisdom, was proved viable both in concept and implementation. These results are extensible and applicable to any refrigeration device employing thermal regenerators when the desired application is gas liquefaction. Each mechanism to improve performance will be summarized in turn.

9.1.1 Theoretical Studies

The theoretical studies can be grouped into two sub-categories describing improvements to the liquefaction performance through consideration of the thermal processes external and fluid and thermal processes internal to the regenerator of the refrigeration device. First, it was demonstrated that for a liquefaction application, a significant reduction in the input power per unit mass liquefied, or equivalently, a significant increase in the liquefaction capacity for equal input power, can be achieved by providing a sensible cooling component in addition to the usual latent cooling component available from a device operating as a refrigerator. That is, an improvement in capacity is available by modifying the refrigeration device to more closely approximate an ideal liquefier than an ideal refrigerator.

The degree of improvement is a function of the specific choice of gas and liquefaction conditions selected, but generally increases as the liquefaction temperature decreases. For the liquefaction of cryogenic gases, the potential improvement in the liquefaction process employing pre-cooling is sufficiently large that it can more than compensate for decreased efficiency of the refrigeration device itself due to any changes required to provide the sensible cooling stream. For GM and AMR systems, a sensible cooling capacity can be provided by operating the regenerator as an asymmetrical and unbalanced regenerator by diverting a portion of the hot blow exit stream to an external counterflow heat exchanger. The diverted flow is termed in this work as "bypass" flow.

For an AMR system, theoretical studies for the liquefaction of ethane at 225 K revealed that bypass flow maximized the liquefaction capacity when the sensible and latent cooling requirements were both closely met. A moderate excess of either latent or sensible capacity still provided increased liquefaction capacity due to the strong impact on capacity provided by the sensible component.

Second, the investigation of the processes internal to the regenerator considered the thermal processes within the AMR regenerator and the flow distribution within both GM and rotary AMR regenerators. For an AMR system, the theoretical studies of the liquefaction of ethane at 225 K revealed that increasing percent bypass flow allowed an increase in the total refrigeration capacity to a maximum value. The optimal bypass maximizing total refrigeration was determined to also be a function of the magnetic field strength. The total refrigeration capacity was defined as the sum of the ideal conversion of the sensible cooling stream flow exergy to cooling at 225 K plus the latent cooling capacity at 225 K. The increase in the total refrigeration capacity was achieved through a change in the temperature profile and resultant redistribution of the work input across the magnetic regenerator bed.

For the simulation of the AMR operating with a 4 Tesla field, the optimal bypass flow of 4% resulted in an increase in total refrigeration capacity of 10.4% and an increase in the total refrigeration coefficient of performance of 11.2%. For the liquefaction of ethane at 225 K, a regenerator bypass flow of 1.25% provided the maximum increase in liquefaction capacity and efficiency. At this bypass setting, the total refrigeration capacity increased by 5.7% from internal improvements in the regenerator and by a further 11% from external improvements in the liquefaction process by provision of the pre-cooling stream for an overall improvement in liquefaction capacity by over 17%.

A general analysis of the effect of flow maldistribution was carried out by simulation of uneven distribution of flow over the cross-section of a regenerator. This work extended and enhanced previously derived efforts to describe the effect of maldistribution on regenerator thermal performance and clarified that maldistribution of flow is detrimental for all values of reduced length and reduced period and is not diminishingly important at high reduced length as previously suggested.

The flow distributions for GM, rotary passive, and AMR regenerators were modelled using a commercially available computational fluid dynamics software package, CFX-TASCFlow. For the GM system, simulation of the flow distribution for a conventional design of a 1st-stage regenerator revealed a tendency for the flow to jet and recirculate in the fluid entrance region. Simulations of a modified design employing conical flow distributors over the flow inlet region and a tapered main regenerator eliminated the recirculation and improved the uniformity of flow over the matrix cross-section. The maximum speed in the entrance region of the main regenerator section was reduced from approximately 9.3 times the homogenous plug-flow speed for the conventional regenerator to approximately 2.6 times the homogenous plug-flow speed for the modified regenerator. After the first 20% of the regenerator length, the maximum speed in the conventional regenerator still exceeded 2.5 times the homogenous plug-flow speed, while the modified regenerator displayed essentially homogenous plug-flow after 17% of the regenerator length.

For the AMR and passive rotary regenerator systems, simulation of the flow distribution within the regenerator ring demonstrated that the simplified pseudo-2-dimensional flow representation is a reasonable approximation except near the circumferential boundaries of the inlet and outlet regions. In these regions, for the models studied, the local angular rotation rate varies by approximately ±80% from the expected rotation rate based on perfect entrainment of the fluid within the porous solid. The deviation is caused by the radial flow tending to diverge from inlet regions and converge towards outlet regions.

It was not possible to fully assess the thermal impact of the differences between the flow profiles calculated by the CFD software and the pseudo-2-dimensional flow representation. For the standard release of the CFD software, the coupling between the solid and fluid equations was insufficient to provide a stable convergence to a solution in a reasonable time frame. For the custom release of the CFD software, a rapid and stable solution convergence was observed, but the solutions exhibited a dependency on the grid definition. Extensive examination of the CFD source code did not reveal the cause of the grid dependency, but did reveal several implementation issues which could have a deleterious effect on the accuracy of the solutions to the rotary regenerator and AMR energy balance equations.

Despite difficulties with grid dependency, it was proven that a commercial CFD package could, in principle, be used to solve both the hydrodynamics and thermal energy equations describing the operation of an active magnetic regenerative refrigerator if the solid and fluid energy equations are fully coupled. If there is some question as to the implementation details of a commercial package, then a custom solver which employs some of the same solution algorithms as the CFX-TASCFlow package could provide a rapid means of solving regenerator problems. In particular, the incomplete lower-upper (ILU) factorization procedure converged rapidly to a solution to the energy equations and the solution time was nearly linearly dependent on the number of nodes in the solution grid. It would be necessary to confirm that the grid dependency issues were not a consequence of the solution procedure.

9.1.2 Experimental Studies

Two groups of experimental studies were performed in this work. In the first group, the cooling performance of a modified commercial Gifford-McMahon (GM) refrigerator was examined in single-stage and two-stage operation using a conventional 1st-stage regenerator and a 1st-stage regenerator modified to reduce flow maldistribution according to design guidelines determined in the theoretical studies. For the single-stage studies, the modified regenerator provided a lower no-load minimum temperature across a broad range of operating frequencies. For the two-stage device operation, using the modified regenerator in the first stage provided a lower no-load minimum temperature at the second stage for all cycle operation frequencies, as well as a lower first stage temperature for the majority of cycle frequencies. Using the modified regenerator when loads were applied to the first and second stages provided lower second stage temperatures for the majority of loads tested.

The second group of experimental studies examined the liquefaction capability of a single-stage GM refrigeration system modified to provide adjustable bypass regenerator flow to give a sensible cooling capacity for the liquefaction of cryogenic gases. Three modes of operation were defined as the

Standard GM cycle, the Bypass GM cycle, and the Combined GM cycle, where the cooling loads provided by the system are latent, sensible, and combined latent and sensible loads, respectively.

The largest total refrigeration capacity, defined as the exergy equivalent cooling power at the cold head temperature, was obtained when there was no bypass flow. If cooling at only a single temperature is required, then bypass regenerator flow should not be employed.

When liquefaction of gases is desired, providing a sensible cooling capacity using the bypass flow stream in conjunction with the latent cooling capacity will provide a greater liquefaction capacity than when no sensible cooling component is provided. That is, the Combined GM cycle will provide a greater liquefaction capacity than the Standard GM cycle. For example, it was demonstrated that operation as a Combined GM cycle could liquefy over 50% more deuterium at ~37 K than operation as a Standard GM cycle. In cases where the selected liquefaction temperature is near the critical point of the gas being liquefied, providing only a sensible cooling component will provide a greater liquefaction capacity than when no sensible cooling component is provided. That is, the Bypass GM cycle will provide a greater liquefaction capacity than the Standard GM cycle only when the liquefaction point is near the gas critical point. For example, it was demonstrated that operation as a Bypass GM cycle could liquefy over 20% more neon at ~44.5 K than operation as a Standard GM cycle.

At low values of bypass flow, there is a modest rise in the cold head temperature compared to the no-load minimum temperature. For values of bypass flow on the order of up to 5% of the total flow through the regenerator or 2-3% of the total system flow, there is an almost linear increase in the cold head temperature by about 10 K. Beyond this bypass flow rate, the cold head temperature rises rapidly. As the cold head temperature rises, the average system pressure increases and the total mass flow through the compressor system decreases. Primarily because of the lower compressor flow rate, the Bypass GM system has a lower ideal compressor input power than the Standard GM system for the same cold head temperature.

Operation of the Bypass GM apparatus as a Bypass GM cycle or Combined GM cycle does not noticeably affect the pressure-volume work cycle at the cold head expansion space, except indirectly by the pressure level changes associated with increased cold head temperatures. Based on the pressure-volume diagrams recorded for the cold head expansion space, valve timing optimization could be performed for the test apparatus which would increase the gross PV work of the system.

9.2 Recommendations

9.2.1 Theoretical Studies

Significant progress has been made in the development of numerical models of the hydrodynamics and thermodynamics of rotary passive and active magnetic regenerators and future efforts should be directed towards refining these models. The hydrodynamics models should be enhanced by consideration of the seals and clearance gaps between the rotating regenerator and its housing, as well as any additional radial dividers within the regenerator ring that serve to limit circumferential flow. With these additions, it would be possible to represent a single pressure source driving the heat transfer circulation fluid flow, rather than the independent hot and cold blow sources represented in this work.

The thermal models should be enhanced by ensuring that the discretization formulation is conservative and thermodynamically consistent with respect to the implementation of solid advection and magnetocaloric terms for all grids employed. For rotary regenerators, this could include representation on a polar rather than Cartesian grid, and directly evaluated material properties at the control volume boundaries rather than interpolated values. The latter criterion would require that magnetic material physical property values be evaluated from values of the independent variables, i.e., temperature and magnetic field, interpolated to the control volume boundaries, rather than control volume average material property values interpolated to the boundaries.

The ILU solution algorithm rapidly solved the regenerator energy equations and scaled approximately linearly with the number of nodes employed in the discretization. This is a substantial improvement compared to LU decomposition which scales as the square of the circumferential size and the cube of the radial size. Development of a theoretical proof that the ILU procedure is valid for the regenerator energy equations should be undertaken to prove that the procedure was not responsible for the observed grid dependency of the thermal solutions. If the ILU solution algorithm validity is established, it should be strongly considered for use in future regenerator studies.

With minor modifications to the boundary condition pre-processor, it would be possible for the custom TASCFlow CFD code to simulate the fully dynamic processes of the operation of a GM regenerator including the full hydrodynamics and thermal energy equations. Cooldown to the minimum temperature and attainment of pseudo-steady-state operation would require simulation of many thermal cycles. Currently, a single ordinary personal computer or workstation would not be capable of performing the simulation rapidly enough for useful design purposes. Several personal computers or workstations, if networked together to tackle the problem cooperatively, would be capable of performing this simulation sufficiently rapidly to be useful as a design tool. If the current trends in the improvement of computer performance continue, such a simulation would be straightforward in the next few years on a single computer. Development of this design tool should be considered.

The concept of bypass flow regenerative cooling cycles for the liquefaction of gases is not limited to cryogenic temperatures or to GM and AMR systems. Benefits of increased capacity or reduced input power requirements are possible for other regenerative cycles. Some of these cycles might exhibit a synergystic effect similar to that observed for the AMR cycle, where the gain in performance due to the external sensible cooling is enhanced by an additional improvement in the regenerator and/or compressor input power requirements of the refrigeration device. Use of bypass flow for these various cycles should be explored, as it may provide a more cost-effective solution to improving liquefier performance than the construction of multiple cooling stages.

9.2.2 Experimental Studies

Studies of the performance of the GM system using a conventional and a modified 1st-stage regenerator showed that the modified design provided superior cooling performance across a wide range of operating conditions for single and two-stage operation. It was not explicitly shown that the observed performance improvements were directly attributable to the improved flow distribution demonstrated in the theoretical simulations. Further studies should directly measure the flow distribution within both the conventional and modified regenerators. Using a single regenerator material for both designs, the thermal performance should be compared and any correlation with the flow maldistribution be determined. These tests would most likely be performed as standalone experiments outside the GM test apparatus.

Without direct measurements of input power and mass flow, it was not determined whether a Bypass GM or Combined GM system experiences improvements in the regenerator internal processes as a result of lower total mass flow and lower void volume losses. There may be an optimal bypass flow to develop a temperature profile which minimizes the sum of the pressure losses from filling the void volume due to a higher average regenerator temperature and the thermal losses from the unbalanced regenerative operation. The complex nature of the GM cycle would likely preclude simulation of these effects with current models and instead direct experimental measurement could be employed.

The Bypass GM apparatus simulated the liquefaction process by the use of electrical heaters. It would be prudent to confirm the increased liquefaction capacity of the Bypass GM and Combined GM cycles compared to the Standard GM cycle by directly employing a process gas to provide the sensible and latent cooling loads. This could be achieved with the current apparatus with modifications to add the necessary process heat exchangers, reservoir for the liquid produced, and flow meters to measure the liquefaction rate. It may be necessary to increase the cold buffer volume to reduce the pressure oscillations at the higher flow rates to achieve the maximum possible efficiency of the bypass flow heat exchanger.

The Bypass GM apparatus employed a simple check valve to achieve the DC bypass flow. This allowed relatively warm, unexpanded gas to enter the cold buffer volume. It should be possible to achieve a lower temperature in the cold buffer volume by the use of an active valve. Additionally, it would be possible for some operating conditions to use an isenthalpic expansion from the cold buffer volume to lower the bypass stream temperature, limited only by the inversion temperature of the GM working fluid and the compressor return line pressure. Last, maintaining the simplicity of the check valve, the bypass gas flow could be cooled to the cold head temperature by heat exchange with the cold head itself. This would not increase the efficiency of a liquefaction process, but would provide a colder bypass stream which could be important for an external process requiring only a sensible cooling load, for example.

Applications for the bypass flow arrangement extend beyond the liquefaction of cryogenic gases to such uses as: thermal radiation shields continuously cooled from room to cryogenic temperatures, active cooling along the length of structures penetrating to cryogenic temperatures, simplified thermal control of material characterization experiments, and active cooling along the length of otherwise undersized current leads during charging/discharging of cryogen-free superconducting magnets. It may also be possible to extend the bypass concept in a GM-like or other regenerative system to gas purification by preferentially freezing out or adsorbing impurities and removing a purified bypass gas stream. Consideration of the benefits of the systems presented here applied to existing systems could yield substantial design breakthroughs.

References

1. Rogner, H.-H., "Natural gas as the fuel of the future", Annual Review of Energy, 14, (1989) pp. 14-73.

2. Intergovernmental Panel on Climate Change (IPPC) (1990), "Climate Change : the IPCC scientific assessment", Cambridge University Press, New York, 1990.

3. Scott, D.S., W. Häfele, "The coming hydrogen age: Preventing world climatic disruption", International Journal of Hydrogen Energy, 15 pp. 727-737.

4. Lee, T.H., H.R. Linden, D.A. Dreyfus, T. Vasko, *The Methane Age*, Kluwer Academic Publishers & IIASA, Dordrecht (1988).

5. Costs, Inpacts, and Benefits of CO_2 Mitigation, Y. Kaya, N. Nakicenovic, W.D. Nordhaus, F.L. Toth, ed., Proceedings of a workshop at IIASA, Laxenburg, Austria (1992).

6. Barclay, J.A., "Prospects for Magnetic Liquefaction of Hydrogen," Proceedings of the 18th International Congress of Refrigeration, Montreal (1991).

7. Petsinger, R.E., "Natural gas quality in North America," Proceedings of Gaseous Fuels for Transportation Conference, Vancouver (1986) pp. 529-571.

8. Buschow, K.H.J., Olijhoek, J.F., and Miedema, A.R., "Extremely Large Heat Capacities between 4 and 10K", *Cryogenics*, 15 (1975) pp. 261-264.

9. Inaguchi, T., Nagao, M., and Yoshimura, H., "Two-stage Gifford-McMahon Cycle Cryocooler Operating at about 2K," Proceedings of the Sixth International Cryocoolers Conference, II:25 (1990).

10. Kuriyama, T., Hakamada, R., Nakagome, H., Tokai, Y., Sahashi, M., Li, R., Yoshida, O., Matsumoto, K., and Hashimoto, T., "High Efficient Two-stage GM Refrigerator with Magnetic Material in the Liquid Helium Temperature Region," Advances in Cryogenic Engineering, 35, Plenum Press, N.Y. (1990).

11. Merida, W.R., and Barclay, J.A. "Monolithic Regenerator Technology for Low Temperature (4 K) Gifford-McMahon Cryocoolers," Advances in Cryogenic Engineering, 43, Plenum Press, N.Y., (1998).

12. Yaron, R., Shokralla, S., Yuan, J., Bradley, P.E., and Radebaugh, R., "Etched Foil Regenerator," Advances in Cryogenic Engineering, 41, Plenum Press, N.Y., (1996).

13. Tsotsas, E., and Martin, H., "Thermal Conductivity of Packed Beds: A Review," Chemical Engineering Processing, 22, (1987).

14. Edwards, M.F., and Richardson, J.F., "Gas dispersion in packed beds", Chemical Engineering Science, 23 (1968).

15. Vortmeyer, D., and Adam, W., "Steady-state measurements and analytical correlations of axial effective thermal conductivities in packed beds at low gas flow rates", International Journal of Heat and Mass Transfer, 27, (1984).

16. Duncan, A.B., G.P. Peterson, L.S. Fletcher, "Effective thermal conductivity within packed beds of spherical particles", ASME Publication HTD 104, Pt. 3 (1988).

17. Walker, G., "Heat Exchangers in Cryocoolers," in *Cryocoolers: Part 2: Applications*, Plenum Press, New York (1983).

18. Schmidt, F.W. and J. John Willmott, *Thermal Energy Storage and Regeneration*, Hemisphere Publishing Corporation, Washington D.C. (1981).

19. Hausen, H., *Heat Transfer in Counterflow, Parallel Flow and Cross Flow*, McGraw-Hill, New York, (1983).

20. Kutchey, J.A., and Julien, H.L., "The Measured Influence of Flow Distribution on Regenerator Performance", SAE paper 740164 (1974).

21. Hofmann, E.E., and Kappelmayer, A., "Mathematical Model of a Hot Blast Stove with External Combustion Chamber", Proceedings of the Conference on Mathematical Methods in Metallurgical Process Development (1970).

22. Schwartz, C.E., and Smith, J.M., "Flow Distribution in Packed Beds", Ind. and Eng. Chem, Perdue University, Lafayette, Ind., 45 (1953).

23. Penney, M.E., "The Modelling and Simulation of Maldistribution in Thermal Regenerators," Doctoral Thesis, The University of York, U.K. (1987).

24. Mitchell, S., "Investigation of the Factors Affecting the Operation of Thermal Regenerators," Doctoral Thesis, The University of Leeds, U.K. (1982).

25. McMahon, H.O., and Gifford, W.E., "A New Low-Temperature Gas Expansion Cycle: Part 1," Advances in Cryogenic Engineering, 5, Plenum Press, N.Y. (1960).

26. Walker, G., "Gifford-McMahon, Solvay, and Postle Cryocoolers," in *Cryocoolers: Part 1: Fundamentals*, Plenum Press, New York (1983).

27. Warburg, E., Ann. Phys. Chem., 13 (1881) p. 141.

28. Weiss, P., and Piccard, A., "On a New Magnetocaloric Effect", C.R. Acad. Sci. (Paris), 166 (1918) p. 352.

29. Debye, P., Ann. Phys. Chem., 81 (1926) p. 1154.

30. Giauque, W.F., J. Amer. Chem Soc., 49 (1927) p. 1864.

31. Giauque, W.F., and MacDougall, D.P., "Attainment of Temprature Below 1 Degree Absolute by Demagnetization of $Gd_2(SO_4)_3 \cdot 8H_2O$," Physics Review, 43 (1933) p. 768.

32. Daunt, J.G., and Heer, C.V. "Addendum: Heat Flow in Metals Below 1 °K and a New Method for Magnetic Cooling," Physical Review, 76 (1949) p. 985.

33. Heer, C.V., Barnes, C.B., and Daunt, J.G., "The Design and Operation of a Magnetic Refrigerator for Maintaining Temperatures below 1 K", Review of Scientific Instruments, 25 (1954) pp. 1088-1098.

34. Benford, S.M., and Brown, G.V., "T-S diagram for Gadolinium Near the Curie Temperature," Journal of Applied Physics, 52, no. 3 (1981) pp. 2110-2112.

35. Steyert, W.A., "Rotating Carnot-Cycle Magnetic Refrigerators for Use Near 2 K", Journal of Applied Physics, 49 (1978) pp. 1227-1231.

36. Barclay, J.A., "Wheel-Type Magnetic Refrigerator", United States Patent #4,408,463 (1983).

37. Lubbock, I., and Bowen, I.G., "The Use of Rotary Heat Regenerators In Gas Turbines," Shell Technical Report No. ICT/5 (1946).

38. Tipler, W., "A Simple Theory of the Heat Regenerator," Shell Technical Report No. ICT/14 (1947).

39. Datskovskii, V.M., "Calculation of Regenerative Heat Exchangers," Teploenergetika, 14 (1967) pp. 88-91.

40. Hausen, H., "Über die Theorie des Wärmeaustausches in Regeneratoren", Z. angew. Math. Mech. 9 (1929).

41. Iliffe, C.E., "Thermal Analysis of the Contra-Flow Regenerative Heat Exchanger," Proc. J. Inst. Mech. Eng., 159 (1948) pp.363-372.

42. Willmott, A.J., and Thomas, R.J., "Analysis of the Long Contra-flow Regenerative Heat Exchanger,"J. Inst. Math. Appl., 14 (1974) pp.267-280.

43. Nahavandi, A.N., and Weinstein, A.S., "A Solution to the Periodic-Flow Regenerative Heat Exchanger Problem," Appl. Sci. Res. A10 (1961) pp.335-348.

44. de Monte, F., "Cyclic Steady Thermal Response of Rapidly Switched Fixed-bed Heat Regenerators in Counterflow," International Journal of Heat and Mass Transfer 42 (1999) pp.2591-2604.

45. Organ, A.J., "Solution of the Classic Thermal Regenerator Problem," Proceedings of the Institute of Mechanical Engineers. 208 No. C3 (1994) pp.187-197.

46. Organ, A.J., "The Wire Mesh Regenerator of the Stirling Cycle Machine," International Journal of Heat and Mass Transfer 37 (1994) pp.2525-2534.

47. Kulakowski, B., and Anielewski, J., "Application of the Closed Methods of Computer Simulation to Non-linear Regenerator Problems", Archiwum Automatykii Telemechaniki, 24 (1979).

48. Lambertson, T.J., "Performance Factors of a Periodic-Flow Heat Exchanger," Trans. ASME, 80 (1958) pp. 586-592.

49. Willmott, A.J., "Digital Computer Simulation of a Thermal Regenerator," International Journal of Heat and Mass Transfer, 7 (1964) pp.1291-1302.

50. Denton, W.H., Robinson, C.H., Tibbs, R.S., "The Heat Transfer and Pressure Loss in Fluid Flow through Randomly Packed Spheres," Harwell Report (UKAEA) AERE-R 4346 (1963).

51. McAdams, W.H., *Heat Transmission*, 3rd Edition, McGraw-Hill, New York (1954).

52. Chang, Zei.-Chi, and Chen, P.H., "Flow Channeling Effect on a Regenerator's Thermal Performance," Cryogenics 38 (1999) pp. 191-196.

53. Jones, J.D. ASME Journal of Engineering for Gas Turbines and Power 111 (1989) pp. 595-600.

54. Kays, W.E., and London, A.L., *Compact Heat Exchangers*, McGraw-Hill Book Company, New York (1964).

55. Hausen, H., "Vervollstandigte Berechnung Des Warmeaustausches In Regeneratoren," Z. Vdi-Deiheft Verahrenstechnik, 2(1942) pp. 31-43.

56. Kern, J., "On the Average Transfer Coefficient in Periodic Heat Exchange -I," International Journal of Heat and Mass Transfer, 19 (1976) pp. 869-878 .

57. Yang, L., Zhou, Y., and Liang, J., "DC Flow Analysis and Second Orifice Version Pulse Tube Refrigerator," Cyrogenics 39 (1999) pp. 187-192.

58. Wang, C., Thummes, G., and Heiden, C., "Control of DC Gas Flow in a Single-stage Double Inlet Pulse Tube Cooler," Cyrogenics 38 (1998) pp. 843-847.

59. Wang, C., "Numerical Analysis of 4 K Pulse Tube Coolers. Part I: Numerical Simulation," Cyrogenics 37 (1997) pp. 207-214.

60. Wang, C., Thummes, G., and Heiden, C., "Effects of DC Gas Flow on Performance of Two-stage 4 K Pulse Tube Coolers," Cyrogenics 38 (1998) pp. 689-695.

61. Smith Jr., J.L., and Nellis, G.F., "Investigation of a Magnetically Augmented Cryogenic Refrigerator," Advances in Cryogenic Engineering, 43 (1998) pp. 1767-1774.

62. Nellis, G.F., and Smith Jr., J.L., "An Experimental GM/Magnetic Refrigerator," Proceedings of the Eighth International Cryocoolers Conference, Plenum Press, New York (1995) pp. 647-656.

63. Gschneidner Jr., K.A., Pecharsky, V.K., and Gailloux, M., "New Ternary Magnetic Lanthanide Regenerator Materials for the Low-Temperature Stage of a Gifford-McMahon (G-M) Cryocooler," Proceedings of the Eighth International Cryocoolers Conference, Plenum Press, New York (1995) pp. 685-694.

64. Hashimoto, T., Nakane, H., Tsukagoshi, T., and Nakagome, H., "Recent Progress in the Application of Magnetic Regenerator Materials," Advances in Cryogenic Engineering 43 (1998) pp. 1541-1547.

65. Hashimoto, T., Tsukagoshi, T., Nitta, H., Yabuki, M., Kuriyama, T., and Nakagome, H., "Excellent Character of Multi-Layer Type Magnetic Regenerator Near 4.2 K," Proceedings of the Eighth International Cryocooler Conference, Plenum Press, New York (1995) pp. 677-683.

66. Lang, A., Häfner, H.-U., and Heiden, C., "Systematic Investigations of Regenerators for 4.2 K-Refrigerators," Advances in Cryogenic Engineering 43 (1998) pp. 1573-1580.

67. Chafe, J.N., and Green, G.F., "Neodymium-Ribbon-Regenerator Cooling Performance in a Two-Stage Gifford-McMahon Refrigerator," Advances in Cryogenic Engineering 43 (1998) pp. 1589-1596.

68. Chafe, J., Green, G., and Hendricks, J., "A Neodymium Plate Regenerator for Low-Temperature Gifford-McMahon Refrigerators," Proceedings of the Ninth International Cryocoolers Conference, Plenum Press, New York (1997).

69. Chafe, J.N., and Green, G.F., "Performance of a Low-Temperature Gifford-McMahon Refrigerator Utilizing a Neodymium Disk Regenerator," Advances in Cryogenic Engineering 43 (1998) pp. 1783-1790.

70. Yaron, R., Shokralla, S., Yuan, J., Bradley, P.E., and Radebaugh, R., "Etched Foil Regenerator," Advances in Cryogenic Engineering 41 (1996) pp. 1339-1346.

71. Li, R., Onishi, A., Satoh, T., and Kanazawa, Y., "Influence of Valve Open Timing and Interval on Performance of 4 K Gifford-McMahon Cycle Cryocooler," Advances in Cryogenic Engineering, 41 (1996) pp. 1601-1607.

72. Inaguchi, T., Nagao, M., Naka, K., and Yoshimura, H., "Effects of Thermal Conductance in the Cooling Stage of a 4K-GM Refrigerator on Refrigeration Capacity," Advances in Cryogenic Engineering, 43, Plenum Press, N.Y. (1998) pp.1807-1814.

73. Wang, L., Xu, X.D., and Zhang, L., "A Numerical Simulation Method of a Two-stage G-M Refrigerator and Comparison with Experiment," Advances in Cryogenic Engineering 43 (1998) pp. 1799-1806.

74. Gschneidner Jr., K.A., Pecharsky, V.K., Pecharsky, A.O., and Zimm, C.B., "Recent Developments in Magnetic Refrigeration," Materials Science Forum 315-317, (1999) pp. 69-76.

75. Giguère, A., Foldeaki, M., Ravi Gopal, B., Chahine, R., Bose, T.K., Frydman, A., and Barclay, J.A., "Direct Measurement of the "Giant" Adiabatic Temperature Change in $Gd_5Si_2Ge_2$,", Physical Review Letters, 83 No. 11, (1999) pp. 2262-2265.

76. Pecharsky, V.K., and Gschneidner Jr., K.A., "Magnetocaloric Effect and Magnetic Refrigeration," Journal of Magnetism and Magnetic Materials 200 (1999) pp. 44-56.

77. DeGregoria, A.J., "Modeling the Active Magnetic Regenerator," Advances in Cryogenic Engineering 37 (1992) pp. 867-873.

78. Schuricht, S.R., DeGregoria, A.J., and Zimm, C.B., "The Effects of a Layered Bed on Active Magnetic Regenerator Performance," Proceedings of the Seventh International Cryocooler Conference, Plenum Press, New York (1993) pp. 614-620.

79. Zhang, L. Sherif, S.A., Veziroglu, T.N., and Sheffield, J.W., "Performance Analysis of Reciprocating Magnetic Liquefiers", International Journal of Hydrogen Energy, 19, (1994) pp. 945-956.

80. Zhang, L. Sherif, S.A., Veziroglu, T.N., and Sheffield, J.W., "On Exergy Losses in AMR Hydrogen Liquefiers", International Journal of Hydrogen Energy, 19, (1994) pp. 447-452.

81. Green G.F., Patton, G., Stevens, J., Humphrey, J., "Magnetocaloric Refrigeration." David Taylor Naval Ship Research and Development Center Report DTNSRDC 87/032 (1987).

82. Hurwitz, M.M., "Additions to the NASTRAN User's Manual and Theoretical Manual for a Thermostructual Capability for NASTRAN Using Isoparametric Finite Elements." DTNSRDC Report CMC-1-73 (1973).

83. Green G.F., and Schroeder, E., "A Finite Element Model of an Experimental Magnetocaloric Refrigerator." Proceedings of the Fifth International Cryocooler Conference, Monterey California (1988) pp.70-80.

84. Schroeder, E., and Green G.F., "Performance Predictions of a Magnetocaloric Refrigerator Using a Finite Element Model." Advances in Cryogenic Engineering, 35 (1990) pp. 1149-1155.

85. Carpetis, C., "An Assessment of Efficiency and Refrigeration Power of Magnetic Refrigerators with Ferromagnetic Refrigerants." Advances in Cryogenic Engineering, 39 (1994) pp. 1407-1415.

86. Spearing, I.G., "A Numerical Model for a Rotary Active Magnetic Regenerative Refrigerator." M.A.Sc. Thesis, University of Victoria, Victoria, B.C., Canada (1994).

87. Crunkleton, J.A., "A New Configuration for Small-Capacity, Liquid-Helium-Temperaure Cryocoolers." Proceedings of the Seventh International Cryocooler Conference, Plenum Press, New York (1993) pp. 187-196.

88. Liepert, A.G., and Crunkleton, J.A., "Application of Boreas Cryocoolers." Proceedings of the Eighth International Cryocooler Conference, Plenum Press, New York (1995) pp. 835-843.

89. DeGregoria, A.J., Zimm, C.R., Janda, D.J., Lubasz, R.A., Jastrab, A.G., Johnson, J.W., and Ludeman, E.M., "Active Magnetic Regenerator Method and Apparatus." United States Patent #5,249,424 (1993).

90. Zimm, C.R., Astronautics Corporation of America, Madison, Wisconsin, United States of America, Private Communication, February 2001.

91. CFX-TASCFlow, AEA Technology Engineering Software Ltd., 554 Parkside Drive, Waterloo, Ontario, Canada, N2L 5Z4.

92. Wysokinski, T.W., Spearing, I.G., Reedeker, P.G., and Barclay, J.A., "Improvement in the Second-stage Cooling Power of a Two-stage GM Refrigerator through Modification of the First-stage Regenerator." Advances in Cryogenic Engineering, 45, Plenum Press, N.Y., (2000).

93. Kuriyama, T., "Technological Research on GM Refrigerators Employing Magnetic Regenerator Materials," (English translation) Doctoral Thesis, Tokyo Engineering University (1994).

94. Bejan, A., *Advanced Engineering Thermodynamics*, John Wiley & Sons, New York (1988).

95. Timmerhaus, K.D., and Flynn, T.M., *Cryogenic Process Engineering*, Plenum Press, New York (1989).

96. MacDonald, I.F., El_Sayed, M.S., Mow, K., and Dullien, F.A.L., "Flow through Porous Media: The Ergun Equation Revisited," Industrial Engineering Chemistry Fundamentals, 18 (1979) pp. 199-208.

97. Patankar, S.V., *Numerical Heat Transfer and Fluid Flow*, W.J. Minkowycz and E.M. Sparrow, ed., Hemisphere Publishing Corporation, New York (1980).

98. Hall, J.L., "A Contaminant Ice Visualization Experiment in a Glass Pulse Tube," Advances in Cryogenic Engineering, 45, Plenum Press, N.Y. (2000).

99. Kurihara, T., Okamoto, M., Sakitani, K., Torii, H., and Morishita, H., "Numerical and Experimental Study of a 4 K Modified-Solvay Cycle Cryocooler," Advances in Cryogenic Engineering, 43, Plenum Press, N.Y. (1998).

100. National Instruments Corporation, 11500 North Mopac Expressway, Austin, Texas, 78759-3504, United States of America.

Appendix A – GM Regenerator Dimensions

Table A.1 Conventional GM regenerator TASCFlow model dimensions.

Geometric Feature of the Conventional GM Regenerator	**Dimension [Inches]**
Major diameter of screen disks filling the porous screen region	1.745
Length of hot end coarse screen section	0.670
Length of middle fine screen section	2.950
Length of cold end coarse screen section	0.250
Diameter of hot end fill tubes (8 fill tubes evenly spaced in 360°, fully open)	0.170
Length of hot end fill tubes	2.750
Diameter of cold end exit tubes (12 exit tubes evenly spaced in 360°, fully open)	0.125
Cold end exit tubes centerline offset from cold end of screens	0.125

Table A.2 Conical GM regenerator TASCFlow model dimensions.

Geometric Feature of the Conical GM Regenerator	**Dimension [Inches]**
Major diameter of tapered stack of screen disks filling the porous screen region	2.500
Minor diameter of tapered stack of screen disks filling the porous screen region	1.250
Length of hot end coarse screen tapered section	1.008
Length of middle fine screen tapered section	2.334
Length of cold end medium coarse screen straight section	0.750
Major diameter of particle bed	2.500
Length of particle bed adjacent to screen region	0.355
Length of particle bed adjacent to regenerator housing	0.200
Sloping offset of particle bed centerline from minor to major diameter	0.250
Diameter of hot end fill tubes (8 fill tubes evenly spaced in 360°, fully open)	0.156
Length of hot end fill tubes (not including conical distributor sections)	2.214
Major diameter of hot end fill tubes conical distributor (fully open)	0.320
Length of fully open conical distributor	0.060
Major diameter of hot end fill tubes conical distributor (porous coarse screens)	0.500
Length of porous coarse screen conical distributor	0.500
Diameter of cold end exit tubes (16 exit tubes evenly spaced in 360°, fully open)	0.125
Cold end exit tubes centerline offset from bottom of particle bed	0.100

Appendix B – Sample AMR Input File

The following text file is a sample input file for the AMR modelling of balanced and unbalanced active magnetic regenerative liquefiers. A complete description of the AMR model and the parameters given in the input file are described by Spearing [86], with revisions described in this work.

```
Unbalanced AMR model.
6 Flow regions: 2 blow regions, 2 no-flow, 2 no-flow with
relaxation on 3rd-order correction scheme.
Note area/volume is 6*(1-porosity)/dp.
Fluid density set by average fluid temperature.

[start]

[operating parameters]

[T hot] 275
[T cold] 225
[T environment] 300
[mu0Hmax] 5.0
[zero offset angle] 50
[frequency w] 25.132741229
[inner radius] 0.2725
[outer radius] 0.3275
[z thickness] 0.05
[average T density?] 1
[radial row size] 30
[total azimuthal rows] 234
[solver iterations] 9
[T update damping iterations] 0
[T update damping factor] 2.5
[ramp field iterations] 0
[ramp field iteration skip] 1

[flow zone definitions]
[flow zone]
  [flow zone azimuthal rows] 65
  [flow zone name type] coldzone
  [flow zone flow rate] 0.5
  [flow zone flow direction] out2in
[end flow zone]
[flow zone]
  [flow zone azimuthal rows] 48
  [flow zone name type] noflowzone
  [flow zone flow rate] 0.5
  [flow zone flow direction] noflow
[end flow zone]
```

```
[flow zone]
  [flow zone azimuthal rows] 4
  [flow zone name type] noflowzone
  [flow zone flow rate] 0.042
  [flow zone flow direction] noflow2out
[end flow zone]
[flow zone]
  [flow zone azimuthal rows] 65
  [flow zone name type] hotzone
  [flow zone flow rate] 0.485
  [flow zone flow direction] in2out
[end flow zone]
[flow zone]
  [flow zone azimuthal rows] 48
  [flow zone name type] noflowzone
  [flow zone flow rate] 0.485
  [flow zone flow direction] noflow
[end flow zone]
[flow zone]
  [flow zone azimuthal rows] 4
  [flow zone name type] noflowzone
  [flow zone flow rate] 0.042
  [flow zone flow direction] noflow2in
[end flow zone]

[end operating parameters]


[results output]

[Tecplot style output] on
[Output description labels] on
[Scientific format output] off
[Extra precise numbers] off

[Magnetic Field Profile] [start list] end [end list]
[Magnetic Field Derivative Profile] [start list] end [end list]
[Fluid Pressure Profile] [start list] never [end list]
[Solid Temperature Profile] [start list] end [end list]
[Solid Temperature Profile Derivative wrt Theta] [start list] end [end list]
[Fluid Temperature Profile] [start list] end [end list]
[Solid Thermal Conductivity Profile] [start list] never [end list]
[Fluid Radial Modified Thermal Conductivity Profile]
        [start list] never [end list]
[Fluid Azimuthal Modified Thermal Conductivity Profile]
        [start list] never [end list]
[Solid Heat Capacity Profile] [start list] end [end list]
[Solid dM/dT Profile] [start list] end [end list]
[Solid dM/dH Profile] [start list] end [end list]
[Solid Magnetization Profile] [start list] end [end list]
[Solid Electrical Resistivity Profile] [start list] never [end list]
[Fluid Heat Capacity Profile] [start list] never [end list]
[Fluid Thermal Conductivity Profile] [start list] never [end list]
[Fluid Density Profile] [start list] end [end list]
[Fluid Viscosity Profile] [start list] never [end list]
[Fluid Heat Transfer Coefficient] [start list] end [end list]
[Solid Dimensionless Coefficient PI] [start list] end [end list]
[Solid Dimensionless Coefficient ZETA] [start list] never [end list]
[Solid Dimensionless Coefficient RAD_LAMBDA] [start list] never [end list]
[Solid Dimensionless Coefficient AZ_LAMBDA] [start list] never [end list]
[Solid Dimensionless Coefficient OMEGA] [start list] never [end list]
[Fluid Dimensionless Coefficient LAMBDA_F] [start list] never [end list]
[Fluid Dimensionless Coefficient AZ_LAMBDA_F] [start list] never [end list]
[Fluid Dimensionless Coefficient CAP_LAMBDA] [start list] end [end list]
[Fluid Dimensionless Coefficient BETA] [start list] never [end list]
[CHT Entropy Generation per unit volume] [start list] end [end list]
```

```
[Eddy Current Entropy Generation per unit volume]
       [start list] never [end list]
[Solid Conduction Entropy Generation per unit volume]
       [start list] end [end list]
[Fluid Conduction Entropy Generation per unit volume]
       [start list] end [end list]
[Power per unit volume] [start list] end [end list]
[Average Refrigeration Temperature] [start list] after end [end list]
[Average Rejection Temperature] [start list] after end [end list]
[Maximum Solid Temperature Change for Iteration]
       [start list] after [end list]
[Maximum Fluid Temperature Change for Iteration]
       [start list] after [end list]
[Net CHT Entropy Generation] [start list] end [end list]
[Net Eddy Current Entropy Generation] [start list] never [end list]
[Net Solid Conduction Entropy Generation] [start list] end [end list]
[Net Fluid Conduction Entropy Generation] [start list] end [end list]
[Net Motor Power] [start list] after end [end list]
[Net Averaged Qdot Load] [start list] after end [end list]
[Net Averaged Qdot Rejected] [start list] after end [end list]
[Residual] [start list] never [end list]

[end results output]


[layer definitions]

[layer]
[# nodes] 30
[radial conduction on/off] on
[azimuthal conduction on/off] on
[eddy currents on/off] off
[material density] fromfile Properties/Soliddata2 Gadolinium_95_325K
[bed porosity]
  (30) [0.4 #]

[heat transfer area/unit volume]
  (30) [36000 #]

[eddy current shape factor]
  (30)  [1.018591636 #]

[eddy current cross sectional area]
  (30) [7.85398163E-9 #]

[eddy current particle contact fudge factor]
  (30) [1.0 #]

[radial thermal conductivity geometry factor]
  (30) [0.6 #]

[azimuthal thermal conductivity geometry factor]
  (30) [0.6 #]

[thermal conductivity temperature variation function]
  fromfile Properties/Soliddata2 Gadolinium_constprops2 linear

[electrial resistivity temperature variation function]
  fromfile Properties/Soliddata2 Gadolinium_constprops2 linear

[heat capacity group]
 fromfile Properties/Gd_multi_2 Gadolinium CHmultitable

[radial fluid conduction modifiers]
   [flow zone] immediate adjust4Re_particles
      [particle diameters] (30) [100e-6 #] [end flow zone]
```

```
   [flow zone] immediate adjust4porosity [end flow zone]
   [flow zone] immediate adjust4porosity [end flow zone]
   [flow zone] immediate adjust4Re_particles
       [particle diameters] (30) [100e-6 #] [end flow zone]
   [flow zone] immediate adjust4porosity [end flow zone]
   [flow zone] immediate adjust4porosity [end flow zone]
[azimuthal fluid conduction modifiers]
   [flow zone] immediate adjust4Re_particles
      [particle diameters] (30) [100e-6 #] [end flow zone]
   [flow zone] immediate adjust4porosity [end flow zone]
   [flow zone] immediate adjust4porosity [end flow zone]
   [flow zone] immediate adjust4Re_particles
     [particle diameters] (30) [100e-6 #] [end flow zone]
   [flow zone] immediate adjust4porosity [end flow zone]
   [flow zone] immediate adjust4porosity [end flow zone]

[heat transfer correlations]
   [flow zone] immediate Timmerhaus_and_Flynn_particles
    [particle diameters] (30) [100e-6 #] [end flow zone]
   [flow zone] immediate No_flow_particles_Nu=2
    [particle diameters] (30) [100e-6 #] [end flow zone]
   [flow zone] immediate No_flow_particles_Nu=2
    [particle diameters] (30) [100e-6 #] [end flow zone]
   [flow zone] immediate Timmerhaus_and_Flynn_particles
    [particle diameters] (30) [100e-6 #] [end flow zone]
   [flow zone] immediate No_flow_particles_Nu=2
    [particle diameters] (30) [100e-6 #] [end flow zone]
   [flow zone] immediate No_flow_particles_Nu=2
    [particle diameters] (30) [100e-6 #] [end flow zone]

[end layer]
[end layer definitions]

[fluid properties functions]
  fromfile Properties/mixedfluidcombos
  Helium_50_atm mixed linear_mix_7
[end fluid properties functions]

[magnetic field profile]
  fromfile Field/Smooth2 smooth7_flat
[end magnetic field profile]

[initial solid temperature profile]
fromfile TProfiles/PhDMag3H5.txt solid_ubal480
[end initial solid temperature profile]

[initial fluid temperature profile]
fromfile TProfiles/PhDMag3H5.txt fluid_ubal480
[end initial fluid temperature profile]

[end]
```

Appendix C – Magnetic Field Profile

The following FORTRAN source code produces a smoothed pulse-shaped magnetic field profile suitable for use in magnetic regenerator studies and employed within the TASCFlow AMR modelling efforts of this work. The field closely approximates the magnetic field profile described by Spearing [86]. Input and output ranges and scaling parameters are described in the comments within the code.

```
*-------------------------------------------------------------------*
      DOUBLE PRECISION FUNCTION EVALCRATL(order, x, c)
*-------------------------------------------------------------------*
      DOUBLE PRECISION x,c(*)
      INTEGER order,i,j,k
      DOUBLE PRECISION xs,n,d,tmp,t2,t1
***** Maximum value is slightly greater than 1.0 without additional scaling.
      DOUBLE PRECISION maxtol/1.00000296736029D0/

      xs=2.0D0*x-1.0D0
      i=order-1
      j=order
      t2=0.0
      t1=0.0
      DO 10 k=i+1,3,-2
        tmp=t1
        t1=2*xs*t1-t2+c(k)
        t2=tmp
 10   CONTINUE
      n=xs*t1-t2+c(1)
      t2=0.0
      t1=0.0
      DO 20 k=j+1,2,-2
        tmp=t1
        t1=2*xs*t1-t2+c(k)
        t2=tmp
 20   CONTINUE
      d=xs*t1-t2+1.0
      IF (d.EQ.0.0) THEN
        EVALCRATL=0.0
      ELSE
        EVALCRATL=n/d/maxtol
      ENDIF
      END
```

```
*------------------------------------------------------------------*
      SUBROUTINE FIELD(xinput,fldscl,dsscal,mag,dmag)
*------------------------------------------------------------------*
***** TableCurve Z:\Amrr\Field\field.f Nov, 1998
***** X= position[valid input from -1 to 1, with peak Y at x=0]
***** Y= field(X)[minimum, and non-zero at -1 and +1]
***** Eqn# 7617  Chebyshev Rational Order 8/9
***** xinput: position, from -1 to 1
***** fldscl: field scaling factor, set to max desired field
***** dsscal: derivative scaling factor, set to 2/(2pi) for rotary bed
*****   set to 2/L for linear bed, L=periodic boundary separation
*****   set to 2/(total cycle time) for transient field on static bed
***** mag:  the scaled magnetic field value at xinput
***** dmag: the scaled magnetic field derivative at xinput
***** NOTE:  NO RANGE ERROR CHECKING ON INPUT IS PERFORMED!*---------------------
-------------------------------------*
      DOUBLE PRECISION c
      DIMENSION c(17+1)
      DATA c(1)/0.6815201834445811D0/
      DATA c(2)/-0.6834904625518209D0/
      DATA c(3)/-1.252191296704689D0/
      DATA c(4)/1.399658009719572D0/
      DATA c(5)/0.9902428592476984D0/
      DATA c(6)/-0.4149281421552129D0/
      DATA c(7)/-0.6617806193058745D0/
      DATA c(8)/0.5066330735524527D0/
      DATA c(9)/0.3744533894564542D0/
      DATA c(10)/-0.1086475225927118D0/
      DATA c(11)/-0.1731183479003018D0/
      DATA c(12)/0.08977986157531714D0/
      DATA c(13)/0.06328453600695742D0/
      DATA c(14)/-0.008610553490674935D0/
      DATA c(15)/-0.01625443761863863D0/
      DATA c(16)/0.003362406916945943D0/
      DATA c(17)/0.002274335517339419D0/
      DATA c(18)/-1.428670842155079D-05/
***** Uncomment one of the following two lines for double or single
***** precision input/output.  Field is calculated as double precision.
***** and downcast to single precision if input/output is specified
***** as single precision.
      DOUBLE PRECISION xinput, fldscl, dsscal, mag, dmag
C      REAL xinput, fldscl, dsscal, mag, dmag
      DOUBLE PRECISION x, xm1, xp1, y, F1, F2
      DOUBLE PRECISION TINY/1.0D-4/
      DOUBLE PRECISION TINY2/2.0D-4/
      DOUBLE PRECISION EVALCRATL

      x=abs(xinput)
      xm1=x-TINY
      xp1=x+TINY

      y=EVALCRATL(17,x,c)
      mag=y*fldscl
      F1=EVALCRATL(17,xm1,c)
      F2=EVALCRATL(17,xp1,c)
      dmag=(F2-F1)/TINY2*(fldscl*dsscal)*SIGN(1.0D0,xinput)
      RETURN
      END
```

Appendix D – Charge Amplifier Circuit

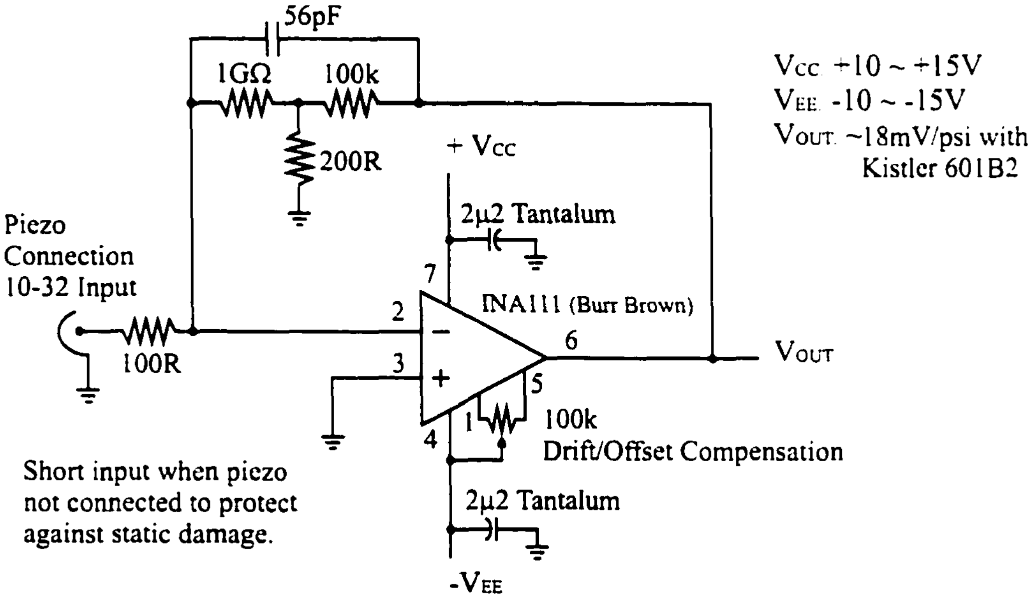

Figure D.1 Custom high impedance charge amplifier circuit used with the Kistler 601B2 piezoelectric pressure transducer.

Appendix E – Bypass GM Components

Table E.1 Bypass GM Apparatus component specifications.

Key	Name	Device
T_{CH}	Cold Head Temperature	Scientific Instruments PRT DIN43760
T_B	Buffer Exit (Heater Entrance) Temperature	Scientific Instruments PRT DIN43760
T_H	Heater Exit Temperature	Scientific Instruments PRT DIN43760
P_B	Cold Buffer Volume Pressure	Omega Instruments PX-613
P_R	Low Pressure Return Line Pressure	Omega Instruments PX-613
P_{CH}	Cold Head Pressure Transducer	Kistler 601B2 Piezoelectric Transducer

Key	Name	Device
	Hall Probe	Lakeshore Cryotronics HGT 2100 Hall Generator
	Bypass Mass Flow Meter	MKS 558A-250
	GM Return Mass Flow Meter	Hastings MFM-200
	Compressor	Leybold UCC 110S
	Bypass Heater (version 1)	Fibreglass-wrapped 28 gage Ni-Cr wire wrapped around 1/4" diameter, 0.028" wall stainless tubing, 2.75 m active length, 1.2 kW max
	Bypass Heater (version 2)	2 parallel lines of 1/8" diameter, 0.028" wall stainless tubing wrapped around and soldered to two 3/4" diameter cartridge heaters, 3.5 m active length, 160 W max
	Cold Head Heater	Omega band heater, 900 W max
	Cold Head Check Valve	Generant CV-250SS-T-3, sealing surfaces polished with 15 micron diamond suspension
	Bypass Metering Valve	Hoke Mille-Mite 1315G4B
	Bypass Metering Safety Valve	Swagelok
	Warm Buffer Bleed Valve	Hoke 3812G6B Needle Valve
	Warm Buffer Shut-Off Valve	1" Ball Valve
	Warm Buffer	7.87 L, 2000 psi compressed gas bottle